

VECTOR CONTROL OF INDUCTION MACHINES USING IMPROVED MACHINE MODELS

MATIJA SOKOLA

**A thesis submitted in partial fulfilment of the requirements of Liverpool John Moores
University for the degree Doctor of Philosophy**

April 1998

ABSTRACT

Basic principles of vector control, introduced in the early Seventies, showed that decoupled control of flux and torque can be theoretically achieved in AC machines. Since then, vector controlled induction machines have become standard means for realisation of high performance AC drives, where very fast and accurate position, speed and torque responses are required. Vector controllers are based on mathematical models that simplify some and totally neglect other phenomena in the complex physical structure of the induction machine. This approach enables design of relatively simple controllers, but at the same time this is a source of detuned operation, that results in performance deterioration.

Objectives of this project are to investigate detuning in the rotor-flux-oriented induction machine drives, to develop improved vector controllers, which compensate this detuning, and to perform experimental investigation that confirms some of the theoretical findings.

A detailed investigation to quantitatively assess detuning in the vector-controlled drive is undertaken. Four detuning phenomena are analysed: main flux saturation, iron loss, variations in the rotor resistance due to temperature effects, and variations in the rotor leakage inductance. Several sets of expressions that describe detuning due to different phenomena are derived, for both torque mode and speed mode of operation. Consequent analytical and simulation studies show that main flux saturation, iron loss and temperature effects can lead to significant detuning.

Several improved induction machine models are further developed and used as a basis for design of several improved vector controllers. The idea is to qualitatively improve two controller parts. The first part is the rotor flux estimator, which is designed to provide open-loop compensation for main flux saturation and for iron loss. The second part is the rotor resistance identifier, which enables closed-loop compensation of thermally induced changes in the rotor resistance. The new identifier obtains some information from the improved estimator and hence accounts for steady-state main flux saturation and for iron loss. Significant reduction in detuning can be achieved when an improved vector controller is employed, as validated by analytical studies and digital simulations. The improved performance of the controller that encompasses the novel rotor resistance identification scheme, is confirmed by simulation studies.

Improved controllers need additional information about the motor they are driving. Hence a novel method for identification of the inverse magnetising curve is developed. The method utilises the same inverter and controller that are employed during normal operation of the drive. Results of analytical studies of detuning effects are confirmed by experiments.

ACKNOWLEDGEMENTS

I would like to sincerely thank my Director of studies, Dr. Emil Levi, for brilliant guidance and lot of patience he showed throughout this project. Many thanks also go to the second supervisor, Prof. David Williams, for invaluable advice.

I would also like to acknowledge the assistance and encouragement provided by all the members of the staff and research colleagues in the School of Engineering (formerly School of Electrical Engineering, Electronics and Physics).

Experimental investigations presented in this study were possible due to unselfish help of Dr. Slobodan Vukosavic from University of Belgrade.

I am also very indebted to Prof. Vladan Vuckovic, from University of Belgrade, and Dr. Radisa Jevremovic, from University of Novi Sad, for getting me into research in the first place.

The moral support and encouragement of my dear friend Mrs. Vesna Levi was crucial at certain stages of the project.

Finally, I could not have managed without continuous support of my wife Zorica.

CONTENTS

ABSTRACT	I
ACKNOWLEDGEMENTS	II
CONTENTS	III
LIST OF FIGURES	XI
NOMENCLATURE	XIX
LIST OF ABBREVIATIONS	XXI
1. INTRODUCTION	1
1.1. A HISTORICAL OVERVIEW OF VECTOR CONTROL OF INDUCTION MACHINES	1
1.2. PROBLEMS EXPERIENCED WITH VECTOR CONTROL OF INDUCTION MACHINES	7
1.2.1. Sources of detuning	7
1.2.2. Approaches to compensation	12
1.3. AIMS OF THE RESEARCH	14
1.3.1. Research objectives	14
1.3.2. Investigation approaches	16
1.3.3. Originality of the research	17
1.4. THESIS OUTLINE	18
2. LITERATURE REVIEW	21
2.1. INTRODUCTION	21
2.2. MATHEMATICAL MODELLING OF AN INDUCTION MACHINE	22
2.2.1. Mathematical model of an induction machine in the three-phase domain	22
2.2.2. Transformation procedure	24
2.2.3. The constant parameter model in a two-phase common reference frame	26
2.2.4. The equivalent circuit for the constant parameter model	29
2.2.5. The i_s - ψ_r mixed current-flux constant parameter model	30
2.2.6. The i_s - ψ_r reduced-order constant parameter model	32

2.3. PRINCIPLES OF VECTOR CONTROL	33
2.3.1. Rotor flux orientation constraints	35
2.3.2. Rotor-flux-oriented control of a current-fed induction machine	36
2.3.2.1. Rotor-flux-oriented constant parameter model of a current-fed induction machine	36
2.3.2.2. Feedback rotor-flux-oriented control of a current-fed machine	37
2.3.2.3. Feed-forward rotor-flux-oriented control of a current-fed machine	39
2.3.3. Rotor-flux-oriented control of a voltage-fed induction machine	39
2.3.4. Other possibilities of orientation	42
2.4. DETUNING IN VECTOR-CONTROLLED INDUCTION MACHINES	44
2.4.1. Consequences of detuning	44
2.4.2. Detuning due to main flux saturation	46
2.4.3. Detuning due to iron loss	49
2.4.4. Detuning due to changes in the rotor time constant (in the rotor resistance)	50
2.4.5. Detuning due to changes in the rotor leakage inductance	55
2.5. REVIEW OF IMPROVED MATHEMATICAL MODELS AND IMPROVED VECTOR CONTROLLERS	56
2.5.1. Mathematical models and estimators with main flux saturation	56
2.5.1.1. The general model with main flux saturation	57
2.5.1.2. The equivalent circuit with main flux saturation	58
2.5.1.3. The i_s - $\underline{\psi}_r$ mixed current-flux model with main flux saturation	59
2.5.1.4. The $\underline{\psi}_m$ - $\underline{\psi}_r$ flux model with main flux saturation	60
2.5.1.5. The $\underline{\psi}_m$ - $\underline{\psi}_r$ reduced-order model with main flux saturation	61
2.5.1.6. The $\underline{\psi}_m$ - $\underline{\psi}_r$ rotor-flux-oriented model with main flux saturation and improved estimators, $i_m(\psi_m)$ representation	62
2.5.2. Mathematical models with iron loss	64
2.5.2.1. The general model with iron loss represented by a resistance placed in parallel with the magnetising branch	65
2.5.2.2. The equivalent circuit with iron loss represented by a resistance placed in parallel with the magnetising branch	65
2.5.2.3. The i_s - i_m - $\underline{\psi}_r$ reduced-order model with iron loss represented by a resistance placed in parallel with the magnetising branch	66
2.5.2.4. The i_s - i_m - $\underline{\psi}_r$ rotor-flux-oriented model with iron loss represented by a resistance placed in parallel with the magnetising branch and improved feed-forward vector controller	67

2.5.2.5. The general model with iron loss represented by a resistance placed after the stator resistance	69
2.5.2.6. The equivalent circuit with iron loss represented by a resistance placed after the stator resistance	69
2.5.3. Rotor resistance and rotor time constant identifiers based on model reference adaptive control theory	70
2.6. SUMMARY.....	73
3. NOVEL IMPROVED MATHEMATICAL MODELS AND ROTOR FLUX ESTIMATORS	74
3.1. INTRODUCTION	74
3.2. NOVEL IMPROVED MODELS AND ESTIMATORS WITH MAIN FLUX SATURATION	74
3.2.1. The $\psi_m - \psi_r$ rotor-flux-oriented model with main flux saturation and improved estimator, $L_m(\psi_m)$ representation	74
3.2.2. The $i_s - \psi_r$ models with main flux saturation and improved estimator, $L_r(\Psi)$ representation	76
3.3. NOVEL IMPROVED MODELS AND ESTIMATORS WITH IRON LOSS ONLY	77
3.3.1. Improved mixed current-flux models with iron loss	78
3.3.1.1. The $i_s - i_m - \psi_r$ mixed current-flux model with iron loss represented by a resistance placed in parallel with the magnetising branch	78
3.3.1.2. The $i_s - \psi_m - \psi_r$ mixed current-flux model with iron loss represented by a resistance placed in parallel with the magnetising branch	79
3.3.1.3. Mixed current-flux models with iron loss represented by a resistance placed after the stator resistance	80
3.3.2. Improved reduced-order models with iron loss	81
3.3.2.1. The $i_s - i_m - \psi_r$ reduced-order model with iron loss represented by a resistance placed in parallel with the magnetising branch	81
3.3.2.2. The $i_s - \psi_m - \psi_r$ reduced-order model with iron loss represented by a resistance placed in parallel with the magnetising branch	82
3.3.2.3. The $i_s - \psi_m - \psi_r$ reduced-order model with iron loss represented by a resistance placed after the stator resistance	83
3.3.3. Improved rotor-flux-oriented models with iron loss	83
3.3.3.1. The $i_s - i_m - \psi_r$ rotor-flux-oriented model with iron loss represented by a resistance placed in parallel with the magnetising branch	84
3.3.3.2. The $i_s - \psi_m - \psi_r$ rotor-flux-oriented model with iron loss represented by a resistance placed in parallel with the magnetising branch	84
3.3.4. Improved estimators with iron loss	85

3.4. NOVEL IMPROVED MODELS AND ESTIMATORS WITH BOTH IRON LOSS AND MAIN FLUX SATURATION	86
3.4.1. The general model with both iron loss and main flux saturation	87
3.4.2. The equivalent circuit with both iron loss and main flux saturation	88
3.4.3. Improved mixed current-flux models with both iron loss and main flux saturation	89
3.4.3.1. The i_s - i_m - ψ_r mixed current-flux model with both iron loss and main flux saturation	89
3.4.3.2. The i_s - ψ_m - ψ_r mixed current-flux model with both iron loss and main flux saturation	90
3.4.4. Improved i_s - ψ_m - ψ_r reduced-order model machine with both iron loss and main flux saturation	91
3.4.5. Improved rotor-flux-oriented models with both iron loss and main flux saturation	92
3.4.6. Improved estimators with both iron loss and main flux saturation	94
3.5. SUMMARY	96
4. DETUNING IN ROTOR-FLUX-ORIENTED INDUCTION MACHINE DRIVES	98
4.1. INTRODUCTION	98
4.2. EXPERIMENTAL IDENTIFICATION OF MACHINE PARAMETERS	98
4.3. CHARACTERISATION OF DETUNING	102
4.4. DETUNING IN STEADY-STATE OPERATION WITH THE CPM-BASED CONTROLLER	103
4.4.1. Steady-state detuning due to rotor resistance variations	105
4.4.2. Steady-state detuning due to rotor leakage inductance variations	110
4.4.2.1. Study with main flux saturation neglected	111
4.4.2.2. Study with main flux saturation included	112
4.4.3. Steady-state detuning due to mutual inductance variations	114
4.4.4. Steady-state detuning due to iron loss	117
4.4.4.1. Detuning with iron loss represented by a resistance placed in parallel with the magnetising branch, main flux saturation neglected	117
4.4.4.2. Detuning with iron loss represented by a resistance placed in parallel with the magnetising branch, main flux saturation included	121
4.4.4.3. Detuning with iron loss represented by a resistance placed after the stator resistance, main flux saturation neglected	123

4.5. COMPARATIVE ANALYSIS OF STEADY-STATE DETUNING WITH THE CPM-BASED CONTROLLER	126
4.6. DETUNING IN TRANSIENT OPERATION WITH THE CPM-BASED CONTROLLER	128
4.6.1. Transient detuning due to rotor resistance variations	128
4.6.2. Transient detuning due to main flux saturation	131
4.6.3. Transient detuning due to iron loss only	135
4.6.3.1. Torque mode of operation, R_{Fe} iron loss representation	135
4.6.3.2. Torque mode of operation, R_{r} iron loss representation	136
4.6.3.3. Speed mode of operation, R_{Fe} iron loss representation	137
4.6.3.4. Speed mode of operation, R_{r} iron loss representation	140
4.6.4. Transient detuning due to both iron loss and main flux saturation, R_{Fe} iron loss representation	141
4.6.4.1. Torque mode of operation	141
4.6.4.2. Speed mode of operation	141
4.7. SUMMARY	144
5. COMPENSATION OF DETUNING USING IMPROVED VECTOR CONTROLLERS.....	145
5.1. INTRODUCTION	145
5.2. DETUNING IN STEADY-STATE OPERATION USING IMPROVED VECTOR CONTROLLERS	145
5.2.1. Analyses of steady-state detuning using improved vector controllers with main flux saturation	145
5.2.1.1. Steady-state detuning due to rotor resistance variations using improved estimator with main flux saturation	146
5.2.1.2. Steady-state detuning due to iron loss using improved estimator with main flux saturation	147
5.2.2. Analyses of steady-state detuning using improved vector controllers with iron loss only	151
5.2.2.1. Steady-state detuning due to main flux saturation using improved estimator with iron loss	152
5.2.2.2. Steady-state detuning in the base speed region due to main flux saturation using improved estimator with iron loss with constant R_{Fe} value	153
5.2.3. Analyses of steady-state detuning using improved vector controllers with both iron loss and main flux saturation	154

5.2.3.1. Steady-state detuning using improved estimator with both iron loss and main flux saturation, R_{Fe} and L_m correctly estimated	155
5.2.3.2. Steady-state detuning using improved estimator with both iron loss and main flux saturation, R_{Fe} incorrectly estimated	155
5.2.3.3. Steady-state detuning using improved estimator with both iron loss and main flux saturation, L_m incorrectly estimated	155
5.3. DETUNING IN TRANSIENT OPERATION USING IMPROVED VECTOR CONTROLLERS	158
5.3.1. Transient detuning using improved estimators with main flux saturation	158
5.3.1.1. Transient detuning due to main flux saturation using improved estimators with main flux saturation	158
5.3.1.2. Transient detuning due to iron loss, torque mode of operation	162
5.3.2. Transient detuning using improved estimators with iron loss only	164
5.3.2.1. Transient detuning during acceleration in the base speed region, torque mode of operation	165
5.3.2.2. Transient detuning during loading and unloading at the rated speed, speed mode of operation	165
5.3.3. Transient detuning using improved vector controllers with both iron loss and main flux saturation	168
5.4. SUMMARY	170
6. ON-LINE IDENTIFICATION OF THE ROTOR RESISTANCE	171
6.1. INTRODUCTION	171
6.2. IDENTIFICATION SCHEME BASED ON THE CONSTANT PARAMETER MODEL	171
6.2.1. Operation in the base speed region	172
6.2.2. Operation in the field-weakening region	176
6.2.3. Sensitivity of the CPM-based identifier	179
6.2.4. Operation with the CPM-based R_r identifier and saturation-adaptive rotor flux estimator	182
6.3. IDENTIFICATION SCHEMES BASED ON THE IMPROVED MODELS	183
6.3.1. Identification scheme based on the improved model with main flux saturation	183
6.3.2. Identification scheme based on the improved model with iron loss	184
6.3.3. Identification scheme based on the improved model with both main flux saturation and iron loss	185
6.4. SUMMARY	187

7. EXPERIMENTAL INVESTIGATION	190
7.1. INTRODUCTION	190
7.2. DESCRIPTION OF THE DRIVE AND OF THE MEASURING EQUIPMENT	190
7.2.1. The vector-controlled drive	190
7.2.2. Measuring equipment	193
7.2.3. Load characteristics	194
7.3. IDENTIFICATION OF MACHINE PARAMETERS BY STANDARD TESTS	194
7.4. NOVEL METHOD FOR MAGNETISING CURVE IDENTIFICATION	196
7.4.1. Overview of the existing methods	196
7.4.2. Approximation of the inverse magnetising curve	199
7.4.3. Theoretical background of the novel procedure	200
7.4.4. Measurement of the currents and voltages	202
7.4.5. Determination of the magnetising curve	206
7.4.6. Accuracy of the proposed identification method	208
7.5. DETERMINATION OF THE SLIP GAIN	210
7.5.1. Procedure	210
7.5.2. Measurements	211
7.5.3. Evaluation of the slip gain	212
7.6. DETUNING OF THE VECTOR-CONTROLLED INDUCTION MACHINE DRIVE IN STEADY-STATE OPERATION	213
7.6.1. Steady-state detuning due to errors in slip gain	214
7.6.1.1. Steady-state detuning in the base speed region	214
7.6.1.2. Steady-state detuning in the field-weakening region	215
7.6.2. Steady-state detuning due to thermal variations	217
7.6.3. Steady-state detuning due to incorrect magnetising curve approximation	218
7.7. DETUNING IN TRANSIENT OPERATION	220
7.7.1. Transients with various slip gain settings	220
7.7.1.1. Transients with the exact slip gain setting, 1500 rpm base speed	220
7.7.1.2. Transients with various slip gain setting, 1500 rpm base speed	222
7.7.1.3. Transients with the exact slip gain setting, 1150 rpm base speed	224
7.7.1.4. Transients with various slip gain setting, 1150 rpm base speed	226

7.7.2. Transients with detuned magnetising curve	228
7.8. SUMMARY	228
8. CONCLUSIONS	231
8.1. SUMMARY	231
8.2. CONCLUSIONS	236
8.3 FURTHER WORK	237
9. REFERENCES	239
APPENDICES	250
APPENDIX A : DATA OF INDUCTION MACHINES	250
APPENDIX B : PUBLISHED PAPERS	252

LIST OF FIGURES

Figure 2.1 : <i>Induction machine dynamic equivalent circuit in arbitrary reference frame, constant parameters</i>	30
Figure 2.2 : <i>Feedback rotor-flux-oriented control of a current-fed induction machine</i>	38
Figure 2.3 : <i>Rotor flux estimator of i_s-ω type, based on the constant parameter model</i>	38
Figure 2.4 : <i>Feed-forward rotor-flux-oriented control of a current-fed induction machine</i>	39
Figure 2.5 : <i>Feedback rotor-flux-oriented control of a voltage-fed induction machine</i>	41
Figure 2.6 : <i>Feedback rotor-flux-oriented control of a voltage-fed induction machine, with current control loops and decoupling circuits</i>	42
Figure 2.7 : <i>Detuned operation of a rotor-flux-oriented vector controller</i>	45
Figure 2.8 : <i>Induction machine dynamic equivalent circuit in an arbitrary reference frame, main flux saturation included</i>	57
Figure 2.9 : <i>Improved rotor flux estimator of i_s-ω type, with main flux saturation represented by the $i_m(\psi_m)$ non-linear function</i>	63
Figure 2.10 : <i>Simplified version of improved rotor flux estimator of i_s-ω type, with main flux saturation represented by the $i_m(\psi_m)$ non-linear function</i>	63
Figure 2.11 : <i>Induction machine dynamic equivalent circuit in an arbitrary reference frame, iron loss represented by a resistor placed in parallel with the magnetising branch</i>	66
Figure 2.12 : <i>The simplified improved feed-forward rotor-flux-oriented controller with iron loss compensation</i>	68
Figure 2.13 : <i>Induction machine dynamic equivalent circuit in an arbitrary reference frame, iron loss represented with a resistor placed after the stator resistance</i>	70
Figure 2.14 : <i>Model reference adaptive control adaptation scheme for the slip gain in feed-forward controller, using the reactive power method</i>	72
Figure 3.1 : <i>Improved rotor flux estimator of i_s-ω type, with main flux saturation represented by the $L_m(\psi_m)$ non-linear relationship</i>	75
Figure 3.2 : <i>Improved rotor flux estimator of i_s-ω type, with main flux saturation represented by the $L_r(\Psi^2)$ non-linear relationship</i>	78
Figure 3.3 : <i>Improved rotor flux estimator of i_s-ω type, with iron loss</i>	86
Figure 3.4 : <i>Simplified improved rotor flux estimator of i_s-ω type, with iron loss</i>	87

Figure 3.5 : Induction machine dynamic equivalent circuit in an arbitrary reference frame, with both iron loss and main flux saturation	88
Figure 3.6 : Improved rotor flux estimator of i_s - ω type, with both iron loss and main flux saturation, $L_m(\psi_m)$ representation	94
Figure 3.7 : Simplified improved rotor flux estimator of i_s - ω type, with both iron loss and main flux saturation, $L_m(\psi_m)$ representation	95
Figure 3.8 : Improved rotor flux estimator of i_s - ω type, with both iron loss and main flux saturation, $i_m(\psi_m)$ representation	95
Figure 3.9 : Simplified improved rotor flux estimator of i_s - ω type, with both iron loss and main flux saturation, $i_m(\psi_m)$ representation	96
Figure 4.1 : Magnetising curve of the 4 kW machine and the mutual inductance (experimentally identified points denoted by crosses)	99
Figure 4.2 : Results of no-load tests, 4 kW machine	100
Figure 4.3 : Steady-state detuning due to R_r variations, operation at the rated speed, load torque in % as parameter, 4 kW machine	109
Figure 4.4 : Steady-state detuning due to R_r variations, operation with the rated load torque, speed in % as parameter, 4 kW machine	109
Figure 4.5 : Steady-state detuning due to L_{lr} variations, operation at the rated speed, main flux saturation neglected, load torque in % as parameter, 4 kW machine	112
Figure 4.6 : Steady-state detuning due to L_{lr} variations, operation in the base speed region, main flux saturation included, load torque in % as parameter, 4 kW machine	113
Figure 4.7 : Steady-state detuning due to L_{lr} variations, operation in a wide speed region with the rated load torque, main flux saturation included, speed in % as parameter, 4 kW machine	113
Figure 4.8 : Steady-state detuning due to L_m variations, operation in the base speed region, load torque in % as parameter, 4 kW machine	116
Figure 4.9 : Steady-state detuning due to L_m variations, operation in a wide speed region with the rated load torque, speed in % as parameter, 4 kW machine	116
Figure 4.10 : Steady-state detuning due to iron loss, R_{Fe} representation, main flux saturation neglected, operation in the base speed region, load torque in % as parameter, 4 kW machine	119
Figure 4.11 : Steady-state detuning due to iron loss, R_{Fe} representation, main flux saturation neglected, motoring and braking in the base speed region, speed in % as parameter, 4 kW machine	119
Figure 4.12 : Steady-state detuning due to iron loss, R_{Fe} representation, main flux saturation neglected, operation in both base speed region and field-weakening, load torque in % (base speed region) and output power in % (field-weakening) as parameters, 4 kW machine	120

Figure 4.13 : Steady-state detuning due to iron loss, R_{Fe} representation, main flux saturation in the machine included, operation in the base speed region, load torque in % as parameter, 4 kW machine	122
Figure 4.14 : Steady-state detuning due to iron loss, R_{Fe} representation, main flux saturation in the machine included, operation a wide speed region, load torque and output power in % as parameters, 4 kW machine	122
Figure 4.15 : Steady-state detuning due to iron loss, R_{ir} representation, main flux saturation in the machine neglected, operation in the base speed region, load torque in % as parameter, 4 kW machine	125
Figure 4.16 : Steady-state detuning due to the iron loss, R_{ir} representation, main flux saturation in the machine neglected, operation a wide speed region, load torque and output power in % as parameters, 4 kW machine	125
Figure 4.17 : Comparative analysis of detuning , operation at the rated speed, with two load torque levels, 4 kW machine	127
Figure 4.18 : Torque and flux responses to step loading and unloading with the rated load torque, influence of the rotor resistance variations, 4 kW machine	130
Figure 4.19 : Torque and flux responses to step loading and unloading with the rated load torque, influence of the rotor resistance variations, 0.75 kW machine	130
Figure 4.20 : Transient responses for fast reversing transient without load, 0.75 kW machine	133
Figure 4.21 : Transient responses for no-load acceleration into the field-weakening region, 0.75 kW machine	133
Figure 4.22 : Transient responses for fast reversing transient without load, 4 kW machine	134
Figure 4.23 : Transient responses for no-load acceleration into the field-weakening region, 4 kW machine	134
Figure 4.24 : Transient detuning due to iron loss (R_{Fe} representation) during no-load acceleration, torque mode of operation, 4 kW machine	136
Figure 4.25 : Transient detuning due to iron loss (R_{ir} representation) during no-load acceleration, torque mode of operation, 4 kW machine	137
Figure 4.26 : Transient detuning due to iron loss (R_{Fe} representation) during loading and unloading at the rated speed, speed mode of operation, 4 kW machine	138
Figure 4.27 : Transient detuning due to iron loss (R_{Fe} representation) for acceleration into the field-weakening region, speed mode of operation, 4 kW machine	139
Figure 4.28 : Transient detuning due to iron loss (R_{ir} representation) during loading and unloading at the rated speed, speed mode of operation, 4 kW machine	140

Figure 4.29 : Transient detuning due to combined influence of iron loss and main flux saturation during no-load acceleration, torque mode of operation, 4 kW machine	142
Figure 4.30 : Transient detuning due to combined influence of iron loss and main flux saturation during loading and unloading at the rated speed, speed mode of operation, 4 kW machine	142
Figure 4.31 : Transient detuning due to combined influence of iron loss and main flux saturation during acceleration into the field-weakening region, speed mode of operation, 4 kW machine	143
Figure 5.1 : Steady-state detuning due to R_r variations, improved estimator with main flux saturation, operation at the rated speed, load torque in % as parameter, 4 kW machine	148
Figure 5.2 : Steady-state detuning due to R_r variations, improved estimator with main flux saturation, operation with the rated load torque, speed in % as parameter, 4 kW machine	148
Figure 5.3 : Steady-state detuning due to iron loss, R_{Fe} representation, improved estimator with main flux saturation, operation in the base speed region, load torque in % as parameter, 4 kW machine	150
Figure 5.4 : Steady-state detuning due to iron loss, R_{Fe} representation, improved estimator with main flux saturation, operation in a wide speed region, load torque and output power in % as parameters, 4 kW machine	150
Figure 5.5 : Steady-state detuning due main flux saturation, improved estimator with iron loss compensation, operation in a wide speed region, load torque in % and output power in % as parameters, 4 kW machine	153
Figure 5.6 : Steady-state detuning due main flux saturation, improved estimator with iron loss represented by a constant value of R_{Fe} , operation in the base speed region, load torque in % as parameter, 4 kW machine	154
Figure 5.7 : Steady-state detuning with improved estimator with both iron loss and main flux saturation, estimated $R_{Fe}(\omega_r)$ 20% greater than actual, operation in a wide speed region, load torque and output power in % as parameters, 4 kW machine	156
Figure 5.8 : Steady-state detuning with improved estimator with both iron loss and main flux saturation, estimated $R_{Fe}(\omega_r)$ 20% smaller than actual, operation in a wide speed region, load torque and output power in % as parameters, 4 kW machine	156
Figure 5.9 : Steady-state detuning with improved estimator with both iron loss and main flux saturation, estimated $L_m(\psi_m)$ 20% greater than actual, operation in a wide speed region, load torque and output power in % as parameters, 4 kW machine	157
Figure 5.10 : Steady-state detuning with improved estimator with both iron loss and main flux saturation, estimated $L_m(\psi_m)$ 20% smaller than actual, operation in a wide speed region, load torque and output power in % as parameters, 4 kW machine	157

Figure 5.11 : Transient responses during fast reversing transient without load, improved estimator with $i_m(\psi_m)$ representation, 0.75 kW machine	159
Figure 5.12 : Transient responses during no-load acceleration into the field-weakening region, improved estimator with $i_m(\psi_m)$ representation, 0.75 kW machine	159
Figure 5.13 : Transient responses during fast reversing transient without load, improved estimator with $L_r(\Psi)$ representation, 0.75 kW machine	160
Figure 5.14 : Transient responses during no-load acceleration into the field-weakening region, improved estimator with $L_r(\Psi)$ representation, 0.75 kW machine	160
Figure 5.15 : Transient responses during fast reversing transient without load, improved estimator with $i_m(\psi_m)$ representation, 4 kW machine	161
Figure 5.16 : Transient responses during no-load acceleration into the field-weakening region, improved estimator with $i_m(\psi_m)$ representation, 4 kW machine	161
Figure 5.17 : Transient detuning due to combined influence of iron loss and main flux saturation during no-load acceleration, torque mode of operation, improved estimator with main flux saturation, 4 kW machine	163
Figure 5.18 : Transient detuning due to combined influence of iron loss and main flux saturation for loading and unloading at the rated speed, speed mode of operation, improved estimator with main flux saturation, 4 kW machine	163
Figure 5.19 : Transient detuning due to combined influence of iron loss and main flux saturation during no-load acceleration into the field-weakening region, speed mode of operation, improved estimator with main flux saturation, 4 kW machine	164
Figure 5.20 : Transient detuning due to combined influence of iron loss and main flux saturation during no-load acceleration, torque mode of operation, the full improved estimator with iron loss, 4 kW machine	166
Figure 5.21 : Transient detuning due to combined influence of iron loss and main flux saturation during no-load acceleration, torque mode of operation, the simplified improved estimator with iron loss, 4 kW machine	166
Figure 5.22 : Transient detuning due to combined influence of iron loss and main flux saturation during loading and unloading at the rated speed, speed mode of operation, the full improved estimator with iron loss, 4 kW machine	167
Figure 5.23 : Transient detuning due to combined influence of iron loss and main flux saturation during loading and unloading at the rated speed, speed mode of operation, the simplified improved estimator with iron loss, 4 kW machine	167

Figure 5.24 : Transient detuning during acceleration into the field-weakening, speed mode of operation, the full improved estimator with both iron loss and main flux saturation, 4 kW machine	169
Figure 5.25 : Transient detuning during acceleration into the field-weakening, speed mode of operation, the simplified improved estimator with both iron loss and main flux saturation, 4 kW machine.....	169
Figure 6.1 : The R_r identification scheme, using the reactive power method	174
Figure 6.2 : Identification of R_r by the CPM-based identifier at the rated speed, $R_r = R_{rn}$, load torque in % as parameter, 4 kW machine	174
Figure 6.3 : Identification of R_r by the CPM-based identifier at the rated speed, $R_r = 1.2 R_{rn}$, load torque in % as parameter, 4 kW machine	174
Figure 6.4 : Identification of R_r by the CPM-based identifier at the rated speed, $R_r = 0.8 R_{rn}$, load torque in % as parameter, 4 kW machine	175
Figure 6.5 : Responses to the changes in load, operation at the rated speed, R_r identification disabled	176
Figure 6.6 : Identification of R_r by the CPM-based identifier in the field-weakening region, 125% speed, load torque in % and the actual value of R_r as parameters, 4 kW machine	178
Figure 6.7 : Identification of R_r by the CPM-based identifier in the field-weakening region, 150% speed, load torque in % and the actual value of R_r as parameters, 4 kW machine	178
Figure 6.8 : Identification of R_r by the CPM-based identifier at the rated speed, $L_m^* = 0.8 L_{mn}$, load torque in % as parameter, 4 kW machine	179
Figure 6.9 : Identification of R_r by the CPM-based identifier at the rated speed, $L_m^* = 1.2 L_{mn}$, load torque in % as parameter, 4 kW machine	179
Figure 6.10 : Identification of R_r by the CPM-based identifier at the rated speed, $L_{ls}^* = 0.8 L_{lsn}$ and $L_{lr}^* = 0.8 L_{lrn}$, load torque in % as parameter, 4 kW machine	181
Figure 6.11 : Identification of R_r by the CPM-based identifier at the rated speed, $L_{ls}^* = 1.2 L_{lsn}$ and $L_{lr}^* = 1.2 L_{lrn}$, load torque in % as parameter, 4 kW machine	181
Figure 6.12 : Identification of R_r by the CPM-based identifier in the field-weakening region, 125% speed, $R_r = R_{rn}$, saturation-adaptive rotor flux estimator, load torque in % as parameter, 4 kW machine	182
Figure 6.13 : Identification of R_r by the saturation-adaptive identifier in the field-weakening region, 125% speed, saturation-adaptive rotor flux estimator, load torque in % as parameter, 4 kW machine	184
Figure 6.14 : Rotor resistance identification with inclusion of iron loss	185
Figure 6.15 : Identification of R_r by the iron-loss-adaptive identifier at the rated speed, rotor flux estimator with iron loss, 4 kW machine	186

Figure 6.16 : Identification of R_r by the iron-loss-adaptive identifier in the field-weakening region, 125% speed, rotor flux estimator with iron loss, 4 kW machine	186
Figure 6.17 : Identification of R_r at the rated speed, both main flux saturation and iron loss included in both rotor flux estimator and R_r identifier, 4 kW machine	188
Figure 6.18 : Identification of R_r in the field-weakening region, 125% speed, both main flux saturation and iron loss included in both rotor flux estimator and R_r identifier, 4 kW machine	188
Figure 7.1 : The indirect RFO scheme implemented in the Vickers drive	193
Figure 7.2 : Variations of output power and output torque with speed for several positions of the resistor bank switch	194
Figure 7.3 : Current and input power during locked rotor test of the 2.3 kW motor	195
Figure 7.4 : Results of no-load experiments with sinusoidal supply, 2.3 kW motor	195
Figure 7.5 : The inverse magnetising curve obtained from no-load experiments with sinusoidal supply, 2.3 kW motor	196
Figure 7.6 : Impact of the coefficient a on the inverse magnetising curve approximation	200
Figure 7.7 : Impact of the coefficient b on the inverse magnetising curve approximation	200
Figure 7.8 : Voltage in PWM no-load operation at 2100 rpm	203
Figure 7.9 : Current waveforms and spectra in PWM no-load operation at 2100 rpm.	203
Figure 7.10: No-load experiments with inverter supply, 1500 rpm base speed	204
Figure 7.11: No-load currents and voltages for two incorrect values of coefficient a , 1150 rpm base speed.	205
Figure 7.12: No-load currents and voltages for different settings of coefficient a , 1150 rpm base speed	206
Figure 7.13: No-load currents and voltages for different settings of coefficient a , 650 rpm base speed	207
Figure 7.14 : The inverse magnetising curve identified by the novel method, comparison with standard no-load test results included in (b).....	208
Figure 7.15: Sensitivity of the proposed identification procedure to incorrect value of the stator leakage inductance.....	209
Figure 7.16: Phase currents (rms fundamental component) with various values of slip gain, operation in the base speed region, 1500 rpm base speed	211
Figure 7.17: Phase currents (rms fundamental component) with various values of slip gain, operation in the base speed region, 1150 rpm base speed	212

Figure 7.18: Estimated I_{qs}^* (rms fundamental component) with various values of slip gain, operation in the base speed region, 1500 rpm base speed	213
Figure 7.19: Estimated I_{qs}^* (rms fundamental component) with various values of slip gain, operation in the base speed region, 1150 rpm base speed	213
Figure 7.20: Phase currents (fundamental component) for detuning due to errors in slip gain settings, 1150 rpm base speed	216
Figure 7.21: Phase currents (fundamental component) for detuning due to errors in slip gain settings, 650 rpm base speed	216
Figure 7.22: Estimated I_{qs}^* (rms fundamental component) with detuning due to errors in slip gain setting, 1150 rpm base speed	217
Figure 7.23: Estimated I_{qs}^* (rms fundamental component) with detuning due to errors in slip gain setting, 650 rpm base speed	217
Figure 7.24: Estimated I_{qs}^* (rms fundamental component) with detuning due to thermal effects	218
Figure 7.25: Phase currents (fundamental component) in no-load operation with various magnetising curves in the controller	219
Figure 7.26: Estimated I_{qs}^* (rms fundamental component) with detuning due to incorrect magnetising curve	219
Figure 7.27: Acceleration transients with the exact slip gain, 1500 rpm base speed	221
Figure 7.28: Deceleration transients with the exact slip gain, 1500 rpm base speed	222
Figure 7.29: Speed responses in acceleration transients with various loads and various slip gains, 1500 rpm base speed	223
Figure 7.30: Speed responses in deceleration transients with various loads and various slip gains, 1500 rpm base speed	223
Figure 7.31: Acceleration transients with the exact slip gain, 1150 rpm base speed	225
Figure 7.32: Deceleration transients with the exact slip gain, 1150 rpm base speed	226
Figure 7.33: Speed responses in acceleration transients with various loads and various slip gains, 1150 rpm base speed	227
Figure 7.34: Speed responses in deceleration transients with various loads and various slip gains, 1150 rpm base speed	227
Figure 7.35: Speed responses for acceleration with three settings of the coefficient a in the vector controller (1, 0.9 and 0.7), the exact slip gain, 1150 rpm base speed	229
Figure 7.36: Speed responses for acceleration with three settings of the coefficient a in the vector controller (1, 0.9 and 0.7), the exact slip gain, 650 rpm base speed	229

NOMENCLATURE

General remarks :

- underlined variables denote matrices,
- overlined variables denote space vectors,

Indices :

a, b, c - phases of the original three-phase system, stator variables,

A, B, C - phases of the original three-phase system, rotor variables,

d, q - axes of the two-phase system,

s - stator,

r - rotor,

m - magnetising (air-gap),

l - leakage,

Fe - iron (the first representation),

ir - iron (the second representation),

L - load,

e - electromagnetic,

sl - slip (angular speed).

Superscripts :

e - estimated value,

t - matrix transposition

$*$ - commanded value.

LIST OF SYMBOLS :

f - frequency,

i - currents,

j - imaginary unit,

J - polar inertia,

L - inductances,

P - number of pole pairs,

R - electrical resistances,

s - Laplace's operator

T_e, T_L - torque (electromagnetic and load, respectively),

T - time constants (in all other cases),

v - voltages,

ψ - flux linkages,

θ - angle,

ω - angular speed.

LIST OF ABBREVIATIONS

DC	direct current
AC	alternative current
RFOC	rotor flux oriented control
SFOC	stator flux oriented control
AFOC	air-gap flux oriented control
PWM	pulse width modulation
MRAC	model reference adaptive control
FL	fuzzy logic
ANN	artificial neural network
DTC	direct torque control
RFO	rotor flux orientation
SFO	stator flux orientation
AFO	air-gap flux orientation
CPM	constant parameter model
DSP	digital signal processor

1. INTRODUCTION

Successful functioning of the modern society heavily relies on variable-speed electric drives. Vast majority of the mankind is not aware of this fact and takes all the available technological advances for granted. However, simple everyday events such as a comfortable elevator ride or a pleasant electric train journey would have not been possible without a variable-speed electric drive. These devices are nowadays present in all aspects of human life, from a washing machine to a space shuttle, from a PC to an electric vehicle, from a simple manufacturing process to a robot.

Variable-speed electric drives make the world go around and this thesis attempts to give a contribution to this area. In particular, one specific approach to obtaining good quality dynamic response of a variable-speed drive, usually termed vector control, is investigated. It is discussed in conjunction with the most frequently used electric motor type, namely an induction machine.

1.1. A HISTORICAL OVERVIEW OF VECTOR CONTROL OF INDUCTION MACHINES

Rapid development of industrial automation requires continuing improvement of different types of electric drives. Manufacturing lines typically involve variable-speed motor drives to power conveyor belts, robot arms, and other types of processing operations. High reliability, good control characteristics, low maintenance requirements, low investment and low running costs are among the important features that are required from a modern drive [Leonhard, 1985]. For simple drives, industry has relied mainly on squirrel-cage induction machines. A major disadvantage of this type of the machine was its inability to be controlled in an efficient manner. Despite this significant drawback, induction motors were industry's principal workhorse, operating in uncontrolled mode. Direct current (DC) machines and wound-rotor induction machines were used only in drives where variable-speed operation was essential. The advent of thyristors in the late Fifties enabled efficient and controlled voltage rectification, making variable-speed drives with DC motors simple to control. However, serious limitations of DC motors such as sparking, extensive maintenance and poor

overloading capability brought attention back to induction motors [Novotny and Lipo, 1996].

Development of thyristor-based inverters, that could provide variable-frequency alternating current (AC) voltage, took place during the Sixties. As a consequence, so-called 'scalar' control techniques emerged, where the frequency and the magnitude of supply voltages are controlled by an inverter. In this way an induction machine was able to operate in a controlled variable-speed mode, obtaining steady-state characteristics similar to those of a DC motor. Systems with scalar control have been replacing DC drives in numerous applications where accuracy and transient response are not crucial requirements (pumps, fans, compressors, etc.), due to the fact that induction motors have a clear competitive edge over DC motors [Leonhard, 1985; Bose, 1986; Trzynadlovski, 1994; Novotny and Lipo, 1996].

Nevertheless, DC machines were still unbeatable in the area of high-performance (servo) drives, where very fast and accurate torque and/or speed responses are required. Furthermore, position servo control was the application area in which DC machines were the only choice. Superior dynamic control characteristics of DC machines are based on decoupled control of flux and torque, utilising quite simple control strategy and equipment. Basic principles of vector control (field orientation), introduced in the early Seventies [Blaschke, 1971], showed that decoupled control of flux and torque was theoretically possible in AC machines as well. Due to their simple structure, robustness, virtually no maintenance and low cost, squirrel-cage induction machines have become especially attractive for vector control.

It should be noted that vector control is not limited to induction machines. Vector control principles are valid for all types of three-phase AC machines [Vas, 1990]. Synchronous motors, particularly the 'brushless' motors with novel high-energy permanent magnets, have found many applications, typically in the areas of machine tools and robotics. Development of vector control theory has even forced manufacturers to build specially designed machines, aimed for vector-controlled drives only. Researchers are still putting a lot of effort in that direction [Slemon, 1994].

Vector control denotes an independent (decoupled) control of the flux and the torque in AC machines [Boldea and Nasar, 1990; Vas, 1990]. This is achieved by controlling the

amplitude of the stator current space vector and its position with respect to the chosen flux space vector. Since there are three flux vectors in an induction machine, three methods of vector control can be distinguished: the stator-flux-oriented control (SFOC), the air-gap-flux-oriented control (AFOC) and the rotor-flux-oriented control (RFOC). The simpler structure, coupled with theoretically infinite maximum (pull-out) torque, has established the RFOC as the most popular method. All vector controllers, regardless of the orientation system, require accurate information about the amplitude and the position of the selected flux vector. This information can be obtained in two ways: directly (by appropriate feedback devices) and indirectly (by feed-forward type estimation). This leads to additional sub-division of vector control schemes into the feedback and the feed-forward schemes.

The first practical realisations of the vector-controlled drives [Flöter, 1971] employed Hall probes in order to obtain information about the amplitude and the position of the air-gap flux. The control system was based on analogue electronics. These drives had a number of drawbacks: Hall probes dictated a special motor design, increasing the cost of the drive; analogue vector controllers were extremely complex, mainly due to the need for the co-ordinate transformation; thyristors were used in power electronic converters and their slow switching meant that current control was poor. The performance and the price of these drives could not compete with DC drives and at that time vector-controlled induction machines did not find many practical applications [Gabriel et al., 1980].

Microprocessors, introduced in the late Seventies, enabled efficient co-ordinate transformation and vector-controlled drives have subsequently become competitive. By the early Eighties the basic concepts of the vector control realisation had been almost resolved [Gabriel et al., 1980]. However, research work has continued very intensively, in order to improve the performance, reduce the cost and enhance the reliability. In fact, the vast majority of work in the area of variable-speed drives has dealt with vector control. The complex structure of vector-controlled drives aggregates knowledge from a number of very different areas of engineering. Their relation to vector control theory and practice is briefly discussed in the following several paragraphs.

Power electronics is an area that has significantly contributed to the evolution of variable-speed drives. The evolution of power electronics is a combination of

inventions and developments in devices, topologies and control techniques. Nowadays there are hundreds of power electronic converter topologies [van Wyk, 1994]. Different semiconductor devices such as metal-oxide-semiconductor field-effect transistor (MOSFET), insulated-gate bipolar transistor (IGBT), MOS-controlled thyristor (MCT), emitter switched thyristor (EST), etc. were invented and their characteristics have been constantly improved [Baliga, 1994]. A variety of methods and techniques aimed for controlling power electronic converters have been developed. Some of them are rather general, while others are specific to either a type of semiconductor device or a topology. Developments in power electronics have had enormous impact on vector controlled drives. Fast switching devices, coupled with sophisticated pulse-width modulation (PWM) techniques, have enabled excellent current control, so that current feeding became a reality [Holtz, 1994]. This in turn has enabled a wider use of current-fed machines, with a vector control systems much simpler than those utilised for voltage-fed machines. Recent theoretical analysis [Bhatnagar and Baliga, 1993] has shown that substitution of silicon by silicon-carbide or by gallium-arsenide could significantly improve electrical characteristics of the devices, increasing the switching frequency and reducing the losses. Thus new developments in power electronics are still expected to come.

Developments in VLSI technology have rapidly enhanced the performance of the microprocessors and other hardware, and reduced costs. Advanced digital signal processors (DSPs), reduced instruction set computing (RISC) processors, application specific integrated circuits (ASICs), and parallel processors (transputers) nowadays provide enough computing power even for the most demanding applications. Motion control algorithms involving coordinated movement along three or even more axes are now performed by a single-chip controller. Computing speed has become so high that the control bandwidth is approaching analogue limits [Le Huy, 1994].

High computing power has opened possibilities to implement modern control theory techniques and artificial intelligence methods in vector-controlled drives. Estimation of flux amplitude and position has become easier and more accurate with implementation of novel observers [Verghese and Sanders, 1988]. Different parameter estimation techniques, such as 'model reference adaptive control' (MRAC) [Garcés, 1980; Krishnan and Pillay, 1986], Kalman filters [Atkinson et al., 1991; Pena and Asher,

1993] or signal injection [Saitoh et al., 1989], have tackled the parameter variation problem, increasing the accuracy and the overall robustness of the drive.

Most recently, artificial intelligence techniques have been applied to control of electric drives. Expert systems and artificial neural networks (ANNs) seem extremely promising for fault diagnosis [Bose, 1994]. Fuzzy logic (FL) theory has been recently introduced to the control of electric drives. FL control can provide a fast response time and good disturbance rejection, without overshoot and with low noise susceptibility [Vas et al., 1995]. Another possible approach is to implement a standard PI controller whose gains are varied by FL [Lee and Pang, 1994]. FL has also been implemented for the optimal efficiency control of flux [Sousa and Bose, 1993] and for slip gain tuning in feed-forward drives [Sousa et al., 1993]. Artificial neural networks (ANNs) are very suitable for controlling highly non-linear processes and electromechanical energy conversion is a non-linear process. ANNs have been implemented for feedback signal processing [Vas et al., 1995; Hofmann and Liang, 1995a; Simões and Bose, 1995], for PWM inverter control [Kazmierowski and Sobczuk, 1994] and for parameter identification [Hofmann and Liang, 1995b; Ba-Razzouk et al., 1996]. It is expected that application of the artificial intelligence techniques in electric drives will usher a new era in motion control in the coming decades [Bose, 1994].

The modern control theory advancements, summarised above, have formed a sound basis for improvement of old and application of new control algorithms for vector control. Schemes that employ manipulation of flux level, in order to maximise efficiency [Kirchen et al., 1987] or to produce high torque pulse [Wallace et al., 1994], have been introduced. Special algorithms for high-power applications, where slow-switching thyristors are still the only possible power electronics devices, have been proposed [Stemmler, 1994]. Introduction of control systems that can adapt their control parameters to an unknown motor through a self-commissioning procedure was a major step towards unification [Shierling, 1988]. Universal vector controllers [De Doncker and Novotny, 1988] can switch between feedback and feed-forward control strategies in order to fully utilise the good characteristics of both schemes. One of the newest directions in research is the realisation of the drive without speed or position sensor [Holtz, 1995], so-called 'sensorless' vector control.

It should be noted that vector control has had some competitors. Several different techniques for control of high-performance electric drives have been proposed. Joensson's method [Joensson, 1989] has very good steady-state characteristics but the dynamic responses are not of a matching quality. So-called 'Field acceleration method' is much simpler than the vector control since it does not need co-ordinate transformation [Yamamura, 1986]. This method can provide good dynamic response [Sharaf et al., 1989]. However, this method has never caught on. The most famous alternative control method, Direct Torque Control (DTC), was first presented by Takahashi and Naguchi [1985], and by Depenbrock, [1988]. The first commercial application of DTC was implemented by the ABB company [Tiitinen et al., 1995; Tiitinen and Surandra, 1996]. The main feature of DTC is the absence of co-ordinate transformation. The inverter switching signals are directly generated on the basis of the errors in flux and torque, by a switching rule table, realised by ASIC hardware. An extremely good performance has been claimed by ABB, but very little information has been disclosed. DTC has the same problem as vector control in that they both require flux and torque estimates. In DTC, estimates are obtained by an adaptive estimator, from measured currents, measured DC bus voltage and information about commanded switching position. It was claimed that the adaptive motor model, stated by the authors to be already known and used, is the key to DTC's unrivalled low speed performance [Tiitinen and Surandra, 1996]. It is not known which particular model is used nor how the model parameters are determined.

Despite the competition, vector control theory and practice has experienced tremendous development and growth in less than three decades. The outcome is that vector control has grown out from being just an interesting research area, useful for building prototypes only. Vector controlled drives have left laboratories and are now commercially available. Their applications are numerous and they are found in a number of industrial applications, covering a wide power range. However, there still are numerous problems to be solved and a lot of research effort is still invested in achieving better drive performance.

1.2 PROBLEMS EXPERIENCED WITH VECTOR CONTROL OF INDUCTION MACHINES

There is a wide variety of vector control schemes, developed over the last 25 years. The orientation of the stator current vector can be performed with respect to the rotor flux vector, the stator flux vector or the air-gap flux vector. The vector control scheme can be feedback or feed-forward. There can be one or several control loops and the appropriate number of controllers, which in turn can be proportional (P), integral (I), a combination of the two (PI), or even fuzzy nowadays. The realisation of the control system can be digital, analogue or hybrid. At the same time, the induction machine can be fed from either voltage or current source.

Each proposed vector control scheme has some advantages and some disadvantages. However, there are certain common features for majority of the schemes. The most important one is that a vector controller operates in a reference frame attached to the chosen flux. Hence the position of the chosen flux must be known, in order to correlate the controller outputs with the inverter and/or to process feedback signals into a form suitable for the controller. Additionally, all vector controllers need to know some machine parameters, in order to perform the required processing of the control signals. Finally, some signals are measured and used as the feedback signals for a controller.

1.2.1 Sources of detuning

Information on the position of the chosen flux is essential for the proper operation of all vector control schemes. This information can be obtained in two ways. The first approach is to directly measure the components of the chosen flux. This is possible for AFOC methods only, where the air-gap flux is measured by Hall probes inserted in the stator teeth. Nevertheless, direct measurement of the air-gap flux is rarely used, due to complications Hall probes introduce and their thermal sensitivity. The second approach, used in the majority of schemes, involves estimation (calculation) of the position of the chosen flux. This is achieved by measuring some other variables, whose measurement is much easier, cheaper and more accurate. Then the position of the chosen flux is estimated (calculated) on the basis of the measured signals [Boldea and Nasar, 1990;

Vas 1990; Vas, 1993]. In all vector controllers, the estimation process relies on a mathematical model of the induction machine.

From the previous paragraph two main sources of operating inaccuracies and operating problems have been identified. Firstly, there are inaccuracies caused by the hardware used for measurement and estimation, which include limited accuracy of sensors, quantization errors, limited resolution of both sensors and digital hardware, electromagnetic interference and selection of the sample rate [Borgard et al., 1995]. The effects of the first three sources of detuning can be reduced by using better sensors and better corresponding hardware, but the cost of the system inevitably increases. Negative effects of electromagnetic interference are tackled by careful design. Finally, since all measured signals are normally time-varying (i.e. AC), the operating sample rate has to be chosen large enough to reduce the sampling errors at high operating speeds (frequencies) to an acceptable level. A high sample rate translates as a requirement for more powerful processing capabilities of the hardware, which again increases the price of a controller. However, the continuing fall in microprocessors prices means that cost is not such a problem. Operating inaccuracies due to the hardware limitations and the digital nature of the controllers are very interesting topics, but they are beyond the scope of this research and will not be discussed further.

The second group of operating inaccuracies and problems has roots in the structure of a vector controller. Estimation of the position of the chosen flux inevitably involves some calculations in which machine parameters are used [Boldea and Nasar, 1990; Vas 1990; Vas, 1993; Slemon, 1994]. Gains and/or time constants of speed, flux and/or torque controllers are also correlated to motor parameters. If there are any discrepancies between the actual motor parameters and the values used in the vector controller, estimation of the flux position is erroneous. This affects the performance and the vector controller operates with an error. In such a situation the vector controller is said to be detuned. Additionally, in certain operating conditions noticeable detuning can arise from phenomena that are considered to be of secondary importance and hence neglected during the control system design. Iron losses are a good example, since they are normally neglected during design of a vector controller. Neglected phenomena, parameter inaccuracies and parameter variations, and their role as detuning sources form the main topic of this thesis.

Which parameter values do vector controllers need? Which phenomena influence the accuracy of a vector controller? How? How much? These questions do not have straightforward answers. Reasons for such an unclear situation can be divided into several groups, which are discussed in the following six paragraphs.

As already noted, there is a huge variety of vector control schemes, stemming from the choice of the flux along which the control is performed, the type of inverter, the utilised induction machine model, the choice of sensors, the choice of other hardware, the performance requirements and so on. Different vector controllers perform different calculations, for which different parameters are used. Therefore the overall sensitivity to parameter variations is heavily dependent on the structure of the controller. Generally, rotor-flux-oriented (RFO) schemes are more sensitive to parameter variations than stator-flux-oriented (SFO) schemes and air-gap-flux-oriented (AFO) schemes [Vas, 1990]. The reason for this lies in the fact that rotor quantities are inaccessible for any measurement and they have to be estimated. Estimation of the rotor quantities requires more calculations involving the machine parameters than the estimation of the quantities needed for the other two types of orientation.

Whatever the type of vector control scheme, it is absolutely crucial to have as accurate knowledge as possible about the parameters involved in the particular vector control scheme. It has to be stressed that initial correct determination of the required parameters is not a guarantee of tuned operation at all times. Each of the parameters is determined for a specific operating point and their values might change when the operating conditions are altered.

There are many phenomena that cause parameter variations in an induction machine and consequently lead to detuned operation of a vector controller. Magnetic saturation affects the values of the inductances in the machine. Variations in temperature and the skin effect change the values of the resistances in the machine. All the above mentioned effects alter the value of the rotor time constant (T_r), which is extensively used for the calculations in many schemes. Iron loss, normally neglected in the control system, takes part in the power balance of the machine and thus reduces the accuracy of the estimation process.

The amount of detuning induced by a specific phenomenon depends on the machine design. Induction machines are built for an extremely wide range of powers and speeds. There are various designs, some rather general, whilst other unique for specific power and/or speed range or for specific performance requirements. Some phenomena concerning parameter variation are more pronounced for certain designs. For instance, design of the rotor bars is a trade-off between the efficiency in normal operation on one side, and the starting current and the starting torque on the other side. However, an induction machine in a vector controlled drive starts under sophisticated controlled conditions so that the starting current and the starting torque are no longer of importance for design. When the induction machine is intended to be used only in vector controlled drives, the rotor bars can be designed for better efficiency. Such a change in rotor design inevitably changes the relative values of the rotor resistance (R_r) and the rotor leakage inductance (L_{lr}). Additionally, various rotor designs will produce diverse variations in these two parameters.

Another example of design consideration is concerned with induction machines of powers in the range of ten or several tens of kW. For the line-starting machines, deep-bar or double-cage rotor designs, where the pronounced skin effect is positively used for increasing the starting torque, are neat solutions. However, deep bars and double cages become obsolete if the machine is intended to operate as a part of a vector controlled drive. Nevertheless, economic reasons might require the replacement of the controller, but not the machine itself, when an existing drive is upgraded. Then a deep-bar or double-cage machine will experience larger parameter variations due to the skin effect, which inevitably influence the operation of the controller.

The pattern of how each parameter varies and how much it influences a vector controller also depends on operating conditions. There are many aspects to be considered. Parameter variations due to magnetic saturation heavily depend on the operating conditions. Magnetic saturation in an induction machine can be separated into main flux saturation, rotor leakage flux saturation and stator leakage flux saturation, causing variations in the mutual (magnetising) inductance (L_m), the rotor leakage inductance (L_{lr}) and the stator leakage inductance (L_{ls}), respectively. Variations in L_m occur when the value of the main flux is changed, which can happen in several cases. Firstly, the main flux can be deliberately reduced or increased. Expansion of the speed range which

a drive should cover means that flux has to be reduced for speeds higher than the rated speed, in order to keep the required voltage within inverter capabilities. Such action is called 'field weakening' and the operating speed region above the rated speed is labelled 'the field-weakening region'. When flux is reduced, main flux saturation becomes less pronounced and the value of L_m increases. Flux level can also be manipulated to achieve better efficiency, to produce a high short-term torque pulse, or to produce maximum torque per ampere. Secondly, there are situations when changes in the magnetising flux are unwanted. One example is a high short-term overloading (for fast acceleration, for instance), when the cross-saturation effect becomes pronounced. Another example is detuned operation due to discrepancies between parameters used in a vector controller and the actual values of these parameters (rotor resistance, for instance). High currents are also responsible for variations in leakage inductances. Furthermore, leakage inductances are dependent on frequency.

As far as R_r variations are concerned, the situation is even more complicated. Firstly, the influence of the skin effect on R_r depends on the geometrical shape of the rotor bars as well as on the amplitude and the frequency of the rotor current (dictated by the loading of the machine). Secondly, thermally induced variations in both R_r and R_s are correlated to operating conditions in a complex manner. On one hand, induction machine is heated by various losses that occur in it. The stator and the rotor currents, dictated by both load and flux requirements, determine the amount of copper losses in both stator and rotor windings. Meanwhile, iron loss is dictated by the flux level and the operating frequency. Both types of losses depend also on the spectra of the voltage and current waveforms that are supplied to the machine by a power electronic converter. Finally, copper losses depend on whether the stator winding is connected into star or delta formation, since the third harmonic component of the current can flow inside delta formation and the copper losses increase. On the other hand, cooling conditions are equally important and equally complex as heating. Operating speed is very influential when the cooling is provided by a fan affixed to the machine shaft. Cooling situation of the machine is quite different when a separate fan provides the flow of cooling air. The ambient temperature is important in both cases. Different duty cycles, that involve specific profiles of the speed and the load, determine the thermal state of the machine and the variations in resistances.

Detailed discussion about the consequences of detuning will be presented in section 2.4. For the moment it is sufficient to say that parameter variations and subsequent detuned operation affect the performance of the drive. The rotor flux amplitude can deviate from the commanded value, torque response can become sluggish or oscillatory, efficiency is decreased, etc. Since high performance is the key advantage of vector controlled drives over scalar drives, serious deterioration in dynamic performance (torque response) is highly undesirable. Various techniques for compensation of detuning have been proposed. Their basic theory is briefly discussed in section 1.2.2 and they are reviewed in detail in Chapter 2.

1.2.2. Approaches to compensation

Detuning problems were noted early in vector control development [Gabriel et al., 1980] and first remedies were proposed [Garcés, 1980]. Variations in R_r and/or T_r due to thermal effects were the first detuning phenomenon to be noted and attempts made to compensate for them. One of the reasons for this is that temperature changes are relatively slow. This meant that relatively slow and not so powerful hardware used at that time was still capable of performing calculations needed for identification and compensation of either R_r or T_r . Various methods for compensation of thermally induced parameter variations have since been developed. Their complexity has increased over the years, as a consequence of the enormous growth in processing power. The common features of these identification techniques are that they operate on-line and are usually operational in steady-states only. The complex nature of both heating and cooling make it difficult to accurately predict the temperature (and hence resistance) of the machine's windings. Consequently, off-line open-loop estimation is practically impossible. In order to keep the identification system as simple as possible, it is usually designed utilising the steady-state machine models. Therefore the identification is performed in steady-state operation only while it is disabled during transients, when the value identified in the previous steady-state is used.

Electromagnetic processes are much faster than the thermal processes, but more predictable. The compensation of electromagnetically induced parameter variations is usually done by open-loop methods. Some of the terminal and/or control variables (currents, fluxes, etc.) are measured and observed and the appropriate parameters are

varied using predetermined functions. From the design point of view, the standard vector controller is substituted with an improved one, that takes into account parameter variations. A number of different improved controllers have been developed over the last ten years. They will be reviewed and the most important ones will be analysed in Chapter 2.

Two main approaches to compensation of detuning due to electromagnetically induced parameter variation can be distinguished. The first approach is to continue designing vector controllers on the basis of the constant parameter model (CPM) and seek performance improvement by resorting to modern control theory techniques, mentioned in section 1.1. In this case vector controllers have additional complex control circuits that compensate the detuning effects. As previously mentioned, such methods are suitable for identifying parameter variations due to thermal effects. However, there are some problems when such an approach is used for identification and compensation of electromagnetically induced parameter variation. The first drawback is the fact that deficiencies in the machine model are being transferred to the additional complexity of vector controllers. Additionally, some of the methods are computationally intensive and the compensation is slow, limiting the successful usage to steady-state operation. Next, one additional circuit can usually compensate for one parameter variation (or even only the effect of one phenomenon on one parameter). Therefore several additional circuits might be needed to provide full compensation. Another serious drawback is that the accuracy of a compensation circuit depends on accurate knowledge of other parameters which are also variable. Finally, compensation circuits can substantially increase controller complexity, requiring more computational power, which inevitably increases the cost of the drive.

The second approach to the compensation of parameter variations is to employ vector controllers based on improved (modified) machine models. The improved models account for some of the phenomena discussed above and therefore can represent the induction machine more faithfully than the CPM model. When these improved models are utilised for the controller design, the controller accounts for the same phenomena and enables compensation of their detuning effects. Such an approach to compensation is more natural than the one employing modern control theory techniques. It has been shown that substantial reduction in detuning can be achieved when improved machine

models are used for a controller design. Hence the performance of such controllers is much enhanced when compared with the CPM-based controllers of similar complexity. Main flux saturation, leakage flux saturation, skin effect and iron loss are amongst phenomena that can be included in the improved model and their detuning effects can be compensated by using this approach. However, since temperature effects cannot be included in the improved models, they cannot be compensated by this approach. Still, improved machine models can be utilised in an on-line R_r identification scheme, in order to enhance its accuracy. In such a case only one additional control circuit is needed.

1.3. AIMS OF THE RESEARCH

1.3.1. Research objectives

Although much research has been done in the area of vector control of induction machines, the ideal control scheme has not yet been established. Such a situation is caused by the complex physical structure of induction machines and the fact that parameters of the machine vary during operation. Many authors in this area appreciate that such a simple device as an induction machine is deceptively difficult to analyse to the degree of accuracy preferred by engineers and designers. As a consequence, detailed design, analysis and operation of vector controlled induction machine drives is a complex problem, particularly when parameter variations are involved. Hence research into parameter variation effects and appropriate schemes that will compensate them deserves further attention.

As mentioned previously, there are two possible approaches for performance improvement and compensation of parameter variations effects. A model-based approach is used in this project. Improved vector controllers, derived from improved induction machine models constitute the basis for this research project. Investigated improved machine models include main flux saturation and/or iron loss. Initially, the improved models are used to represent the induction machine, in order to investigate and evaluate detuning that occurs when the above phenomena are included in the machine model while neglected in the controller. Next, the improved models are utilised to design improved vector controllers, in order to compensate detuning effects

caused by the above phenomena. Since it is necessary to have knowledge about the magnetising curve of a machine, a novel method for identification of the inverse magnetising curve has been developed. Finally, improved models are utilised for derivation of two novel MRAC-based circuits for identification of thermally induced parameter variations. Novel identification schemes operate in conjunction with improved controllers.

In accordance with the previous discussion, the main objectives of this study are as follows :

- 1) To derive various improved induction machine models that include main flux saturation and iron loss.
- 2) To quantitatively investigate detuning effects introduced by main flux saturation, iron loss and temperature effects in standard vector control schemes. In addressing this problem, the induction machine is represented by improved models, while the vector controller is based on the CPM.
- 3) To systematically develop novel vector controllers, based on improved mathematical models of induction machines. Several novel controllers will be studied, with one or more improvements over the CPM-based controller. The aim of novel controllers is to reduce or eliminate detuning and hence improve the overall performance of the drive.
- 4) To perform quantitative investigation into the accuracy of the novel controllers and into sensitivity of the novel controllers to remaining parameter variation.
- 5) To evaluate theoretical performance improvement achieved by novel vector controllers in both steady-state and transient operation.
- 6) To develop an auxiliary control circuit that will identify thermally induced changes of the R_r and hence compensate the temperature effects. Since neither CPM-based nor novel controllers can include temperature effects, it is necessary to employ some sort of R_r identifier. A novel R_r identifier must be based on the same improved model that is used for the development of the novel controller.
- 7) To develop a simple experimental procedure for identification of the inverse magnetising curve, that can be easily implemented in the actual vector controller.

- 8) To experimentally confirm the results obtained in objective 2.

1.3.2. Investigation approaches

In agreement with the above research objectives, the research is divided into several stages, during which different investigative approaches are utilised.

- 1) Derivation of improved machine models encompasses :
 - a) Inclusion of main flux saturation and/or iron loss in general induction machine models in arbitrary reference frame.
 - b) Derivation of mixed current-flux models and their reduction.
 - c) Application of rotor flux orientation constraints onto the reduced models, which result in the rotor-flux-oriented improved models.
- 2) Quantitative investigation of detuning effects includes :
 - a) Experimental identification of the parameters of an induction machine. This procedure involves measuring some variables in the machine and calculating some parameters on the basis of an adopted machine model.
 - b) Analysis of detuning effects in steady-state operation of the drive is based on the steady-state detuning expressions. These expressions are derived by an already known mathematical methodology, from steady-state mathematical models of both induction machine and vector controller, adopting certain assumptions. The expressions are obtained for each detuning source and then for several combinations of sources.
 - c) Quantitative study of detuning due to different detuning sources. This is done for specific induction machines using the appropriate detuning expressions. Since the detuning expressions involve an equation of up to the fifth order and parameter variations are non-linear, the results are obtained using the iterative procedure incorporated into custom-made FORTRAN programs.
 - d) Studies of detuning effects in transient operation are based on simulation of the whole vector controlled induction machine drive. A simulation model consists of an appropriate dynamic machine model and a full model of a control system,

along with simplified models of supply converter and feedback devices. In this part of the work an appropriate simulation package is used.

- 3) Design of improved vector controllers by applying steady-state simplifications on the improved rotor-flux-oriented models, developed under objective 1.
- 4) For analyses of detuning when the improved estimators are implemented, the approaches 2.b to 2.d. are used, but now in conjunction with improved machine models and improved vector controllers.
- 5) Comparison of performance obtained by CPM-based and improved vector controllers.
- 6) An auxiliary control circuit for R_r identification is derived using an existing approach, but is here based on the equations obtained from improved machine models. The operation of the improved R_r is investigated by dynamic simulations, using a simulation package.
- 7) Using the experimental rig, a novel identification procedure suitable for vector controlled drives is devised.
- 8) Experimental verification of the theoretically established consequences of detuning is realised by changing the control parameters of the experimental rig, so that detuned operation occurs. The variables are recorded and the actual detuning is assessed.

1.3.3. Originality of the research

Investigation of parameter variations is not a revolutionary new research topic. However, it has been noted that research into detuning effects induced by iron loss has attracted research interest only recently and only the tip of an iceberg has been revealed. Hence there is a wide scope for further research. Original research results constitute major portions of Chapters 3, 4, 5, 6 and 7. The originality of this thesis lies in the following areas:

- 1) Evaluation of detuning in the vector-controlled induction machine drive due to iron loss in the field-weakening region.

- 2) Evaluation of detuning in the vector-controlled induction machine drive introduced by combined influence of main flux saturation and iron loss.
- 3) Comparative analysis of detuning due to different phenomena.
- 4) Investigation of the accuracy and convergence speed of a specific MRAC-based R_r identification scheme, regarding impact of parameter variations on its accuracy.
- 5) Development of several novel vector controllers.
- 6) Development of novel R_r identification scheme that is to be used in conjunction with the improved vector controllers.
- 7) Development of a novel procedure for identification of the magnetising curve.

1.4. THESIS OUTLINE

An overview of existing knowledge in the area of vector control is given in Chapter 2. In order to thoroughly explain the vector control theory, the whole derivation procedure is presented, starting with mathematical modelling of induction machines, which is presented in section 2.2. The CPM in the three-phase domain is discussed first, then transformed into a general CPM in the two-phase domain and the corresponding equivalent scheme is derived. The mixed current-flux CPM is derived next and a possibility to reduce the number of equations, by treating the induction machine as current-fed, is explained. In section 2.3. principles of vector control are discussed and the rotor flux orientation constraints are given. Their application to the mixed current-flux models results in RFO models, which constitute the basis for design of estimator for feedback vector control schemes or for determination of gains in feed-forward schemes. Rotor-flux-oriented control with voltage feeding is then presented, followed by a brief description of SFO and AFO. Existing work on detuning in vector controlled induction machine drives is overviewed in section 2.4. Consequences of detuning are discussed first, followed by the detailed discussion on work published so far concerning detuning due to three particular phenomena : main flux saturation, iron loss and R_r variations. Finally, section 2.5. presents an overview of the improved mathematical models and the improved vector controllers, that have been proposed for reduction and eventual elimination of detuning. In accordance with the discussion from sub-section

1.2.2, the improved models and the compensation techniques are grouped depending on which detuning source they are designed to compensate for.

This research project has resulted in development of novel improved mathematical models and novel improved rotor flux estimators, which are presented in Chapter 3. Step-by-step procedure for derivation of improved models and for the design of improved estimators is given. Models and estimators with main flux saturation, utilising two different representations of saturation, are presented in section 3.2. Section 3.3. presents improved models and improved estimators with iron loss. Two ways of iron loss representation are discussed and the one that results in simpler models is utilised for the design of an improved estimator. As inclusion of iron loss increases the order of the models and the complexity of the estimator, a possible way of simplifying the estimator is shown. Inclusion of both iron loss and main flux saturation is presented in section 3.4. Two representations of main flux saturation are combined with the simpler representation of iron loss, yielding two improved RFO models and two improved estimators. Simplifications similar to those used in conjunction with the estimators with iron loss are adopted and simplified versions of both estimators are obtained. Contributions of the chapter 3 are summarised in section 3.5.

Detailed analysis of detuning due to different phenomena, that occurs when the CPM-based estimator is employed, is presented in chapter 4. Experimental determination of the machine parameters is presented in section 4.2. The methods and quantities by which detuning is assessed are explained in section 4.3. Section 4.4 presents analyses of detuning in steady-state operation that occurs due to four detuning sources. For each analysis, the detuning expressions are derived first, followed by quantitative assessment of detuning in different operating regimes for a particular machine. Comparison of steady-state detuning that occurs due to different phenomena is performed in section 4.5. Detuning in transient operation of the drive is investigated by means of simulation in section 4.6. Contributions of the chapter are summarised in the section 4.7.

Compensation of detuning, obtainable when novel improved rotor flux estimators are employed, is investigated in chapter 5. Steady-state detuning with improved estimators is investigated in section 5.2, for estimators with main flux saturation, with iron loss and with both these phenomena. It is shown that they can successfully compensate detuning in some operating regimes. The behaviour of the improved estimators is then simulated

in transient operation and results are given in section 5.3. The summary of the chapter is given in the section 5.4.

Chapter 6 presents identification of rotor resistance using the MRAC approach, with the identification schemes based on the reactive power. Identification utilising CPM-based R_r identification scheme in the feedback RFOC is investigated in section 6.2. It is shown that CPM-based identifier manages to eliminate detuning in steady-state operation in the base speed region but exhibits poor performance in other operating conditions. Therefore two improved R_r identification schemes are proposed and their improved performance is confirmed in section 6.3. Finally, section 6.4 summarises the contributions of the chapter.

Experimental investigation is presented in Chapter 7. The experimental rig, which consists of a feed-forward vector-controlled drive and the DC machine operating as generator, and the measuring equipment are described in section 7.2, while section 7.3. covers identification of the machine parameters from standard tests. For correct operation of the drive in the field-weakening region, it is necessary to incorporate the magnetising curve of the motor into the control algorithm. In section 7.4. existing identification procedures are reviewed and a novel method for identification of the inverse magnetising curve, that utilises the PWM inverter used for normal operation, is proposed. The proposed procedure is verified by comparing the results with the results obtained using standard no-load tests. Section 7.5. presents the experiments concerned with determination of the slip gain. The results of experiments concerned with detuning in the RFO drive due to parameter variation, due to inaccurate slip gain setting, and due to main flux saturation are presented in sections 7.6 for steady-state operation and in section 7.7 for transient operation. Section 7.8. summarises the Chapter 7.

Chapter 8 is the concluding chapter. The thesis summary is given in section 8.1. The outcomes of the research and the main conclusions are presented in section 8.2, while section 8.3 elaborates several possibilities for further work.

The list of referenced literature is given in chapter 9.

Appendix A contains the data of the three induction machines used throughout the thesis, while Appendix B contains copies of the research publications that are direct result of this project.

2. LITERATURE REVIEW

2.1. INTRODUCTION

Vector controllers are designed on the basis of induction machine mathematical models. Dynamic mathematical models, that describe dynamic operation, under arbitrary supply voltage (or current) waveforms, have to be used for the design, since voltages and currents supplied to a vector controlled induction machine are not sinusoidal, even in a steady-state operation. Induction machine models and vector controllers presented in this chapter are already known in the literature.

As discussed previously, huge variety of vector control schemes exists and it is an almost impossible task to comprehensively analyse all of them. The thesis concentrates on rotor-flux-oriented control applied to a current-fed induction machine. Some other orientation schemes are briefly presented as well.

Majority of existing vector controllers for induction machines are based on the dynamic constant parameter model (CPM) in a two-phase common reference frame. Hence detailed procedure for deriving the CPM is presented in section 2.2. The adopted assumptions and idealisations are presented at first, and model in the three-phase domain is given. This is followed by an explanation of the transformation procedure, which transforms the three-phase domain model into the two-phase domain model. The resulting CPM in a two-phase common reference frame is presented next. Then the space vectors are introduced and utilised for construction of the equivalent circuit. Finally, the mixed current-flux CPM in state-space form is presented and accordingly utilised for derivation of the reduced-order CPM, suitable for representing current-fed machines.

Basic principles of vector control are presented in section 2.3. Rotor-flux-oriented control of an induction machine is discussed in detail. Rotor flux orientation constraints are presented and consequently applied to the reduced-order CPM, which results in the rotor-flux oriented constant parameter model (RFO CPM). On the basis of this model, both feedback and feed-forward RFO control schemes are derived for a current-fed machine. After this, RFO control of a voltage-fed machine is described. Finally, other orientation possibilities like SFOC and AFOC are briefly reviewed.

Theoretical considerations and previous work on detuning in vector controlled induction machine drives are reviewed in section 2.4. Detuning due to main flux saturation, due to iron loss, due to variations in rotor time constant and due to variations in rotor leakage inductance are discussed separately.

Improved mathematical models and improved vector controllers, proposed in literature so far, are reviewed in section 2.5. Improved models and improved estimators for RFO control with main flux saturation, improved models and improved feed-forward controller with iron loss and a rotor resistance identifier based on the model reference adaptive control theory are discussed. Finally, section 2.6 brings the summary of the chapter.

2.2. MATHEMATICAL MODELLING OF AN INDUCTION MACHINE

Electrical machines are physical objects aimed for conversion of the electrical energy into the mechanical energy and vice versa. Electrical, magnetic and mechanical phenomena interact in a machine in a complex manner. The general theory of electrical machines [Krause, 1990; Vas, 1992; Vuckovic, 1992] attempts to represent the phenomena in these physical objects by mathematical models. Mathematical models are sets of equations that mathematically describe physical relationships between certain quantities in machines. Mathematical models have to fulfil two contradictory requirements - faithfully represent the phenomena in electrical machines and be simple to use and analyse. In accordance with the latter requirement, they are derived with a number of assumptions and simplifications. The simplification procedure results in the loss of information about phenomena that are postulated to be of the secondary importance [Vuckovic, 1992].

2.2.1. Mathematical model of an induction machine in the three-phase domain

The procedure of mathematical modelling of an induction machine starts with adopting the following assumptions and idealisations : stator phase windings are identical with the mutual space displacement of exactly 120 electrical degrees; magnetomotive force of a winding is sinusoidally distributed along the air-gap circumference; parasitic capacitances are neglected; air-gap is constant (impact of stator and rotor slots is

neglected); the rotor cage winding can be substituted with the balanced three-phase winding; resistances and leakage inductances of the windings are constant parameters; iron loss is neglected; and the magnetising curve is treated as a linear function i.e. main flux saturation is neglected.

When these assumptions are adopted, the mathematical model of an induction machine in the three-phase domain, in terms of instantaneous variables, is given with the following expressions :

$$\underline{v}_{abc} = R_s \underline{i}_{abc} + \frac{d\underline{\psi}_{abc}}{dt} \quad (2.1)$$

$$\underline{v}_{ABC} = 0 = R_r \underline{i}_{ABC} + \frac{d\underline{\psi}_{ABC}}{dt} \quad ,$$

$$\underline{\psi}_{abc} = \underline{L}_s \underline{i}_{abc} + \underline{L}_{sr} \underline{i}_{ABC} \quad (2.2)$$

$$\underline{\psi}_{ABC} = \underline{L}_r \underline{i}_{ABC} + \underline{L}'_{sr} \underline{i}_{abc} \quad ,$$

$$T_e = \frac{P}{2} \underline{i}' \frac{d\underline{L}}{d\theta} \underline{i} = P \underline{i}'_{abc} \frac{d\underline{L}_{sr}}{d\theta} \underline{i}_{ABC} \quad , \quad (2.3)$$

$$T_e - T_L = \frac{J}{P} \frac{d\omega}{dt} + \frac{1}{P} k\omega \quad . \quad (2.4)$$

In equations (2.1) - (2.4) the lower case indices apply to the stator quantities, while the upper case indices denote the rotor quantities. Matrices in (2.1) - (2.3) are :

$$\underline{v}_{abc} = \begin{bmatrix} v_a \\ v_b \\ v_c \end{bmatrix} \quad ; \quad \underline{i}_{abc} = \begin{bmatrix} i_a \\ i_b \\ i_c \end{bmatrix} \quad ; \quad \underline{\psi}_{abc} = \begin{bmatrix} \psi_a \\ \psi_b \\ \psi_c \end{bmatrix} \quad (2.5)$$

$$\underline{v}_{ABC} = \begin{bmatrix} v_A \\ v_B \\ v_C \end{bmatrix} = \begin{bmatrix} 0 \\ 0 \\ 0 \end{bmatrix} \quad ; \quad \underline{i}_{ABC} = \begin{bmatrix} i_A \\ i_B \\ i_C \end{bmatrix} \quad ; \quad \underline{\psi}_{ABC} = \begin{bmatrix} \psi_A \\ \psi_B \\ \psi_C \end{bmatrix} \quad ,$$

$$\underline{i} = \begin{bmatrix} \underline{i}_{abc} \\ \underline{i}_{ABC} \end{bmatrix} \quad ; \quad \underline{L} = \begin{bmatrix} \underline{L}_s & \underline{L}_{sr} \\ \underline{L}'_{sr} & \underline{L}_r \end{bmatrix} \quad , \quad (2.6)$$

where the sub-matrices of the inductance matrix \underline{L} are :

$$\underline{L}_{sr} = L_{sa} \begin{bmatrix} \cos\theta & \cos\left(\theta + \frac{2\pi}{3}\right) & \cos\left(\theta - \frac{2\pi}{3}\right) \\ \cos\left(\theta - \frac{2\pi}{3}\right) & \cos\theta & \cos\left(\theta + \frac{2\pi}{3}\right) \\ \cos\left(\theta + \frac{2\pi}{3}\right) & \cos\left(\theta - \frac{2\pi}{3}\right) & \cos\theta \end{bmatrix} \quad , \quad (2.7.a)$$

$$\underline{L}_s = \begin{bmatrix} L_{aa} & L_{ab} & L_{ac} \\ L_{ba} & L_{bb} & L_{bc} \\ L_{ca} & L_{cb} & L_{cc} \end{bmatrix} = L_{aa} \begin{bmatrix} 1 & -1/2 & -1/2 \\ -1/2 & 1 & -1/2 \\ -1/2 & -1/2 & 1 \end{bmatrix} \quad (2.7.b)$$

$$\underline{L}_r = \begin{bmatrix} L_{AA} & L_{AB} & L_{AC} \\ L_{BA} & L_{BB} & L_{BC} \\ L_{CA} & L_{CB} & L_{CC} \end{bmatrix} = L_{AA} \begin{bmatrix} 1 & -1/2 & -1/2 \\ -1/2 & 1 & -1/2 \\ -1/2 & -1/2 & 1 \end{bmatrix}$$

The angle θ in (2.3) and (2.7.a) denotes the instantaneous position of the revolving magnetic axis of the rotor phase 'A' winding with respect to the stationary magnetic axis of the stator phase 'a' winding. The angle θ is correlated with the rotor electrical speed of rotation ω through dependence :

$$\theta = \theta(0) + \int \omega dt \quad (2.8)$$

Substitution of (2.5) - (2.7) into (2.3) gives the torque equation in the developed form :

$$T_e = -PL_{aa} \left\{ \sin\theta(i_a i_A + i_b i_B + i_c i_C) + \sin\left(\theta - \frac{2\pi}{3}\right)(i_a i_C + i_b i_A + i_c i_B) + \sin\left(\theta + \frac{2\pi}{3}\right)(i_a i_B + i_b i_C + i_c i_A) \right\} \quad (2.9)$$

The mathematical model of an induction machine in the three-phase domain is given with (2.1)-(2.8). In a developed form, it consists of seven first-order non-linear differential equations, one integral equation and seven algebraic equations. Some coefficients in these 15 equations are time-varying, because the rotor position θ changes as the rotor revolves. As such, the three-phase time-domain model is inconvenient even for simulation of an induction machine, needless to mention control system design. Furthermore, principles of vector control cannot be explained and understood from this model.

2.2.2. Transformation procedure

Inconvenience of the three-phase time-domain mathematical model can be mastered by applying an appropriate mathematical transformation that will transform it into a simpler model. The most commonly used transformation is the irregular Blondel's (or Park's) transformation [Krause, 1990]. The irregular Blondel's transformation is performed by transforming the stator equations and the rotor equations by means of \underline{B}_s and \underline{B}_r transformation matrices, respectively :

$$\underline{B}_s = \frac{2}{3} \begin{bmatrix} \cos \theta_s & \cos\left(\theta_s - \frac{2\pi}{3}\right) & \cos\left(\theta_s + \frac{2\pi}{3}\right) \\ -\sin \theta_s & -\sin\left(\theta_s - \frac{2\pi}{3}\right) & -\sin\left(\theta_s + \frac{2\pi}{3}\right) \end{bmatrix}, \quad (2.10.a)$$

$$\underline{B}_r = \frac{2}{3} \begin{bmatrix} \cos \theta_r & \cos\left(\theta_r - \frac{2\pi}{3}\right) & \cos\left(\theta_r + \frac{2\pi}{3}\right) \\ -\sin \theta_r & -\sin\left(\theta_r - \frac{2\pi}{3}\right) & -\sin\left(\theta_r + \frac{2\pi}{3}\right) \end{bmatrix}. \quad (2.10.b)$$

The angles introduced in the transformation matrices are defined and mutually correlated through the following expressions :

$$\theta_s = \theta_s(0) + \int_0^t \omega_a dt \quad ; \quad \theta_r = \theta_s - \theta = \theta_r(0) + \int_0^t (\omega_a - \omega) dt, \quad (2.11)$$

where ω_a is an arbitrary angular speed.

The transformation procedure may be viewed as a substitution of the actual stator and rotor three-phase windings ($a-b-c$ and $A-B-C$, respectively) with the new, fictitious, two-phase windings ($ds-qs$ and $dr-qr$, respectively). The new windings are mutually perpendicular, so that there is no magnetic coupling between a d -axis winding and a q -axis winding. The transformation given with (2.10) is called irregular since the zero sequence components are omitted. This is appropriate when the machine windings are connected in star connection without neutral lead and/or when a machine is supplied from a balanced three-phase source.

The transformation matrices for the stator windings (2.10.a) and for the rotor windings (2.10.b) differ in the sense that different angles are met in \sin and \cos terms in them. Selection of angles according to (2.11) removes relative motion between the new stator windings and the new rotor windings. In this way both stator and rotor $d-q$ windings rotate with the same arbitrary angular speed (ω_a) and single $d-q$ axis system is valid for both stator and rotor. These are the reasons why this type of transformation is usually termed 'transformation to the common arbitrary reference frame' and the models obtained are referred to as 'models in a two-phase common reference frame'. Due to the non-salient nature of an induction machine, any angular speed can be chosen as the angular speed of the common reference frame.

For transforming d - q quantities back into the original three-phase domain, the inverse irregular Blondel's transformation is used, which can be given as :

$$\underline{B}_s^{-1} = \begin{bmatrix} \cos \theta_s & -\sin \theta_s \\ \cos \left(\theta_s - \frac{2\pi}{3} \right) & -\sin \left(\theta_s - \frac{2\pi}{3} \right) \\ \cos \left(\theta_s + \frac{2\pi}{3} \right) & -\sin \left(\theta_s + \frac{2\pi}{3} \right) \end{bmatrix}, \quad (2.10.c)$$

$$\underline{B}_r^{-1} = \begin{bmatrix} \cos \theta_r & -\sin \theta_r \\ \cos \left(\theta_r - \frac{2\pi}{3} \right) & -\sin \left(\theta_r - \frac{2\pi}{3} \right) \\ \cos \left(\theta_r + \frac{2\pi}{3} \right) & -\sin \left(\theta_r + \frac{2\pi}{3} \right) \end{bmatrix}. \quad (2.10.d)$$

2.2.3. The constant parameter model in a two-phase common reference frame

Application of the transformation (2.10.a) and (2.10.b) on the model in the three-phase domain (2.1)-(2.3) results in the mathematical model in an arbitrary two-phase reference frame, consisting of the following expressions [Krause, 1990; Vuckovic, 1992] :

$$\underline{v}_s = R_s \underline{i}_s + \frac{d\underline{\psi}_s}{dt} + \omega_a \underline{G} \underline{\psi}_s \quad (2.12)$$

$$\underline{v}_r = 0 = R_r \underline{i}_r + \frac{d\underline{\psi}_r}{dt} + (\omega_a - \omega) \underline{G} \underline{\psi}_r$$

$$\underline{\psi}_s = L_s \underline{i}_s + L_m \underline{i}_r \quad (2.13)$$

$$\underline{\psi}_r = L_m \underline{i}_s + L_r \underline{i}_r$$

$$T_e = \frac{3}{2} P \underline{i}_s^t \underline{G} \underline{\psi}_s \quad (2.14)$$

where the matrices are :

$$\begin{aligned} \underline{v}_s &= \underline{B}_s \underline{v}_{abc} = \begin{bmatrix} v_{ds} \\ v_{qs} \end{bmatrix} ; & \underline{i}_s &= \underline{B}_s \underline{i}_{abc} = \begin{bmatrix} i_{ds} \\ i_{qs} \end{bmatrix} ; & \underline{\psi}_s &= \underline{B}_s \underline{\psi}_{abc} = \begin{bmatrix} \psi_{ds} \\ \psi_{qs} \end{bmatrix} \\ \underline{v}_r &= \begin{bmatrix} v_{dr} \\ v_{qr} \end{bmatrix} = \begin{bmatrix} 0 \\ 0 \end{bmatrix} ; & \underline{i}_r &= \underline{B}_r \underline{i}_{ABC} = \begin{bmatrix} i_{dr} \\ i_{qr} \end{bmatrix} ; & \underline{\psi}_r &= \underline{B}_r \underline{\psi}_{ABC} = \begin{bmatrix} \psi_{dr} \\ \psi_{qr} \end{bmatrix} \quad (2.15) \\ \underline{G} &= \begin{bmatrix} 0 & -1 \\ 1 & 0 \end{bmatrix} \end{aligned}$$

In equations (2.13) the two-phase inductances are correlated with the three-phase inductances by the following expressions :

$$L_s = L_{aa} - L_{ab} = \frac{3}{2}L_{aa} \quad ; \quad L_r = L_{AA} - L_{AB} = \frac{3}{2}L_{AA} \quad ; \quad L_m = \frac{3}{2}L_{aA} \quad . \quad (2.16)$$

The mechanical equation of motion remains unchanged :

$$T_e - T_L = \frac{J}{P} \frac{d\omega}{dt} + \frac{1}{P} k\omega \quad . \quad (2.4)$$

The electromagnetic torque, expressed in terms of d - q variables, becomes :

$$T_e = \frac{3}{2} P (\psi_{ds} i_{qs} - \psi_{qs} i_{ds}) \quad . \quad (2.17.a)$$

The model, given with (2.4), (2.11)-(2.13) and (2.17.a), is denoted as the constant parameter model, since it is assumed that all the parameters do not change. It is much simpler than the model in the three-phase domain, due to several reasons. The time dependence in the mutual inductances, that occurs due to rotor revolution, has been eliminated (inductances in (2.13) and (2.16) are not dependent on angle θ any more). Due to the omission of the zero sequence variables, the number of equations is reduced to five differential and five algebraic equations. The equations themselves have become much simpler. In particular, the torque equation (2.17.a) is significantly simpler than (2.9). The simplicity of this model enables its successful application for control purposes, for analyses, for dynamic simulation, for derivation of the equivalent circuits, etc. Another important feature of this model is that it provides an easy explanation of the vector control principles, as well as an easy derivation of models with vector control constraints and subsequent design of vector controllers.

The CPM in an arbitrary frame of reference yields a unique model for any specified value of the angular velocity of the common reference frame (ω_a). Models in the stationary (stator) reference frame, in the synchronous reference frame, in the rotor reference frame, in reference frames fixed to the space vectors of the rotor flux, the stator flux or the air-gap flux can be derived by appropriate setting of ω_a . All variables (voltages, currents and flux linkages) are transformed, so that the correlation between three-phase (a - b - c) and two-phase (d - q) variables, given with (2.10), has to be accounted for in any application of the model.

There are several possible alternative forms of the CPM presented above. One of the alternative forms can be obtained by introducing the leakage inductances as :

$$\begin{aligned} L_{ls} &= L_s - L_m \\ L_{lr} &= L_r - L_m \end{aligned} \quad (2.18)$$

and the magnetising current and the magnetising flux as :

$$i_m = i_s + i_r \quad (2.19)$$

$$\underline{\psi}_m = L_m i_m \quad (2.20)$$

where the matrices are :

$$i_m = \begin{bmatrix} i_{dm} \\ i_{qm} \end{bmatrix} ; \quad \underline{\psi}_m = \begin{bmatrix} \psi_{dm} \\ \psi_{qm} \end{bmatrix} \quad (2.21)$$

Implementing (2.18)-(2.20), flux equations (2.13) become :

$$\begin{aligned} \underline{\psi}_s &= L_{ls} i_s + L_m (i_s + i_r) = L_{ls} i_s + L_m i_m = L_{ls} i_s + \underline{\psi}_m \\ \underline{\psi}_r &= L_{lr} i_r + L_m (i_r + i_s) = L_{lr} i_r + L_m i_m = L_{lr} i_r + \underline{\psi}_m \end{aligned} \quad (2.22)$$

Substitution of (2.22) into voltage equations (2.12) gives :

$$\begin{aligned} v_s &= R_s i_s + \frac{d(L_{ls} i_s)}{dt} + \frac{d\underline{\psi}_m}{dt} + \omega_a L_{ls} \underline{G} i_s + \omega_a \underline{G} \underline{\psi}_m \\ 0 &= R_r i_r + \frac{d(L_{lr} i_r)}{dt} + \frac{d\underline{\psi}_m}{dt} + \omega_a L_{lr} \underline{G} i_r + \omega_a \underline{G} \underline{\psi}_m - \omega \underline{G} \underline{\psi}_r \end{aligned} \quad (2.23)$$

while substitution of (2.22) into the torque equation (2.17.a) results in several alternative expressions for the electromagnetic torque [Vuckovic, 1992] :

$$T_e = \frac{3}{2} P \frac{L_m}{L_r} (\psi_{dr} i_{qs} - \psi_{qr} i_{ds}) \quad (2.17.b)$$

$$T_e = \frac{3}{2} P \frac{1}{L_{lr}} (\psi_{dr} \psi_{qm} - \psi_{qr} \psi_{dm}) \quad (2.17.c)$$

$$T_e = \frac{3}{2} P L_m (i_{dr} i_{qs} - i_{qr} i_{ds}) \quad (2.17.d)$$

$$T_e = \frac{3}{2} P (\psi_{dm} i_{qs} - \psi_{qm} i_{ds}) \quad (2.17.e)$$

$$T_e = \frac{3}{2} P \frac{L_m}{L_{lr}} (\psi_{dr} i_{qm} - \psi_{qr} i_{dm}) \quad (2.17.f)$$

In this way one of the alternative forms of the model is given by equations (2.4), (2.19), (2.20), (2.22), (2.23) and one of the (2.17). This model, that uses the mutual inductance and the leakage inductances, is convenient for derivation of the equivalent circuits.

2.2.4. The equivalent circuit for the constant parameter model

Equivalent circuits are another way to represent phenomena in electrical machines. Their benefit is that a circuit consisting of resistors, inductors and voltage sources is an explanation tool that is much easier to comprehend than a set of equations. This is especially true in steady-state operation with sine-wave supply, when equivalent circuits become very simple. Equivalent circuits are normally derived from mathematical models in a two-phase common reference frame. If the d - q components are used for equivalent circuit representation, it would be necessary to have two very similar equivalent circuits, one for d -axis and one for q -axis. Hence space vectors [Vas, 1992] are more suitable for derivation of equivalent circuits. In general, a space vector is a complex variable consisting of a d -axis component as the real part and a q -axis component as the imaginary part of a space vector. Thus space vectors are defined as :

$$\bar{f}_i = f_{di} + j f_{qi} , \quad (2.24)$$

where f can denote voltage, current or flux ($f = v, i, \psi$), while index i can denote stator, rotor or magnetising variable ($i = s, r, m$). Using the space vector representation, and adopting that all the parameters are constant, voltage equations (2.23) become:

$$\begin{aligned} \bar{v}_s &= R_s \bar{i}_s + L_{ls} \frac{d\bar{i}_s}{dt} + j\omega_a L_{ls} \bar{i}_s + L_m \frac{d\bar{i}_m}{dt} + j\omega_a L_m \bar{i}_m \\ 0 &= R_r \bar{i}_r + L_{lr} \frac{d\bar{i}_r}{dt} + j\omega_a L_{lr} \bar{i}_r + L_m \frac{d\bar{i}_m}{dt} + j\omega_a L_m \bar{i}_m - j\omega \bar{\psi}_r \end{aligned} \quad (2.25)$$

and the torque equation becomes :

$$T_e = \frac{3}{2} P \operatorname{Im}(\bar{i}_s \bar{\psi}_s^*) , \quad (2.17.g)$$

where the asterisk represents complex conjugation.

On the basis of (2.25) it is possible to construct the dynamic equivalent circuit of an induction machine. The Ri terms correspond to voltage drops across resistors, the $L \frac{di}{dt}$

terms correspond to voltage drops across inductances, while the $j\omega\psi$ and the $j\omega_a\psi$ terms correspond to induced electromotive forces. It should be noted that the existence of the terms containing ω_a depends on the chosen angular speed of the reference frame. The equivalent circuit of an induction machine, based on equation (2.25), is shown in Fig. 2.1. Although the appearance of the equivalent circuit resembles the steady-state equivalent circuit of an induction machine, there are several differences. The main one is that the variables in the circuit of Fig. 2.1 are space vectors, while in the steady-state circuit phasors are used. Hence this circuit is valid not only for a symmetrical sine-wave supply (as the steady-state circuit is), but for any type of voltage excitation (i.e. for inverter supply as well). The second important feature of this equivalent circuit is that it is valid not only for steady state-operation, but for transient operation as well.

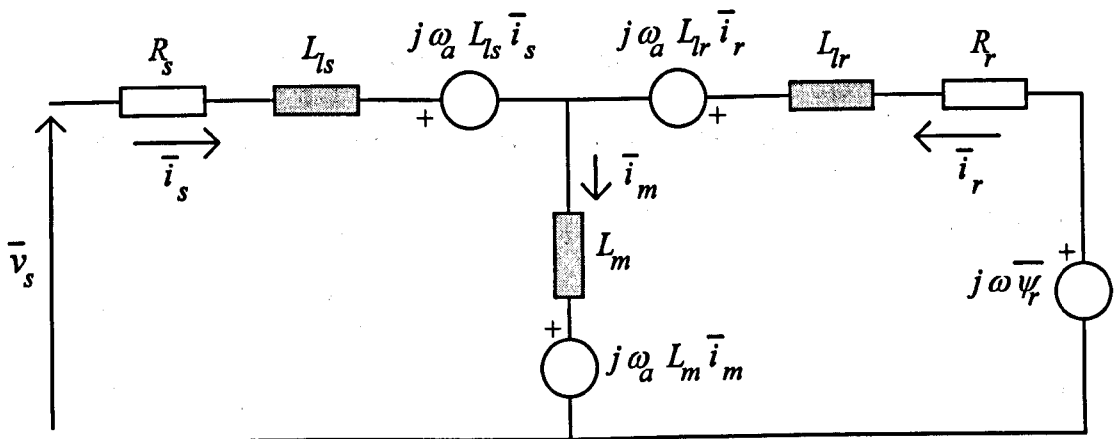


Figure 2.1 : Induction machine dynamic equivalent circuit in an arbitrary reference frame, constant parameters.

2.2.5. The \bar{i}_s - $\bar{\psi}_r$ mixed current-flux constant parameter model

The form of the CPM presented in sub-section 2.2.3., although convenient for derivation of the equivalent circuit, is not very beneficial for analytical studies of dynamics, for simulations or for control purposes. Thus the model should be reformulated in a state-space form, where a state vector, consisting of four state variables, is used to represent machine's electromagnetic behaviour. The equation of mechanical motion is treated separately. Different sets of state variables can be used and there are fourteen possible combinations [Levi, 1995a], usually arranged in three groups. Flux-based models feature fluxes, current-based models feature currents, while mixed current-flux models

feature a current (stator, rotor, or magnetising) and a flux (stator, rotor or magnetising) as state variables [Levi and Krzeminski, 1996].

The mixed current-flux model where the stator current and the rotor flux are chosen as state variables (i_s - ψ_r model) is best suited for the RFOC with supply from a current source. The suitability stems from the fact that the stator current is the input to a vector controlled machine and the rotor flux is the variable to be controlled. Procedure for derivation of the i_s - ψ_r mixed current-flux model involves selecting the stator current and the rotor flux as state variables, expressing all other variables in terms of them and substituting these expressions in the general model. Mixed current-flux models can be represented in a form :

$$\underline{v} = \underline{A} \frac{d\underline{x}}{dt} + \underline{B}\underline{x} \quad , \quad (2.26)$$

where \underline{x} is a state vector and \underline{v} is an input vector of voltages.

For the i_s - ψ_r mixed current-flux CPM, the vector of voltages is :

$$\underline{v} = [v_{ds} \quad v_{qs} \quad 0 \quad 0]^t \quad , \quad (2.27)$$

and the state vector is :

$$\underline{x} = [i_{ds} \quad i_{qs} \quad \psi_{dr} \quad \psi_{qr}]^t \quad . \quad (2.28)$$

The matrices \underline{A} and \underline{B} are :

$$\underline{A} = \begin{bmatrix} \sigma L_s & 0 & \frac{L_m}{L_r} & 0 \\ 0 & \sigma L_s & 0 & \frac{L_m}{L_r} \\ 0 & 0 & 1 & 0 \\ 0 & 0 & 0 & 1 \end{bmatrix} \quad , \quad (2.29)$$

$$\underline{B} = \begin{bmatrix} R_s & -\omega_a \sigma L_s & 0 & -\omega_a \frac{L_m}{L_r} \\ \omega_a \sigma L_s & R_s & \omega_a \frac{L_m}{L_r} & 0 \\ -\frac{L_m}{T_r} & 0 & \frac{1}{T_r} & -(\omega_a - \omega) \\ 0 & -\frac{L_m}{T_r} & \omega_a - \omega & \frac{1}{T_r} \end{bmatrix} \quad , \quad (2.30)$$

where the total leakage inductance of the machine σ is defined as :

$$\sigma = 1 - \frac{L_m^2}{L_s L_r} , \quad (2.31)$$

and the rotor time constant T_r is :

$$T_r = \frac{L_r}{R_r} . \quad (2.32)$$

Equation that describes developed electromagnetic torque :

$$T_e = \frac{3}{2} P \frac{L_m}{L_r} (\psi_{dr} i_{qs} - \psi_{qr} i_{ds}) , \quad (2.17.b)$$

and the equation of mechanical motion, that can be rearranged as :

$$\frac{d\omega}{dt} = \frac{P}{J} (T_e - T_L) - \frac{1}{J} k\omega , \quad (2.33)$$

complete the model.

2.2.6. The i_s - ψ_r reduced-order constant parameter model

An induction machine in a vector controlled drive is very often supplied from a current-controlled PWM inverter that may be treated as a current source. In this case the stator current is known while the stator voltage is not known, but is not needed either. Thus the stator voltage equation can be omitted from consideration. Such mathematical models may be called reduced-order models, as the number of the differential equations (and hence the order of the model) is reduced. This differs from the definition of a reduced-order model commonly used in general theory of electrical machines, where the order of the model is reduced by neglecting some of the phenomena that are less influential on machine dynamics.

The i_s - ψ_r reduced-order CPM model is therefore derived from the i_s - ψ_r mixed current-flux CPM model, by reducing the state vector to the d - q rotor flux components and by omitting the stator voltage equations (the first two rows in matrices A and B). The d - q components of the stator current are considered as the input variables. When the flux derivatives are transferred to the left-hand side of the equations, the reduced-order CPM in developed form is given with :

$$\frac{d\psi_{dr}}{dt} = -\frac{1}{T_r} \psi_{dr} + \frac{1}{T_r} L_m i_{ds} + (\omega_a - \omega) \psi_{qr} \quad (2.34)$$

$$\frac{d\psi_{qr}}{dt} = -\frac{1}{T_r} \psi_{qr} + \frac{1}{T_r} L_m i_{qs} - (\omega_a - \omega) \psi_{dr}$$

$$\frac{d\omega}{dt} = \frac{P}{J} (T_e - T_L) - \frac{1}{J} k\omega \quad (2.33)$$

$$T_e = \frac{3}{2} P \frac{L_m}{L_r} (\psi_{dr} i_{qs} - \psi_{qr} i_{ds}) \quad (2.17.b)$$

This model is used as a basis for derivation of the RFO CPM and for design of vector controllers with orientation along the rotor flux space vector.

2.3. PRINCIPLES OF VECTOR CONTROL

Decoupled flux and torque control is realised by controlling the position and the amplitude of the stator current space vector with respect to the chosen flux space vector. The stator current space vector can be oriented with respect to the space vectors of either the rotor flux, the stator flux or the air-gap flux. At the same time, the induction machine can be fed from either voltage or current source [Vas, 1990; Trzynadlovski, 1994]. If SFOC or AFOC methods are employed, an appropriate decoupling circuit has to be inserted in the control part of the system, no matter whether the machine is fed from voltage or current source. A similar conclusion is valid for the voltage-fed induction machine with a RFOC method.

This leaves the RFOC of a current-fed induction machine as the only control method that does not need any decoupling circuit. Another advantage of the RFOC is that it offers a theoretically infinite maximal (pull-out) torque. In practice, however, the pull-out torque will have a finite value, due to magnetic saturation, possible parameter variations and, of course, capabilities of the inverter.

Orientation along the air-gap flux space vector did not get much attention until very recently. Apart from expensive and temperature-sensitive Hall probes, measurement of the position and the amplitude of the air-gap flux can be obtained by using a tapped stator windings [Lipo and Chang, 1988]. This approach to flux sensing is robust to changes in the stator resistance (R_s) and changes in L_{ls} since the taps can be arranged to cancel the voltage drops across R_s . Flux sensing by the tapped windings is convenient

for the AFOC schemes. It was also used in conjunction with the universal field controller operating in the reference frame attached to the air-gap flux [De Doncker et al., 1994]. Additionally, machines with either deep-bar or double cage rotor construction are usually modelled with a ladder network representing the rotor winding by two or more branches [Vas, 1992]. In this case there are at least two rotor fluxes and the dilemma which one should be used for the orientation is posed. This leaves the AFOC as an attractive orientation possibility [De Doncker, 1992; Healey, 1995; Williamson and Healey, 1996].

Orientation along the stator flux also remained beyond the scope of interest for a long time. However, recent advancements in microprocessors and DSPs have enabled significantly easier implementation of the decoupling circuits. As a consequence, there is a certain increase in the amount of research devoted to the orientation along the stator flux [Vas, 1990].

An advanced achievement in the vector control of induction machines is the universal vector controller [De Doncker and Novotny, 1988]. It enables combined application of the feed-forward and the feedback vector control methods, with orientations along the rotor flux, the air-gap flux and the stator flux in different operating regimes. Appropriate decoupling circuits are available for different orientation types. A possible combination, suggested in [De Doncker and Novotny, 1988], consists of the feed-forward RFOC at low speeds and the feedback SFOC at medium speeds and in the field-weakening region.

Already introduced notions of feedback and feed-forward vector control need further explanation. These terms are related to the way in which orientation is achieved, but they are not related to any specific choice of the flux along which the orientation is performed. Vector control schemes are classified depending on the signals that are utilised for calculating the position of the chosen flux space vector. Classification used here is that feedback schemes utilise some electromagnetic feedback signals (i.e. measured quantities like currents, fluxes, etc.) while feed-forward schemes perform this calculation on the basis of feed-forward signals (i.e. commanded currents) and measured rotor speed (position). Feedback and feed-forward vector control are often termed as direct and indirect control, respectively [Vas, 1990; Vas, 1992].

The research presented in the thesis will mostly address the feedback RFOC of a current-fed machine, with an i_s - ω estimator. As the PWM inverter is assumed to be an ideal current source, all steady-state results are valid for the corresponding feed-forward RFOC. Hence these two schemes will be elaborated in detail in sub-section 2.3.2.

2.3.1. Rotor flux orientation constraints

For the RFO vector control schemes, the reference frame attached to rotor flux is adopted as a common reference frame. This reference frame is fixed to the space vector of the rotor flux, so that the d -axis of the common reference frame coincides with the rotor flux space vector. This is achieved when the angles in the transformation matrices \underline{B}_s and \underline{B}_r (2.10) are chosen as:

$$\theta_s = \varphi_r \quad ; \quad \theta_r = \varphi_r - \theta \quad ; \quad \omega_a = \omega_r = \frac{d\varphi_r}{dt} \quad , \quad (2.35)$$

where φ_r is the instantaneous position of the rotor flux space vector and ω_r is the angular speed of the rotor flux. In this special reference frame the q -axis component of the rotor flux becomes zero, i.e. the rotor flux space vector becomes a real variable :

$$\psi_{dr} = \psi_r \quad ; \quad \psi_{qr} = 0 \quad ; \quad \underline{\psi}_r = \begin{bmatrix} \psi_r \\ 0 \end{bmatrix} \quad ; \quad \bar{\psi}_r = \psi_{dr} + j\psi_{qr} = \psi_r \quad , \quad (2.36.a)$$

so that
$$\frac{d\psi_{qr}}{dt} = 0 \quad . \quad (2.36.b)$$

The difference between the angular speed of the reference frame and the rotor speed is the angular slip speed :

$$\omega_{sl} = \omega_a - \dot{\omega} = \omega_r - \omega \quad . \quad (2.37)$$

Application of RFO constraints onto the mixed current-flux CPM results in a model of induction machine in the rotor-flux-oriented reference frame. This model will be called rotor-flux-oriented model.

2.3.2. Rotor-flux-oriented control of a current-fed induction machine

2.3.2.1. Rotor-flux-oriented constant parameter model of a current-fed induction machine

Taking into account RFO constraints (2.36), the electromagnetic torque equations (2.17.b), (2.17.c) and (2.17.f), respectively, in this reference frame become :

$$T_e = \frac{3}{2} P \frac{L_m}{L_r} \psi_r i_{qs} , \quad (2.38.a)$$

$$T_e = \frac{3}{2} P \frac{1}{L_{lr}} \psi_r \psi_{qm} , \quad (2.38.b)$$

$$T_e = \frac{3}{2} P \frac{L_m}{L_{lr}} \psi_r i_{qm} . \quad (2.38.c)$$

The torque equations (2.38) are of the same form as the torque equation met in DC machines theory. Equation (2.38.a) suggests that if the magnitude of the rotor flux is kept at a constant value, the torque can be independently controlled by the q -axis component of the stator current. Equations (2.38.b) and (2.38.c) are at present irrelevant. They will become important once when main flux saturation and/or iron loss are included in the model (section 2.5 onwards).

Since a current-fed induction machine is discussed, RFO constraints (2.35)-(2.36) are applied to the i_s - ψ_r reduced-order CPM from section 2.2.6. The rotor flux equations (2.34) become:

$$\psi_r + T_r \frac{d\psi_r}{dt} = L_m i_{ds} , \quad (2.39)$$

$$\omega_{sl} \psi_r T_r = L_m i_{qs} , \quad (2.40)$$

where the rotor time constant T_r is defined by (2.32). The developed torque is :

$$T_e = \frac{3}{2} P \frac{L_m}{L_r} \psi_r i_{qs} , \quad (2.38.a)$$

and the equation of mechanical motion remains unchanged :

$$\frac{d\omega}{dt} = \frac{P}{J} (T_e - T_L) - \frac{1}{J} k\omega . \quad (2.33)$$

All the machine parameters (resistances, inductances, the rotor time constant) used in the model are considered to be time-invariant. The above model is well known in literature and often represents the starting point for vector controller design and for analyses of vector controlled drives with rotor flux orientation.

Equation (2.39) reveals that, in this special reference frame, fixed to the rotor flux space vector, the magnitude of the rotor flux (ψ_r) can be controlled by the stator d -axis current (i_{ds}). As there is some magnetic inertia, the responses of ψ_r will lag the changes in i_{ds} according to the rotor time constant T_r . The common vector control strategy is to keep ψ_r at the content level, by keeping i_{ds} constant. In such a case, both angular slip speed ω_{sl} and developed torque are proportional to the stator q -axis current (i_{qs}), according to equations (2.40) and (2.38.a), respectively. Consequently, the developed torque is proportional to the angular slip speed and the torque can be instantaneously altered by changing i_{qs} as there is no lag. This is the key feature that enables fast (theoretically instantaneous) torque response and high performance of the drive. Note that there is no torque limit (the maximum torque is theoretically infinite) and any desired value of the torque can be obtained by applying an appropriate value of i_{qs} , while maintaining the rotor flux on a certain constant level.

2.3.2.2. Feedback rotor-flux-oriented control of a current-fed induction machine

The feedback RFO vector control scheme is shown in Fig. 2.2. It consist of a control system, current-controlled PWM inverter and induction machine. The control system has three proportional-integral (PI) controllers (the torque controller can be omitted and in such a case the speed controller produces the i_{qs}^* reference), the field-weakening block, the co-ordinate transformation block (\underline{B}_s^{-1} , as defined by (2.10.c)), and a rotor flux estimator.

On the basis of the measured motor signals and the machine's parameters, the rotor flux estimator provides estimated signals of the rotor flux amplitude (ψ_r^e), electromagnetic torque (T_e^e) and the rotor flux position (φ_r^e). If the control system does not have a torque controller, T_e^e calculation can be omitted in the estimator. The structure of the estimator is determined by which mathematical model of the induction machine is employed and by which motor signals are measured. The estimator elaborated in this

research is the one that has stator currents and rotor angular speed as input (i_s - ω type). The CPM-based i_s - ω estimator, based on (2.35), (2.37), (2.38.a), (2.39) and (2.40), is shown in Fig. 2.3. It includes the \underline{B}_s co-ordinate transformation, in accordance with (2.10.a). All parameters in the estimator are assumed to be constant and hence they bear an asterisk as superscript. The time derivative is denoted by the Laplace's operator 's'. The estimator operates in the reference frame attached to the estimated rotor flux position.

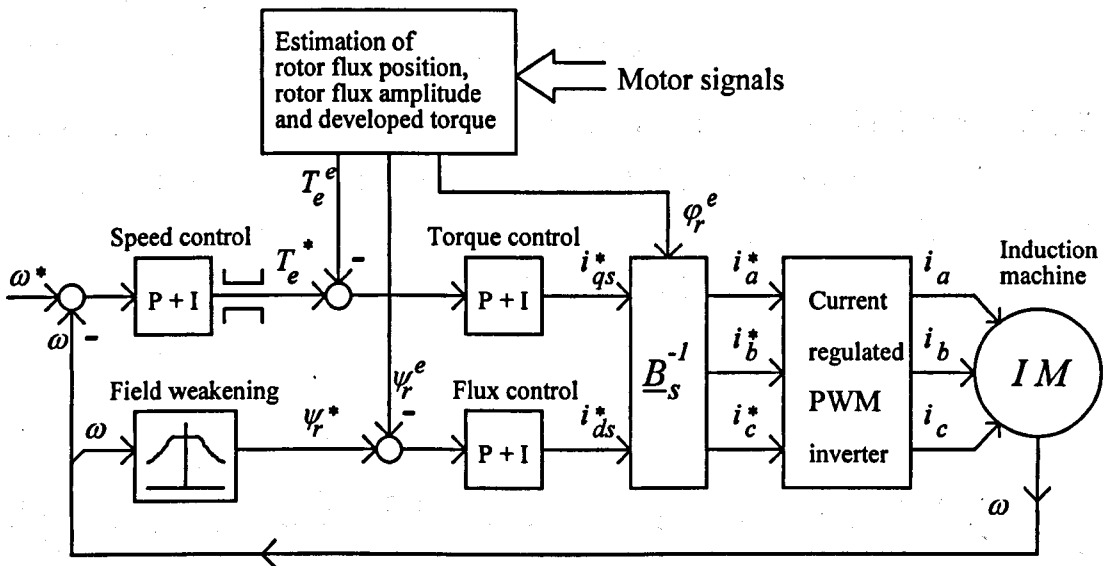


Figure 2.2 : Feedback rotor-flux-oriented control of a current-fed induction machine

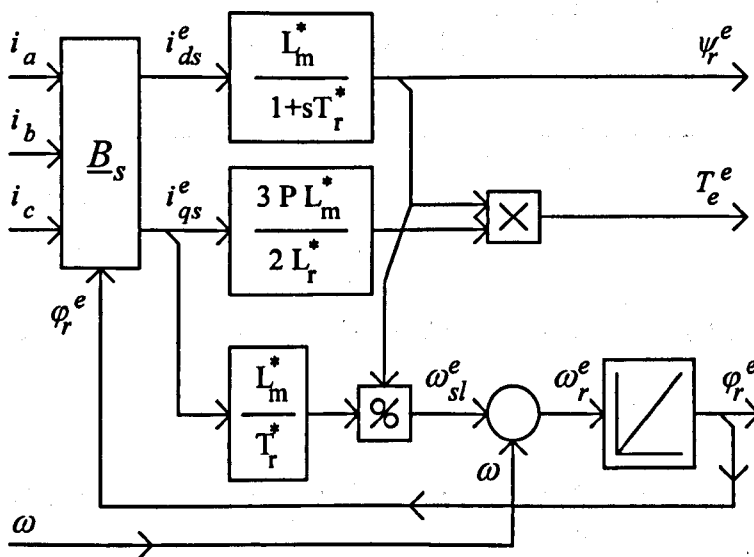


Figure 2.3 : Rotor flux estimator of i_s - ω type, based on the constant parameter model.

2.3.2.3. Feed-forward rotor-flux-oriented control of a current-fed induction machine

The feed-forward RFO vector control scheme is shown in Fig. 2.4. It is again based on eqs. (2.35), (2.37), (2.38.a), (2.39) and (2.40). In this structure, the control system consist of a speed PI controller, the field-weakening block, one differential block, two gain blocks, angular slip speed calculator and \underline{B}_s^{-1} co-ordinate transformation. The slip angular speed is calculated on the basis of the commanded (reference) stator current components. Estimated position of the rotor flux is obtained by integrating the sum of the calculated slip angular speed and the measured rotor speed. Parameters used in the feed-forward controller are constant and hence denoted by an asterisk.

Since both feedback scheme of Figs. 2.2 and 2.3 and feed-forward scheme of Fig. 2.4. are based on the identical set of equations, their behaviour in steady-states is identical. Hence although feedback vector control scheme is studied, all steady-state detuning expressions and detuning characteristics of chapter 4 are equally applicable to feed-forward scheme as well.

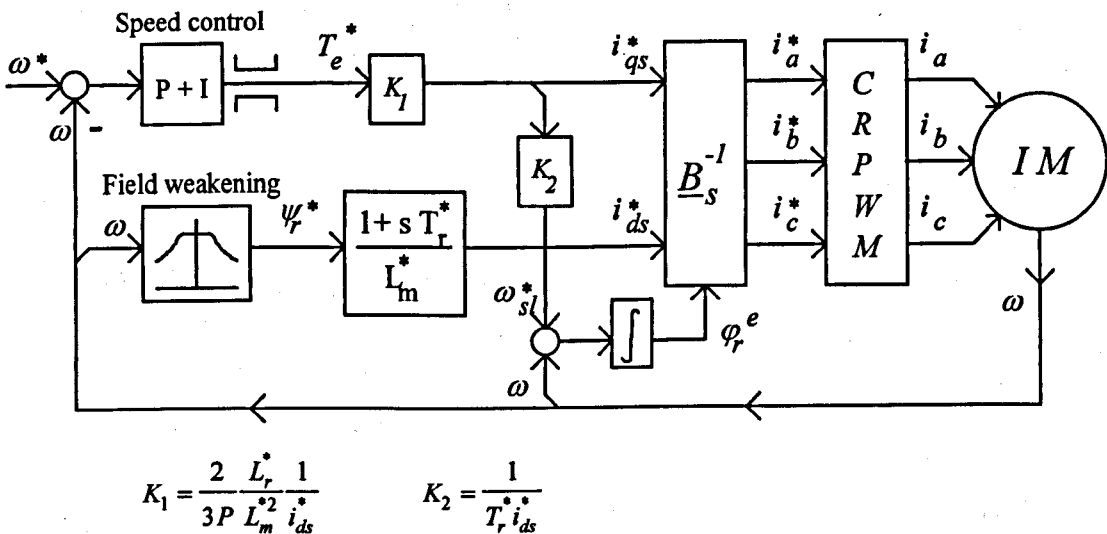


Figure 2.4 : Feed-forward rotor-flux-oriented control of a current-fed induction machine.

2.3.3. Rotor-flux-oriented control of a voltage-fed induction machine

If the current control is performed in the two-phase rotational $d-q$ reference frame, the machine can not be treated as being current-fed. Also, it is possible that the control

system does not have any current control loops. In such cases the induction machine is considered to be voltage-fed and the full mixed current-flux CPM of section 2.5.5 must be used for vector controller design. The final goal of RFOC remains orientation of the stator current space vector with respect to the rotor flux space vector. As straightforward control of the stator current space vector is not possible any more, the appropriate stator voltage space vector by which vector control is achieved has to be determined. In other words, the applied stator voltage space vector has to have such a magnitude and has to be put in such a position that the resulting stator current space vector attains exactly the magnitude and the position with respect to the rotor flux space vector that are needed to realise decoupled flux and torque control. This means that the stator current is controlled not directly as in the case of current feeding, but indirectly, by controlling the stator voltage. Due to complex relationships between stator voltage d - q components and stator current d - q components, this is not an easy task.

Applying RFO constraints (2.36) on the equations of the full mixed current-flux CPM (2.26)-(2.30), the voltage equations are obtained as :

$$\begin{aligned} v_{ds} &= R_s i_{ds} + \sigma L_s \frac{di_{ds}}{dt} + \frac{L_m}{L_r} \frac{d\psi_r}{dt} - \omega_r \sigma L_s i_{qs} \\ v_{qs} &= R_s i_{qs} + \sigma L_s \frac{di_{qs}}{dt} + \omega_r \frac{L_m}{L_r} \psi_r + \omega_r \sigma L_s i_{ds} \end{aligned} \quad (2.41)$$

Consequently, the RFO model of a voltage-fed induction machine is obtained as :

$$i_{ds} + T_s' \frac{di_{ds}}{dt} = \frac{1}{R_s} v_{ds} - \frac{1}{R_s} \frac{L_m}{L_r} \frac{d\psi_r}{dt} + \omega_r T_s' i_{qs} \quad , \quad (2.42)$$

$$i_{qs} + T_s' \frac{di_{qs}}{dt} = \frac{1}{R_s} v_{qs} - \omega_r \frac{1}{R_s} \frac{L_m}{L_r} \psi_r + \omega_r T_s' i_{ds} \quad , \quad (2.43)$$

$$\psi_r + T_r \frac{d\psi_r}{dt} = L_m i_{ds} \quad , \quad (2.39)$$

$$\omega_{sl} \psi_r T_r = L_m i_{qs} \quad , \quad (2.40)$$

where the time constant T_s' is defined as :

$$T_s' = \frac{\sigma L_s}{R_s} \quad . \quad (2.44)$$

Equations (2.42)-(2.43) show that d -axis and q -axis components of the stator voltage and the stator current are cross-coupled by $\omega_r T_s' i_{qs}$ and $\omega_r T_s' i_{ds}$ terms. Hence the components of the stator current cannot be controlled directly by the corresponding components of the stator voltage. However, there are several ways to achieve decoupled control of stator d -axis and q -axis currents. One way is to introduce an appropriate decoupling circuit in the control system. The structure of such controller is shown in Fig. 2.5. Note that scheme of Fig. 2.5. does not have any current control loops. The complete decoupling circuit is rather complicated as it is based on voltage equations (2.41). However, the decoupling circuit can be simplified by omitting the derivative terms in (2.41). This simplification does not affect controller's steady-state performance, but transient performance slightly deteriorates.

Another way to tackle the cross-coupling problem is to introduce current control loops with PI controllers in the d - q axis reference frame and simplify or even completely omit the decoupling circuit. The current controllers are able to fully compensate the coupling between the axes and enable proper operation if the switching frequency of the inverter is high. To reduce the complexity of the control system, the torque control loop can be omitted. Such a controller structure is shown in Fig. 2.6.

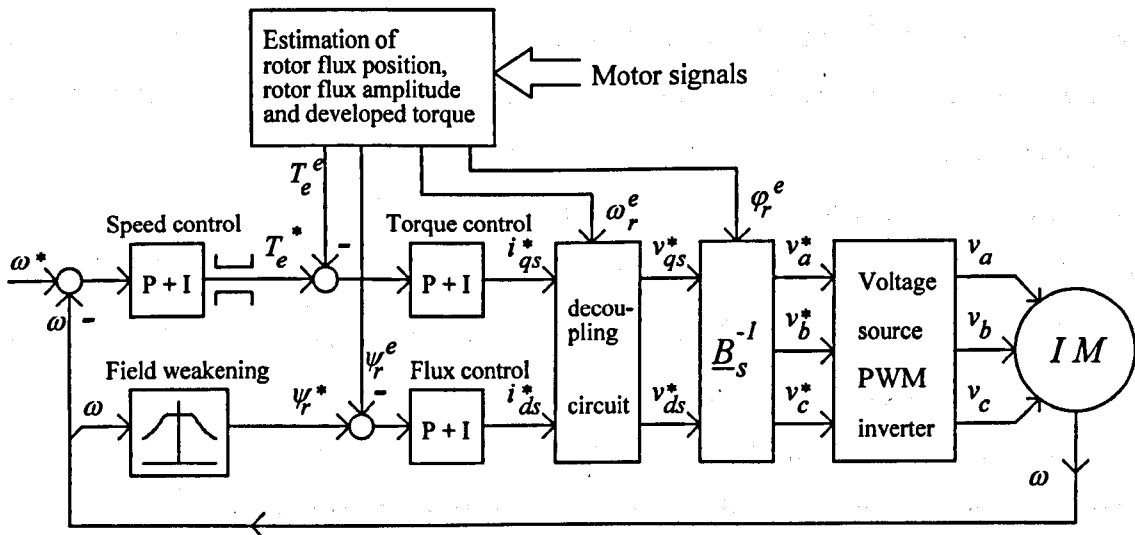


Figure 2.5 : Feedback rotor-flux-oriented control of a voltage-fed induction machine.

If the machine cannot be considered as current-fed, equations for the stator voltage d - q components, based on (2.12) have to be included in the SFO model. This additionally complicates the SFO model, resulting in even more complex control system, since the stator current components are driven by the stator voltage. Depending on the type of the supply, different decoupling circuits are employed in order to achieve correct vector control. The need for decoupling circuits makes orientation along the stator flux less popular choice than orientation along the rotor flux.

However, several good features of SFOC should be mentioned. If the flux space vector is to be estimated from the measured values of the stator currents and the stator voltages (by the v_s - i_s estimator), then the stator flux can be estimated more accurately than the rotor flux, due to inevitable parameter variation in the machine. This is the vector control scheme where the SFOC is suggested to be a better solution than the RFOC [Vas, 1990]. If the machine's rotor is of such design that L_r and/or R_r variations are very pronounced, the SFOC becomes especially advantageous. However, although robust to changes in the rotor parameters, the SFOC schemes are sensitive to R_s variations.

For the AFO vector control schemes, the air-gap (magnetising) flux reference frame is adopted as a common reference frame. Equivalently to the other two types of orientation, the reference frame is fixed to the space vector of the air-gap flux, so that the d -axis of the common reference frame coincides with the air-gap flux space vector.

Similarly to the SFOC, the torque in AFOC schemes can be independently controlled by i_{qs} if the magnitude of the magnetising flux is kept at a constant value. The main problem with AFOC is that i_{ds} , its derivative and i_{qs} all play a role in building the magnetising flux. As in the SFO case, decoupled control of flux and torque is impossible, because i_{qs} influences both stator flux and developed torque. Slip calculation is again a complex task. Voltage feeding worsens the situation, since the additional equations for stator voltage components, based on (2.23), increase the complexity of the model. As it was the case with both SFOC and RFOC with voltage feeding, decoupling circuits and/or additional current control loops are a possible remedy.

2.4. DETUNING IN VECTOR-CONTROLLED INDUCTION MACHINES

Information on the position of the chosen flux is essential for the proper operation of all vector control schemes. As shown in the previous sub-section, this information is obtained by using a mathematical model of the induction machine. Different vector controllers obtain this information in different ways, but practically all controllers use some machine parameters for the calculation [Boldea and Nasar, 1990; Vas 1990; Vas, 1993]. If there are any discrepancies between the actual motor parameters and the values used in the controller, detuned operation occurs. In certain operating conditions, noticeable detuning can arise from the phenomena that are considered to be of the secondary importance and hence are neglected during the control system design. Limited accuracy of the measurement system and discrete nature of the power electronic converter actions represent yet another group of detuning sources [Vas, 1993; Borgard et al., 1995], but their influence is beyond the scope of interest in this research.

2.4.1. Consequences of detuning

As different vector controllers use different parameters, the overall sensitivity to parameter variations depends on the structure of the controller. Additionally, the influence of each parameter variation varies with operating conditions. Generally speaking, RFOC schemes are more sensitive to parameter variations than SFOC and AFOC schemes. The reason for this lies in the fact that rotor quantities are inaccessible for any measurement. Hence some other quantities are measured and then the rotor flux vector is calculated. In feedback RFOC schemes stator currents, and/or stator voltages, and/or rotor speed (or position) are measured and used in the rotor flux estimator. In feed-forward RFOC schemes the measured rotor speed (or position) and the commanded values of the stator currents are used. In all RFOC schemes the calculation process uses certain motor parameters and therefore the estimation accuracy (hence the performance of the whole drive) depends on the accurate knowledge of these parameters.

Situation in detuned steady-state operation of a RFO vector controller with orientation along the rotor flux is schematically shown in Fig. 2.7 [Novotny and Lipo, 1996]. The controller operates in the reference (commanded) d - q reference frame (denoted as d^* - q^*),

which is determined by the estimated position of the rotor flux (angle φ_r^e). In this reference frame, control of flux and torque should be decoupled. On the basis of the commanded flux (ψ_r^*) and the commanded speed (or torque), the control system produces the d - q stator current commands (i_{ds}^* , i_{qs}^*) as its output. These two are then transformed into the current commands in the three-phase domain (i_a^* , i_b^* , i_c^*). It is assumed that fast current control in the PWM inverter ensures that the actual phase currents (i_a , i_b , i_c) are equal to the commanded. In this way the machine is assumed to be fed from an ideal current source.

Due to mismatch between the actual motor parameters and the values used in the controller and/or due to effects of the neglected phenomena, the actual rotor flux (ψ_r) is not aligned with the commanded d^* -axis. The ψ_r is shifted from the ψ_r^* by an angle $\Delta\varphi_r$. This means that the actual d - q co-ordinates, attached to the actual flux, do not coincide with the reference d^* - q^* co-ordinates. Another consequence of this phase shift is that the actual d -axis current and the actual q -axis current (i_{ds} and i_{qs} , respectively) do not match their commanded values. Thus the amplitude of the actual flux deviates from the commanded value. The actual i_{ds} in Fig. 2.7 is smaller than the commanded and hence the actual flux ψ_r is smaller than commanded as well. The developed torque, being proportional to the cross-product of the stator current vector and the rotor flux vector, also differs from its commanded value.

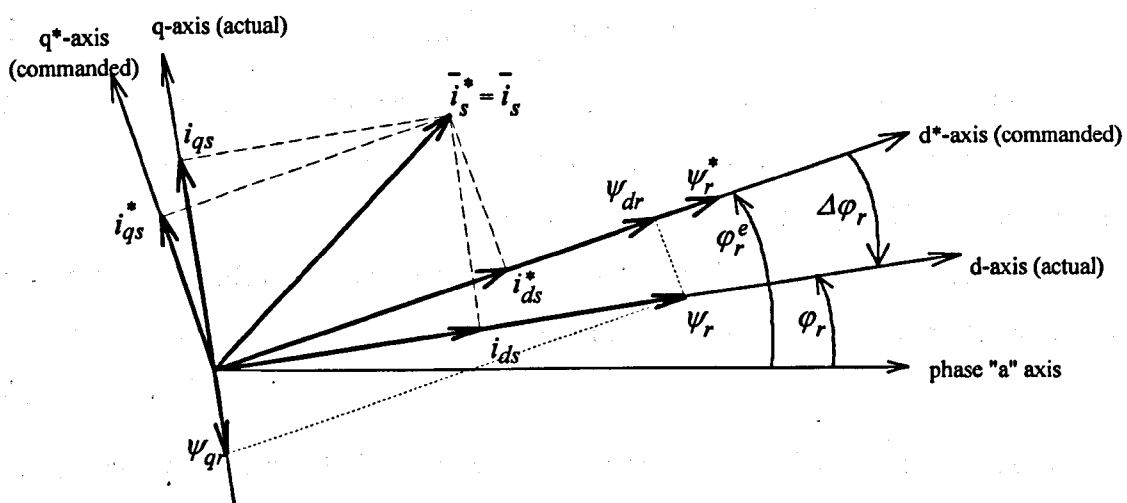


Figure 2.7: Detuned operation of a rotor-flux-oriented vector controller.

Detuned operation of a vector controller has several consequences. Some of them are :

- All transients that follow a stepwise change in the speed command (acceleration, deceleration) or a stepwise change in load will have oscillatory nature, instead of smooth stepwise response. In extreme detuning conditions, unstable operation might occur.
- If the actual flux is lower than the commanded and the machine is heavily loaded, higher q -axis current is required to produce enough torque. This increases copper losses in windings and reduces the efficiency. Additionally, the acceleration rate is reduced due to reduced torque capability [Kirchen et al., 1987].
- If the actual flux is greater than the commanded, iron loss is increased. This again reduces the efficiency [Kirchen et al., 1987]. Additionally, the machine operates in the region of high saturation.
- In the field-weakening region, the actual flux may be higher than the commanded, leading to an increase in the required voltage. If this becomes more pronounced, the voltage limit of the inverter is reached and the inverter is not able to maintain good current control.

All these problems have been noticed early in the evolution of the vector controlled drives [Gabriel et al., 1980; Garcés, 1980] and lot of research work has been directed towards compensation of detuning effects.

2.4.2. Detuning due to main flux saturation

Magnetic saturation is a phenomenon met in all electromagnetic devices. In induction machines it can be separated into main flux saturation and leakage flux saturation. As far as modelling and parameter variations are concerned, the net effects are that main flux saturation influences the value of the mutual inductance (L_m) while leakage flux saturation influences the values of the stator and the rotor leakage inductances (L_{ls} and L_{lr} , respectively).

Induction machines are designed to experience some level of main flux saturation when obtaining the rated flux level. Therefore the value of L_m that corresponds to the rated flux level (the saturated value, L_{msat}) is used by a controller for operation up to rated speed. However, it is necessary to reduce the flux level for operation above the rated

speed in order to keep the required voltage within capabilities of the supply. If the value of L_m is not adapted in accordance with the flux changes, detuning will occur [Levi, 1994a]. This means that operation above the rated speed is one of the cases when main flux saturation is a source of significant detuning. Main flux saturation also affects the process of the flux build-up, even though the machine is at standstill during this process. Some detuning also occurs when the machine develops high torque (fast acceleration, deceleration or reversal), due to the cross-saturation effect [Levi, 1994a]. Finally, there are some vector control strategies that employ operation with a variable flux command even below the rated speed. These strategies are used to enable faster acceleration [Sangwongwanich et al., 1988], to produce a high short-term torque [Wallace et al., 1994], or to improve the efficiency [Kirchen et al., 1987].

If an induction machine is represented by the CPM, main flux saturation is neglected and maximal torque-per-ampere ratio is achieved when $i_{ds} = i_{qs}$ [Khater et al., 1987]. This is not true any more when main flux saturation is pronounced and a saturated induction machine model should be used in order to select the rotor flux level for different load circumstances. Steady-state characteristics of a saturated current-fed induction machine with RFOC were presented in [Lorentz and Novotny, 1990]. It was shown that saturation reduces torque-per-ampere ratio (especially at high currents) and that the peak torque occurs at some value $i_{ds} < i_{qs}$. Grotstollen and Wiesing [1995] have studied the torque capability of an induction motor drive over a wide range of flux weakening, with current and voltage limited by a power converter. They have shown that it is necessary to include main flux saturation for a proper choice of flux levels in the field-weakening region.

Main flux saturation also plays a significant role in thermally induced detuning, in an indirect manner. A study of detuning in two feed-forward RFOC induction machines due to thermal effects has been done in [Nordin et al., 1985]. A more general analysis of detuning in vector-controlled machines [Ojo et al., 1994] has presented expressions for determination of steady-state detuning for SFOC, AFOC and RFOC. In both of these papers it was shown that main flux saturation has to be acknowledged for proper evaluation of detuning due to R_r variations (i.e. temperature effects and skin-effects). Otherwise, unrealistic results are obtained.

Detailed analyses of detuning due to main flux saturation in transient operation of the RFOC induction machine drive were presented in [Levi and Vuckovic, 1993; Levi, 1994a]. It was shown that the actual level of the rotor flux differs from the commanded value during aforementioned transients.

A number of different schemes that compensate the effects of main flux saturation have been proposed. Improved (also called modified, advanced or adaptive) rotor flux estimators, derived from improved mathematical models, are used for the feedback schemes. The conventional T-model of the induction machine, with main flux saturation included, is usually utilised for the improved estimators, in which the estimated value of L_m is varied in accordance with the estimated value of the magnetising flux. Implementation of improved estimators can significantly reduce detuning and thus improve the performance of the drive, with rather small additional complexity of the control algorithm, as shown in [Levi and Vuckovic, 1993; Levi, 1994a]. The ladder network with two saturable inductances (main flux saturation and rotor leakage flux saturation), has been proposed and experimentally verified for an AFOC scheme with a machine with deep rotor bars [Williamson and Healey, 1996].

Since a magnetising curve constitutes an important part of the improved estimator, it has to be known in advance. Detailed discussion on methods for identification of the magnetising curve are given in section 7.4.1. For the moment, it suffices to say that it is usually determined from no-load tests [Vas, 1993], although several other methods have been developed.

It is also possible to employ alternative models of saturated induction machines. One of these is a suggestion that L_m could be made a function of the rotor flux [Vas and Alakula, 1990], but it has no experimental verification. Sullivan and Sanders [1995] have proposed a novel π -model, with two saturable inductances. The π -model has been used to develop modified rotor flux estimators and the improved performance has been reported [Sullivan et al., 1996]. Similar model with saturation has been proposed in [Slemon, 1996]. It includes two (stator and rotor) saturable inductances. Choice of values of the stator current components for producing high torque for short periods in vector controllers that use this model has been suggested and compared with the choices when both conventional saturated T-model and non-saturated models are used.

2.4.3. Detuning due to iron loss

Another magnetic phenomenon is iron loss. It occurs in the presence of the time-varying magnetic field [Stoll, 1974] and inevitably takes part in the power balance of an induction machine. When the machine is lightly loaded and flux kept at rated level, iron loss can represent a significant part of the total power loss. Iron loss as a source of detuning in vector-controlled drives has attracted attention only in recent years.

Investigation of the vector-controlled synchronous reluctance machine [Xu et al., 1991] has indicated that iron loss can play an important detuning role. This work has initiated similar investigations concerning the vector-controlled induction machines. In [Hintze and Schröder, 1992] it was mentioned that detuning due to iron loss is significant at light loads. Since the vector control scheme elaborated in [Hintze and Schröder, 1992] had a R_r identifier, it was also revealed that iron loss affects the identification process. Unfortunately, this work has no results (simulation or experimental) regarding the influence of iron loss on the accuracy of either vector orientation or R_r identification. The first published quantitative results regarding the steady-state detuning of the vector-controlled induction machines [Jaderko, 1992] are obtained by simulation. The analytical expressions for steady-state detuning characteristics for RFOC, AFOC and SFOC have been presented in [Levi, 1995b]. This paper also presents a comparative study of steady-state detuning for the three orientation strategies and a study of transient detuning for the RFOC scheme. A comparative study for several induction machines has been introduced in [Levi et al., 1995a]. In the two papers [Levi, 1995b; Levi et al., 1995a] main flux saturation and temperature effects are not considered and only operation at the rated speed with the rated commanded flux is presented. In [Garcia et al., 1994], a theoretical study of detuning due to iron loss over a wide speed region (from zero up to twice the rated speed) was presented. It appears that this analysis was performed without taking into consideration the common field-weakening strategy for operation above the rated speed.

Compensation of detuning due to iron loss is commonly based on the improved machine models. Simple changes in estimator equations, consisting of subtracting the d - q components of the 'equivalent iron loss current', have been suggested in [Hintze and Schröder, 1992]. Models of the current-fed induction machine, that include iron loss, have been developed for all three possible orientation strategies [Levi, 1994a]. Out of

these models, the one with RFO strategy was utilised for design of the improved rotor flux estimator for the feedback RFOC scheme. The increase in the complexity of the improved controller is moderate [Levi, 1994a].

The control system presented in [Kubota and Matsuse, 1992] employs an adaptive flux observer that accounts for iron loss. The influence of iron loss on the estimation accuracy has been investigated and the iron loss compensation technique was proposed.

2.4.4. Detuning due to changes in the rotor time constant (in the rotor resistance)

The temperatures of induction motor parts change during operation, affecting the values of the resistances of all windings. The cooling system of an induction machine usually employs a fan that blows the air over the stator surface. Consequently, the rotor is warmer than the stator and changes of the resistance are more pronounced in the rotor. Additionally, R_r may change due to changes in the rotor slip frequency. The rotor winding is of such design that it is more receptive to the skin effect, which becomes more pronounced with the increase in the slip frequency. The influence of the skin effect on R_r is generally negligible.

The rotor time constant is intensively used for calculations in vector controllers. The value of T_r is dependent on both the rotor self-inductance (L_r) and R_r . This means that the value of T_r is influenced by main flux saturation, rotor leakage flux saturation, changes in temperature and changes in slip angular speed (frequency). All these phenomena can produce a significant difference between the actual value of T_r and the value used in the RFOC controller (T_r^*). This discrepancy leads to inaccurate calculations and results in detuned operation. The problem of detuning due to changes in the T_r was recognised in the early days of vector control [Garcés, 1980] and has subsequently attracted substantial research attention.

Expressions that describe detuning effects in the feed-forward RFOC scheme, due to errors in T_r , presented in [Garcés, 1980], have considered constant flux operation and thus only variations of R_r due to thermal effects were elaborated. Sivakumar et al. [1986] presented the analysis of detuning in the feed-forward RFOC scheme, caused by changes in L_m and R_r . Detuning expressions and characteristics for steady-state operation were presented, as well as a study of detuning in transients. However, it

appears that changes in L_m and R_r were assumed to be independent, which is not the case in reality. Nevertheless, this fact was recognised by Nordin et al. [1985] and detuning characteristics for feed-forward RFOC, with main flux saturation included, are presented for two machines. A comprehensive study of detuning due to R_r variations in RFOC, SFOC and AFOC schemes, with main flux saturation included, has been done in [Ojo et al., 1994]. Sensitivity of the observer for the feedback RFOC to changes in R_r has been elaborated in [Hori and Umeno, 1989], showing the strong influence of the rotor speed on the amount of detuning.

Temperature-related variations in R_r are dependent on the operating speed, load torque at the shaft and duty cycle of the machine, so that any attempt to compensate for R_r variation necessarily consists of on-line identification. A considerable number of solutions for on-line identification have been suggested and published. They may be classified on the basis of the utilised approach into the following three groups :

- schemes based on thermal models,
- schemes based on injected signals,
- schemes that use modern control theory methods.

They are discussed in the following paragraphs. Some other methods of on-line rotor resistance adaptation that strictly speaking do not belong into any of these three groups are described in [Toliyat et al., 1995; Chan and Wang, 1990].

Employment of an induction machine thermal model, in conjunction with measurements of the temperature of easily accessible parts (usually different parts of stator), was proposed in [De Doncker et al., 1986]. With methods of this kind it is possible to simultaneously estimate temperatures and resistances of both stator and rotor windings. Drawbacks of such methods are: temperature sensors are in general not available in the machine; their installation is highly undesirable as it increases cost and reduces robustness of the machine; a reliable thermal model is needed to estimate temperature of the rotor; and the relationship between R_r and the rotor temperature has to be known. Thus the most straightforward approach is at the same time the least desirable and is of no practical value.

The second group of R_r identification techniques encompasses methods that employ the injection of special signals [Leonhard, 1985; Saitoh et al., 1989] and obtain the estimate

of T_r (or R_r) by measuring the response generated by the injected signal(s). The injected signal is of higher frequency, usually superimposed on the d -axis current command. However, the disturbances in flux, torque and speed, induced by the test signal, are undesirable in most drives. As a result, methods with very small disturbances have been developed. The one described in [Wade et al., 1997] uses just occasional short pulses of the commanded d -axis current and adapts R_r on the basis of recorded disturbances in torque command. If R_r is correctly identified, the torque disturbance will diminish. The identification scheme for a sensorless vector controller, described in [Kubota and Matsuse, 1994], utilises two injected signals of different frequencies in order to simultaneously estimate R_r and angular speed.

In the third group of schemes, R_r identification is performed by resorting to the modern control theory. Different techniques have been implemented: model reference adaptive control (MRAC) techniques [Garcés, 1980; Rowan et al., 1991], observer-based control schemes [Wade et al., 1997], Kalman filters [Atkinson et al., 1991; Pena and Asher, 1993], neural networks [Hofmann and Liang, 1995b; Ba-Razzouk et al., 1996], etc.

Model reference adaptive control theory is the approach that has attracted most of the attention due to its relatively simple implementation. The basic idea is that one quantity can be calculated in two different ways. The adaptive value is calculated from references inside the control system, on the basis of the machine model. The reference (feedback) value is calculated from measured signals. The difference between the two is an error signal, whose existence is assigned entirely to the discrepancy between the actual value of one parameter and the value of the same parameter used in the control system. This parameter can be R_r , T_r or K_{sl} (slip gain, $K_{sl} = 1/T_r$). The error signal is utilised to drive an adaptive mechanism with PI or I controller, which provides correction of the chosen parameter.

The number of MRAC-based T_r identification schemes is vast and they primarily differ with respect to which quantity is selected for adaptation (identification) purposes. Method based on reactive power [Garcés, 1980; Rowan et al., 1991] is probably the most frequently applied. Its good features are that it is independent of R_r variations and the calculations are relatively simple as no integration is involved. Next, the air-gap power can be selected as the quantity on which adaptation is based [Dalal and Krishnan, 1987]. The reference air-gap power is calculated from reference values of torque and

frequency, while the actual air-gap power is calculated from the measured input power and estimated stator losses in the machine. Alternatively, the DC link power can be measured instead of the machine's input power. In both cases the accuracy of the method is seriously undermined by the need to precisely estimate stator losses (and inverter losses if the DC link power is measured), which is a tricky task when the machine is fed from an inverter. Other possibilities include selection of torque [Rowan et al., 1991; Lorenz and Lawson, 1990], rotor back emf [Kazmierkowski and Sulkowski, 1986], rotor flux magnitude [Rowan et al., 1991], rotor flux d - and q -components [Ganji and Lataire, 1995], stored magnetic energy [Tungpimolrut et al., 1994], product of stator q -axis current and rotor flux [Umanand and Bhat, 1994], stator d -axis or q -axis voltage components [Umanand and Bhat, 1994], or a special criterion function [Vukosavic and Stojic, 1993].

There are several common features of MRAC schemes. First of all, adaptation is usually operational in steady-states only and disabled during transients, when the last identified value is used. In this way the adaptation scheme can be based on a steady-state model of the machine, which reduces the computational burden. Secondly, in the majority of cases the stator voltages are required for calculation of the adaptive quantity. They are either measured or reconstructed from the inverter firing signals and the measured DC link voltage [Vas, 1993]. Thirdly, identification does not work at zero speed and at zero load torque. And finally, the accuracy relies on the accuracy of the employed machine model, in which, most frequently, all the other parameters are treated as constants. As some other parameters are involved in calculation of the adaptive and/or the reference quantity, they also influence the error signal. This is the major drawback of MRAC methods. Indeed, an analysis of the parameter variation influence on accuracy of R_r adaptation [Krishnan and Pillay, 1986] has shown that when the MRAC identifier based on the rotor flux magnitude is applied and the actual leakage inductances deviate by 40% from the values used in MRAC adaptation, R_r is estimated with such an error that the response of the drive becomes worse than with no adaptation at all. A similar study with very much the same conclusions is presented in [Dittrich, 1994], where parameter sensitivity is examined for four MRAC adaptation methods, namely d -axis stator voltage method, q -axis stator voltage method, air gap power method and reactive power method.

Due to high sensitivity to other parameter variation effects it is desirable to account for at least some of these in the process of R_r adaptation. Variation of L_m with saturation is for this reason sometimes taken into account, so that accuracy of R_r identification is improved [Sivakumar et al., 1986; Sul, 1989; Sumner et al., 1993; Vukosavic and Stojic, 1993]. Inclusion of iron loss in the T_r identifier can also reduce the parameter sensitivity [Sumner et al., 1993] and improve the performance of the RFOC drive. The other drawback of MRAC methods, impossibility of adaptation at zero speed and zero load torque, is successfully eliminated in certain cases. For example, the schemes of [Vukosavic and Stojic, 1993; Umanand and Bhat, 1994] are operational at zero speed and at light loads although they do fail at zero load.

It is worth noting that in many cases T_r adaptation essentially reduces to R_r adaptation as variations of inductances are usually neglected. An excellent review of R_r identification schemes is available in [Krishnan and Bharadwaj, 1991]. It should be also noted that methods for R_r identification have been proposed [Umanand and Bhat, 1995], as R_r plays an important role in establishing accurate vector control in a number of schemes. However, R_s variations have no effect on the accuracy of RFO control schemes elaborated here and R_r adaptation methods are therefore not discussed in detail.

The universal vector controller [De Doncker and Novotny, 1988] was developed as a combination of a feedback and a feed-forward controller, generalised for any selected flux. The feed-forward universal controller needs the values of T_r and the rotor leakage time constant (T_{lr}). Thus it is sensitive to uncertainties in T_r , L_m , and T_{lr} . The study of the parameter sensitivity of this control scheme [De Doncker, 1994] has shown that changes in T_{lr} have far less detuning effects than changes in T_r , especially for light loads or when T_r is accurately identified. The universal controller for motors with tapped stator winding [De Doncker et al., 1994] proposed an original method for T_r identification. The idea was to run both feedback and feed-forward control algorithms all the time, with the commanded output currents being a sum of weighted output currents of the two control schemes. The weight factors are dependent on speed so that the feedback scheme is preferred for higher speeds, typically above 5 Hz. During such operation it is possible to adapt T_r by comparing the outputs of the two schemes and making them equal by changing T_r in the feed-forward scheme.

Some of the feedback vector controllers based on the improved machine models also use T_{lr} instead of T_r [Levi, 1994a; Levi, 1994b]. The sensitivity of these schemes to parameter variations has not been presented so far.

2.4.5. Detuning due to changes in the rotor leakage inductance

The rotor leakage inductance can change due to saturation of leakage flux and due to skin effect. The amount of variations depends on the design of rotor bars. If an induction machine has deep-bar design, L_{lr} variations in due to skin effect are more pronounced. If the machine has closed rotor slots, leakage flux saturation is more pronounced.

Analysis of the parameter sensitivity of universal vector controllers [De Doncker, 1994] has shown that T_{lr} inaccuracies have much smaller influence than T_r inaccuracies. The stability limits of the universal vector controllers were also investigated in the above paper. It was shown that they are normally reached at high loads and they depend on the accuracy of estimation of both T_r and T_{lr} . The influence of T_{lr} is generally smaller than the influence of T_r . However, when T_r is equal to or bigger than the commanded value (T_r^*), and T_{lr} is equal or smaller than the commanded value (T_{lr}^*), the influence of T_{lr} inaccuracies becomes more significant and the stability limits of the drive are reached at lower loads than usual.

Deep-bar and double-cage rotor constructions are used for medium-power and high-power induction machines, in order to increase the machine efficiency, while achieving high starting torque [Vas, 1992]. The idea used for modelling these types of rotor constructions is to represent the rotor windings by a ladder network with at least two branches [Vas, 1992]. The common leakage flux in rotor is modelled by a common rotor leakage inductance (which can be saturable, [Williamson and Healey, 1996]), while the end-ring resistance between the two cages is represented by a common rotor resistance. Each of the two rotor windings is modelled by a branch containing a resistance and a leakage inductance. This directly corresponds to the two cages in double-cage machines. The deep-bar rotor is modelled by dividing the cage into outer part and inner part. In certain cases, more than two ladder branches can be used to model the deep-bar rotor [Healey et al., 1995].

The ladder model of the rotor with leakage flux saturation has been used for vector control of deep-bar induction machines [De Doncker, 1992; Williamson and Healey, 1996]. Since there are two rotor fluxes, the RFOC cannot be used and either SFOC or AFOC scheme should be employed. The AFOC schemes are presented in these two papers and improvements of torque responses' accuracy has been demonstrated.

Rotor leakage flux saturation and deep-bar effects are not investigated in this project. The reason for this is that the induction machines dealt with here have such a design of rotor bars that neither of these two phenomena are pronounced and it is not expected that they will have a significant effect on the machine performance. Nevertheless, saturation of rotor leakage flux and corresponding L_{lr} variation will be included in the steady-state analyses of detuning, presented in chapter 4, in order to show that its detuning influence is quite small.

2.5. REVIEW OF IMPROVED MATHEMATICAL MODELS AND IMPROVED VECTOR CONTROLLERS

A number of compensation schemes that tackle the problem of detuning in vector controlled induction machine drives were mentioned in the previous section. In this section, ones that are strongly connected with this research are presented in detail. They include improved models and improved estimators with main flux saturation, improved models and improved feed-forward RFO controller with iron loss and improved controllers that have a rotor resistance or a rotor time constant identifier.

2.5.1. Mathematical models and estimators with main flux saturation

Compensation of main flux saturation detuning effects is usually based on employing improved machine models that include main flux saturation. The design of the control system is therefore based on improved machine models. The last assumption in subsection 2.2.1, about the linear magnetising curve, means that main flux saturation is neglected, i.e. L_m is assumed to be constant. This is quite true for a number of operating regimes and the CPM will faithfully represent the behaviour of the machine. On the other hand, as discussed in section 2.4.2, there are also a number of operating regimes in which this assumption is not truly satisfied. To obtain more accurate representation of

the machine's behaviour in such cases, it is necessary to include main flux saturation in the mathematical model of the induction machine.

A number of mathematical models that attempt to represent main flux saturation have been proposed. Generalised analyses of main flux saturation in d - q axis models of electrical machines [Boldea and Nasar, 1987a] have presented a current-based state-space model with saturation, valid for any electrical machine. Current state-space models with main flux saturation contain terms that explicitly describe cross-saturation effect. Flux-based models [Vas, 1992], generally simpler than current-based ones, have no terms that explicitly describe cross-saturation. Mixed current-flux models [Levi and Krzeminski, 1996] are sometimes more convenient than the other two types. From these mixed models, improved vector controllers are designed by applying the RFO constraints as the next stage. This results in improved RFO models with main flux saturation, from which improved rotor flux estimators with main flux saturation are developed.

2.5.1.1. The general model with main flux saturation

The general model of an induction machine with main flux saturation is well known in the literature [Vas, 1992]. It consist of the same equations as the CPM model, presented in sub-section 2.2.3 :

$$\underline{v}_s = R_s \underline{i}_s + \frac{d(L_{ls} \underline{i}_s)}{dt} + \frac{d\underline{\psi}_m}{dt} + \omega_a L_{ls} \underline{G} \underline{i}_s + \omega_a \underline{G} \underline{\psi}_m \quad (2.23)$$

$$0 = R_r \underline{i}_r + \frac{d(L_{lr} \underline{i}_r)}{dt} + \frac{d\underline{\psi}_m}{dt} + \omega_a L_{lr} \underline{G} \underline{i}_r + \omega_a \underline{G} \underline{\psi}_m - \omega \underline{G} \underline{\psi}_r$$

$$\underline{\psi}_s = L_{ls} \underline{i}_s + \underline{\psi}_m \quad (2.22)$$

$$\underline{\psi}_r = L_{lr} \underline{i}_r + \underline{\psi}_m$$

$$T_e = \frac{3}{2} P \frac{L_m}{L_r} (\psi_{dr} i_{qs} - \psi_{qr} i_{ds}) \quad (2.17.b)$$

$$T_e - T_L = \frac{J}{P} \frac{d\omega}{dt} + \frac{1}{P} k\omega \quad (2.4)$$

In order to express the above model in a state-space form, it is necessary to eliminate one of the \underline{i}_s , \underline{i}_r or $\underline{\psi}_m$ vectors. This model is therefore not in the state-space form. However, it can be used to design the equivalent circuit, as discussed in 2.5.1.2. The

only difference between the general model with main flux saturation and the general CPM (sub-section 2.2.3) is an additional equation that describes the magnetising curve. However, once the model is given in the state-space form, differences become substantial.

The exact shape of the magnetising curve is an individual feature of a machine. Main flux saturation can be represented with one of the non-linear functions :

$$i_m = f(\psi_m) , \quad (2.45.a)$$

$$L_m = f(i_m) , \quad (2.45.b)$$

$$L_m = f(\psi_m) , \quad (2.45.c)$$

where

$$\psi_m = \sqrt{\psi_{dm}^2 + \psi_{qm}^2} , \quad (2.46)$$

$$i_m = \sqrt{i_{dm}^2 + i_{qm}^2} . \quad (2.47)$$

In order to analyse induction machines' dynamics, some models use the dynamic mutual inductance, which represents the rate of change of the main flux with the magnetising current :

$$L_m' = L = \frac{d\psi_m}{di_m} . \quad (2.48)$$

2.5.1.2. The equivalent circuit with main flux saturation

The equivalent circuit for this case is derived from the general model with main flux saturation. The voltage equations, in terms of space vectors, are :

$$\begin{aligned} \bar{v}_s &= R_s \bar{i}_s + L_{ls} \frac{d\bar{i}_s}{dt} + j\omega_a L_{ls} \bar{i}_s + \frac{d\bar{\psi}_m}{dt} + j\omega_a \bar{\psi}_m \\ 0 &= R_r \bar{i}_r + L_{lr} \frac{d\bar{i}_r}{dt} + j\omega_a L_{lr} \bar{i}_r + \frac{d\bar{\psi}_m}{dt} + j\omega_a \bar{\psi}_m - j\omega \bar{\psi}_r \end{aligned} \quad (2.49)$$

The dynamic equivalent circuit of the saturated induction machine, in an arbitrary reference frame, based on (2.49), is shown in Fig 2.8. It differs from the CPM-based equivalent circuit only in one detail - the mutual inductance is a variable parameter, as described by (2.45). However, dynamic models, needed for improved vector controller design, differ significantly, as will be seen later in this section.

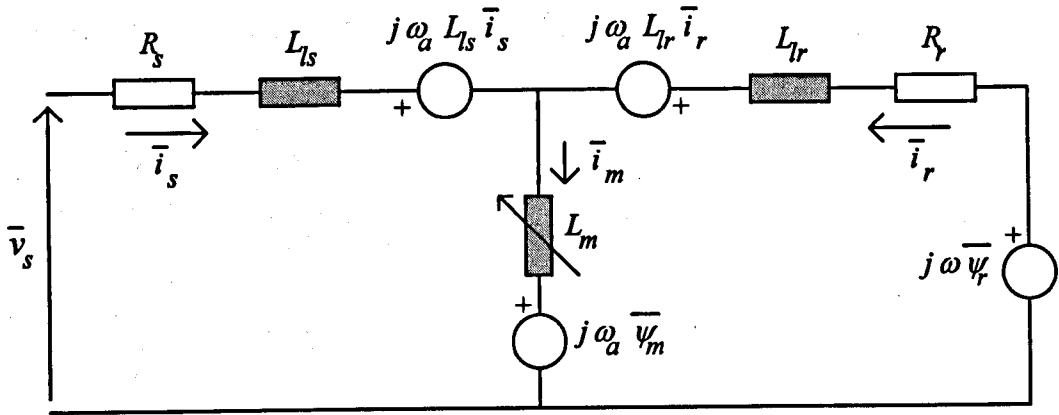


Figure 2.8 : Induction machine dynamic equivalent circuit in an arbitrary reference frame, main flux saturation included.

2.5.1.3. The \underline{i}_s - $\underline{\psi}_r$ mixed current-flux model with main flux saturation

The \underline{i}_s - $\underline{\psi}_r$ mixed current-flux model [Levi and Krzeminski, 1996] is best suited for RFOC. The model is derived from the general model, by elimination of rotor current vector \underline{i}_r and magnetising flux vector $\underline{\psi}_m$. The model is represented in the state-space form, in accordance with (2.26). The vector of voltages is :

$$\underline{v} = [v_{ds} \quad v_{qs} \quad 0 \quad 0]^T, \quad (2.27)$$

and the state vector is :

$$\underline{x} = [i_{ds} \quad i_{qs} \quad \psi_{dr} \quad \psi_{qr}]^T. \quad (2.28)$$

In this case the matrices \underline{A} and \underline{B} are :

$$\underline{A} = \begin{bmatrix} L_{ls} + L_{lr} - \frac{L_{lr}^2}{L_{dd}} & -\frac{L_{lr}^2}{L_{dq}} & 1 - \frac{L_{lr}}{L_{dd}} & -\frac{L_{lr}}{L_{dq}} \\ -\frac{L_{lr}^2}{L_{dq}} & L_{ls} + L_{lr} - \frac{L_{lr}^2}{L_{qq}} & -\frac{L_{lr}}{L_{dq}} & 1 - \frac{L_{lr}}{L_{qq}} \\ 0 & 0 & 1 & 0 \\ 0 & 0 & 0 & 1 \end{bmatrix}, \quad (2.50)$$

$$\underline{B} = \begin{bmatrix} R_s & -\omega_a \left(L_{ls} + L_{lr} - \frac{L_{lr}^2}{L_r} \right) & 0 & -\omega_a \frac{L_m}{L_r} \\ \omega_a \left(L_{ls} + L_{lr} - \frac{L_{lr}^2}{L_r} \right) & R_s & \omega_a \frac{L_m}{L_r} & 0 \\ -\frac{L_m}{T_r} & 0 & \frac{1}{T_r} & -(\omega_a - \omega) \\ 0 & -\frac{L_m}{T_r} & \omega_a - \omega & \frac{1}{T_r} \end{bmatrix}. \quad (2.51)$$

The saturation-dependent coefficients in (2.50) are :

$$\begin{aligned} \frac{1}{L_{dd}} &= \frac{1}{L_r'} \left(\frac{\Psi_d}{\Psi} \right)^2 + \frac{1}{L_r} \left(\frac{\Psi_q}{\Psi} \right)^2 \\ \frac{1}{L_{qq}} &= \frac{1}{L_r'} \left(\frac{\Psi_q}{\Psi} \right)^2 + \frac{1}{L_r} \left(\frac{\Psi_d}{\Psi} \right)^2, \\ \frac{1}{L_{dq}} &= \left(\frac{1}{L_r'} - \frac{1}{L_r} \right) \frac{\Psi_d}{\Psi} \frac{\Psi_q}{\Psi} \end{aligned} \quad (2.52)$$

where the generalised flux is defined as :

$$\begin{aligned} \Psi_d &= \psi_{dr} + L_{lr} i_{ds} \equiv L_r i_{dm} \\ \Psi_q &= \psi_{qr} + L_{lr} i_{qs} \equiv L_r i_{qm}, \\ \Psi &= \sqrt{\Psi_d^2 + \Psi_q^2} \end{aligned} \quad (2.53)$$

and L_r' is dynamic (rotor) inductance, defined as :

$$L_r' = L_{lr} + L = \frac{d\Psi}{di_m} \quad (2.54)$$

The torque equation (2.17.b) and mechanical equation (2.4) complete the model.

The above mixed current-flux model is much more complicated than the CPM mixed current-flux model presented in section 2.2.5, as a consequence of the inclusion of main flux saturation. However, explicit terms that describe dynamic cross-saturation appear only in the stator voltage equations (the first two rows of \underline{A}). This is a very beneficial feature for design of improved rotor flux estimators with main flux saturation, when the current-fed induction machine is considered. This issue is addressed in sub-section 3.2.2.

2.5.1.4. The $\underline{\psi}_m$ - $\underline{\psi}_r$ flux model with main flux saturation

This model, presented in [Levi, 1995c], is derived from the general model by selecting the d - q components of the magnetising flux and the rotor flux as state variables. The vector of voltages is again given with (2.27), while the state vector is now :

$$\underline{x} = \left[\psi_{dm} \quad \psi_{qm} \quad \psi_{dr} \quad \psi_{qr} \right]^T \quad (2.55)$$

In such a case the matrices \underline{A} and \underline{B} become :

$$\underline{A} = \begin{bmatrix} 1 + \frac{L_{ls}}{L_{lr}} + \frac{L_{ls}}{L_{dd}} & \frac{L_{ls}}{L_{dq}} & -\frac{L_{ls}}{L_{lr}} & 0 \\ \frac{L_{ls}}{L_{dq}} & 1 + \frac{L_{ls}}{L_{lr}} + \frac{L_{ls}}{L_{dd}} & 0 & -\frac{L_{ls}}{L_{lr}} \\ 0 & 0 & 1 & 0 \\ 0 & 0 & 0 & 1 \end{bmatrix}, \quad (2.56)$$

$$\underline{B} = \begin{bmatrix} \frac{L_r}{L_m L_{lr}} R_s & -\omega_a \left(L_s + \frac{L_{ls}}{L_{lr}} \right) & -\frac{R_s}{L_{lr}} & -\omega_a \frac{L_{ls}}{L_{lr}} \\ \omega_a \left(L_s + \frac{L_{ls}}{L_{lr}} \right) & \frac{L_r}{L_m L_{lr}} R_s & -\omega_a \frac{L_{ls}}{L_{lr}} & -\frac{R_s}{L_{lr}} \\ -\frac{1}{T_{lr}} & 0 & \frac{1}{T_{lr}} & -(\omega_a - \omega) \\ 0 & -\frac{1}{T_{lr}} & \omega_a - \omega & \frac{1}{T_{lr}} \end{bmatrix}, \quad (2.57)$$

where the leakage rotor time constant T_{lr} is defined as

$$T_{lr} = \frac{L_{lr}}{R_r}. \quad (2.58)$$

The saturation-dependent coefficients in (2.57) are :

$$\begin{aligned} \frac{1}{L_{dd}} &= \frac{1}{L_m'} \left(\frac{\psi_{dm}}{\psi_m} \right)^2 + \frac{1}{L_m} \left(\frac{\psi_{qm}}{\psi_m} \right)^2 \\ \frac{1}{L_{qq}} &= \frac{1}{L_m'} \left(\frac{\psi_{qm}}{\psi_m} \right)^2 + \frac{1}{L_m} \left(\frac{\psi_{dm}}{\psi_m} \right)^2, \\ \frac{1}{L_{dq}} &= \left(\frac{1}{L_m'} - \frac{1}{L_m} \right) \frac{\psi_{dm}}{\psi_m} \frac{\psi_{qm}}{\psi_m} \end{aligned} \quad (2.59)$$

where the dynamic (mutual) inductance L_m' is defined by (2.48). The torque equation (2.17.c) and mechanical equation (2.4) complete the model.

2.5.1.5. The $\underline{\psi}_m$ - $\underline{\psi}_r$ reduced-order model with main flux saturation

The $\underline{\psi}_m$ - $\underline{\psi}_m$ reduced-order, valid for current-fed machines, is obtained from the above model by reducing the state variable vector to ψ_{dr} and ψ_{qr} and omitting the first two rows in matrices \underline{A} (2.56) and \underline{B} (2.57). Since dynamic saturation-dependent coefficients feature only in the omitted equation, the obtained reduced-order model is:

$$\begin{aligned} \frac{d\psi_{dr}}{dt} &= -\frac{1}{T_{lr}} \psi_{dr} + \frac{1}{T_{lr}} \psi_{dm} + (\omega_a - \omega) \psi_{qr} \\ \frac{d\psi_{qr}}{dt} &= -\frac{1}{T_{lr}} \psi_{qr} + \frac{1}{T_{lr}} \psi_{qm} - (\omega_a - \omega) \psi_{dr} \end{aligned}, \quad (2.60)$$

$$\frac{d\omega}{dt} = \frac{P}{J}(T_e - T_L) - \frac{1}{J}k\omega \quad , \quad (2.33)$$

$$T_e = \frac{3}{2}P \frac{L_m}{L_r} (\psi_{dr} i_{qs} - \psi_{qr} i_{ds}) \quad , \quad (2.17.b)$$

2.5.1.6. The $\underline{\psi}_m$ - $\underline{\psi}_r$ rotor-flux-oriented model with main flux saturation and improved estimators, $i_m(\psi_m)$ representation

Application of the rotor flux orientation constraints (2.35)-(2.36) to the $\underline{\psi}_m$ - $\underline{\psi}_r$ reduced-order model with main flux saturation, presented in the previous sub-section, yields the model in the rotor-flux-oriented reference frame, described with :

$$\psi_r + T_{lr} \frac{d\psi_r}{dt} = \psi_{dm} \quad , \quad (2.61)$$

$$\omega_{sl} T_{lr} \psi_r = \psi_{qm} \quad , \quad (2.62)$$

$$\psi_{dm} = \psi_r + L_{lr} (i_{ds} - i_{dm}) \quad , \quad (2.63)$$

$$\psi_{qm} = L_{lr} (i_{qs} - i_{qm}) \quad , \quad (2.64)$$

$$\psi_m = \sqrt{\psi_{dm}^2 + \psi_{qm}^2} \quad , \quad (2.46)$$

$$i_m = f(\psi_m) \quad , \quad (2.45.a)$$

$$i_{dm} = i_m \frac{\psi_{dm}}{\psi_m} \quad , \quad (2.65)$$

$$i_{qm} = i_m \frac{\psi_{qm}}{\psi_m}$$

$$T_e = \frac{3}{2}P \frac{1}{L_{lr}} \psi_r \psi_{qm} \quad , \quad (2.38.b)$$

The improved saturation-adaptive rotor flux estimator with $i_m(\psi_m)$ representation is based on the above RFO model. The estimator's structure is depicted in Fig 2.9 [Levi, 1994a]. Parameters that are assumed to be constant are denoted by an asterisk, while estimated ones are denoted by an 'e' as a superscript. This estimator is more complex than the CPM-based estimator (Fig. 2.3). There are more calculations to be done and the $i_m(\psi_m)$ relationship valid for the particular machine has to be known. The estimator fully compensates detuning due to main flux saturation, as shown in [Levi, 1994a].

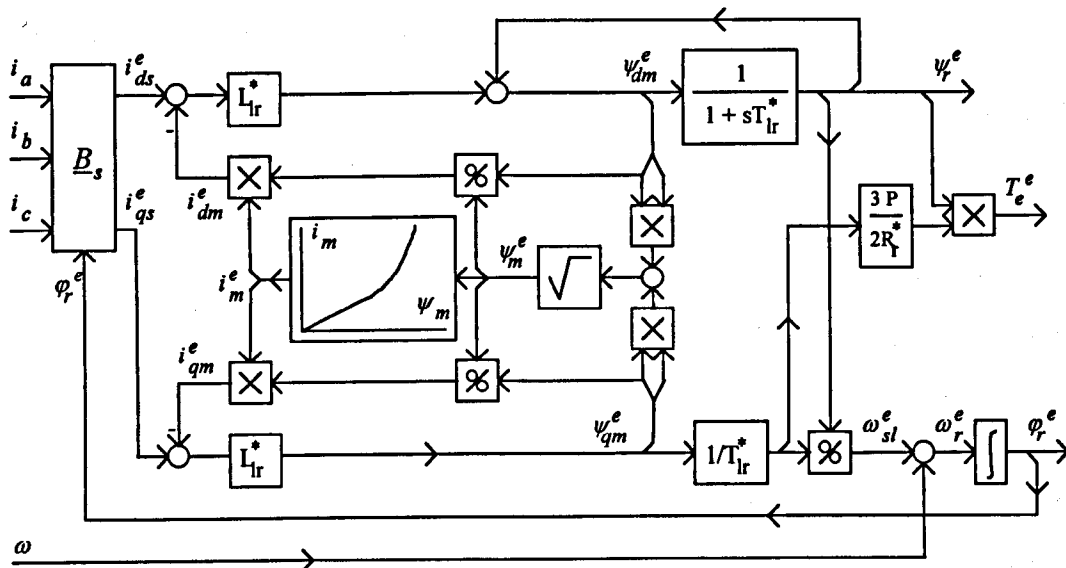


Figure 2.9 : Improved rotor flux estimator of i_s - ω type, with main flux saturation represented by the $i_m(\psi_m)$ non-linear function.

In order to reduce the complexity and the calculation burden that the above estimator can place on the control system, the simplified estimator has been proposed in [Levi, 1994a]. It is obtained by neglecting the influence of cross-saturation and neglecting the changes in the ratio L_m/L_r . The first assumption is justified for operation of the drive with torque up to twice rated, when influence of q -axis magnetising flux component on the total magnetising flux is small. The second assumption is justified because the rotor leakage inductance is at least 10 times smaller than the mutual inductance. The simplified estimator, shown in Fig. 2.10, is capable of providing partial but still very good compensation of main flux saturation, as shown in [Levi, 1994a].

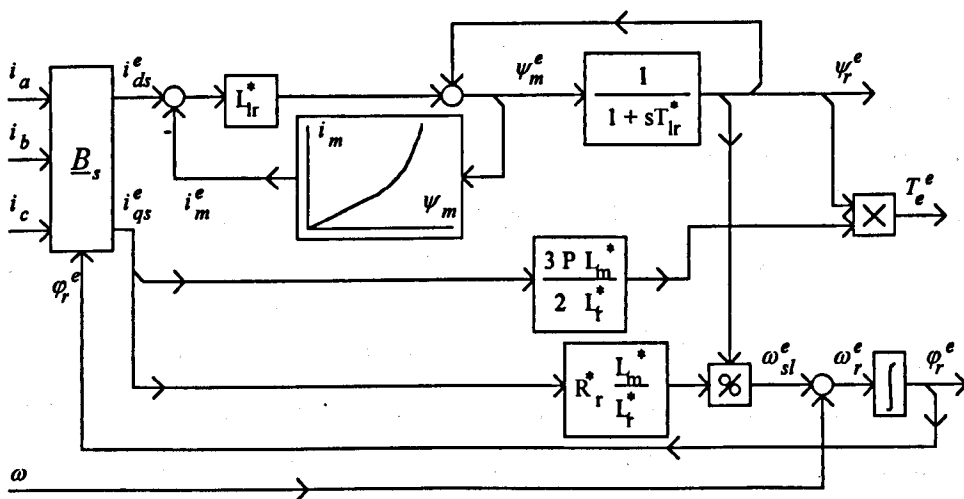


Figure 2.10 : Simplified version of improved rotor flux estimator of i_s - ω type, with main flux saturation represented by $i_m(\psi_m)$ non-linear function.

2.5.2. Mathematical models with iron loss

One of the assumptions adopted in sub section 2.2.1 was that iron loss can be neglected. Iron loss has magnetic nature and hence it cannot be described by means of electric circuits in a completely exact way. Nevertheless, it is possible to include iron loss in the induction machine model in an approximate manner, by adding a fictitious winding. The fictitious winding is usually modelled by an equivalent iron loss resistance [Kubota and Matsuse, 1992; Hintze and Schröder, 1992; Vas, 1992], which represents the power lost as iron loss. For more accurate representation, the value of the equivalent iron loss resistance is changed with the stator frequency and with the flux level. Such an approach will be used in this research. Some authors have proposed to represent iron loss by both equivalent iron loss resistance and equivalent iron loss leakage inductance [Boldea and Nasar, 1987b]. Equivalent iron loss leakage inductance tries to model the rate of change of the eddy current iron loss. Such representation additionally increases the complexity of the model while it does not substantially increase the accuracy, as shown in [Sokola et al., 1996]. Therefore the equivalent iron loss inductance is not considered in models given in this section.

As discussed in sub-section 2.4.3, inclusion of iron loss in induction machine models has been done by some authors. Studies presented in [Jaderko, 1992; Garcia et al., 1994; Levi, 1995b] utilise improved $d-q$ models with iron loss, in a reference frame dictated by CPM-based controller. Iron loss compensation technique described in [Hintze and Schröder, 1992] consist of approximate adjusting of the magnetising current components. It appears that no substantial work on either iron loss modelling or development of improved vector controllers has been published. Thus only two general models, two equivalent circuits, a reduced-order model, a RFO model and an improved feed-forward controller will be presented in this sub-section. The rest of work concerned with models with iron loss and improved estimators with iron loss will be presented in chapter 3, as an original contribution of this research project.

There are two possible placements for the equivalent iron loss resistance in the dynamic equivalent circuit. It can be placed either in parallel with the magnetising branch or immediately after the stator resistance. In the former case the equivalent resistance bears the index ' Fe ' and in the latter case the equivalent resistance bears the index ' ir '. In accordance with this, two types of general model and mixed models are presented.

2.5.2.1. The general model with iron loss represented by a resistance placed in parallel with the magnetising branch

The general model with iron loss represented by a resistance placed in parallel with the magnetising branch can be given as [Vas, 1992, Levi, 1994b] :

$$\underline{v}_s = R_s \underline{i}_s + \frac{d(L_{ls} \underline{i}_s)}{dt} + \frac{d\underline{\psi}_m}{dt} + \omega_a L_{ls} \underline{G} \underline{i}_s + \omega_a \underline{G} \underline{\psi}_m \quad (2.23)$$

$$0 = R_r \underline{i}_r + \frac{d(L_{lr} \underline{i}_r)}{dt} + \frac{d\underline{\psi}_m}{dt} + \omega_a L_{lr} \underline{G} \underline{i}_r + \omega_a \underline{G} \underline{\psi}_m - \omega \underline{G} \underline{\psi}_r$$

$$R_{Fe} \underline{i}_{Fe} = \frac{d\underline{\psi}_m}{dt} + \omega_a \underline{G} \underline{\psi}_m \quad (2.66)$$

$$\underline{\psi}_s = L_{ls} \underline{i}_s + \underline{\psi}_m \quad (2.22)$$

$$\underline{\psi}_r = L_{lr} \underline{i}_r + \underline{\psi}_m$$

$$\underline{i}_m + \underline{i}_{Fe} = \underline{i}_s + \underline{i}_r \quad (2.67)$$

$$\underline{\psi}_m = L_m \underline{i}_m \quad (2.20)$$

$$T_e = \frac{3}{2} P \frac{1}{L_{lr}} (\psi_{dr} \psi_{qm} - \psi_{qr} \psi_{dm}) \quad (2.17.c)$$

$$\text{or } T_e = \frac{3}{2} P \frac{L_m}{L_{lr}} (\psi_{dr} i_{qm} - \psi_{qr} i_{dm}) \quad (2.17.f)$$

$$T_e - T_L = \frac{J}{P} \frac{d\omega}{dt} + \frac{1}{P} k\omega \quad (2.4)$$

The model is of higher order than the previous two general models, since the additional winding introduces two more differential equations. The value of the equivalent iron loss resistance is in general dependent on the frequency and the flux level :

$$R_{Fe} = f(f, \psi_m) \quad (2.68)$$

2.5.2.2. The equivalent circuit with iron loss represented by a resistance placed in parallel with the magnetising branch

Applying space vector representation, voltage equations (2.23) and (2.66) become :

$$\bar{v}_s = R_s \bar{i}_s + L_{ls} \frac{d\bar{i}_s}{dt} + j\omega_a L_{ls} \bar{i}_s + L_m \frac{d\bar{i}_m}{dt} + j\omega_a L_m \bar{i}_m \quad (2.25)$$

$$0 = R_r \bar{i}_r + L_{lr} \frac{d\bar{i}_r}{dt} + j\omega_a L_{lr} \bar{i}_r + L_m \frac{d\bar{i}_m}{dt} + j\omega_a L_m \bar{i}_m - j\omega \bar{\psi}_r$$

$$R_{Fe} \bar{i}_{Fe} = \frac{d\bar{\psi}_m}{dt} + j\omega_a \bar{\psi}_m \quad (2.69)$$

The dynamic equivalent circuit of an induction machine, in an arbitrary reference frame, based on (2.25) and (2.69), is shown in Fig. 2.11 [Vas, 1992; Levi, 1994b]. The circuit is more complicated than the CPM-based circuit since there is the additional branch with the equivalent iron loss resistance. It is depicted as a variable parameter, in accordance with (2.68).

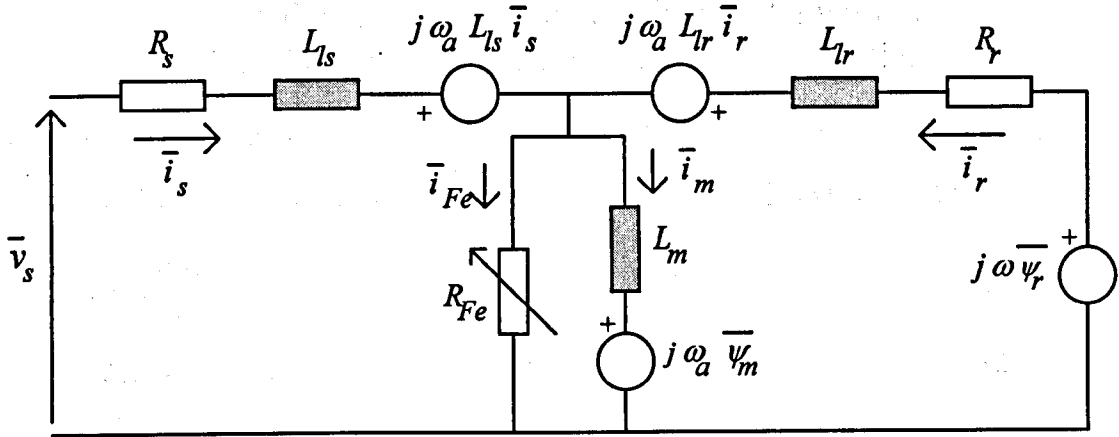


Figure 2.11 : Induction machine dynamic equivalent circuit in an arbitrary reference frame, iron loss represented by a resistor placed in parallel with the magnetising branch.

2.5.2.3. The \underline{i}_s - \underline{i}_m - $\underline{\psi}_r$ reduced-order model with iron loss represented by a resistance placed in parallel with the magnetising branch

This model is obtained from the general model of sub-section 2.5.2.1, eliminating \underline{i}_r and \underline{i}_{Fe} and assuming that \underline{i}_s is known input to the current-fed machine. In developed form, the \underline{i}_s - \underline{i}_m - $\underline{\psi}_r$ reduced-order model consist of [Levi, 1994b] :

$$\frac{d\psi_{dr}}{dt} = -\frac{1}{T_{lr}} \psi_{dr} + \frac{1}{T_{lr}} L_m i_{dm} + (\omega_a - \omega) \psi_{qr} \quad (2.70)$$

$$\frac{d\psi_{qr}}{dt} = -\frac{1}{T_{lr}} \psi_{qr} + \frac{1}{T_{lr}} L_m i_{qm} - (\omega_a - \omega) \psi_{dr}$$

$$\frac{di_{dm}}{dt} = -\frac{1}{T_{Fe}} \frac{L_r}{L_{lr}} i_{dm} + \frac{1}{T_{Fe}} \frac{1}{L_{lr}} \psi_{dr} + \frac{1}{T_{Fe}} i_{ds} + \omega_a i_{qm} \quad (2.71)$$

$$\frac{di_{qm}}{dt} = -\frac{1}{T_{Fe}} \frac{L_r}{L_{lr}} i_{qm} + \frac{1}{T_{Fe}} \frac{1}{L_{lr}} \psi_{qr} + \frac{1}{T_{Fe}} i_{qs} - \omega_a i_{dm}$$

$$\frac{d\omega}{dt} = \frac{P}{J}(T_e - T_L) - \frac{1}{J}k\omega, \quad (2.33)$$

$$T_e = \frac{3}{2}P \frac{L_m}{L_{lr}} (\psi_{dr} i_{qm} - \psi_{qr} i_{dm}), \quad (2.17.f)$$

where the time constant T_{Fe} is defined as :

$$T_{Fe} = \frac{L_m}{R_{Fe}}. \quad (2.72)$$

2.5.2.4. The i_s - i_m - ψ_r rotor-flux-oriented model with iron loss represented by a resistance placed in parallel with the magnetising branch and improved feed-forward vector controller

When the rotor flux orientation constraints (2.35)-(2.36) are applied on the above reduced-order model, the following RFO model is obtained [Levi, 1994b; Levi, 1995b] :

$$\psi_r + T_{lr} \frac{d\psi_r}{dt} = L_m i_{dm}, \quad (2.73)$$

$$\omega_{sl} T_{lr} \psi_r = L_m i_{qm}, \quad (2.74)$$

$$\frac{L_r}{L_{lr}} i_{dm} + T_{Fe} \frac{di_{dm}}{dt} = i_{ds} + \frac{1}{L_{lr}} \psi_r + \omega_r T_{Fe} i_{qm}, \quad (2.75)$$

$$\frac{L_r}{L_{lr}} i_{qm} + T_{Fe} \frac{di_{qm}}{dt} = i_{qs} - \omega_r T_{Fe} i_{dm}, \quad (2.76)$$

$$T_e = \frac{3}{2}P \frac{L_m}{L_{lr}} \psi_r i_{qm}, \quad (2.38.c)$$

$$\frac{d\omega}{dt} = \frac{P}{J}(T_e - T_L) - \frac{1}{J}k\omega. \quad (2.33)$$

This model differs from all the previously introduced RFO models. Introduction of the equivalent iron loss resistance has influenced the equations for the magnetising current components, which have become differential and the cross-coupling between the d -axis and the q -axis has been introduced. The cross-coupling terms are dependent on the angular speed of the rotor flux. Additionally, the time constant T_{Fe} is dependent on the rotor flux angular speed, as iron loss changes with the frequency. All other parameters are assumed to be constant.

It should be stressed that the torque equation (2.38.c) should be used, since the expression (2.38.a) is not valid for this model. If the torque is calculated in accordance with (2.38.a), iron loss would be incorrectly included in the developed torque.

2.5.2.5. The general model with iron loss represented by a resistance placed after the stator resistance

The other possible placement of the equivalent iron loss resistance is immediately after the stator resistance, i.e. between the stator resistance and the stator leakage inductance.

In this case the general model with iron loss becomes :

$$v_s = R_s i_s + \frac{d\psi_s'}{dt} + \omega_a \underline{G} \psi_s' \quad (2.82)$$

$$0 = R_r i_r + \frac{d\psi_r}{dt} + (\omega_a - \omega) \underline{G} \psi_r$$

$$R_r i_{ir} = v_s - R_s i_s \quad (2.83.a)$$

or
$$R_r i_{ir} = L_{ls} \frac{di_s'}{dt} + \omega_a L_{ls} \underline{G} i_s' + \frac{d\psi_m}{dt} + \omega_a \underline{G} \psi_m \quad (2.83.b)$$

$$\psi_s' = L_{ls} i_s' + \psi_m \quad (2.84)$$

$$\psi_r = L_r i_r + \psi_m$$

$$i_s' = i_s - i_{ir} \quad (2.85)$$

$$i_m = i_s' + i_r$$

$$\psi_m = L_m i_m \quad (2.20)$$

$$T_e = \frac{3}{2} P \frac{L_m}{L_{lr}} \left(\psi_{dr} i_{qm} - \psi_{qr} i_{dm} \right) \quad (2.17.f)$$

$$T_e - T_L = \frac{J}{P} \frac{d\omega}{dt} + \frac{1}{P} k\omega \quad (2.4)$$

The value of the equivalent iron loss resistance is dependent on frequency and flux :

$$R_{ir} = f(f, \psi_s') \quad (2.86)$$

The above model has not been utilised for design of improved vector controllers. Hence further processing of this model will be presented in chapter 3. The equivalent scheme of an induction machine with R_{ir} iron loss representation is given next.

2.5.2.6. The equivalent circuit with iron loss represented by a resistance placed after the stator resistance

Application of space vectors on voltage equations (2.82) and (2.83.a) yields :

$$\bar{v}_s = R_s \bar{i}_s + L_{ls} \frac{d\bar{i}_s'}{dt} + j\omega_a L_{ls} \bar{i}_s' + \frac{d\bar{\psi}_m}{dt} + j\omega_a \bar{\psi}_m \quad (2.87)$$

$$0 = R_r \bar{i}_r + L_{lr} \frac{d\bar{i}_r}{dt} + j\omega_a L_{lr} \bar{i}_r + \frac{d\bar{\psi}_m}{dt} + j\omega_a \bar{\psi}_m - j\omega \bar{\psi}_r$$

$$\bar{v}_s = R_s \bar{i}_s + R_r \bar{i}_r \quad (2.88)$$

Dynamic equivalent circuit of an induction machine, in an arbitrary reference frame, based on (2.87) and (2.88), is shown in Fig. 2.13. Iron loss resistance in Fig. 2.13 is given as variable parameter, since its value changes in different operating conditions.

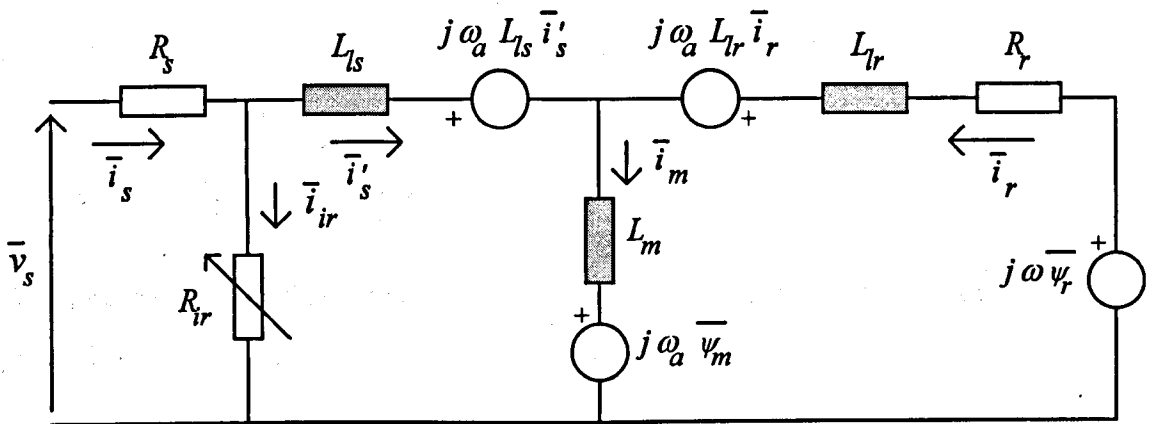


Figure 2.13 : Induction machine dynamic equivalent circuit in an arbitrary reference frame, iron loss represented with a resistor placed after the stator resistance.

2.5.3. Rotor resistance and rotor time constant identifiers based on model reference adaptive control theory

Temperature-related variation of the machine resistances is a slow process, in contrast to fast-changing electromagnetic phenomena such as magnetic saturation and iron loss. Therefore the approach to identification and compensation of rotor resistance variations differs from the approach used for compensation of main flux saturation and iron loss. A number of various methods, discussed in 2.4.4, have been proposed in the literature. As the compensation based on the MRAC theory appears to be the mainstream one, it is elaborated next, using the reactive power as the reference and adaptive quantity.

Identification of T_r , R_r or K_{sl} is normally based on a steady-state model of the induction machine. All the other parameters of the induction machine are assumed to be constant.

The input reactive power of an induction machine is given in terms of d - q axis quantities with the following expression :

$$Q^* = \frac{3}{2} (v_{qs} i_{ds} - v_{ds} i_{qs}) \quad (2.89)$$

The above expression is used for calculation of the reference reactive power. As it is based on the measured stator voltages and currents, no machine parameters are involved. The calculation is independent of the chosen reference frame, and it is convenient to perform the above calculation in the stationary reference frame, avoiding any co-ordinate transformations. On the other hand, the stator voltage d - q axis components in any steady state follow from (2.41) in the form :

$$\begin{aligned} v_{ds} &= R_s i_{ds} - \omega_r \sigma L_s i_{qs} \\ v_{qs} &= R_s i_{qs} + \omega_r \sigma L_s i_{ds} + \omega_r \frac{L_m}{L_r} \psi_r \end{aligned} \quad (2.90)$$

When expressions (2.90) are substituted into (2.89), another expression for the reactive power is obtained as :

$$Q^a = \frac{3}{2} (\omega + \omega_{sl}) L_s (i_{ds}^2 + \sigma i_{qs}^2) \quad (2.91)$$

This expression is called adaptive reactive power. The adaptation mechanism is constructed using (2.89) and (2.91). The difference between the two reactive powers is called the error signal (ΔQ). It is assumed that the error signal stems purely from discrepancy of R_r value used in the controller and the actual R_r value. The error signal is processed through a controller (typically PI or I), whose output represents the updated R_r (or T_r or K_{sl}) value, that is subsequently used in calculation of the slip command. The MRAC adaptation scheme based on the reactive power method is illustrated in Fig. 2.14, together with the slip calculator for feed-forward RFO controller. The output of the corrective PI controller is the slip gain (i.e. inverse of T_r).

The adaptation scheme based on reactive power is independent of R_r , which is a good feature of this method. It is however dependent on machine's inductances, through both inductance L_s and coefficient σ . This means that accurate operation of the adaptation scheme relies on the accurate knowledge of the machine inductances.

2.6. SUMMARY

Basics of mathematical modelling of induction machines were presented in the first instance. Adoption of numerous assumptions and idealisations and subsequent change of co-ordinate system have enabled representation of a complicated electromechanical device by relatively simple mathematical models and equivalent circuits. Models can be simplified further if current feeding, that is very often employed in vector controlled induction machine drives, is analysed. Resultant models are called reduced-order models.

The basics of vector control theory were reviewed and orientation along different flux vectors were explained. Orientation along the rotor flux, in conjunction with current feeding, being the simplest and hence the most common group of vector control methods, was discussed in detail. On the basis of the RFO CPM, obtained when the rotor flux constraints were applied to the reduced-order CPM, vector control principles were discussed. The same RFO CPM was utilised for design of two vector controlled schemes (feedback and feed-forward ones).

Since vector controllers are supposed to operate in the reference system attached to the chosen flux, accurate information on the position of the chosen flux is essential for proper operation. If there are any inaccuracies in obtaining this information, performance of the vector controlled machine deteriorates and the controller is said to be detuned. Sources and consequences of detuned operation were explained. Detuning due to main flux saturation, iron loss and temperature effects, as well as compensation techniques for these three phenomena, were discussed in detail. Two types of compensation techniques were distinguished : open-loop compensation of either main flux saturation and iron loss and closed-loop compensation of thermally induced variations in the rotor resistance.

A detailed review of several improved mathematical models and improved rotor flux estimators revealed that rotor flux estimators with compensation of either main flux saturation or iron loss can be derived using the same procedure that was used for derivation of the CPM-based estimator. Finally, a possible way of using the MRAC theory for on-line adaptation of slip gain was explained for the reactive power method.

3. NOVEL IMPROVED MATHEMATICAL MODELS AND ROTOR FLUX ESTIMATORS

3.1. INTRODUCTION

In order to compensate the detuning in vector controlled drives, different improved mathematical models of induction machines have been developed and proposed in literature. Still, it is felt that there is much more to be done. This research project has resulted in development of several novel improved mathematical models of induction machines and several novel rotor flux estimators. They are presented in this chapter. For each estimator, the step-by-step design procedure, analogous to the one utilised in chapter 2 for design of the CPM-based estimator, is followed. Since most of the proposed novel estimators are quite complex, means of simplifying them in a way which will not compromise the performance improvement are investigated.

The improved models are consequently used for representation of induction machines for quantitative analyses of detuning that occur when the CPM-based estimator is employed in a RFO controller (chapter 4). The improved estimators are incorporated in improved vector controllers, whose operation is analysed in chapter 5.

Novel mathematical models that include main flux saturation and corresponding improved rotor flux estimators are presented in section 3.2. Section 3.3 describes improved models and rotor flux estimators with iron loss. Models and estimators that account for both main flux saturation and iron loss are presented in section 3.4. Section 3.5. summarises the contributions of the chapter.

3.2. NOVEL IMPROVED MODELS AND ESTIMATORS WITH MAIN FLUX SATURATION

3.2.1. The $\psi_m - \psi_r$ rotor-flux-oriented model with main flux saturation and improved estimator, $L_m(\psi_m)$ representation

This model is essentially the same as the $\psi_m - \psi_r$ RFO model from sub-section 2.5.1.6. However, main flux saturation is here represented by the $L_m(\psi_m)$ non-linear relationship (2.45.c). In order to use this representation, the expressions for the magnetising flux

components (2.63)-(2.64) are reformulated in such a way that they do not contain the magnetising current components. From (2.22), adopting (2.36), it can be obtained :

$$\psi_{dm} = \frac{L_m}{L_r} (\psi_r + L_{lr} i_{ds}^e) , \quad (3.1)$$

$$\psi_{qm} = \frac{L_m}{L_r} L_{lr} i_{qs}^e . \quad (3.2)$$

The following equations complete the model :

$$\psi_r + T_{lr} \frac{d\psi_r}{dt} = \psi_{dm} , \quad (2.61)$$

$$\omega_{sl} T_{lr} \psi_r = \psi_{qm} , \quad (2.62)$$

$$\psi_m = \sqrt{\psi_{dm}^2 + \psi_{qm}^2} , \quad (2.46)$$

$$T_e = \frac{3}{2} P \frac{1}{L_{lr}} \psi_r \psi_{qm} , \quad (2.38.b)$$

$$\frac{d\omega}{dt} = \frac{P}{J} (T_e - T_L) - \frac{1}{J} k\omega . \quad (2.33)$$

The saturation-adaptive improved estimator is constructed on the basis of the above model. The structure of the estimator is shown in Fig. 3.1 [Sokola and Levi, 1996]. In this configuration, the estimator requires the non-linear $L_m(\psi_m)$ relationship (2.45.c) to be known. The above RFO model and estimator of Fig. 3.1. are derived for this non-

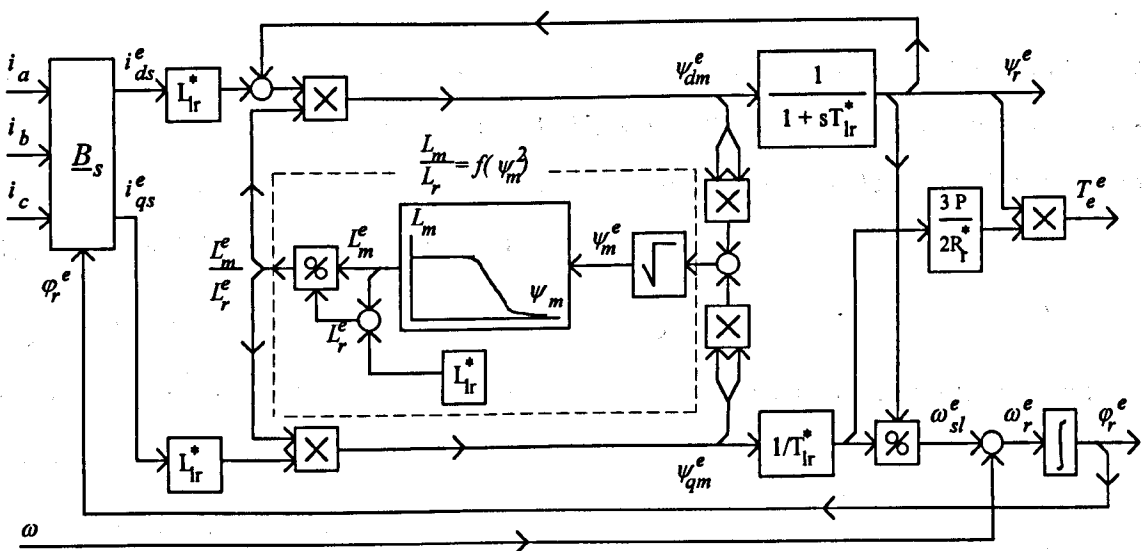


Figure 3.1 : Improved rotor flux estimator of i_s - ω type, with main flux saturation represented by $L_m(\psi_m)$ non-linear relationship.

linear relationship. The amount of computation within the estimator can be reduced by representing main flux saturation by either the non-linear function $L_m = f(\psi_m^2)$, or the non-linear function $\frac{L_m}{L_r} = f(\psi_m^2)$. The latter representation results if all the blocks within dashed lines in Fig. 3.1. are substituted by a block that describes the non-linear function $\frac{L_m}{L_r} = f(\psi_m^2)$.

3.2.2. The \underline{i}_s - $\underline{\psi}_r$ models with main flux saturation and improved estimator, $L_r(\Psi)$ representation

The \underline{i}_s - $\underline{\psi}_r$ reduced-order model, valid for current-fed induction machines, is presented first. It is obtained from the \underline{i}_s - $\underline{\psi}_r$ mixed current-flux model described in the subsection 2.5.1.3, by omitting the first two rows in matrices \underline{A} (2.50) and \underline{B} (2.51). The \underline{i}_s - $\underline{\psi}_r$ reduced-order model in developed form is given with :

$$\frac{d\psi_{dr}}{dt} = -\frac{1}{T_r} \psi_{dr} + \frac{1}{T_r} L_m i_{ds} + (\omega_a - \omega) \psi_{qr} \quad (2.34)$$

$$\frac{d\psi_{qr}}{dt} = -\frac{1}{T_r} \psi_{qr} + \frac{1}{T_r} L_m i_{qs} - (\omega_a - \omega) \psi_{dr}$$

$$\frac{d\omega}{dt} = \frac{P}{J} (T_e - T_L) - \frac{1}{J} k\omega \quad (2.33)$$

$$T_e = \frac{3}{2} P \frac{L_m}{L_r} (\psi_{dr} i_{qs} - \psi_{qr} i_{ds}) \quad (2.17.b)$$

The rotor flux equations for the above reduced-order model have the same appearance as those of the \underline{i}_s - $\underline{\psi}_r$ reduced-order CPM. However, there is one important difference - the rotor inductance (and hence L_m and T_r) in this case is a variable parameter, as given by one of the following two non-linear relationship :

$$L_r = f(\Psi) \quad \text{or} \quad L_r = f(\Psi^2) \quad (3.3)$$

where the generalised flux components under rotor flux orientation constraints and the amplitude of generalised flux are defined with :

$$\begin{aligned} \Psi_d &= \psi_r + L_{lr} i_{ds} \equiv L_r i_{dm} \\ \Psi_q &= L_{lr} i_{qs} \equiv L_r i_{qm} \quad , \\ \Psi &= \sqrt{\Psi_d^2 + \Psi_q^2} \end{aligned} \quad (2.53)$$

and then the mutual inductance is calculated as :

$$L_m = L_r - L_{lr} , \quad (3.4)$$

while the rotor time constant is calculated according to (2.32).

The next two stages in design of the saturation-adaptive improved rotor flux estimator are application of the rotor flux orientation constraints (2.35)-(2.36) to the above reduced-order model and consequent construction of the estimator. The i_s - ψ_r RFO model and the saturation-adaptive estimator with $L_r(\Psi)$ representation are proposed in [Levi and Sokola, 1997] and they follow from the work presented in [Levi, 1995a; Levi and Krzeminski, 1996].

The i_s - ψ_r RFO model is derived from the above reduced-order model by applying the rotor flux orientation constraints (2.35)-(2.36), so that the rotor flux and developed torque under the rotor flux constraints are :

$$\psi_r + T_r \frac{d\psi_r}{dt} = L_m i_{ds} , \quad (2.39)$$

$$\omega_{sl} \psi_r T_r = L_m i_{qs} , \quad (2.40)$$

$$T_e = \frac{3}{2} P \frac{1}{L_{lr}} \psi_r \psi_{qm} . \quad (2.38.b)$$

Equations (3.3), (2.53), (3.4) and (2.32) complete the i_s - ψ_r RFO model. The rotor flux equation (2.39) and the slip equation (2.40) are the same as in the CPM model, but the differences are that L_m and T_r are varied in accordance with changes in the rotor flux.

From this RFO model, the improved saturation-adaptive estimator, depicted in Fig. 3.2 [Levi and Sokola, 1997] is constructed. The relationship $L_r(\Psi^2)$, which saves some computing time, is shown.

3.3. NOVEL IMPROVED MODELS AND ESTIMATORS WITH IRON LOSS ONLY

Although several models with iron loss have been proposed in literature, there was a lot of scope for research and development to be done in this project. Several mixed current-flux models with iron loss will be presented at first, followed by reduced-order

models and RFO models. The section will be concluded with derivation of novel estimators with iron loss, aimed for use in feedback RFO control schemes.

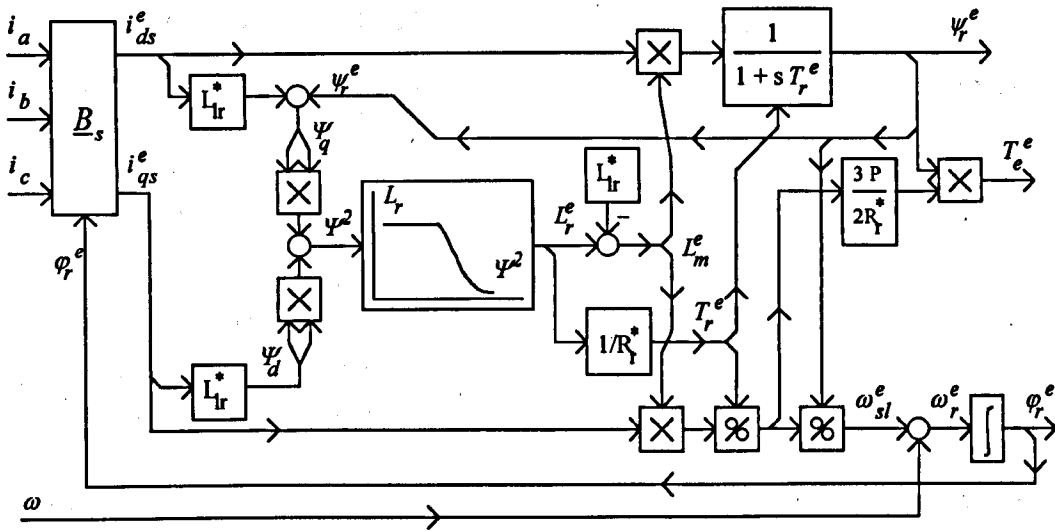


Figure 3.2 : Improved rotor flux estimator of i_s - ω type, with main flux saturation represented by $L_r(\Psi^2)$ non-linear relationship.

3.3.1. Improved mixed current-flux models with iron loss

3.3.1.1. The i_s - i_m - ψ_r mixed current-flux model with iron loss represented by a resistance placed in parallel with the magnetising branch

Inclusion of iron loss has introduced an additional differential matrix equation (2.66) in the general model, increasing the order of the model. Consequently, it is necessary to increase the number of state variables. One of the possible combinations is to use d - q components of the stator current, the magnetising current, and the rotor flux as state variables. This model will be denoted as the i_s - i_m - ψ_m model. The model is again given in state-space form of :

$$\underline{v} = \underline{A} \frac{dx}{dt} + \underline{Bx} \quad , \quad (2.26)$$

where the vector of voltages is :

$$\underline{v} = [v_{ds} \quad v_{qs} \quad 0 \quad 0 \quad 0 \quad 0]^T \quad , \quad (3.5)$$

and the state vector is :

$$\underline{x} = [i_{ds} \quad i_{qs} \quad i_{dm} \quad i_{qm} \quad \psi_{dr} \quad \psi_{qr}]^T \quad . \quad (3.6)$$

The matrices \underline{A} and \underline{B} are:

$$\underline{A} = \begin{bmatrix} L_{ls} & 0 & L_m & 0 & 0 & 0 \\ 0 & L_{ls} & 0 & L_m & 0 & 0 \\ 0 & 0 & 0 & 0 & 1 & 0 \\ 0 & 0 & 0 & 0 & 0 & 1 \\ 0 & 0 & L_m & 0 & 0 & 0 \\ 0 & 0 & 0 & L_m & 0 & 0 \end{bmatrix}, \quad (3.7)$$

$$\underline{B} = \begin{bmatrix} R_s & -\omega_a L_{ls} & 0 & -\omega_a L_m & 0 & 0 \\ \omega_a L_{ls} & R_s & \omega_a L_m & 0 & 0 & 0 \\ 0 & 0 & -\frac{L_m}{T_{lr}} & 0 & \frac{1}{T_{lr}} & -(\omega_a - \omega) \\ 0 & 0 & 0 & -\frac{L_m}{T_{lr}} & \omega_a - \omega & \frac{1}{T_{lr}} \\ -R_{Fe} & 0 & \frac{L_r}{T_{lFe}} & -\omega_a L_m & -\frac{1}{T_{lFe}} & 0 \\ 0 & -R_{Fe} & \omega_a L_m & \frac{L_r}{T_{lFe}} & 0 & -\frac{1}{T_{lFe}} \end{bmatrix}, \quad (3.8)$$

where the time constant T_{lFe} is defined as :

$$T_{lFe} = \frac{L_{lr}}{R_{Fe}}. \quad (3.9)$$

In this case the developed torque is :

$$T_e = \frac{3}{2} P \frac{L_m}{L_{lr}} (\psi_{dr} i_{qm} - \psi_{qr} i_{dm}). \quad (2.17.f)$$

3.3.1.2. The i_s - ψ_m - ψ_r mixed current-flux model with iron loss represented by a resistance placed in parallel with the magnetising branch

Another possible combination is to use d - q components of stator current, magnetising flux and rotor flux as state variables. This model is denoted as i_s - ψ_m - ψ_r mixed model.

In this case, the vector of voltages is again defined by (3.5) while the state vector is :

$$\underline{x} = [i_{ds} \quad i_{qs} \quad \psi_{dm} \quad \psi_{qm} \quad \psi_{dr} \quad \psi_{qr}]^T. \quad (3.10)$$

The matrices \underline{A} and \underline{B} for this model are easily obtained from (3.7) and (3.8), by dividing the third and the fourth columns by L_m , yielding :

$$\underline{A} = \begin{bmatrix} L_{ls} & 0 & 1 & 0 & 0 & 0 \\ 0 & L_{ls} & 0 & 1 & 0 & 0 \\ 0 & 0 & 0 & 0 & 1 & 0 \\ 0 & 0 & 0 & 0 & 0 & 1 \\ 0 & 0 & 1 & 0 & 0 & 0 \\ 0 & 0 & 0 & 1 & 0 & 0 \end{bmatrix}, \quad (3.11)$$

$$\underline{B} = \begin{bmatrix} R_s & -\omega_a L_{ls} & 0 & -\omega_a & 0 & 0 \\ \omega_a L_{ls} & R_s & \omega_a & 0 & 0 & 0 \\ 0 & 0 & -\frac{1}{T_{lr}} & 0 & \frac{1}{T_{lr}} & -(\omega_a - \omega) \\ 0 & 0 & 0 & -\frac{1}{T_{lr}} & \omega_a - \omega & \frac{1}{T_{lr}} \\ -R_{Fe} & 0 & \frac{L_r}{L_m} \frac{1}{T_{lFe}} & -\omega_a & -\frac{1}{T_{lFe}} & 0 \\ 0 & -R_{Fe} & \omega_a & \frac{L_r}{L_m} \frac{1}{T_{lFe}} & 0 & -\frac{1}{T_{lFe}} \end{bmatrix}. \quad (3.12)$$

For such a choice of state variables, the torque equation (2.17.c) should be used :

$$T_e = \frac{3}{2} P \frac{1}{L_{lr}} (\psi_{dr} \psi_{qm} - \psi_{qr} \psi_{dm}). \quad (2.17.c)$$

3.3.1.3. Mixed current-flux models with iron loss represented by a resistance placed after the stator resistance

These models are derived from the general model with R_{ir} iron loss representation, given in sub-section 2.5.2.5. When the machine is fed from a current source, it is convenient to use (2.83.b) for derivation of mixed current-flux models, since the stator voltage does not feature in this equation. As it was the case with R_{Fe} iron loss representation, two mixed models can be formed, namely the $\underline{i}_s - \underline{i}_m - \underline{\psi}_r$ model and the $\underline{i}_s - \underline{\psi}_m - \underline{\psi}_r$ model. For the mixed $\underline{i}_s - \underline{i}_m - \underline{\psi}_r$ model, the vector of voltages is given by (3.5) and the state vector is defined by (3.6). Then the matrices \underline{A} and \underline{B} are :

$$\underline{A} = \begin{bmatrix} 0 & 0 & k_1 L_m & 0 & -\frac{L_{ls}}{L_{lr}} & 0 \\ 0 & 0 & 0 & k_1 L_m & 0 & -\frac{L_{ls}}{L_{lr}} \\ 0 & 0 & 0 & 0 & 1 & 0 \\ 0 & 0 & 0 & 0 & 0 & 1 \\ 0 & 0 & k_1 L_m & 0 & -\frac{L_{ls}}{L_{lr}} & 0 \\ 0 & 0 & 0 & k_1 L_m & 0 & -\frac{L_{ls}}{L_{lr}} \end{bmatrix}, \quad (3.13)$$

$$\underline{B} = \begin{bmatrix} R_s & 0 & 0 & -\omega_a k_1 L_m & 0 & \omega_a \frac{L_{ls}}{L_{lr}} \\ 0 & R_s & \omega_a k_1 L_m & 0 & -\omega_a \frac{L_{ls}}{L_{lr}} & 0 \\ 0 & 0 & -\frac{L_m}{T_{lr}} & 0 & \frac{1}{T_{lr}} & -(\omega_a - \omega) \\ 0 & 0 & 0 & -\frac{L_m}{T_{lr}} & \omega_a - \omega & \frac{1}{T_{lr}} \\ -R_{lr} & 0 & \frac{L_r}{T_{lir}} & -\omega_a k_1 L_m & -\frac{1}{T_{lir}} & \omega_a \frac{L_{ls}}{L_{lr}} \\ 0 & -R_{lr} & \omega_a k_1 L_m & \frac{L_r}{T_{lir}} & -\omega_a \frac{L_{ls}}{L_{lr}} & -\frac{1}{T_{lir}} \end{bmatrix}, \quad (3.14)$$

where :

$$k_1 = 1 + \frac{L_{ls}}{L_{lr}} \frac{L_r}{L_m} \quad \text{and} \quad T_{lir} = \frac{L_{lr}}{R_{lr}}. \quad (3.15)$$

The torque equation (2.17.f) and the equation of mechanical motion (2.4) complete the model.

The $\underline{i}_s - \underline{\psi}_m - \underline{\psi}_r$ mixed current-flux model with iron loss is easily derived from the above $\underline{i}_s - \underline{i}_m - \underline{\psi}_r$ mixed model, by choosing (3.10) as the state vector, using the torque expression (2.17.c) and dividing the third and the fourth column in matrices \underline{A} (3.13) and \underline{B} (3.14) by L_m .

Comparison of the presented four mixed current-flux models with different iron loss representation reveals that R_{Fe} iron loss representation (models in 3.3.1.1 and 3.3.1.2) yield simpler models than the R_{lr} representation (models in this sub-section). The additional complexity in models with R_{lr} representation is essentially the appearance of additional terms that contain the coefficient k_1 or the L_{ls}/L_{lr} ratio.

3.3.2. Improved reduced-order models with iron loss

3.3.2.1. The $\underline{i}_s - \underline{i}_m - \underline{\psi}_r$ reduced-order model with iron loss represented by a resistance placed in parallel with the magnetising branch

This model is almost the same as the model presented in 2.5.2.3. It is repeated here with a minor modification - instead of the equivalent iron loss time constant T_{Fe} (2.72), the equivalent leakage iron loss time constant T_{lFe} (3.9) is used. It will be shown later that models and estimators using T_{lFe} are more convenient in certain cases, especially if both

main flux saturation and iron loss are analysed. The $i_s - i_m - \psi_r$ reduced-order model is derived from the mixed model of 3.3.1.1, by assuming that stator current components are known and therefore omitting the first two rows in matrices \underline{A} (3.7) and \underline{B} (3.8). Such manipulation results in the following expressions :

$$\begin{aligned} \frac{d\psi_{dr}}{dt} &= -\frac{1}{T_{lr}} \psi_{dr} + \frac{1}{T_{lr}} L_m i_{dm} + (\omega_a - \omega) \psi_{qr} \\ \frac{d\psi_{qr}}{dt} &= -\frac{1}{T_{lr}} \psi_{qr} + \frac{1}{T_{lr}} L_m i_{qm} - (\omega_a - \omega) \psi_{dr} \end{aligned} \quad (2.70)$$

$$\begin{aligned} \frac{di_{dm}}{dt} &= -\frac{1}{T_{lFe}} \frac{L_r}{L_m} i_{dm} + \frac{1}{T_{lFe}} \frac{1}{L_m} \psi_{dr} + \frac{R_{Fe}}{L_m} i_{ds} + \omega_a i_{qm} \\ \frac{di_{qm}}{dt} &= -\frac{1}{T_{lFe}} \frac{L_r}{L_m} i_{qm} + \frac{1}{T_{lFe}} \frac{1}{L_m} \psi_{qr} + \frac{R_{Fe}}{L_m} i_{qs} - \omega_a i_{dm} \end{aligned} \quad (3.16)$$

$$\frac{d\omega}{dt} = \frac{P}{J} (T_e - T_L) - \frac{1}{J} k\omega \quad (2.33)$$

$$T_e = \frac{3}{2} P \frac{L_m}{L_{lr}} (\psi_{dr} i_{qm} - \psi_{qr} i_{dm}) \quad (2.17.f)$$

3.3.2.2. The $i_s - \psi_m - \psi_r$ reduced-order model with iron loss represented by a resistance placed in parallel with the magnetising branch

This model is derived from the mixed current-flux model described in 3.3.1.2. Thus the model consist of :

$$\begin{aligned} \frac{d\psi_{dr}}{dt} &= -\frac{1}{T_{lr}} \psi_{dr} + \frac{1}{T_{lr}} \psi_{dm} + (\omega_a - \omega) \psi_{qr} \\ \frac{d\psi_{qr}}{dt} &= -\frac{1}{T_{lr}} \psi_{qr} + \frac{1}{T_{lr}} \psi_{qm} - (\omega_a - \omega) \psi_{dr} \end{aligned} \quad (2.60)$$

$$\begin{aligned} \frac{d\psi_{dm}}{dt} &= -\frac{1}{T_{lFe}} \frac{L_r}{L_m} \psi_{dm} + \frac{1}{T_{lFe}} \psi_{dr} + R_{Fe} i_{ds} + \omega_a \psi_{qm} \\ \frac{d\psi_{qm}}{dt} &= -\frac{1}{T_{lFe}} \frac{L_r}{L_m} \psi_{qm} + \frac{1}{T_{lFe}} \psi_{qr} + R_{Fe} i_{qs} - \omega_a \psi_{dm} \end{aligned} \quad (3.17)$$

$$\frac{d\omega}{dt} = \frac{P}{J} (T_e - T_L) - \frac{1}{J} k\omega \quad (2.33)$$

$$T_e = \frac{3}{2} P \frac{1}{L_{lr}} (\psi_{dr} \psi_{qm} - \psi_{qr} \psi_{dm}) \quad (2.17.c)$$

3.3.2.3. The i_s - ψ_m - ψ_r reduced-order model with iron loss represented by a resistance placed after the stator resistance

For this way of iron loss representation, the mixed model from 3.3.1.3. is used as a basis for derivation. Elimination of the first two rows in (3.13) and (3.14) yields :

$$\begin{aligned} \frac{d\psi_{dr}}{dt} &= -\frac{1}{T_{lr}} \psi_{dr} + \frac{1}{T_{lr}} \psi_{dm} + (\omega_a - \omega) \psi_{qr} \\ \frac{d\psi_{qr}}{dt} &= -\frac{1}{T_{lr}} \psi_{qr} + \frac{1}{T_{lr}} \psi_{qm} - (\omega_a - \omega) \psi_{dr} \end{aligned} \quad (2.60)$$

$$\begin{aligned} k_1 \frac{d\psi_{dm}}{dt} - \frac{L_{ls}}{L_{lr}} \frac{d\psi_{dr}}{dt} &= R_{lr} i_{ds} - \frac{1}{T_{lir}} \frac{L_r}{L_m} \psi_{dm} + \omega_a k_1 \psi_{qm} + \frac{1}{T_{lir}} \psi_{dr} - \omega_a \frac{L_{ls}}{L_{lr}} \psi_{qm} \\ k_1 \frac{d\psi_{qm}}{dt} - \frac{L_{ls}}{L_{lr}} \frac{d\psi_{qr}}{dt} &= R_{lr} i_{qs} - \frac{1}{T_{lir}} \frac{L_r}{L_m} \psi_{qm} - \omega_a k_1 \psi_{dm} + \frac{1}{T_{lir}} \psi_{qr} + \omega_a \frac{L_{ls}}{L_{lr}} \psi_{dm} \end{aligned} \quad (3.18)$$

$$\frac{d\omega}{dt} = \frac{P}{J} (T_e - T_L) - \frac{1}{J} k \omega \quad (2.33)$$

$$T_e = \frac{3}{2} P \frac{1}{L_{lr}} (\psi_{dr} \psi_{qm} - \psi_{qr} \psi_{dm}) \quad (2.17.c)$$

Substitution of (2.60) into (3.18) results in the following expressions for the magnetising flux components :

$$\begin{aligned} \frac{d\psi_{dm}}{dt} &= \frac{\left(-\frac{1}{T_{lir}} \frac{L_r}{L_m} + \frac{1}{T_{lr}} \frac{L_{ls}}{L_{lr}} \right) \psi_{dm} + \left(\frac{1}{T_{lir}} - \frac{1}{T_{lr}} \frac{L_{ls}}{L_{lr}} \right) \psi_{dr} - \omega \frac{L_{ls}}{L_{lr}} \psi_{qr} + R_{lr} i_{ds}}{k_1} + \omega_a \psi_{qm} \\ \frac{d\psi_{qm}}{dt} &= \frac{\left(-\frac{1}{T_{lir}} \frac{L_r}{L_m} + \frac{1}{T_{lr}} \frac{L_{ls}}{L_{lr}} \right) \psi_{qm} + \left(\frac{1}{T_{lir}} - \frac{1}{T_{lr}} \frac{L_{ls}}{L_{lr}} \right) \psi_{qr} + \omega \frac{L_{ls}}{L_{lr}} \psi_{dr} + R_{lr} i_{qs}}{k_1} - \omega_a \psi_{dm} \end{aligned} \quad (3.19)$$

The magnetising flux equations (3.19) are considerably more complex than the (3.17), making this model significantly more complicated than the reduced-order model with R_{Fe} iron loss representation. Eventual utilisation of this model for design of improved rotor flux estimators would result in a highly complex estimator structure. This is the main reason why this model is not elaborated further.

3.3.3. Improved rotor flux-oriented models with iron loss

Improved RFO models with iron loss are derived from the reduced-order models, applying the rotor flux orientation constraints (2.35)-(2.36). Two RFO models, both with R_{Fe} iron loss representation, will be presented.

3.3.3.1. The $\underline{i}_s - \underline{i}_m - \underline{\psi}_r$ rotor-flux-oriented model with iron loss represented by a resistance placed in parallel with the magnetising branch

A RFO model of this type has been described already in sub-section 2.5.2.4, where the equivalent iron loss time constant T_{Fe} was used. On the other hand, the equivalent leakage iron loss time constant T_{lFe} is used in the mixed current-flux model of sub-section 3.3.1.1 and the reduced-order model of 3.3.2.1. Hence the $\underline{i}_s - \underline{i}_m - \underline{\psi}_r$ RFO model with iron loss presented here slightly differs from the $\underline{i}_s - \underline{i}_m - \underline{\psi}_r$ RFO model with iron loss from 2.5.2.4. When the rotor flux orientation constraints (2.35)-(2.36) are applied on the reduced-order model of 3.3.2.1, the following RFO model is obtained :

$$\psi_r + T_{lr} \frac{d\psi_r}{dt} = L_m i_{dm} \quad , \quad (2.73)$$

$$L_m i_{qm} = \omega_{sl} T_{lr} \psi_r \quad , \quad (2.74)$$

$$i_{dm} + T_{lFe} \frac{L_m}{L_r} \frac{di_{dm}}{dt} = \frac{1}{L_r} \left(\psi_r + L_{lr} i_{ds} + \omega_r T_{lFe} L_m i_{qm} \right) \quad , \quad (3.20)$$

$$i_{qm} + T_{lFe} \frac{L_m}{L_r} \frac{di_{qm}}{dt} = \frac{1}{L_r} \left(L_{lr} i_{qs} - \omega_r T_{lFe} L_m i_{dm} \right) \quad , \quad (3.21)$$

$$T_e = \frac{3}{2} P \frac{L_m}{L_{lr}} \psi_r i_{qm} \quad , \quad (2.38.c)$$

$$\frac{d\omega}{dt} = \frac{P}{J} (T_e - T_L) - \frac{1}{J} k\omega \quad . \quad (2.33)$$

Similarly to the model of 2.5.2.4, the cross-coupling terms are dependent on the angular speed of the rotor flux, i.e. on the frequency of the supply. Additionally, the time constant T_{lFe} is dependent on the rotor flux angular speed, as iron loss changes with the frequency.

3.3.3.2. The $\underline{i}_s - \underline{\psi}_m - \underline{\psi}_r$ rotor-flux-oriented model with iron loss represented by a resistance placed in parallel with the magnetising branch

This RFO model is obtained from the reduced-order model of sub-section 3.2.2.2. It can also be derived from the $\underline{i}_s - \underline{i}_m - \underline{\psi}_r$ RFO model from the previous sub-section, by using (2.20). The model consist of the following equations :

$$\psi_r + T_{lr} \frac{d\psi_r}{dt} = \psi_{dm} \quad , \quad (2.61)$$

$$\omega_{sl} T_{lr} \psi_r = \psi_{qm} \quad , \quad (2.62)$$

$$\psi_{dm} + T_{lFe} \frac{L_m}{L_r} \frac{d\psi_{dm}}{dt} = \frac{L_m}{L_r} (\psi_r + L_{lr} i_{ds} + \omega_r T_{lFe} \psi_{qm}) \quad , \quad (3.22)$$

$$\psi_{qm} + T_{lFe} \frac{L_m}{L_r} \frac{d\psi_{qm}}{dt} = \frac{L_m}{L_r} (L_{lr} i_{qs} - \omega_r T_{lFe} \psi_{dm}) \quad , \quad (3.23)$$

$$T_e = \frac{3}{2} P \frac{1}{L_{lr}} \psi_r \psi_{qm} \quad , \quad (2.38.b)$$

$$\frac{d\omega}{dt} = \frac{P}{J} (T_e - T_L) - \frac{1}{J} k\omega \quad . \quad (2.33)$$

The above model is similar to the RFO model introduced in the previous sub-section, with cross-coupling between the two components of the magnetising flux.

3.3.4. Improved estimators with iron loss

Since the three RFO models presented in 2.5.2.3, 3.3.3.1 and 3.3.3.2. are very similar, the structure of the corresponding estimators would be very similar. The $i_s - \psi_m - \psi_r$ RFO model from sub-section 3.3.3.2, slightly less complex than the other two RFO models, is utilised here for the design of the improved estimator with iron loss, resulting in more compact estimator than in the other two cases. The improved rotor flux estimator with iron loss is shown in Fig. 3.3 [Levi et al., 1996a]. The equivalent iron loss leakage time constant is assumed to be dependent on the angular speed of the rotor flux. The non-linear relationship $T_{lFe} = f(\omega_r)$ can be entered as a look-up table. The estimator is more complex than the CPM-based estimator as there are several more calculations to be performed.

The complexity of this estimator can be critical for real-time application. This is the reason for seeking a possible simpler version, which will feature less calculations while still enabling iron loss compensation. If the estimator parameters are analysed, it can be concluded that the time constant T_{lFe} (and subsequently the equivalent time constant $\frac{L_m}{L_r} T_{lFe}$) is always at least two orders (100 times) smaller than the rotor leakage time constant T_{lr} . This means that the influence of the first-order delay elements containing T_{lFe} on the machine dynamics is negligible when compared with the influence of the first-order delay element that contains T_{lr} . With such a justification, the equivalent time

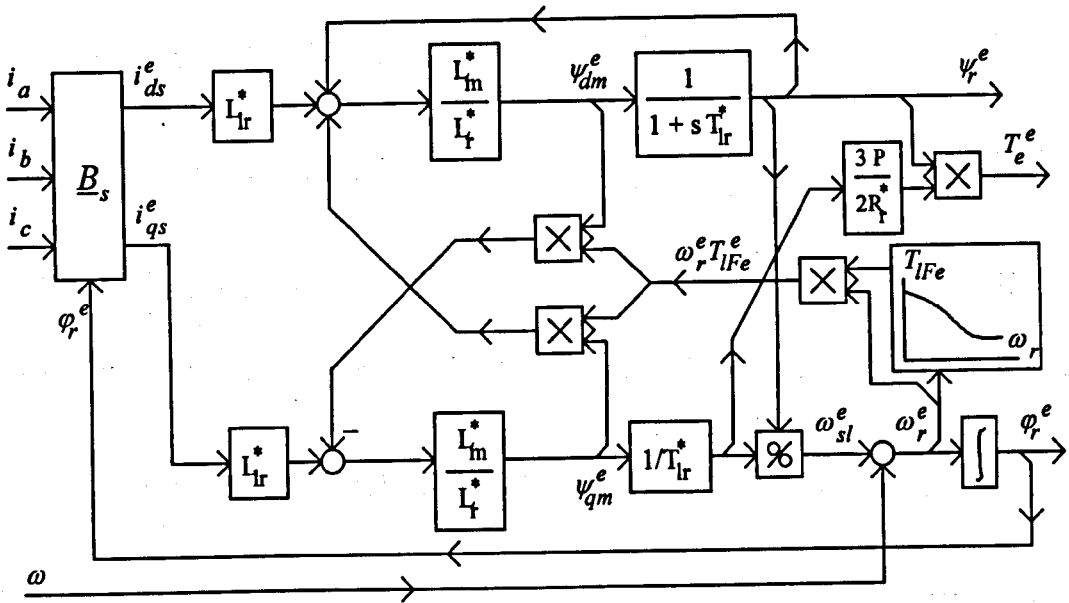


Figure 3.4 : Simplified improved rotor flux estimator of i_s - ω type, with iron loss.

3.4.1. The general model with both iron loss and main flux saturation

The general model of the induction machine with iron loss represented by a resistance placed in parallel with the magnetising branch and with main flux saturation is [Boldea and Nasar, 1987b] :

$$\underline{v}_s = R_s \underline{i}_s + \frac{d(L_{ls} \underline{i}_s)}{dt} + \frac{d\underline{\psi}_m}{dt} + \omega_a L_{ls} \underline{G} \underline{i}_s + \omega_a \underline{G} \underline{\psi}_m \quad , \quad (2.23)$$

$$0 = R_r \underline{i}_r + \frac{d(L_{lr} \underline{i}_r)}{dt} + \frac{d\underline{\psi}_m}{dt} + \omega_a L_{lr} \underline{G} \underline{i}_r + \omega_a \underline{G} \underline{\psi}_m - \omega \underline{G} \underline{\psi}_r$$

$$R_{Fe} \underline{i}_{Fe} = \frac{d\underline{\psi}_m}{dt} + \omega_a \underline{G} \underline{\psi}_m \quad , \quad (2.66)$$

$$\underline{\psi}_s = L_{ls} \underline{i}_s + \underline{\psi}_m \quad (2.22)$$

$$\underline{\psi}_r = L_{lr} \underline{i}_r + \underline{\psi}_m \quad ,$$

$$\underline{i}_m + \underline{i}_{Fe} = \underline{i}_s + \underline{i}_r \quad , \quad (2.67)$$

$$\underline{\psi}_m = L_m \underline{i}_m \quad , \quad (2.20)$$

$$\underline{i}_m = f(\underline{\psi}_m) \quad \text{or} \quad L_m = f(\underline{i}_m) \quad \text{or} \quad L_m = f(\underline{\psi}_m) \quad , \quad (2.45)$$

$$R_{Fe} = f(f, \underline{\psi}_s) \quad , \quad (2.68)$$

$$T_e = \frac{3}{2} P \frac{1}{L_{lr}} (\psi_{dr} \psi_{qm} - \psi_{qr} \psi_{dm}) , \quad (2.17.c)$$

$$\text{or } T_e = \frac{3}{2} P \frac{L_m}{L_{lr}} (\psi_{dr} i_{qm} - \psi_{qr} i_{dm}) , \quad (2.17.f)$$

$$T_e - T_L = \frac{J}{P} \frac{d\omega}{dt} + \frac{1}{P} k\omega . \quad (2.4)$$

On the first sight, the above model is almost identical to the model given in 2.5.2.1. This is because the model is not in the state-space form. The difference is that main flux saturation is accounted for, by one of the (2.45) non-linear relationships.

3.4.2. The equivalent circuit with both iron loss and main flux saturation

The equivalent circuit with both iron loss and main flux saturation can be constructed from :

$$\bar{v}_s = R_s \bar{i}_s + L_{ls} \frac{d\bar{i}_s}{dt} + j\omega_a L_{ls} \bar{i}_s + L_m \frac{d\bar{i}_m}{dt} + j\omega_a L_m \bar{i}_m \quad (2.25)$$

$$0 = R_r \bar{i}_r + L_{lr} \frac{d\bar{i}_r}{dt} + j\omega_a L_{lr} \bar{i}_r + L_m \frac{d\bar{i}_m}{dt} + j\omega_a L_m \bar{i}_m - j\omega \bar{\psi}_r$$

$$R_{Fe} \bar{i}_{Fe} = \frac{d\bar{\psi}_m}{dt} + j\omega_a \bar{\psi}_m . \quad (2.69)$$

The corresponding equivalent circuit is shown in Fig. 3.5. Both equivalent iron loss resistance and mutual inductance are variable parameters, as given by (2.45) and (2.68).

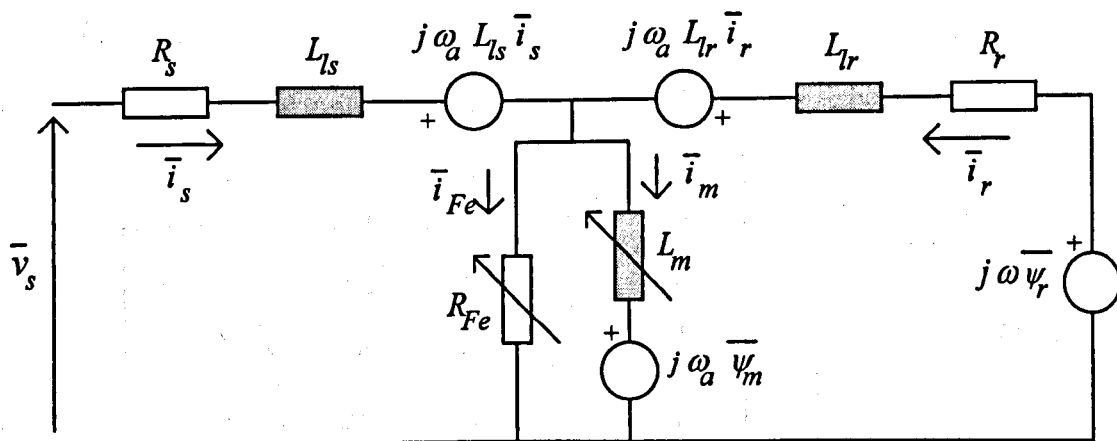


Figure 3.5 : Induction machine dynamic equivalent circuit in an arbitrary reference frame, with both iron loss and main flux saturation.

3.4.3. Improved mixed current-flux models with both iron loss and main flux saturation

3.4.3.1. The $\underline{i}_s - \underline{i}_m - \underline{\psi}_r$ mixed current-flux model with both iron loss and main flux saturation

This model is an original contribution of the research. Like in the case without main flux saturation (sub-section 3.3.1.1), the vector of voltages is :

$$\underline{v} = [v_{ds} \quad v_{qs} \quad 0 \quad 0 \quad 0 \quad 0]^t, \quad (3.5)$$

and the state vector is :

$$\underline{x} = [i_{ds} \quad i_{qs} \quad i_{dm} \quad i_{qm} \quad \psi_{dr} \quad \psi_{qr}]^t. \quad (3.6)$$

Because of main flux saturation, some coefficients in the matrix \underline{A} (3.7) change, so that matrix \underline{A} becomes :

$$\underline{A} = \begin{bmatrix} L_{ls} & 0 & L_{dd} & L_{dq} & 0 & 0 \\ 0 & L_{ls} & L_{dq} & L_{qq} & 0 & 0 \\ 0 & 0 & 0 & 0 & 1 & 0 \\ 0 & 0 & 0 & 0 & 0 & 1 \\ 0 & 0 & L_{dd} & L_{dq} & 0 & 0 \\ 0 & 0 & L_{dq} & L_{qq} & 0 & 0 \end{bmatrix}. \quad (3.26)$$

Saturation dependent coefficients are defined as :

$$\begin{aligned} L_{dd} &= L_m' \frac{i_{dm}^2}{i_m^2} + L_m \frac{i_{qm}^2}{i_m^2} \\ L_{qq} &= L_m' \frac{i_{qm}^2}{i_m^2} + L_m \frac{i_{dm}^2}{i_m^2}, \\ L_{dq} &= (L_m' - L_m) \frac{i_{dm} i_{qm}}{i_m^2} \end{aligned} \quad (3.27)$$

where dynamic mutual inductance is defined by (2.48). The matrix \underline{B} remains :

$$\underline{B} = \begin{bmatrix} R_s & -\omega_a L_{ls} & 0 & -\omega_a L_m & 0 & 0 \\ \omega_a L_{ls} & R_s & \omega_a L_m & 0 & 0 & 0 \\ 0 & 0 & -\frac{L_m}{T_r} & 0 & \frac{1}{T_r} & -(\omega_a - \omega) \\ 0 & 0 & 0 & -\frac{L_m}{T_r} & \omega_a - \omega & \frac{1}{T_r} \\ -R_{Fe} & 0 & \frac{L_r}{T_{IFe}} & -\omega_a L_m & -\frac{1}{T_{IFe}} & 0 \\ 0 & -R_{Fe} & \omega_a L_m & \frac{L_r}{T_{IFe}} & 0 & -\frac{1}{T_{IFe}} \end{bmatrix}, \quad (3.8)$$

while the developed torque is given with :

$$T_e = \frac{3}{2} P \frac{L_m}{L_r} (\psi_{dr} i_{qm} - \psi_{qr} i_{dm}) \quad (2.17.f)$$

This model contains saturation dependent coefficients in both the first two and the last two rows, which make it inconvenient for either detailed analysis of dynamics and simulations. Because of this, the $i_s - \underline{\psi}_m - \underline{\psi}_r$ mixed current-flux model is derived in the next sub-section.

3.4.3.2. The $i_s - \underline{\psi}_m - \underline{\psi}_r$ mixed current-flux model with both iron loss and main flux saturation

Another possible combination is to use d - q components of stator current, magnetising flux and rotor flux as the state variables. The idea of using the magnetising flux instead of the magnetising current relies on the earlier mentioned fact that in certain cases flux-based models do not contain terms that explicitly describe cross-saturation. Thus the $i_s - \underline{\psi}_m - \underline{\psi}_r$ mixed current-flux model should be simpler than the $i_s - i_m - \underline{\psi}_r$ one. The equations that constitute the $i_s - \underline{\psi}_m - \underline{\psi}_r$ mixed current-flux model with both iron loss and main flux saturation are essentially identical to the equations of the $i_s - \underline{\psi}_m - \underline{\psi}_r$ mixed current-flux model with iron loss only, presented in sub-section 3.3.1.2. The only difference is that main flux saturation is included as well. Hence the model is given with :

$$\underline{v} = [v_{ds} \quad v_{qs} \quad 0 \quad 0 \quad 0 \quad 0]^t, \quad (3.5)$$

$$\underline{x} = [i_{ds} \quad i_{qs} \quad \psi_{dm} \quad \psi_{qm} \quad \psi_{dr} \quad \psi_{qr}]^t. \quad (3.10)$$

$$\underline{A} = \begin{bmatrix} L_{ls} & 0 & 1 & 0 & 0 & 0 \\ 0 & L_{ls} & 0 & 1 & 0 & 0 \\ 0 & 0 & 0 & 0 & 1 & 0 \\ 0 & 0 & 0 & 0 & 0 & 1 \\ 0 & 0 & 1 & 0 & 0 & 0 \\ 0 & 0 & 0 & 1 & 0 & 0 \end{bmatrix}, \quad (3.11)$$

$$\underline{B} = \begin{bmatrix} R_s & -\omega_a L_{ls} & 0 & -\omega_a & 0 & 0 \\ \omega_a L_{ls} & R_s & \omega_a & 0 & 0 & 0 \\ 0 & 0 & -\frac{1}{T_{lr}} & 0 & \frac{1}{T_{lr}} & -(\omega_a - \omega) \\ 0 & 0 & 0 & -\frac{1}{T_{lr}} & \omega_a - \omega & \frac{1}{T_{lr}} \\ -R_{Fe} & 0 & \frac{L_r}{L_m} \frac{1}{T_{lFe}} & -\omega_a & -\frac{1}{T_{lFe}} & 0 \\ 0 & -R_{Fe} & \omega_a & \frac{L_r}{L_m} \frac{1}{T_{lFe}} & 0 & -\frac{1}{T_{lFe}} \end{bmatrix}, \quad (3.12)$$

$$T_e = \frac{3}{2} P \frac{1}{L_{lr}} (\psi_{dr} \psi_{qm} - \psi_{qr} \psi_{dm}) . \quad (2.17.c)$$

Main flux saturation is described by one of the (2.45) non-linear relationships.

3.4.4. Improved i_s - ψ_m - ψ_r reduced-order model machine with both iron loss and main flux saturation

Due to the existence of saturation-dependent coefficients, the i_s - ψ_m - ψ_r mixed model (given in 3.4.3.1) is more complex than the i_s - ψ_m - ψ_r mixed model (given in 3.4.3.2).

Thus the latter is used for derivation of the reduced-order model, which is obtained as :

$$\frac{d\psi_{dr}}{dt} = -\frac{1}{T_{lr}} \psi_{dr} + \frac{1}{T_{lr}} \psi_{dm} + (\omega_a - \omega) \psi_{qr} \quad (2.60)$$

$$\frac{d\psi_{qr}}{dt} = -\frac{1}{T_{lr}} \psi_{qr} + \frac{1}{T_{lr}} \psi_{qm} - (\omega_a - \omega) \psi_{dr}$$

$$\frac{d\psi_{dm}}{dt} = -\frac{1}{T_{lFe}} \frac{L_r}{L_m} \psi_{dm} + \omega_a \psi_{qm} + \frac{1}{T_{lFe}} \psi_{dr} + R_{Fe} i_{ds} \quad (3.28)$$

$$\frac{d\psi_{qm}}{dt} = -\frac{1}{T_{lFe}} \frac{L_r}{L_m} \psi_{qm} - \omega_a \psi_{dm} + \frac{1}{T_{lFe}} \psi_{qr} + R_{Fe} i_{qs}$$

$$\frac{d\omega}{dt} = \frac{P}{J} (T_e - T_L) - \frac{1}{J} k\omega , \quad (2.33)$$

$$T_e = \frac{3}{2} P \frac{1}{L_{lr}} (\psi_{dr} \psi_{qm} - \psi_{qr} \psi_{dm}) , \quad (2.17.c)$$

Main flux saturation is described by one of the (2.54) non-linear relationships.

3.4.5 Improved rotor flux-oriented models with both iron loss and main flux saturation

Two RFO models with both iron loss and main flux saturation will be presented. They are both i_s - ψ_m - ψ_r RFO models, derived from the above reduced-order model. The difference between the two models is concerned with the representation of main flux saturation. Models with $L_m(\psi_m)$ and $i_m(\psi_m)$ representations are given. Although their equations differ, both models produce the same simulation results. Iron loss in both models is represented by the equivalent iron loss resistance R_{Fe} .

The first model that is elaborated here is the i_s - ψ_m - ψ_r RFO model with both iron loss and main flux saturation, with main flux saturation represented by $L_m(\psi_m)$ non-linear function. This model is obtained from the reduced-order model of 3.4.4 when $L_m(\psi_m)$ representation of main flux saturation (2.45.c) is utilised. The RFO constraints (2.35)-(2.36) are applied to the reduced-order model, resulting in the following model :

$$\psi_r + T_{lr} \frac{d\psi_r}{dt} = \psi_{dm} \quad , \quad (2.61)$$

$$\psi_{qm} = \omega_{sl} T_{lr} \psi_r \quad , \quad (2.62)$$

$$\psi_{dm} + T_{lFe} \frac{L_m}{L_r} \frac{d\psi_{dm}}{dt} = \frac{L_m}{L_r} \left(\psi_r + L_{lr} i_{ds} + \omega_r T_{lFe} \psi_{qm} \right) \quad , \quad (3.20)$$

$$\psi_{qm} + T_{lFe} \frac{L_m}{L_r} \frac{d\psi_{qm}}{dt} = \frac{L_m}{L_r} \left(L_{lr} i_{qs} - \omega_r T_{lFe} \psi_{dm} \right) \quad , \quad (3.21)$$

$$T_e = \frac{3}{2} P \frac{1}{L_{lr}} \psi_r \psi_{qm} \quad , \quad (2.38.b)$$

$$\frac{d\omega}{dt} = \frac{P}{J} (T_e - T_L) - \frac{1}{J} k\omega \quad , \quad (2.33)$$

$$L_m = f(\psi_m) \quad , \quad (2.45.c)$$

$$\psi_m = \sqrt{\psi_{dm}^2 + \psi_{qm}^2} \quad . \quad (2.46)$$

The model is almost identical to the RFO model with iron loss only, presented in sub-section 3.3.3.2. The differences are that magnetising inductance and hence the rotor inductance will assume different values at different operating conditions. As it was discussed for the model in sub-section 3.3.3.2, relationships $L_m(\psi_m^2)$ or $L_m/L_r(\psi_m^2)$ can be used to reduce the number of mathematical operations.

The second elaborated model is the $i_s - \psi_m - \psi_r$ RFO model of an induction machine with both iron loss and main flux saturation, when saturation is represented by $i_m(\psi_m)$ non-linear function. This model is obtained from the reduced-order model presented in the previous sub-section. The equations for the rotor flux components remain :

$$\psi_r + T_{lr} \frac{d\psi_r}{dt} = \psi_{dm} \quad , \quad (2.61)$$

$$\psi_{qm} = \omega_{sl} T_{lr} \psi_r \quad . \quad (2.62)$$

In order to utilise $i_m(\psi_m)$ representation, it is necessary to modify the equations for the magnetising flux components. Combining the rotor flux equation (2.22) with (2.67) and (2.66), the equations for the magnetising flux components are obtained as :

$$\psi_{dm} + T_{lFe} \frac{d\psi_{dm}}{dt} = \psi_r + L_{lr}(i_{ds} - i_{dm}) + \omega_r T_{lFe} \psi_{qm} \quad , \quad (3.29)$$

$$\psi_{qm} + T_{lFe} \frac{d\psi_{qm}}{dt} = L_{lr}(i_{qs} - i_{qm}) - \omega_r T_{lFe} \psi_{dm} \quad , \quad (3.30)$$

where the components of the magnetising current are :

$$i_{dm} = i_m \frac{\psi_{dm}}{\psi_m} \quad (2.65)$$

$$i_{qm} = i_m \frac{\psi_{qm}}{\psi_m}$$

Main flux saturation is described by the non-linear relationship :

$$i_m = f(\psi_m) \quad , \quad (2.45.a)$$

and the developed torque and the equation of mechanical motion are :

$$T_e = \frac{3}{2} P \frac{1}{L_{lr}} \psi_r \psi_{qm} \quad , \quad (2.38.b)$$

$$\frac{d\omega}{dt} = \frac{P}{J} (T_e - T_L) - \frac{1}{J} k\omega \quad . \quad (2.33)$$

The model is similar to the RFO model with main flux saturation from sub-section 2.5.1.6. But, when the expressions for magnetising flux components in these two models are compared, it can be seen that expressions (3.29)-(3.30) are more complicated than (2.63)-(2.64). Due to inclusion of iron loss, they have become differential equations and cross-coupling terms have appeared.

3.4.6. Improved estimators with both iron loss and main flux saturation

Four rotor flux estimators with both iron loss and main flux saturation will be presented in this sub-section. The first two are with $L_m(\psi_m)$ representation of the main flux saturation and they are based on the first model given in sub-section 3.4.5. The structure of the full estimator is shown in Fig. 3.6 [Sokola and Levi, 1996]. It is quite complex, involving a number of calculations and two look-up tables, for the non-linear relationships $L_m(\psi_m)$ and $T_{lFe}(\omega_r)$. Similarly to the improved estimator with main flux saturation only, non-linear relationships, $L_m = f(\psi_m^2)$ or $\frac{L_m}{L_r} = f(\psi_m^2)$ can be utilised, as shown by the dashed lines in Fig. 3.6. Changes in iron loss are represented by the non-linear relationship $T_{lFe}(\omega_r)$.

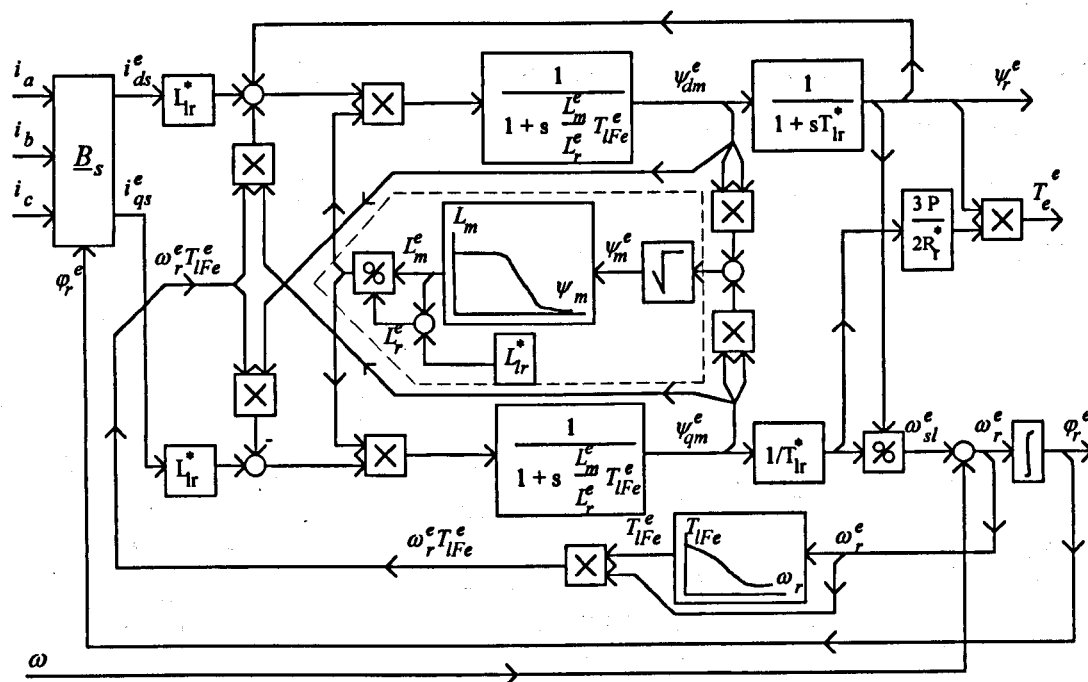


Figure 3.6 : Improved rotor flux estimator of i_s - ω type, with both iron loss and main flux saturation, $L_m(\psi_m)$ representation.

As it was the case with the estimator with iron loss only (sub-section 3.3.4), the influence of the equivalent time constant $(L_m/L_r) T_{lFe}$ on the machine dynamics is small and can be neglected in first-order delay elements [Sokola et al., 1996]. This approximation dictates that expressions (3.24)-(3.25) are used for the magnetising flux rather than (3.22)-(3.23). The simplified estimator is shown in Fig. 3.7.

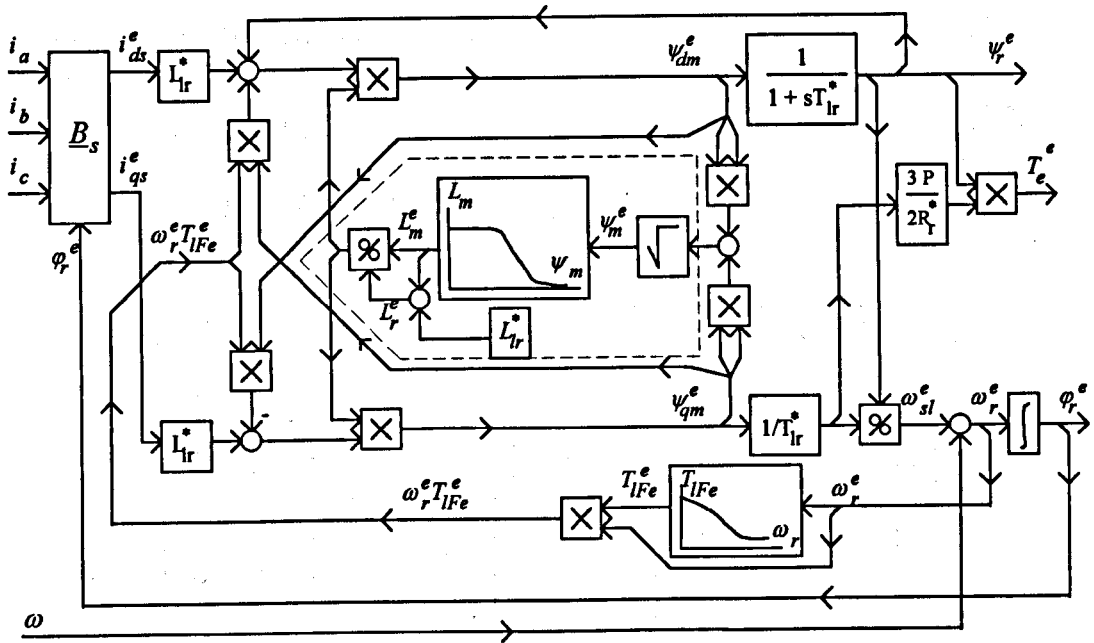


Figure 3.7 : Simplified improved rotor flux estimator of i_s - ω type, with both iron loss and main flux saturation, $L_m(\psi_m)$ representation.

The other two improved estimators with both iron loss and main flux saturation are with $i_m(\psi_m)$ representation. They are based on the second RFO model from sub-section 3.4.5. The structure of the full estimator is shown in Fig. 3.8. When the first-order delay blocks containing the time constant T_{IFe} are neglected, equations (3.29) and (3.30) become :

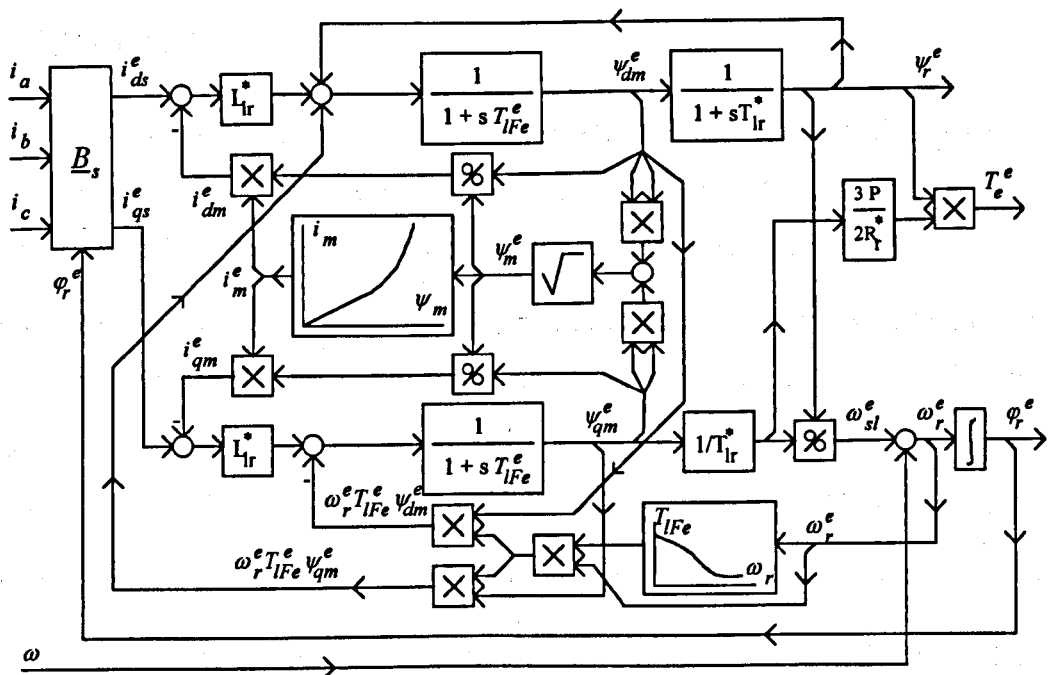


Figure 3.8 : Improved rotor flux estimator of i_s - ω type, with both iron loss and main flux saturation, $i_m(\psi_m)$ representation .

$$\psi_{dm} = \psi_r + L_{lr}(i_{ds} - i_{dm}) + \omega_r T_{lFe} \psi_{qm} \quad (3.31)$$

$$\psi_{qm} = L_{lr}(i_{qs} - i_{qm}) - \omega_r T_{lFe} \psi_{dm} \quad (3.32)$$

Utilisation of (3.31)-(3.32) results in the simplified estimator, shown in Fig. 3.9.

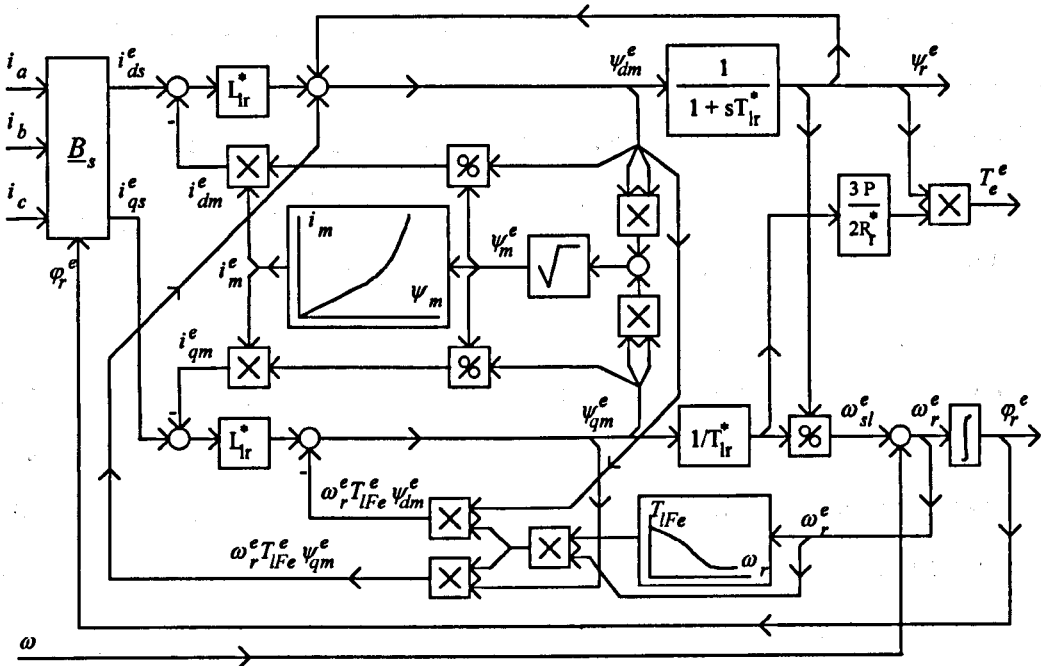


Figure 3.9 : Simplified improved rotor flux estimator of i_s - ω type, with both iron loss and main flux saturation, $i_m(\psi_m)$ representation.

3.5. SUMMARY

A number of novel improved mathematical models of induction machines and novel improved rotor flux estimators were proposed in this chapter. Main flux saturation, iron loss and then both these phenomena were included in improved models.

Two novel models and estimators with main flux saturation were developed, using two different non-linear relationships to represent main flux saturation. The first model, using $L_m(\psi_m)$ representation, is obtained from the already known model with $i_m(\psi_m)$ representation, by merely changing equations for the magnetising flux components.

However, utilisation of the non-linear relationship $\frac{L_m}{L_r} = f(\psi_m^2)$ reduces the number of calculation needed to execute the estimation process with respect to the estimator with $i_m(\psi_m)$ representation. The second representation of main flux saturation, $L_r(\Psi)$, uses

the generalised flux and results in improved estimator of the similar complexity as the estimator that uses $L_m(\psi_m)$ representation with $\frac{L_m}{L_r} = f(\psi_m^2)$ non-linear function.

Improved mixed current-flux models and improved reduced-order models with R_{Fe} iron loss representation were shown to be simpler than the corresponding models with R_r iron loss representation, when the current feeding is considered. Out of the two analysed sets of state variables, the $\underline{i}_s - \underline{\psi}_m - \underline{\psi}_r$ combination resulted in more compact rotor-flux-oriented model and simpler improved estimator than it was the case with the $\underline{i}_s - \underline{i}_m - \underline{\psi}_r$ combination. As the improved estimator with iron loss compensation was still quite complicated, a simplification that does not compromise the achieved iron loss compensation was proposed.

Models that include both iron loss and main flux saturation were derived as well. Following the suggestions about simplicity of the models from previous considerations, R_{Fe} iron loss representation and $\underline{i}_s - \underline{\psi}_m - \underline{\psi}_r$ combination of the state variables was used throughout the derivation. As both $L_m(\psi_m)$ and $i_m(\psi_m)$ representations of the main flux saturation were elaborated, two full improved estimators are designed. Both estimators were simplified using the same approximation that was already used for improved estimator with iron loss only.

4. DETUNING IN ROTOR-FLUX-ORIENTED INDUCTION MACHINE DRIVES

4.1. INTRODUCTION

The aim of this chapter is to evaluate and compare detuning due to different phenomena in both steady-state and transient operation of the vector-controlled induction machine drive, when the controller is based on the CPM. First, parameters of the machines, that are later used for quantitative analysis of detuning, are experimentally determined. The identification procedure is presented in section 4.2. Methods and quantities by which detuning will be assessed are explained in section 4.3. Section 4.4 presents analyses of steady-state detuning that occurs due to four detuning sources. In each analysis, detuning expressions are derived first, followed by a quantitative assessment of detuning in different operating regimes for the particular machine. Comparison of steady-state detuning that occurs due to different phenomena is performed in section 4.5. Detuning in transient operation is investigated in section 4.6. Contributions of the chapter are summarised in the section 4.7.

4.2. EXPERIMENTAL IDENTIFICATION OF MACHINE PARAMETERS

In order to evaluate detuning in different operating regimes, it is necessary to have knowledge on the magnetising curve and the equivalent iron loss resistance (how it changes with frequency). For any machine, these relationships have to be identified experimentally.

Two induction machines are utilised in the following studies. Analyses are mostly performed for the induction machine with rating of 4 kW, that showed high sensitivity to iron loss induced detuning [Levi et al., 1995b]. Additionally, some of the detuning studies in transient operation are performed for the 0.75 kW machine, utilised in [Levi, 1994a; Levi et al., 1995a].

Parameters of the 4 kW induction machine are determined as follows. After the DC test for identification of the stator resistance and the blocked-rotor test for identification of the leakage inductances, the machine is subjected to two types of no-load tests. The first

no-load test is a standard one, conducted with supply from a sine-wave variable-voltage 50 Hz source. The purpose of this test is to determine the magnetising curve of the machine. The identified magnetising curve is then approximated using the least squares fitting, as shown in Fig. 4.1. The same figure also depicts the change in the mutual inductance (L_m) with the magnetising current and the rated saturated value of the mutual inductance ($L_{msat} \equiv L_{mn}$).

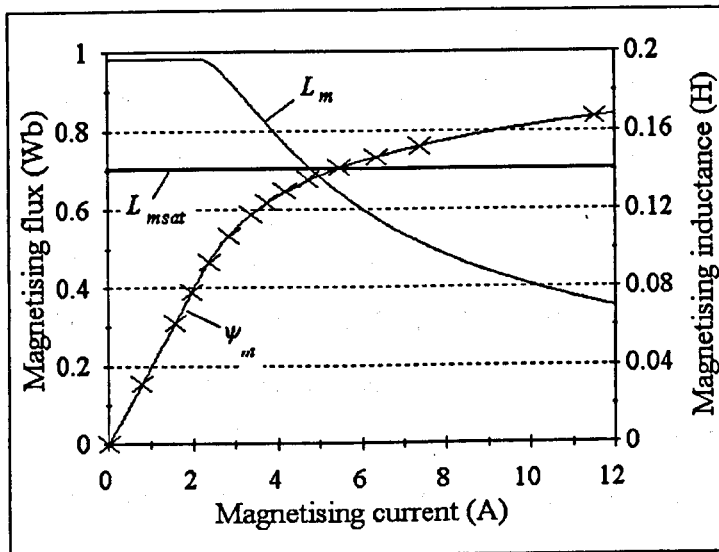


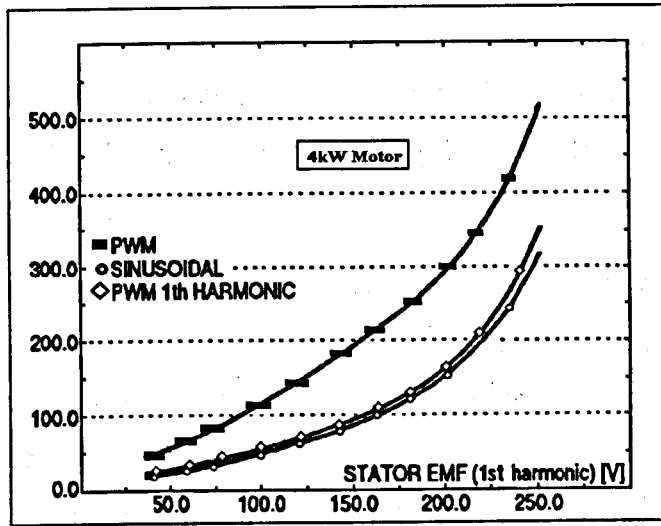
Figure 4.1 : Magnetising curve of the 4 kW machine and the mutual inductance (experimentally identified points denoted by crosses).

The induction machine in a vector-controlled drive is fed by a PWM power electronic converter. Losses with the PWM supply are significantly higher than with a sinusoidal supply. This is especially true for iron loss and this topic has been elaborated in [De Buck et al., 1984; Boglietti et al., 1996]. As a PWM voltage consist of a series of pulses, it can be subjected to spectrum analysis and viewed as a combination of different spectrum components. Beside the fundamental harmonic, the voltage spectrum contains pronounced high-frequency harmonics, with frequency close to switching frequency and its multiples. These high-frequency harmonics are responsible for the increase in iron loss [Undeland and Mohan, 1988; Boglietti et al., 1996]. However, since vector controllers control only the fundamental harmonic of currents, then only the fundamental harmonic of iron loss has an influence on the accuracy [Levi, 1995b].

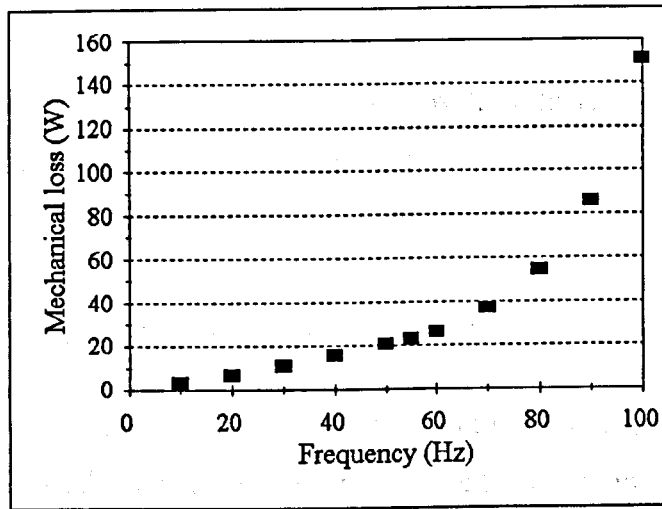
Hence the second group of no-load tests utilises supply from a PWM inverter [Levi et al., 1996a,b] and the purpose of these tests is to determine the first harmonic of iron loss

at different fundamental frequencies. At first, the machine is operated under no-load conditions with PWM inverter feeding at rated 50 Hz fundamental frequency. The employed PWM technique is the sinusoidal ramp comparison method with carrier frequency of 1047 Hz. The DC link voltage is such that the rated fundamental voltage at machine terminals is obtained with the modulation index of 0.63. The first harmonic of input power and the total no-load power are measured by a power analyser. Deduction of copper loss from these two powers give the sum of mechanical loss and the first harmonic of iron loss and the sum of mechanical loss and the total iron loss, respectively. These two sums, as well as the sum of mechanical and iron loss for no-load test with sinusoidal supply, all for 50 Hz, are shown in Fig. 4.2.a. [Levi et al., 1996a,b]. The curves are plotted against the first harmonic of the stator e.m.f. (first harmonic of stator voltage minus volt-drop across the stator resistance). It can be seen that the first harmonic of the no-load losses obtained with PWM supply is essentially the same as the no-load losses with sinusoidal supply.

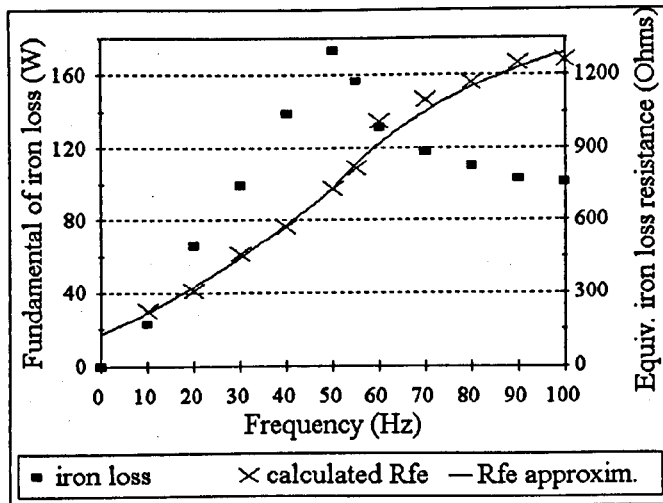
The second set of no-load tests with PWM supply is performed at various fundamental frequencies, using another PWM inverter. This inverter operates with switching frequency of 5 kHz. The modulation index is controlled in such a way that the first harmonic voltage rises linearly with the frequency up to the value of 0.95 at 50 Hz and is kept at a constant value of 0.95 for frequencies higher than 50 Hz. Such test conditions resemble the common vector control strategy that is met in normal operation of a RFO induction machine. As the fundamental voltage in the field-weakening region is kept constant, change of iron loss with change in flux density is automatically accounted for. The fundamental frequency range encompassed by the tests was from 10 Hz to 100 Hz. In order to calculate the equivalent iron loss resistance, mechanical losses at different frequencies have to be known. They are determined at each operating frequency from a set of no-load tests with variable DC link voltage at that particular frequency. For the 4 kW motor, change of mechanical loss with the frequency is depicted in Fig. 4.2.b while the results of the experimental identification of iron loss are shown in Fig. 4.2.c. The fundamental iron loss and the calculated equivalent iron loss resistance R_{Fe} are shown for discrete points obtained by measurement. The continuous approximation of the function $R_{Fe}(f)$, that is consequently utilised in analytical studies, is shown as well.



a. sum of iron loss and mechanical loss at 50 Hz, with PWM and sinusoidal supply.



b. mechanical loss against frequency.



c. fundamental iron loss and equivalent iron loss resistance R_{Fe} for the common vector control strategy (experimental and approximation).

Figure 4.2 : Results of no-load tests, 4 kW machine.

It should be noted that the experimentally determined fundamental iron loss for the rated first harmonic voltage and the rated frequency is not identical in the two experiments (Figs. 4.2.a and 4.2.c). However, the discrepancy is below 10% and such accuracy is believed to be satisfactory.

To enable calculation of detuning effects over a wider speed range, the equivalent iron loss resistance is extrapolated in the region ranging from twice the rated frequency up to five times the rated frequency. A precise extrapolation is possible as the results of Fig. 4.2.c enable an accurate subdivision of iron losses into hysteresis and eddy-current losses. This is done by splitting iron loss into two parts - one proportional to the frequency (hysteresis) and the other proportional to the square of the frequency (eddy currents).

All parameter values for the analysed machines, as well as the analytical function for R_{Fe} approximation for the 4 kW machine and magnetising inductances for both machines, are shown in the Appendix A.

4.3. CHARACTERISATION OF DETUNING

Several ways to characterise detuning can be found in the literature. The method used here for analyses of steady-state detuning is to observe the following three quantities :

1. The orientation angle error, defined as :

$$\Delta\varphi_r = \varphi_r^e - \varphi_r , \quad (4.1)$$

2. The torque ratio, defined as :

$$\text{Torque ratio} = \frac{T_e}{T_e^*} , \quad (4.2)$$

3. The rotor flux ratio, defined as :

$$\text{Rotor flux ratio} = \frac{\psi_r}{\psi_r^*} . \quad (4.3)$$

The commanded values of the rotor flux and the torque assume different values for different operation conditions. The commanded rotor flux is equal to the rated rotor flux in the base speed region, while it is reduced in the field-weakening region. The

commanded torque is dictated by the load conditions and also by the amount of detuning, as it will be seen later in the chapter.

In analyses of transient detuning, the following three quantities are observed :

1. The orientation angle error, defined by 4.1.
2. The torque error, defined as :

$$\text{Torque error} = \frac{T_e^* - T_e}{T_e^*} \times 100 \text{ [\%]} , \quad (4.4)$$

3. The rotor flux error, defined as :

$$\text{Rotor flux error} = \frac{\psi_r^* - \psi_r}{\psi_r^*} \times 100 \text{ [\%]} . \quad (4.5)$$

4.4. DETUNING IN STEADY-STATE OPERATION WITH THE CPM-BASED CONTROLLER

To quantitatively assess detuning in steady-state operation, the following investigation approach is utilised. Behaviour of a CPM-based RFO vector controller in steady-state operation is analysed and described by mathematical expressions that constitute steady-state controller model. On the other hand, an appropriate improved steady-state induction machine model, that includes some of the detuning sources, is derived from a corresponding improved reduced-order machine model. These two steady-state models are then combined, yielding detuning expressions for the orientation angle error, the torque ratio and the rotor flux ratio. These three expressions suffice when the vector-controlled drive operates in the torque mode. An additional equation (usually a polynomial of third or fourth order), necessary for detuning analyses in the speed mode of operation, is then derived. The full set of equations is solved for a particular machine using the numerical Newton-Raphson method and detuning characteristics are obtained. The procedure for solving the detuning expressions is iterative and the solutions are found using custom-made FORTRAN programs.

Analyses of steady-state detuning are performed in the reference frame determined by the control system ($d^* - q^*$ axis commanded reference frame). Because of that, steady-state models have to be valid for this reference frame. The steady-state model of the

CPM-based vector controller is in the d^*-q^* axis commanded reference frame by the nature of things. The steady-state model of the induction machine is valid in the d^*-q^* commanded reference frame when the commanded speed of the rotor flux is chosen for the arbitrary speed ($\omega_r^* = \omega_a$). Due to detuning, the actual $d-q$ axes are not ideally aligned with the commanded d^*-q^* axes ($\omega_r \neq \omega_r^*$). This is the reason why RFO models cannot be used for machine representation in the following analyses.

The steady-state model of the vector controller is presented next. The model is valid for both feedback and feed-forward RFOC schemes from sub-sections 2.3.2.2 and 2.3.2.3. In the all cases discussed in this section, the control system encompasses the CPM-based estimator of i_s , $-\omega$ type, described in 2.3.2.2. In any steady-state, PI controllers ensure that the commanded values of torque and rotor flux are equal to the corresponding estimated values (used as feedback signals for control loops). This results in the following expressions ::

$$\psi_r^e = \psi_r^* = L_m^* i_{ds}^* , \tag{4.6}$$

$$T_e^e = T_e^* = \frac{3}{2} P \frac{L_m^*}{L_r^*} \psi_r^* i_{qs}^* , \tag{4.7}$$

where superscript ‘e’ stands for estimated values, while superscript ‘*’ denotes both the commanded quantities and the machine parameters used in the estimator. The commanded speed and the actual speed of the induction machine are equal, so that the actual, the commanded and the estimated slip angular speeds are equal :

$$\omega_{sl} = \omega_{sl}^* = \omega_{sl}^e = \frac{L_m^* i_{qs}^*}{T_r^* \psi_r^*} . \tag{4.8}$$

Combining (4.6) and (4.8), the relationship between the commanded value of q -axis current and the commanded value of d -axis current is obtained as :

$$i_{qs}^* = \omega_{sl}^* T_r^* i_{ds}^* . \tag{4.9}$$

Since the current-regulated PWM inverter is assumed to be ideal, the actual and the commanded values of current components are equal :

$$i_{qs} = i_{qs}^* \quad ; \quad i_{ds} = i_{ds}^* . \tag{4.10}$$

In the following sub-sections the above steady-state controller model is utilised for derivation of detuning expressions and for analyses of steady-state detuning due to four

different phenomena. The analysed phenomena include rotor resistance variations, rotor leakage inductance variations, mutual inductance variations and iron loss.

4.4.1. Steady-state detuning due to rotor resistance variations

The actual value of the rotor resistance (R_r) changes during operation, due to thermal effects. On the other hand, a CPM-based RFO controller is designed to use always the same rotor resistance value (R_r^*). Additionally, the value used in the controller might be initially wrong, as a consequence of inaccurate commissioning procedure. Whatever the reason, a discrepancy between the above two values leads to detuned operation. Hence the amplitude and the position of the rotor flux, as well as the developed torque, are wrongly estimated. The commanded currents assume non-optimal values. As a consequence, the actual rotor flux and the developed torque differ from their commanded values.

Significant research efforts, discussed in section 2.4.3., have been devoted to compensation of detuning caused by R_r variations. To properly evaluate detuning due to R_r variations, it is necessary to recognise that changes in the flux level cause different levels of main flux saturation. Thus the saturated machine model has to be utilised for a correct analysis, as suggested by [Nordin et al., 1985; Ojo et al., 1994].

First, it is necessary to derive the appropriate induction machine model. It is the i_s - ψ_r reduced-order steady-state model, in the d^* - q^* axis reference frame determined by the RFO controller. In order to use the $L_m(\psi_m)$ representation of main flux saturation, the reduced-order model from sub-section 3.2.2 is combined with (2.22), acknowledging that all the derivatives are zeroes in steady states. This yields the following model :

$$\begin{aligned} \psi_{dr} &= \psi_{dm} + \omega_{sl} T_{lr} \psi_{qr} \\ \psi_{qr} &= \psi_{qm} - \omega_{sl} T_{lr} \psi_{dr} \end{aligned} \quad (4.11)$$

$$\psi_{dm} = \frac{L_m}{L_r} (\psi_{dr} + L_{lr} i_{ds}^*) \quad (4.12)$$

$$\psi_{qm} = \frac{L_m}{L_r} (\psi_{qr} + L_{lr} i_{qs}^*)$$

$$T_e = \frac{3}{2} P \frac{1}{L_{lr}} (\psi_{dr} \psi_{qm} - \psi_{qr} \psi_{dm}) \quad (2.17.c)$$

Main flux saturation is represented by the $L_m(\psi_m)$ non-linear function :

$$L_m = f(\psi_m) , \quad (2.45.c)$$

$$\psi_m = \sqrt{\psi_{dm}^2 + \psi_{qm}^2} . \quad (2.46)$$

In order to derive the relationship between the rotor flux d - q components and the stator current d - q components, (4.11) and (4.12) are combined, yielding :

$$\psi_{dr} = L_m \dot{i}_{ds} + \omega_{sl} T_r \psi_{qr} \quad (4.13)$$

$$\psi_{qr} = L_m \dot{i}_{qs} - \omega_{sl} T_r \psi_{dr}$$

From (4.13), the rotor flux components are obtained as :

$$\psi_{dr} = L_m \frac{\dot{i}_{ds} + \omega_{sl} T_r \dot{i}_{qs}}{1 + \omega_{sl}^2 T_r^2} \quad (4.14)$$

$$\psi_{qr} = L_m \frac{-\omega_{sl} T_r \dot{i}_{ds} + \dot{i}_{qs}}{1 + \omega_{sl}^2 T_r^2}$$

Detuning expressions are derived by combining the above model with the estimator model (4.6)-(4.10). As discussed in 2.4.1, the vector controller assumes that the perfect orientation is achieved and that the estimated position of the rotor flux (φ_r^e) determines the instantaneous position of the rotor flux, i.e. the position of the commanded d^* - q^* reference frame. On the other hand, the position of the actual rotor flux (φ_r) is determined by the stator current components and by the actual motor parameters. If parameter variations take place, the actual flux is not aligned along the d^* -axis and the ψ_{qr} component exists. The error in the orientation angle is :

$$\Delta\varphi_r = \arctan \frac{\psi_{qr}}{\psi_{dr}} = \arctan \frac{\omega_{sl} (T_r^* - T_r)}{1 + \omega_{sl}^2 T_r^* T_r} . \quad (4.15)$$

Another consequence of detuning is that the amplitude of the actual rotor flux differs from the commanded (estimated) value of rotor flux amplitude. The ratio of these two amplitudes is the rotor flux ratio, expressed as :

$$\frac{\psi_r}{\psi_r^*} = \frac{\sqrt{\psi_{dr}^2 + \psi_{qr}^2}}{L_m \dot{i}_{ds}} . \quad (4.16)$$

Substitution of (4.14) and (4.9) into (4.16) yields :

$$\frac{\psi_r}{\psi_r^*} = \frac{L_m}{L_m^*} \sqrt{\frac{1 + \omega_{sl}^{*2} T_r^{*2}}{1 + \omega_{sl}^{*2} T_r^2}} \quad (4.17)$$

There is also a difference between the developed torque and the commanded torque. The torque ratio in the case of R_r variations is :

$$\frac{T_e}{T_e^*} = \frac{R_r^*}{R_r} \left(\frac{\psi_r}{\psi_r^*} \right)^2 = \frac{R_r^*}{R_r} \left(\frac{L_m}{L_m^*} \right)^2 \frac{1 + \omega_{sl}^{*2} T_r^{*2}}{1 + \omega_{sl}^{*2} T_r^2} \quad (4.18)$$

Expressions (4.15), (4.17) and (4.18) describe detuning due to R_r variations for steady-state operation in the torque mode, when the speed control loop is open and when the reference torque (or the reference q -axis current component) is imposed to the control system as an input.

When the speed control loop is closed, the actual speed is equal to the reference speed and the developed torque is equal to the load torque. The commanded torque becomes an unknown variable and an additional equation is needed. Substituting T_e with T_L in (4.18) and then combining (4.18) with (4.6)-(4.8), the expression for the commanded torque in the speed mode of operation is obtained as :

$$T_e^{*3} g^2 \frac{R_r^*}{R_r} \left(\frac{L_m}{L_m^*} \right)^2 T_r^{*2} - T_e^{*2} g^2 T_L T_r^2 + T_e^* \frac{R_r^*}{R_r} \left(\frac{L_m}{L_m^*} \right)^2 - T_L = 0 \quad (4.19)$$

where :

$$g = \frac{2 R_r^*}{3P \psi_r^{*2}} = \frac{\omega_{sl}^*}{T_e^*} \quad (4.20)$$

Detuning as given by (4.15), (4.17)-(4.19) appears to be speed-independent and this is true in the base speed region. However, for operation in the field-weakening region, dependence on speed exists in an indirect manner, as it will be seen shortly.

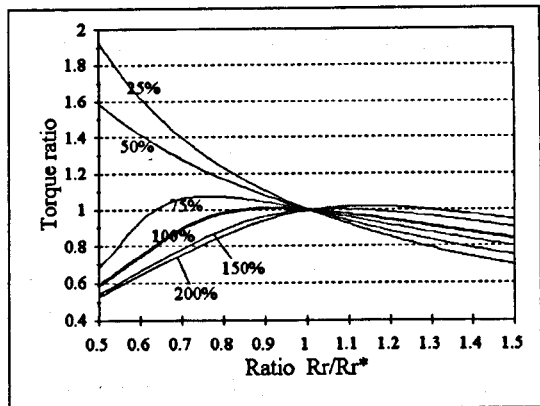
On the basis of the above detuning expressions, a quantitative study of steady-state detuning due to R_r variations is performed for the 4 kW machine. The results are shown in Figs. 4.3 and 4.4. Figure 4.3 shows operation with different load torque at the rated speed, while Fig. 4.4 shows operation at different speeds with the rated load torque. The torque ratio, the rotor flux ratio and the orientation angle error are shown, all versus the ratio of actual to estimated rotor resistance (R_r/R_r^*). If the value of the R_r/R_r^* ratio is smaller than unity, the rotor resistance is over-estimated (R_r is smaller

than R_r^*), while the value bigger than unity means that the rotor resistance is underestimated (R_r is bigger than R_r^*).

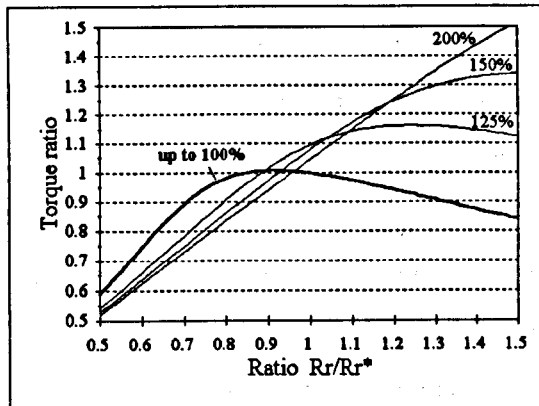
From Fig. 4.3.a. it can be seen that the torque ratio significantly deviates from the desired value for over-estimated values of R_r . The actual torque is either higher or smaller than the commanded torque, depending on whether the load is light or heavy, respectively. When R_r is under-estimated, the actual torque is always smaller than the commanded torque. The torque error decreases with loading and is generally smaller than for over-estimated R_r . It should be noted that characteristics are valid for the constant load torque, which means that the developed torque and the load torque along a characteristic remain constant, while the commanded torque changes. The rotor flux ratio, depicted in Fig. 4.3.b, exhibits different behaviour when compared with the torque ratio. If R_r is over-estimated, the actual rotor flux is smaller than the commanded flux, and vice versa. In both cases errors increase with the load, but if R_r is under-estimated, errors are relatively smaller. This is a consequence of main flux saturation and it can be stated that main flux saturation has a damping effect on detuning. The orientation angle error is illustrated in Fig. 4.3.c. When R_r is over-estimated, the orientation angle error is always negative, relatively smaller for light loads, bigger for moderate loads and again smaller for heavy loads. In the case of R_r under-estimation, the orientation angle error is always positive, increasing with load and with the level of R_r under-estimation.

Figure 4.4 presents detuning characteristics for operation with the rated load torque, for different speeds. The studied speed region is from the rated speed to twice the rated speed. As expected, detuning in the field-weakening region differs from detuning in the base speed region. Torque errors and rotor flux errors in the field-weakening region (Figs. 4.4.a and 4.4.b) are bigger than in the base speed region. Additionally, there is some detuning even when R_r is exactly equal to R_r^* , because the estimated and the actual values of the mutual inductance differ due to lower level of main flux saturation. This means that the actual values of L_m , L_r and T_r also differ from the values used in the estimator. At twice the rated speed (200% characteristics) the commanded flux is half of the rated and the machine operates in unsaturated region of the magnetising curve, even when the rotor flux ratio reaches 1.5. This is the reason why torque ratio and flux ratio detuning characteristic for 200% speed are straight lines. The orientation angle error for operation in the field-weakening region (Fig. 4.4.c) is generally smaller

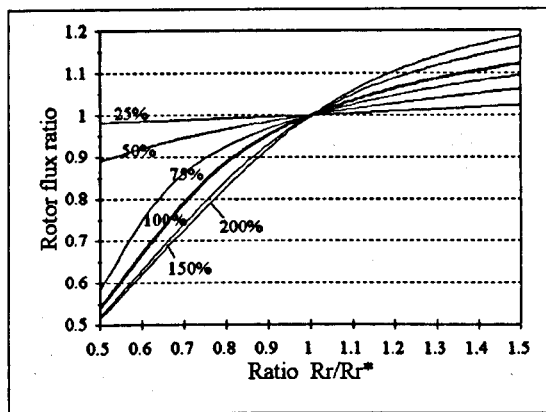
than in the base speed region if over-estimation and under-estimation of R_r is significant, but it is bigger for small over-estimation.



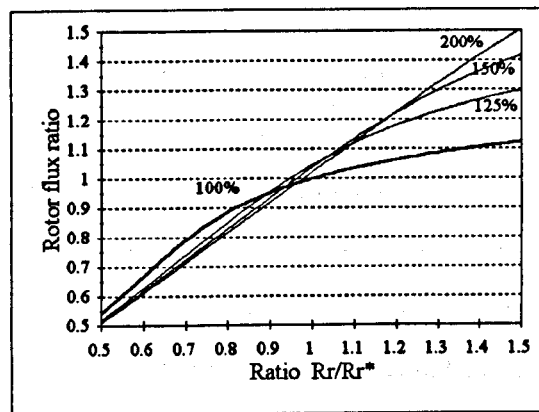
a. torque ratio



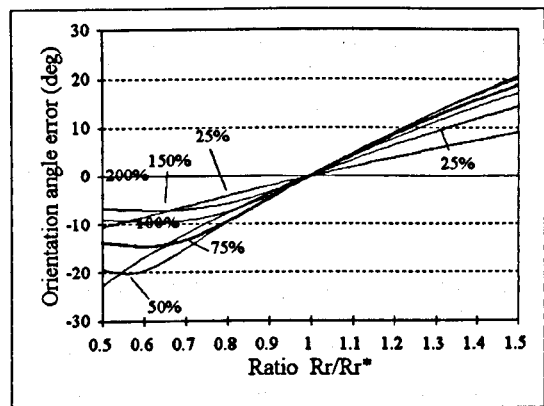
a. torque ratio



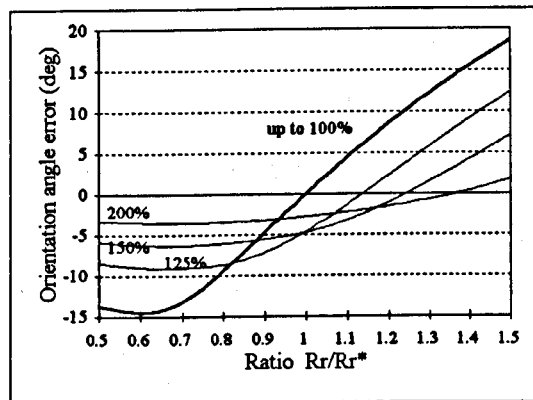
b. rotor flux ratio



b. rotor flux ratio



c. orientation angle error



c. orientation angle error

Figure 4.3 : Steady-state detuning due to R_r variations, operation at the rated speed, load torque in % as parameter, 4 kW machine.

Figure 4.4 : Steady-state detuning due to R_r variations, operation with the rated load torque, speed in % as parameter, 4 kW machine.

4.4.2. Steady-state detuning due to rotor leakage inductance variations

Leakage inductances in the machine change due to saturation of the leakage flux paths, which can occur when the current is high, i.e. when the machine develops high torque. In such a case the actual values of leakage inductances decrease with an increase in saturation. Another cause for uncertainties in leakage inductances is that distribution of the total leakage inductance (calculated from the blocked-rotor test) into stator leakage inductance and rotor leakage inductance might not be accurate since it involves some idealisations based on empirical knowledge. In this case the value used in the controller (L_{lr}^*) differs from the nominal value of L_{lr} . Both above sources of L_{lr} variations are elaborated here. The assumed approximation of L_{lr} variations due to saturation is given in Appendix A for the 4 kW machine, as a $L_{lr}(i_r)$ relationship.

Two analyses of detuning due to L_{lr} variations have been performed. The difference between them is whether main flux saturation in the machine is neglected or not. In both studies it is assumed that both estimated and actual rotor resistances are of rated value ($R_r = R_r^* = R_{rn}$), and the commanded mutual inductance is of rated value ($L_m^* = L_{mn}$). Meanwhile, the commanded and the actual value of the rotor leakage inductance (L_{lr}^* and L_{lr} , respectively) can assume values different than the rated one (L_{lrn}). In the first study, the actual value of the mutual inductance is considered constant and equal to the rated value ($L_m = L_{mn}$), i.e. main flux saturation in the machine is neglected. In the second study, main flux saturation is included and the mutual inductance in the machine is adapted in accordance with the magnetising curve.

Derivation of the detuning expressions for L_{lr} variations, with main flux saturation included, is presented here, as such a case is more general. Detuning expressions for the case when main flux saturation is neglected are easily derived from them, by setting $L_m = L_{mn}$. As in the previous sub-section, derivation procedure is based on combining steady-state models of the induction machine and the CPM-based estimator. Therefore the derivation procedure closely parallels the one from sub-section 4.4.1. The expressions that describe detuning due to L_{lr} variations are :

$$\Delta\varphi_r = \arctan \frac{\psi_{qr}}{\psi_{dr}} = \arctan \frac{\omega_{sl}^* (T_r^* - T_r)}{1 + \omega_{sl}^{*2} T_r^* T_r}, \quad (4.15)$$

$$\frac{\psi_r^*}{\psi_r} = \frac{L_m}{L_m^*} \sqrt{\frac{1 + \omega_{sl}^{*2} T_r^{*2}}{1 + \omega_{sl}^{*2} T_r^2}}, \quad (4.17)$$

$$\frac{T_e^*}{T_e} = \left(\frac{\psi_r^*}{\psi_r} \right)^2 = \left(\frac{L_m}{L_m^*} \right)^2 \frac{1 + \omega_{sl}^{*2} T_r^{*2}}{1 + \omega_{sl}^{*2} T_r^2}, \quad (4.21)$$

$$T_e^{*3} g^2 \left(\frac{L_m}{L_m^*} \right)^2 T_r^{*2} - T_e^{*2} g^2 T_L T_r^2 + T_e^* \left(\frac{L_m}{L_m^*} \right)^2 - T_L = 0, \quad (4.22)$$

where g is given with (4.20).

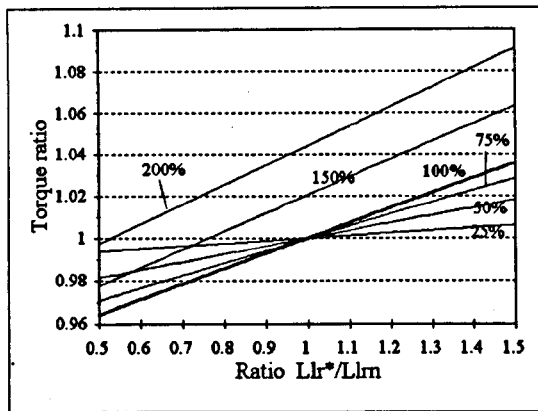
As in the previous case, detuning expressions are independent of speed in the base speed region while an indirect dependence exists in the field-weakening region.

4.4.2.1. Study with main flux saturation neglected

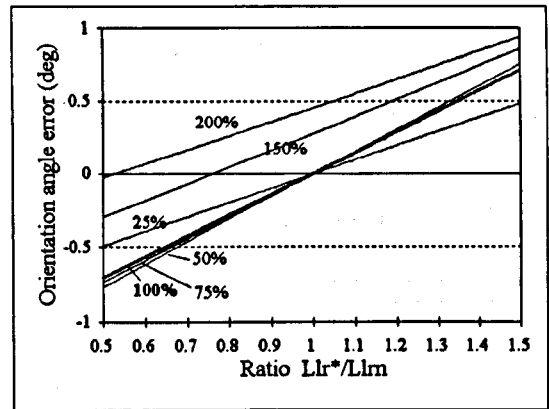
A quantitative study of detuning due to L_{lr} variations, based on the above detuning expressions, is performed for the 4 kW machine. Both sources of L_{lr} uncertainties are simultaneously elaborated. The commanded value of the rotor leakage inductance (L_{lr}^*) is varied from 50% to 150% of the nominal leakage inductance (L_{lrn}). The actual value of the rotor leakage inductance is varied in accordance with the assumed L_{lr} (i_r) relationship. Detuning characteristics for closed-speed-loop operation at the rated speed, with different loads, are shown in Fig. 4.5.

Figure 4.5 indicates that detuning due to the L_{lr} variations is significantly smaller than detuning due to R_r variations. The reason for this is that L_{lr} represents only about 5% of the total rotor inductance (L_r). Errors in L_{lr}^* therefore yield quite small discrepancies between L_{lr}^* and L_{lr} (and thus T_r^* and T_r as well). As it can be seen in Figs. 4.5, detuning characteristics have a linear shape. For loads up to the rated, all detuning parameters increase with load and with the errors in the ratio L_{lr}^*/L_{lrn} . Detuning is quite small, since it is assumed that leakage flux saturation does not occur at such levels of rotor current. For loads above the rated, detuning becomes more pronounced due to leakage flux saturation in the machine. Errors in torque and rotor flux reach 9% and 4.5%, respectively, for operation with twice the rated load. Orientation angle error is very small, staying within ± 1 degree.

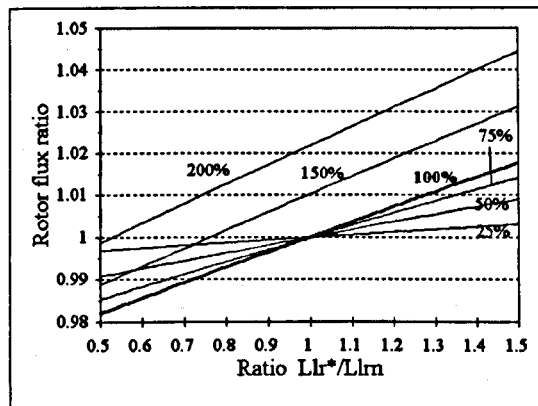
Analysis of detuning when the machine operates in the field-weakening region was also performed. Due to omission of main flux saturation in the machine model, the results are exactly the same as in the base speed region (Fig. 4.5) and therefore not repeated.



a. torque ratio



c. orientation angle error

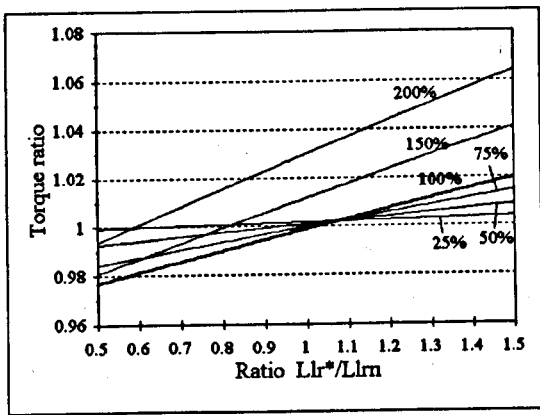


b. rotor flux ratio

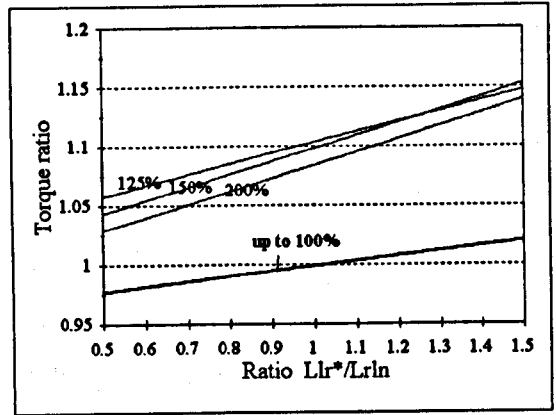
Figure 4.5 : Steady-state detuning due to L_{lr} variations, operation at the rated speed, main flux saturation neglected, load torque in % as parameter, 4 kW machine.

4.4.2.2. Study with main flux saturation included

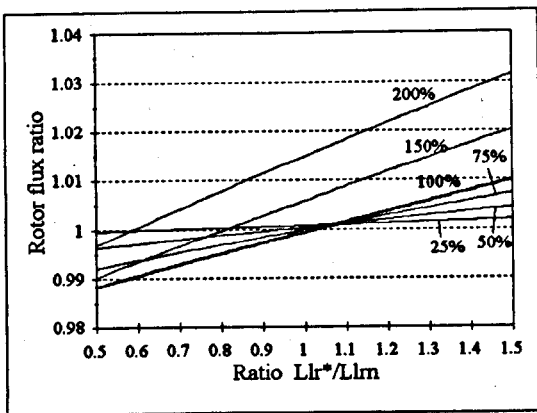
The second study of steady-state detuning due to L_{lr} variations is performed with main flux saturation included in the machine model. The results are shown in Fig. 4.6, for operation in the base speed region [Sokola et al., 1997] and in Fig. 4.7 for operation in both base speed and field-weakening regions. Detuning characteristics for the base speed region (Fig. 4.6) are very similar to the ones obtained with main flux saturation neglected (Fig. 4.5). However, values differ. Errors in the torque and the rotor flux are smaller than in the previous case, reaching 6.5% and 3%, respectively. On the other hand, the orientation angle error is bigger than in the previous case as it ranges from -1° to 2.5° . It can be concluded that main flux saturation has a damping effect on the torque error and the rotor flux error, while it increases the orientation angle error.



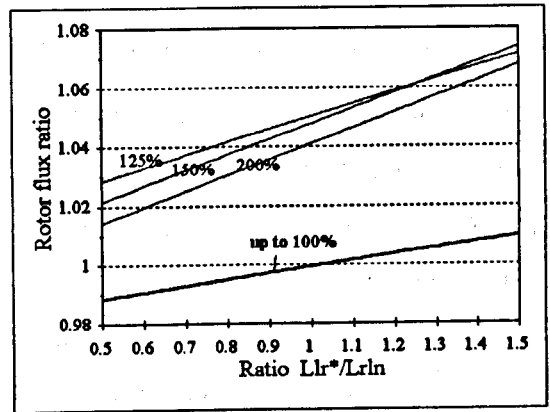
a. torque ratio



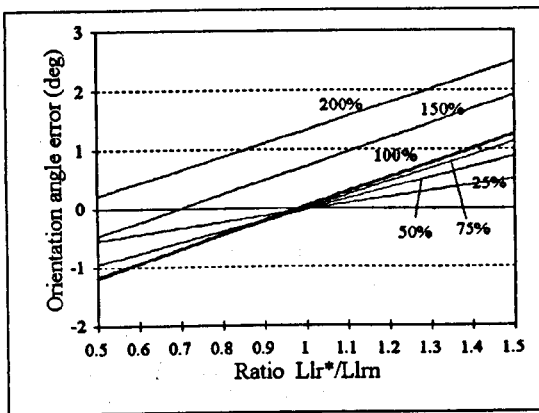
a. torque ratio



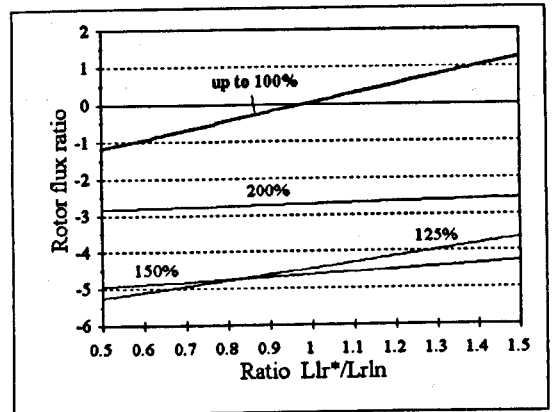
b. rotor flux ratio



b. rotor flux ratio



c. orientation angle error



c. orientation angle error

Figure 4.6 : Steady-state detuning due to L_{lr} variations, operation in the base speed region, main flux saturation included, load torque in % as parameter, 4 kW machine.

Figure 4.7 : Steady-state detuning due to L_{lr} variations, operation in a wide speed region with rated load torque, main flux saturation included, speed in % as parameter, 4 kW machine.

In the field-weakening region (Figs. 4.7), detuning characteristics become different and detuning becomes more pronounced. The actual torque and the actual flux are always bigger than the commanded values, with deviations increasing with L_{lr}^*/L_{lrn} ratio and reaching about 15% and 7%, respectively. The orientation angle error is always negative, smaller for 200% speed than for 125% and 150% speeds. The main reason for an increase in detuning can be found in the fact that as the rotor flux is decreased, higher level of torque-producing current is necessary to produce the required torque and leakage flux saturation in rotor occurs even at rated torque.

4.4.3. Steady-state detuning due to mutual inductance variations

Variations in the value of the mutual inductance are amongst major causes for detuned operation of a vector-controlled drive. Detuning may occur because of three reasons. First of all, the commanded (estimated) value of the mutual inductance ($L_m^* = L_m^e$) may be not equal to the rated (nominal) value of the mutual inductance (L_{mn}). Secondly, the actual value of L_m can change because of variations in the stator q -axis current, due to the cross-saturation effect. Finally, the actual value of L_m changes when the machine operates with reduced flux command in the field-weakening region.

The procedure for deriving the expressions for detuning due to the L_m variations is exactly the same as the procedure presented in the previous sub-section, so that steady-state detuning is described by :

$$\Delta\phi_r = \arctan \frac{\psi_{qr}}{\psi_{dr}} = \arctan \frac{\omega_{sl}^* (T_r^* - T_r)}{1 + \omega_{sl}^{*2} T_r^* T_r} , \quad (4.15)$$

$$\frac{\psi_r}{\psi_r^*} = \frac{L_m}{L_m^*} \sqrt{\frac{1 + \omega_{sl}^{*2} T_r^{*2}}{1 + \omega_{sl}^{*2} T_r^2}} , \quad (4.17)$$

$$\frac{T_e}{T_e^*} = \left(\frac{\psi_r}{\psi_r^*} \right)^2 = \left(\frac{L_m}{L_m^*} \right)^2 \frac{1 + \omega_{sl}^{*2} T_r^{*2}}{1 + \omega_{sl}^{*2} T_r^2} , \quad (4.21)$$

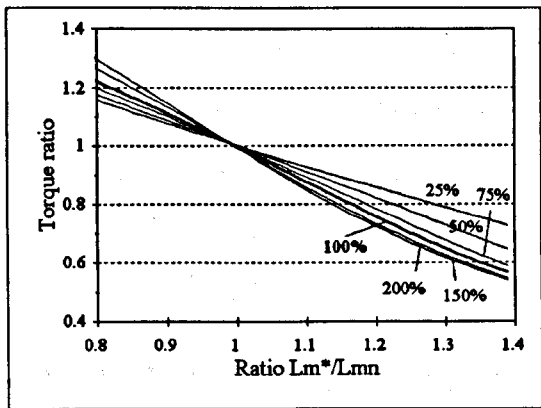
$$T_e^{*3} g^2 \left(\frac{L_m}{L_m^*} \right)^2 T_r^{*2} - T_e^{*2} g^2 T_L T_r^2 + T_e^* \left(\frac{L_m}{L_m^*} \right)^2 - T_L = 0 , \quad (4.22)$$

where g is given with (4.20). As in previous analyses, the speed does not appear in the detuning expressions, but detuning is dependent on speed in the field-weakening region in an indirect manner, due to reduced flux level.

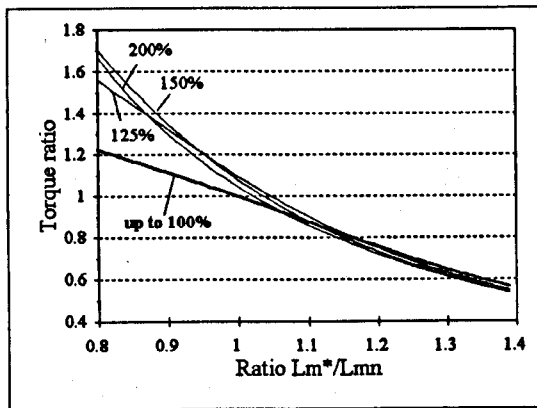
In this part of study, leakage flux saturation and temperature effects are neglected. This means that both the actual value of the rotor leakage inductance and the value used in the estimator are equal to the rated value ($L_{lr} = L_{lr}^* = L_{lrm}$). The same stands for the rotor resistance ($R_r = R_r^* = R_{rm}$). These assumptions are adopted in order to investigate the sole influence of L_m variations and inaccuracies. In the analysis, the value used in the estimator (L_m^*) is varied from $0.8 \times L_{mn}$ (deep saturation) to $1.4 \times L_{mn}$ (unsaturated region). The actual value of L_m is varied in accordance with the magnetising curve of the analysed machine.

Detuning characteristics caused by L_m variations are shown in Figs. 4.8 and 4.9, for closed-speed-loop operation in the base speed region and in a wide speed region, respectively. In the base speed region the torque ratio (Fig. 4.8.a) and the rotor flux ratio (Fig. 4.8.b) are basically linear functions, with errors increasing with load torque and with deviations of L_m^*/L_{mn} ratio from unity. The orientation angle error (Fig. 4.8.c) increases with the load level if deep saturation ($L_m^*/L_{mn} < 1$) is assumed in the controller. If a less saturated value is used in the controller ($L_m^*/L_{mn} > 1$), the orientation angle error increases proportionally to L_m^*/L_{mn} ratio for any given load. Dependence of the orientation angle error on the load level is more complicated. The angle error is relatively smaller for light loads and heavy loads, while it is bigger for medium (50% and 75%) loads.

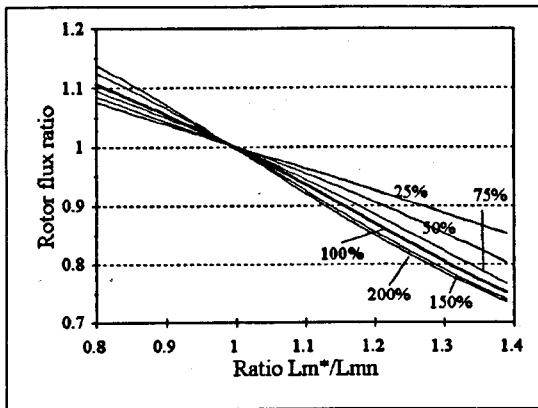
Figure. 4.9 represents operation with rated load torque, but for various speeds. In the field-weakening region (125% speed, 150% speed and 200% speed), the torque ratio and the rotor flux ratio are considerably greater than unity when deep saturation is assumed in the controller ($L_m^*/L_{mn} < 1$). The errors are almost independent of speed when unsaturated value is used in the estimator ($L_m^*/L_{mn} > 1$). The orientation angle errors in the field weakening region are relatively small for both low and high values of L_m^*/L_{mn} ratio; however in the regions of L_m^*/L_{mn} close to unity, error in orientation angle takes place.



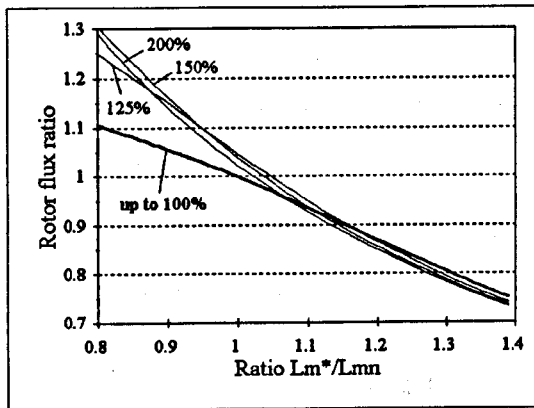
a. torque ratio



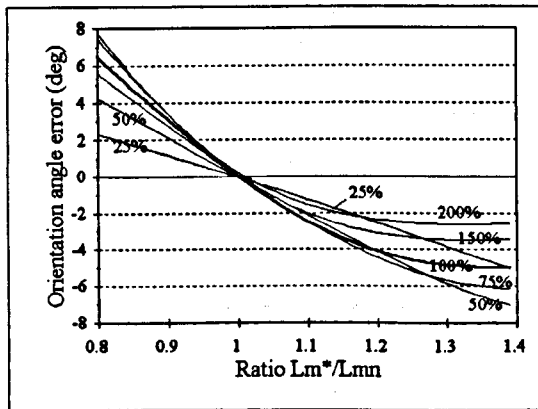
a. torque ratio



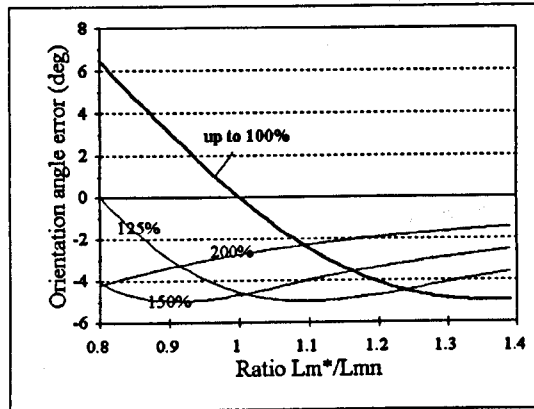
b. rotor flux ratio



b. rotor flux ratio



c. orientation angle error



c. orientation angle error

Figure 4.8 : Steady-state detuning due to L_m variations, operation in the base speed region, load torque in % as parameter, 4 kW machine.

Figure 4.9 : Steady-state detuning due to L_m variations, operation in a wide speed region with the rated load torque, speed in % as parameter, 4 kW machine.

4.4.4. Steady-state detuning due to iron loss

This sub-section mostly deals with novel research. Majority of the work presented in this sub-section has been published in several papers during the last three years [Sokola et al., 1995; Sokola and Levi, 1996; Sokola et al., 1996; Levi et al., 1996a, 1996b; Sokola et al., 1997].

4.4.4.1. Detuning with iron loss represented by a resistance placed in parallel with the magnetising branch, main flux saturation neglected

In this part of study, all other phenomena (thermal effects, leakage flux saturation, main flux saturation) are neglected, in order to investigate the sole influence of iron loss. The i_s - ψ_m - ψ_r reduced-order model with iron loss, given in sub-section 3.3.2.2, is used as the basis for the modelling of the induction machine. In a steady state the induction machine model in the d^*-q^* reference frame (where $\omega_a = \omega_r^*$) becomes :

$$\begin{aligned} \psi_{dr} &= \psi_{dm} + \omega_{sl}^* T_{lr} \psi_{qr} \\ \psi_{qr} &= \psi_{qm} - \omega_{sl}^* T_{lr} \psi_{dr} \end{aligned} \quad (4.11)$$

$$\begin{aligned} \psi_{dm} &= \frac{L_m}{L_r} \left(\psi_{dr} + L_{lr} i_{ds}^* + \omega_r^* T_{lFe} \psi_{qm} \right) \\ \psi_{qm} &= \frac{L_m}{L_r} \left(\psi_{qr} + L_{lr} i_{qs}^* - \omega_r^* T_{lFe} \psi_{dm} \right) \end{aligned} \quad (4.23)$$

$$T_e = \frac{3}{2} P \frac{1}{L_{lr}} \left(\psi_{dr} \psi_{qm} - \psi_{qr} \psi_{dm} \right) \quad (2.17.c)$$

Substitution of (4.23) and (4.9) into (4.11) yields:

$$\begin{aligned} \psi_{dr} &= L_m \frac{A i_{ds}^* + B i_{qs}^*}{A^2 + B^2} \\ \psi_{qr} &= L_m \frac{-B i_{ds}^* + A i_{qs}^*}{A^2 + B^2} \end{aligned} \quad (4.24)$$

$$\text{where } A = 1 - \omega_r^* \omega_{sl}^* T_{Fe} T_{lr} \text{ and } B = \omega_{sl}^* T_r + \omega_r^* T_{Fe} \quad (4.25)$$

Combining the above machine model with the controller model (4.6)-(4.10), the expressions that describe detuning due to iron loss are obtained as [Levi, 1995b; Levi et al., 1996a] :

$$\Delta\varphi_r = \arctan \frac{\psi_{qr}}{\psi_{dr}} = \arctan \frac{-B + \omega_{sl}^* T_r^* A}{A + \omega_{sl}^* T_r^* B}, \quad (4.26)$$

$$\frac{\psi_r^*}{\psi_r} = \sqrt{\frac{1 + \omega_{sl}^{*2} T_r^{*2}}{A^2 + B^2}}, \quad (4.27)$$

$$\frac{T_e}{T_e^*} = \left(\frac{\psi_r}{\psi_r^*} \right)^2 = \frac{1 + \omega_{sl}^{*2} T_r^{*2}}{A^2 + B^2}, \quad (4.28)$$

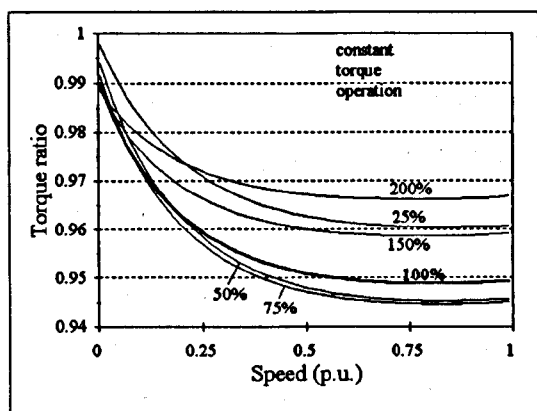
$$\begin{aligned} & T_e^{*4} g^4 T_L T_{Fe}^2 T_{lr}^2 + T_e^{*3} g^2 \left(2g T_L \omega T_{Fe}^2 T_{lr}^2 - T_r^{*2} \right) + \\ & + T_e^{*2} g^2 T_L \left((T_r + T_{Fe})^2 + \omega^2 T_{Fe}^2 T_{lr}^2 - 2T_{Fe} T_{lr} \right) + \\ & + T_e^* \left(2g T_L \omega T_{Fe} (T_{Fe} + T_r - T_{lr}) - 1 \right) + T_L (1 + \omega^2 T_{Fe}^2) = 0 \end{aligned} \quad (4.29)$$

where g is given with (4.20).

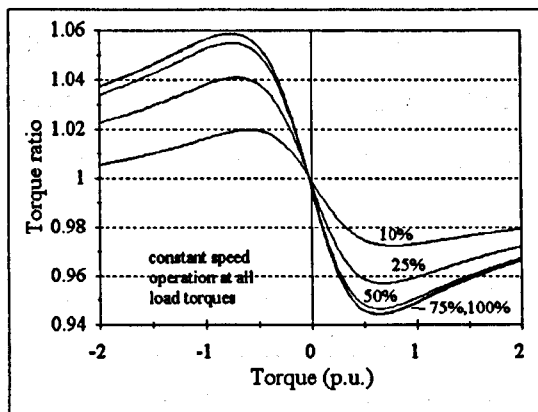
As iron loss is dependent on the frequency, R_{Fe} and T_{Fe} are dependent on the operating frequency as well. Hence detuning will exhibit dependence on speed not only in the field-weakening region, but also in the base speed region.

A number of quantitative detuning studies are performed for the 4 kW induction machine and some of the results are presented in Figs. 4.10 to 4.12. Figure 4.10 represents dependence of detuning on speed, with the load torque as parameter, for operation in the base speed region. It can be seen that detuning due to iron loss is quite small at low speeds, non-linearly increasing with the speed. Dependence of detuning on load level is more complicated. The errors in the torque and in the rotor flux are smaller for both light and heavy loads than for medium loads. The orientation angle error is greatest for light loads and decreases as the load torque increases.

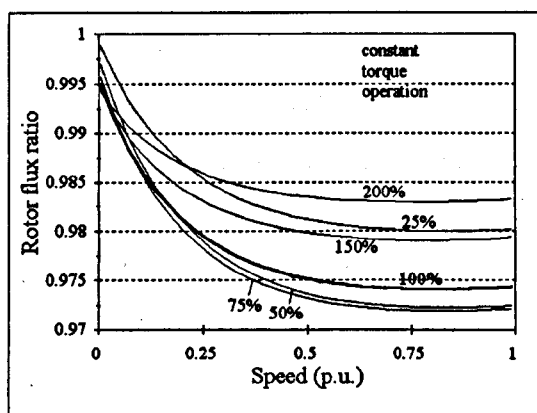
Figure 4.11. depicts dependence of detuning on load, with speed as parameter. Both motoring (positive torque) and braking (negative torque) operation in the base speed region are encompassed. As expected, detuning is most severe at the rated speed. Figure 4.11 also reveals that maximum deviations in the torque and in the rotor flux occur when the load torque is about 60% and about 70% of the rated torque, for motoring and braking, respectively. As the study presented in [Levi et al., 1996a] has shown, load torque at which maximum errors in the torque and in the rotor flux occur is an individual feature of the particular machine, while maximum error in the orientation angle always occurs at no-load operation.



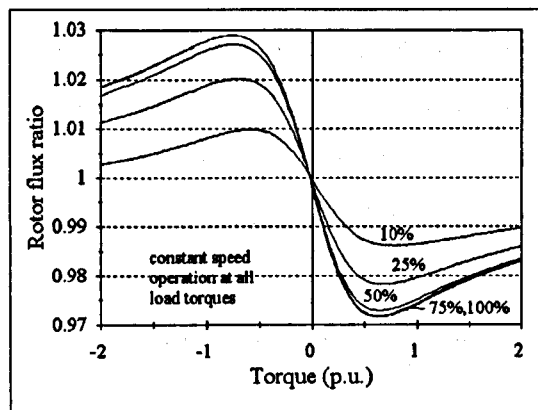
a. torque ratio



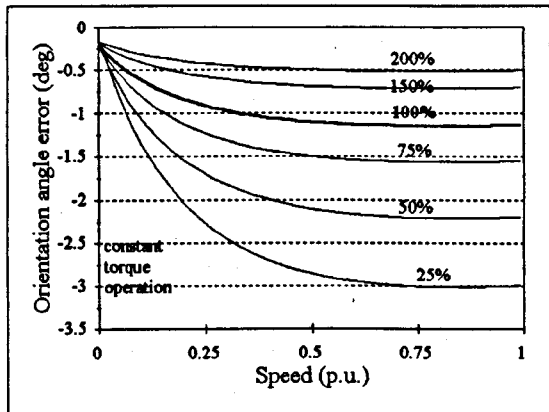
a. torque ratio



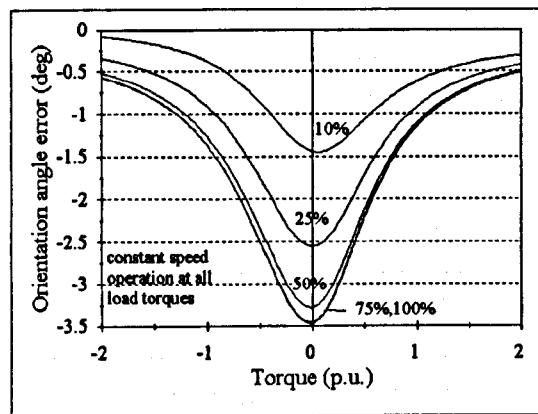
b. rotor flux ratio



b. rotor flux ratio



c. orientation angle error



c. orientation angle error

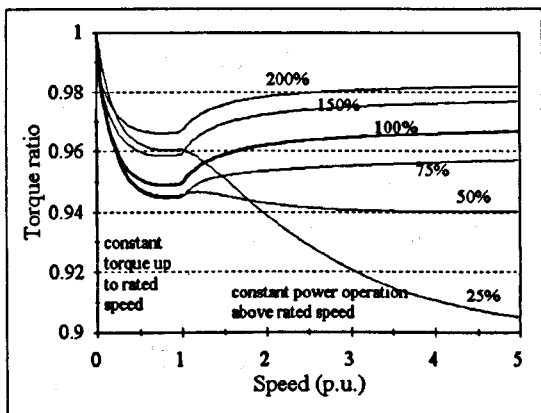
Figure 4.10 : Steady-state detuning due to iron loss, R_{Fe} representation, main flux saturation neglected, operation in the base speed region, load torque in % as parameter, 4 kW machine.

Figure 4.11 : Steady-state detuning due to iron loss, R_{Fe} representation, main flux saturation neglected, motoring and braking in the base speed region, speed in % as parameter, 4 kW machine.

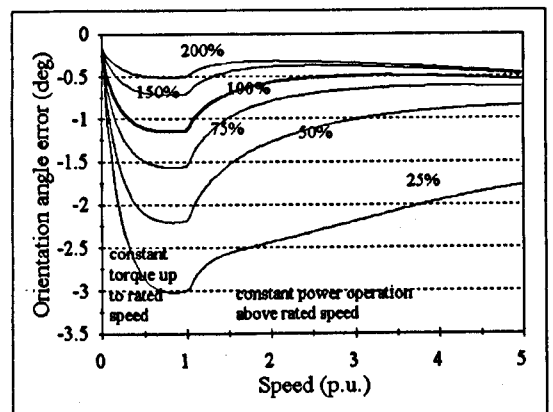
The torque ratio and the rotor flux ratio in Fig. 4.11 are close to be odd functions with respect to the zero torque, while the orientation angle error is close to be an even function. The explanation is that iron loss in motoring operation appears as an unrecognised power that has to be covered by the inverter. In this way the commanded

torque (power) has to be higher than the actual torque (power). In contrast to this, iron loss is covered from the converted mechanical power during braking operation. In this case the actual torque (power) is greater than the commanded torque (power) [Levi et al., 1996a].

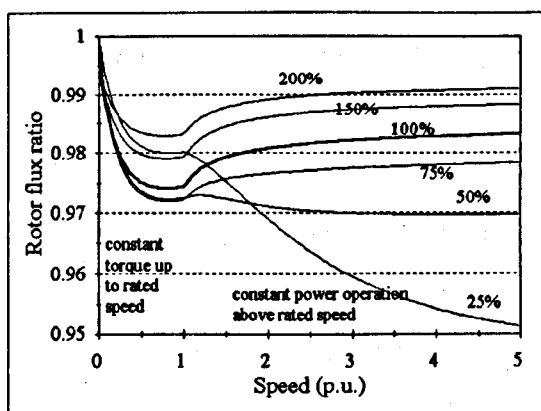
Figure 4.12 depicts detuning characteristics for motoring operation only, for a wide speed range [Sokola et al., 1995]. Parameters for these characteristics are load torque (output torque) in the base speed region and output power in the field-weakening region. More specifically, 100% curve denotes that the load torque is of rated level until the rated speed is reached and then the output power is of rated level beyond the rated speed. For instance, 100% curve means that at speed of say 3 p.u. the load torque is one third of the rated torque and the output power is rated. Figure 4.12 reveals that detuning due to iron loss in the field-weakening region is smaller than detuning at the rated speed for medium and heavy loads. The opposite is true for light load operation. The orientation angle error is always smaller in field-weakening than at the rated speed.



a. torque ratio



c. orientation angle error



b. rotor flux ratio

Figure 4.12 : Steady-state detuning due to iron loss, R_{Fe} representation, main flux saturation neglected, operation in both base speed region and field-weakening, load torque in % (base speed region) and output power in % (field-weakening) as parameters, 4 kW machine.

4.4.4.2. Detuning with iron loss represented by a resistance placed in parallel with the magnetising branch, main flux saturation included

In this part of study, both iron loss and main flux saturation are included in the machine model, while thermal effects and leakage flux saturation are neglected. Therefore the $i_s - \psi_m - \psi_r$ reduced-order model with both iron loss and main flux saturation, presented in sub-section 3.4.4, is utilised as the starting point for derivation. The steady-state model consists of (4.11), (4.23), (2.17.c), (2.46) and one of (2.45). The difference between this model and model from 4.4.4.1 is that the actual values of the mutual inductance, the rotor inductance and the rotor time constant are variable parameters, as a consequence of main flux saturation. Recognising these facts and following the same procedure as in the previous sub-section, the expressions that describe detuning due to iron loss are obtained as [Sokola and Levi, 1996] :

$$\Delta\varphi_r = \arctan \frac{\psi_{qr}}{\psi_{dr}} = \arctan \frac{-B + \omega_{sl}^* T_r^* A}{A + \omega_{sl}^* T_r^* B} , \quad (4.26)$$

$$\frac{\psi_r}{\psi_r^*} = \frac{L_m}{L_m^*} \sqrt{\frac{1 + \omega_{sl}^{*2} T_r^{*2}}{A^2 + B^2}} , \quad (4.30)$$

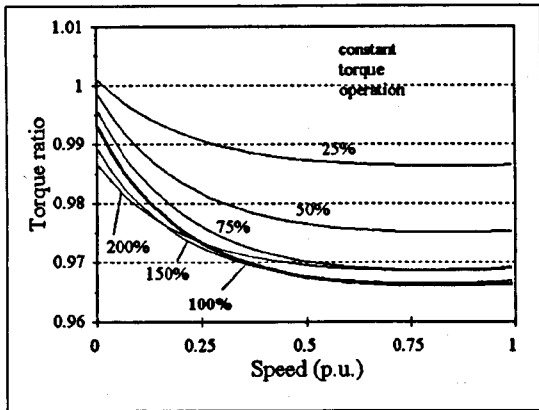
$$\frac{T_e}{T_e^*} = \left(\frac{\psi_r}{\psi_r^*} \right)^2 = \left(\frac{L_m}{L_m^*} \right)^2 \frac{1 + \omega_{sl}^{*2} T_r^{*2}}{A^2 + B^2} , \quad (4.31)$$

$$\begin{aligned} & T_e^{*4} g^4 T_L T_{Fe}^2 T_{lr}^2 + T_e^{*3} g^2 \left(2g T_L \omega T_{Fe}^2 T_{lr}^2 - T_r^{*2} \frac{L_m^2}{L_m^{*2}} \right) + \\ & + T_e^{*2} g^2 T_L \left((T_r + T_{Fe})^2 + \omega^2 T_{Fe}^2 T_{lr}^2 - 2T_{Fe} T_{lr} \right) + \\ & + T_e^* \left(2g T_L \omega T_{Fe} (T_{Fe} + T_r - T_{lr}) - \frac{L_m^2}{L_m^{*2}} \right) + T_L (1 + \omega^2 T_{Fe}^2) = 0 \end{aligned} \quad (4.32)$$

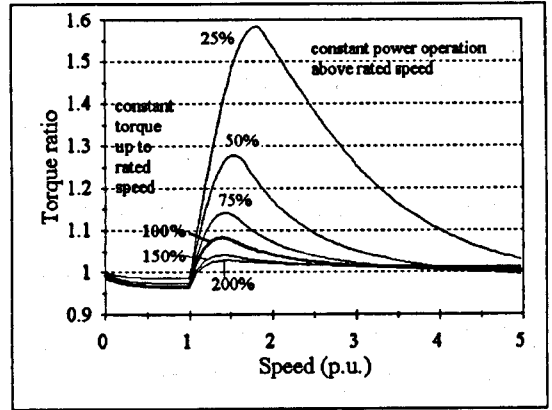
where A and B are defined by (4.25) while g is given with (4.20).

The above detuning expressions are dependent on speed, as a consequence of two phenomena. The first one is that iron loss (and thus R_{Fe}) is dependent on the operating frequency, while the second one is that the mutual inductance will change its value in different operating conditions, particularly in the field-weakening region.

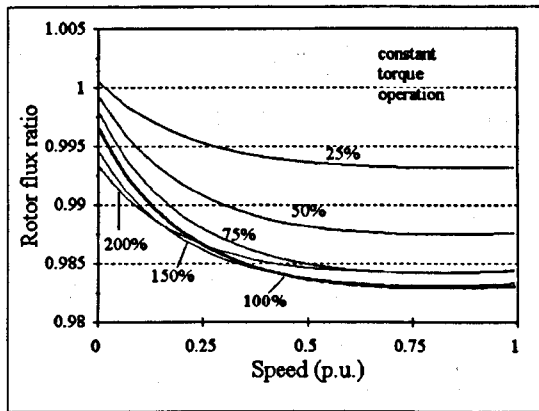
The results of quantitative detuning study for this case are shown in Fig. 4.13 for the base speed region and in Fig. 4.14 for a wide speed region [Sokola and Levi, 1996].



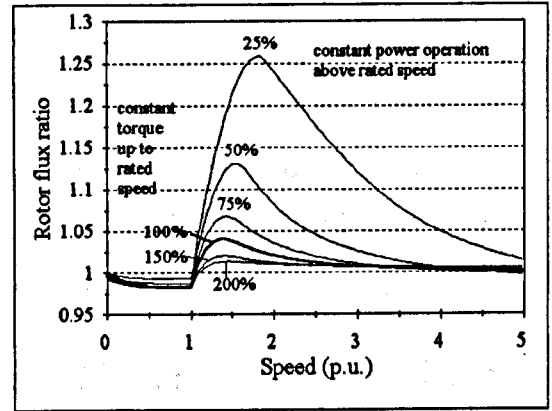
a. torque ratio



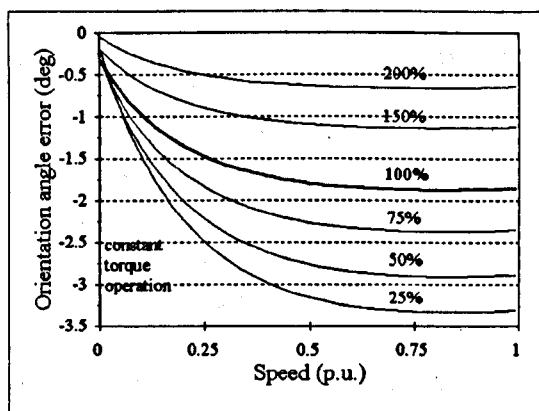
a. torque ratio



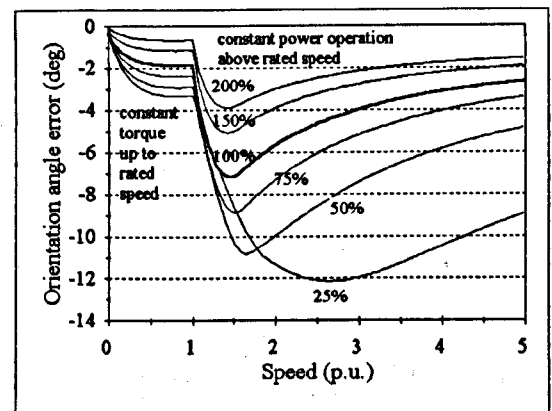
b. rotor flux ratio



b. rotor flux ratio



c. orientation angle error



c. orientation angle error

Figure 4.13 : Steady-state detuning due to iron loss, R_{Fe} representation, main flux saturation in the machine included, operation in the base speed region, load torque in % as parameter, 4 kW machine.

Figure 4.14 : Steady-state detuning due to iron loss, R_{Fe} representation, main flux saturation in the machine included, operation in a wide speed region, load torque and output power in % as parameters, 4 kW machine.

Motoring operation of the 4 kW machine is analysed. In the base speed region, errors in the torque and in the rotor flux increase with the speed and with the load. Maximum errors occur roughly at the rated load. Comparison of Figs. 4.10 and 4.13 indicates that main flux saturation has a damping effect on detuning in the base speed region, reducing the errors in the torque and the rotor flux. The orientation angle error becomes slightly bigger when the main flux saturation is included.

However, main flux saturation has a major detuning role in the field-weakening region. Figure 4.14 suggest that detuning in the field-weakening region is severe, especially at light loads. Errors in the torque and in the rotor flux reach about 58% and 26%, respectively, while the orientation angle error exceeds 12 degrees. For each output power curve, maximum errors in the torque and in the rotor flux occur at speeds between 1.3 p.u. (for 200% output power) and 2 p.u. (for 25% output power). Maximum in the orientation angle error occur at roughly same speeds, exception being light load operation, when the maximum error occurs at somewhat higher speed of 2.6 p.u. When detuning characteristics from Fig. 4.14 are compared with the detuning characteristics solely due to iron loss, Fig. 4.12, it can be concluded that main flux saturation has dominant influence in the field-weakening region.

4.4.4.3. Detuning with iron loss represented by a resistance placed after the stator resistance, main flux saturation neglected

Iron loss can also be represented by a resistance placed immediately after the stator resistance. Detuning expressions for R_{lr} iron loss representation can be derived from the corresponding $i_s - \psi_m - \psi_r$ reduced-order model, described in sub-section 3.3.2.3, by adopting $\omega_a = \omega_r^*$. In a steady state, the rotor flux equations are :

$$\begin{aligned} \psi_{dr} &= \psi_{dm} + \omega_{sl}^* T_{lr} \psi_{qr} \\ \psi_{qr} &= \psi_{qm} - \omega_{sl}^* T_{lr} \psi_{dr} \end{aligned} \quad (4.11)$$

while the expressions for the magnetising flux in steady states are obtained from (3.21) as:

$$\begin{aligned} 0 &= R_{lr} i_{ds} - \frac{1}{T_{lr}} \frac{L_r}{L_m} \psi_{dm} + \omega_a \frac{L_s}{L_m} \psi_{qm} + \frac{1}{T_{lr}} \psi_{dr} \\ 0 &= R_{lr} i_{qs} - \frac{1}{T_{lr}} \frac{L_r}{L_m} \psi_{qm} - \omega_a \frac{L_s}{L_m} \psi_{dm} + \frac{1}{T_{lr}} \psi_{qr} \end{aligned} \quad (4.33)$$

Combining (4.11) and (4.33), the rotor flux components are obtained as :

$$\begin{aligned}\psi_{dr} &= L_m \frac{C i_{ds}^* + D i_{qs}^*}{C^2 + D^2} \\ \psi_{qr} &= L_m \frac{-D i_{ds}^* + C i_{qs}^*}{C^2 + D^2}\end{aligned}\quad (4.34)$$

Coefficients C and D in (4.34) are :

$$C = 1 - \omega_r \omega_{sl} T_{sir} T_{lr} \quad \text{and} \quad D = \omega_{sl} T_r + \omega_r T_{sir} \quad , \quad (4.35)$$

where the time constant T_{sir} is defined as :

$$T_{sir} = \frac{L_s}{R_{ir}} \quad . \quad (4.36)$$

Combining the above steady-state model with the steady-state estimator model, given by (4.6) - (4.10), the expressions that describe detuning due to iron loss are obtained as :

$$\frac{\psi_r}{\psi_r^*} = \sqrt{\frac{1 + \omega_{sl}^2 T_r^{*2}}{C^2 + D^2}} \quad , \quad (4.37)$$

$$\Delta\phi_r = \arctan \frac{\psi_{qr}}{\psi_{dr}} = \arctan \frac{-D + \omega_{sl} T_r^* C}{C + \omega_{sl} T_r^* D} \quad , \quad (4.38)$$

$$\frac{T_e}{T_e^*} = \left(\frac{\psi_r}{\psi_r^*} \right)^2 = \frac{1 + \omega_{sl}^2 T_r^{*2}}{C^2 + D^2} \quad , \quad (4.39)$$

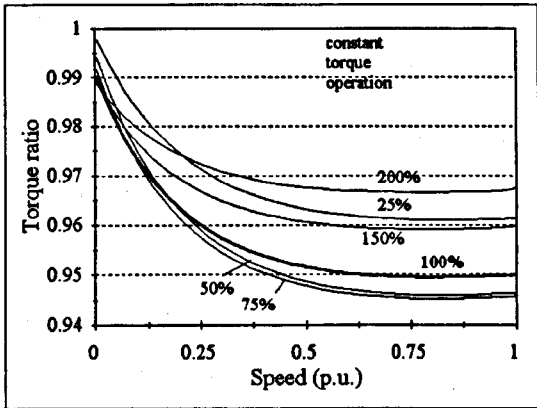
$$\begin{aligned}T_e^{*4} g^4 T_L T_{sir}^2 T_{lr}^2 + T_e^{*3} g^2 (2g T_L \omega T_{sir}^2 T_{lr}^2 - T_r^2) + T_e^{*2} g^2 T_L ((T_r + T_{sir})^2 + \omega^2 T_{sir}^2 T_{lr}^2 - 2T_{sir} T_{lr}) + \\ + T_e^* (2g T_L \omega T_{sir} (T_{sir} + T_r - T_{lr}) - 1) + T_L (1 + \omega^2 T_{sir}^2) = 0\end{aligned}\quad , \quad (4.40)$$

where g is given with (4.20).

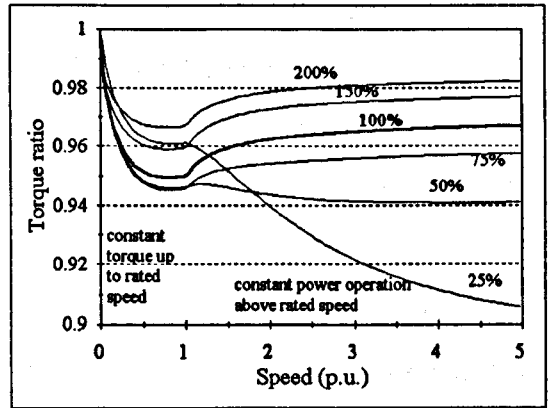
The values of the equivalent iron loss resistance R_{ir} at different operating frequencies are re-calculated from values of R_{Fe} shown in Fig. 4.2.c. As R_{ir} is dependent on frequency, the above detuning expressions will be speed-dependent in any operating region.

The quantitative study of steady-state detuning due to iron loss when R_{ir} representation is utilised is performed for the 4 kW machine. The results are shown in Figs. 4.15 and 4.16, for operation in the base speed region and in a wide speed region, respectively. It can be seen that these detuning characteristics are practically identical to the ones obtained with R_{Fe} iron loss representation (Figs. 4.10 and 4.12). It can be concluded that the way of iron loss representation does not influence the results of detuning

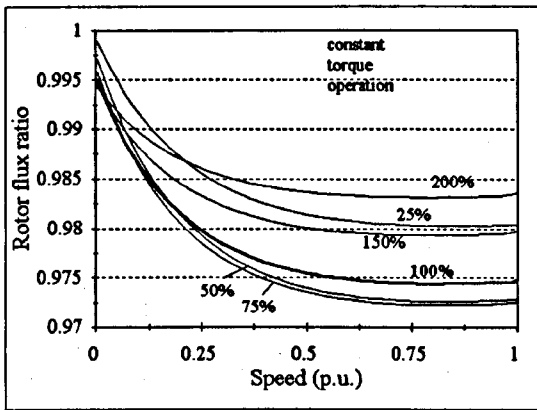
studies. This justifies lack of more detailed treatment of R_{ir} method of iron loss representation in Chapters 3 and 5.



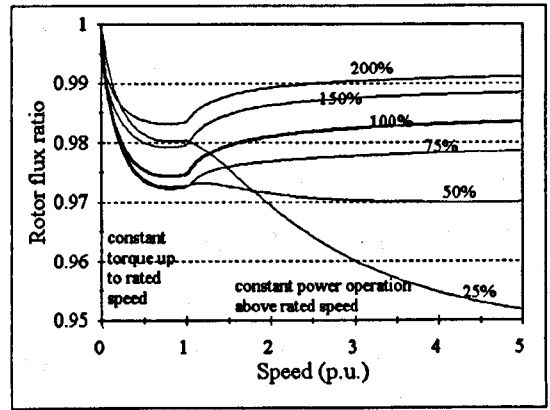
a. torque ratio



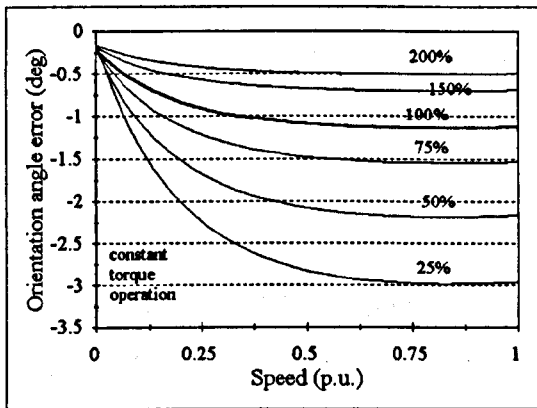
a. torque ratio



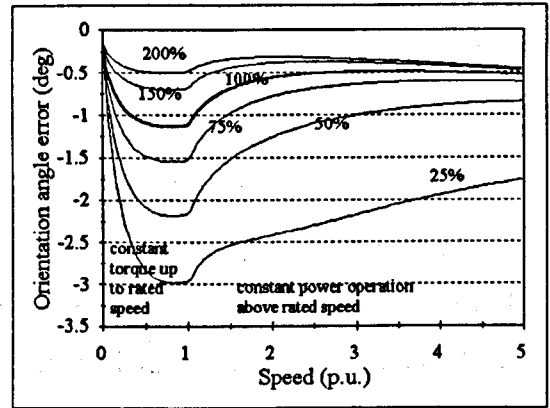
b. rotor flux ratio



b. rotor flux ratio



c. orientation angle error



c. orientation angle error

Figure 4.15 : Steady-state detuning due to iron loss, R_{ir} representation, main flux saturation in the machine neglected, operation in the base speed region, load torque in % as parameter, 4kW machine.

Figure 4.16 : Steady-state detuning due to iron loss, R_{ir} representation, main flux saturation in the machine neglected, operation in a wide speed region, load torque and output power in % as parameters, 4 kW machine.

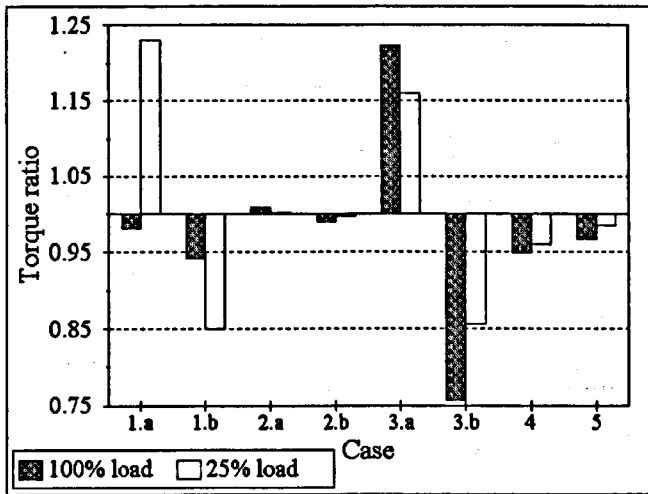
4.5. COMPARATIVE ANALYSIS OF STEADY-STATE DETUNING WITH THE CPM-BASED CONTROLLER

Studies of detuning due to different phenomena were presented in the previous section. Although these phenomena very often occur simultaneously, previous studies analysed influence of only one or at most two phenomena at a time. In this way it is attempted to extract the detuning effects of each phenomenon, in order to enable the following comparative analysis.

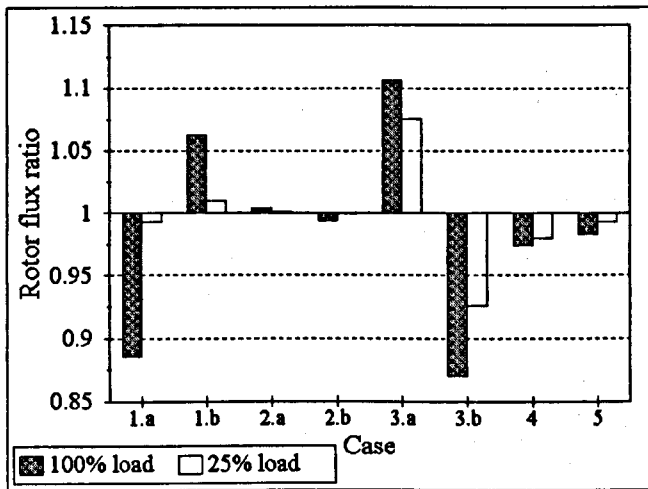
Figure 4.17 [Sokola et al., 1997] shows an extract of results presented in the section 4.4 (Figs. 4.3 - 4.16). Eight cases altogether are displayed. Although studies presented in previous sections encompassed very wide ranges of parameter variations, moderate errors in parameters are chosen for these eight cases, because extreme values of parameter variations would not enable a fair comparison. The first two cases represent detuning due to R_r variations, when the actual value is 80% of the estimated value (case 1.a) and when the actual value is 120% of the estimated value (case 1.b). The next two cases represent detuning due to L_{lr} variations, when the actual value is 80% of the estimated value (case 2.a) and when the actual value is 120% of the estimated value (case 2.b). The fifth and the sixth case represent detuning due to L_m inaccuracies, when the estimated value of the mutual inductance is 80% of nominal value L_{mn} (case 3.a) and when the estimated value is 120% of L_{mn} (case 3.b). Finally, the last two cases represent detuning due to iron loss, with main flux saturation neglected (case 4) and with main flux saturation included (case 5), both with R_{Fe} iron loss representation.

Figure 4.17 depicts results for operation at the rated speed with the load torque levels of 25% and 100% of the rated torque. The torque ratio is shown in Fig. 4.17.a., the rotor flux ratio in Fig. 4.17.b. and the orientation angle error in Fig. 4.17.c. First of all, it can be concluded that L_{lr} variations produce negligible detuning for these loads. As far as the torque ratio is concerned, L_m variation at both loads and R_r variation at light loads cause significant errors. At the rated load, both L_m and R_r variations result in significant errors in the rotor flux, while iron loss has smaller influence. At the light load, the rotor flux error due L_m variations is the greatest, while iron loss and R_r variation have much smaller influence. As far as the orientation angle error is concerned, at the rated load, R_r variations are most influential, followed by L_m

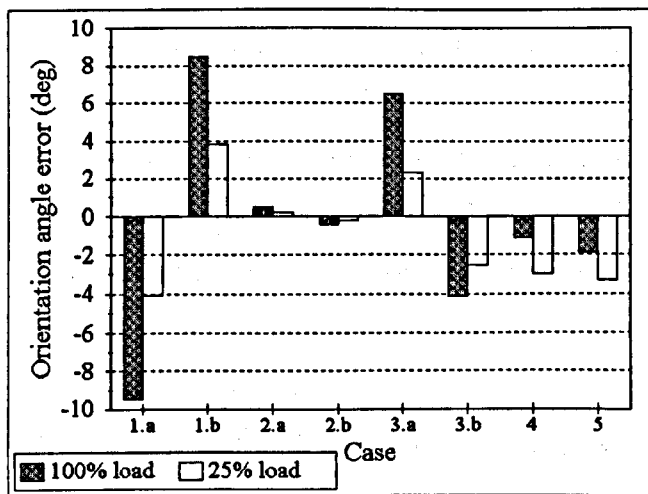
variations and iron loss. However, at 25% load the errors in the orientation angle are comparable for these three phenomena.



a. torque ratio



b. rotor flux ratio



c. orientation angle error

Figure 4.17 : Comparative analysis of detuning, operation at the rated speed, with two load torque levels, 4 kW machine.

Cases:

1 : R_r variations,

1.a : $R_r / R_r^* = 0.8$

1.b : $R_r / R_r^* = 1.2$

2 : L_{lr} variations,

2.a : $L_{lr}^* / L_{lrn} = 0.8$

2.b : $L_{lr}^* / L_{lrn} = 1.2$

3 : L_m variations,

3.a : $L_m^* / L_{mn} = 0.8$

3.b : $L_m^* / L_{mn} = 1.2$

4 : Detuning due to iron loss at rated speed, main flux saturation neglected in the machine model,

5 : Detuning due to iron loss at rated speed, main flux saturation included in the machine model.

4.6. DETUNING IN TRANSIENT OPERATION WITH THE CPM-BASED CONTROLLER

As controlled transition between two steady-states is one of the key features of a vector controlled drive, it is important to analyse the influence of detuning phenomena on the transient performance. To predict the performance of a drive in detuned transient conditions, an investigation approach different to the one used for analyses of steady-state detuning has to be utilised. Analyses of detuning in transients are based on simulation of the whole drive, using a software package for digital simulation. Feedback vector control system of Figs. 2.2. and 2.3. is simulated and the induction machine is represented by an appropriate dynamic model. As current feeding is assumed, improved dynamic reduced-order models in the d^*-q^* reference frame are utilised. Current-regulated PWM inverter is assumed to be an ideal current source and is modelled by a first-order delay element with the time constant of 200 μs . In certain cases only torque mode of operation (speed control loop open) is elaborated, while in other cases the full closed-speed-loop vector control is analysed. As L_{lr} variations are the least important source of detuning, having only a minor influence when compared with the other three detuning sources, they are omitted from analysis of transient detuning.

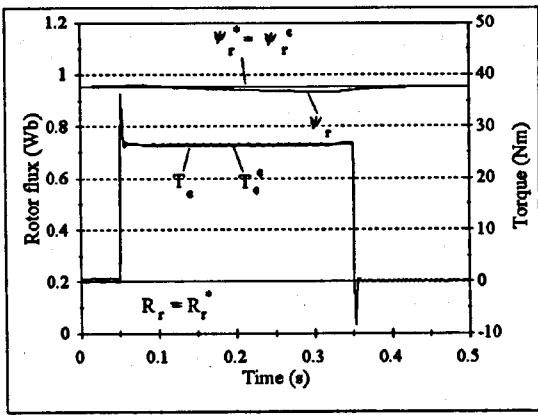
4.6.1. Transient detuning due to rotor resistance variations

For simulation studies of transient detuning due to R_r variations, the induction machine is represented by the $\psi_m - \psi_r$ reduced-order model with main flux saturation, given in 2.5.1.4. Main flux saturation is represented by the $i_m (\psi_m)$ non-linear relationship. Operation with accurately identified R_r is analysed first, followed by simulation of the drive responses with wrongly identified R_r . The vector controller operates in the speed mode. This differs from the usual approach in which detuning due to R_r variations is analysed in the torque mode of operation, where a stepwise torque command is applied and the speed response is observed. As most vector-controlled drives normally operate with closed-loop speed control, the approach used here is more realistic for majority of vector-controlled induction machine drives. The simulated transients are sudden application and removal of the rated load torque. The initial and the final steady state

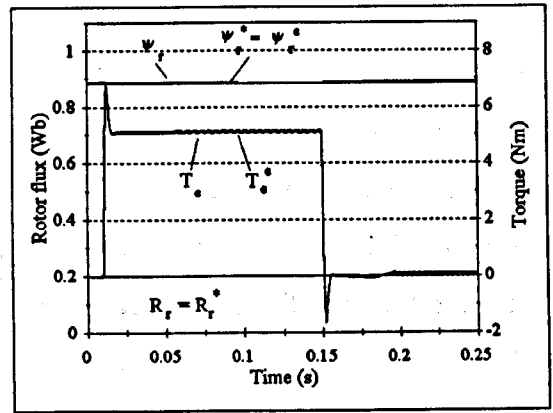
correspond to operation with the rated rotor flux command, 80% of the rated speed and zero load torque. The application of the load initiates a transient which brings the machine into the operation with the rated rotor flux command, 80% of the rated speed and rated load torque. The removal of the load initiates the other transient, which returns the machine into the no-load operation.

Simulation results for the 4 kW machine are shown in Fig. 4.18, for three cases. In all cases the estimated rotor resistance (the value used in the controller) is of rated value ($R_r^* = R_{rn}$). The actual rotor resistance assumes different values. In the case a. the actual rotor resistance is equal to the rated, in the case b. it is 20% greater than the rated and in the case c. it is 20% smaller than the rated. As these variations in R_r are not known to the estimator, detuned operation occurs in cases b. and c. Due to actions of the PI speed controller, speed is maintained at the commanded level of 80% of the rated and the developed torque equals the load torque, apart of short-term spikes at the beginnings of both transients. However, the estimated (and the commanded) torque differs from the rated value in detuned cases. In the case b. it is bigger and in the case c. it is smaller than the actual torque. Moreover, the response in the case c. is oscillatory, although well damped. Similar behaviour can be observed for the rotor flux. The flux level is in all cases estimated to be constant and equal to the commanded flux, while the actual flux experiences significant swing in both detuned cases. Bigger swing in the rotor flux can be noticed in the case c. , since main flux saturation dampens the flux increase in the case b. When transients are finished, the amount of detuning corresponds to the values predicted by the steady-state analysis, Fig. 4.4.

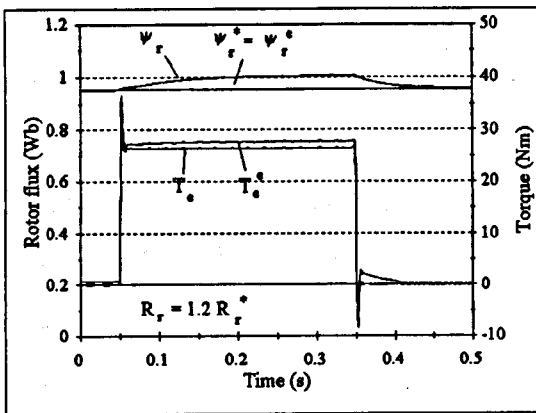
Similar analysis of transient detuning is performed for the 0.75 kW machine (data given in the Appendix A), but for two greater errors in the rotor resistance than it was the case for the 4 kW machine. The results are shown in Fig. 4.19. In the case a. the actual rotor resistance is equal to the rated resistance, in the case b. it is 50% greater than the rated and in the case c. it is 34% smaller than the rated. Trends of detuning are the same as for the 4 kW machine, but, as expected, detuning is more pronounced. In the case c. responses are oscillatory and this is an indication that proper rotor-flux-oriented control is lost.



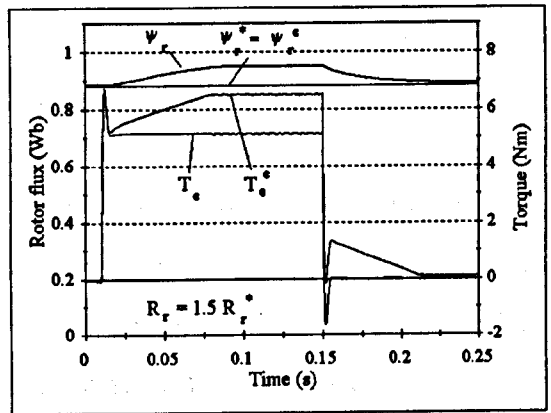
a. $R_r = R_{rn} = R_r^*$



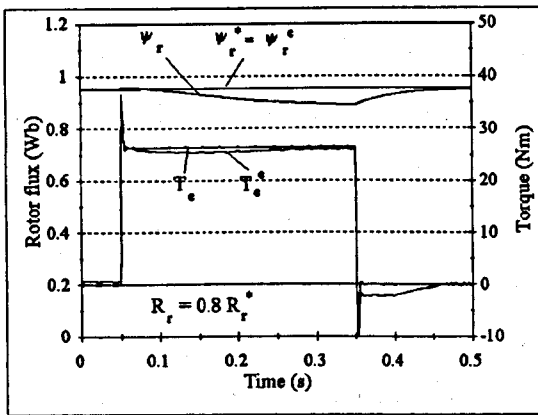
a. $R_r = R_{rn} = R_r^*$



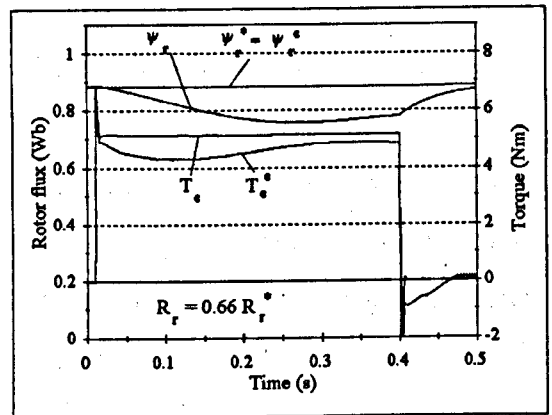
b. $R_r = 1.2 \times R_r^*$



b. $R_r = 1.5 \times R_r^*$



c. $R_r = 0.8 \times R_r^*$



c. $R_r = 0.66 \times R_r^*$

Figure 4.18 : Torque and flux responses to step loading and unloading with the rated load torque, influence of the rotor resistance variations, $R_r^* = R_m$, 4 kW machine.

Figure 4.19 : Torque and flux responses to step loading and unloading with the rated load torque, influence of the rotor resistance variations, $R_r^* = R_m$, 0.75 kW machine.

4.6.2. Transient detuning due to main flux saturation

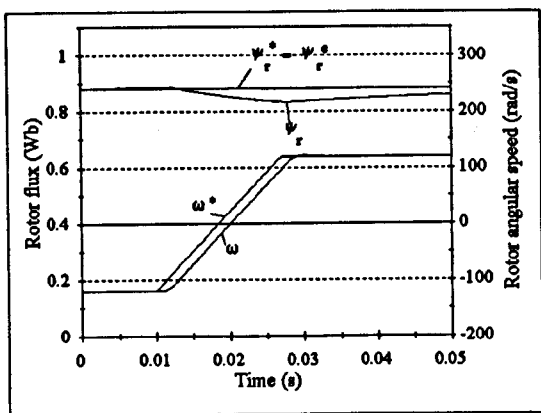
In order to simulate the behaviour of a RFO induction machine drive in the presence of main flux saturation, a convenient dynamic model of an induction machine is required. The reduced-order model from sub-section 2.5.1.4., with any representation of main flux saturation can be utilised for a simulation study. The feedback vector control system of Figs. 2.2 and 2.3 is analysed again, for two transients during which main flux saturation is typically pronounced. The first transient is a very fast speed reversal in the base speed region. In such a case, very high torque is required, so that the q -axis current is very high and the cross-saturation effect is pronounced. The second analysed transient is acceleration into the field-weakening region, where the flux is reduced and machine becomes less saturated than with the rated flux, affecting the actual value of the mutual inductance. In both cases it is assumed that transients occur without load. This study can be found in [Levi, 1994a] for the 0.75 kW machine and it is repeated here in order to be compared later on with the drive performance when novel saturation-adaptive estimators are employed. Additionally, the same transients are simulated for the 4 kW machine.

Reversing transient for the 0.75 kW machine is shown in Fig. 4.20. The commanded speed is rapidly changed in a ramp-wise manner from -40% to +40% of the rated speed. The rotor flux command is kept at the rated level. Change in the commanded speed leads to extremely fast rise in the stator q -axis current, which reaches seven times the rated q -axis current. High current in turn produces very high torque (almost seven times rated torque), that is needed for harsh acceleration. The magnetising q -axis current becomes significant and the machine becomes more saturated, yielding a drop in the actual value of the mutual inductance. As this change of magnetic conditions is not recognised by the CPM-based rotor flux estimator, decrease in the rotor flux is not detected and the commanded d -axis stator current is unchanged. Therefore a decrease in the rotor flux is not compensated. Consequently, the developed torque is smaller than the estimated (commanded). After the reversal is performed, the q -axis stator current is returned to its low no-load value, the cross-saturation effect diminishes and the rotor flux slowly returns to the commanded level.

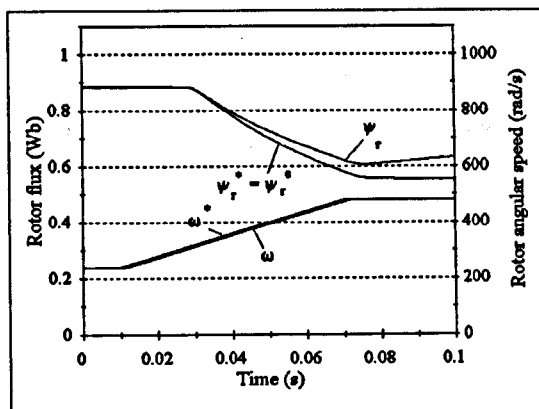
Simulation results for acceleration into the field-weakening region for the 0.75 kW machine are shown in Fig. 4.21. The commanded speed is increased from 80% to 160% of the rated speed in a relatively slow manner, so that torque of about 180% is required for the acceleration. In this way the influence of cross-saturation is suppressed as the intention is to analyse detuning due to the reduced flux command during operation above the rated speed. When the rated speed is surpassed, detuning starts to occur. As the commanded flux is lowered, magnetic saturation becomes less pronounced, the mutual inductance increases, the rotor flux is greater than the commanded and the developed torque is greater than estimated (commanded) torque. After the final speed is reached, the actual value of the rotor flux deviates even more from the commanded value.

The results of 4.20 and 4.21 indicate that some detuning occurs in the analysed transients even when the mutual inductance in the CPM estimator (L_m^*) is correctly set to the rated value. If L_m^* was incorrectly set, as analysed in sub-section 4.4.1 for steady-state operation, the transient performance of the drive would deteriorate further.

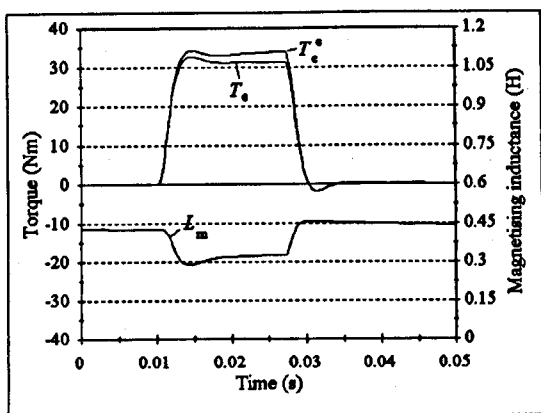
The same transient analyses are repeated for the 4 kW machine and the results are shown in Figs. 4.22 and 4.23. Due to much higher inertia, acceleration lasts for longer time than for the 0.75 kW machine. During the reversing transient, Fig. 4.22, the developed torque is almost 5 times rated and the q -axis stator current is about 5 times rated. The cross-saturation effect is less pronounced than in the previous case. Thus the increase in the magnetising current and the drop in the mutual inductance are smaller in relative terms. As far as acceleration into the field-weakening region is concerned, Fig. 4.23, the rate of change in the commanded speed is such that torque level of about 190% is required. Differences between the commanded torque and the actual torque are quite small, but the actual rotor flux significantly deviates from the commanded value after the final speed is reached and no acceleration is required any more.



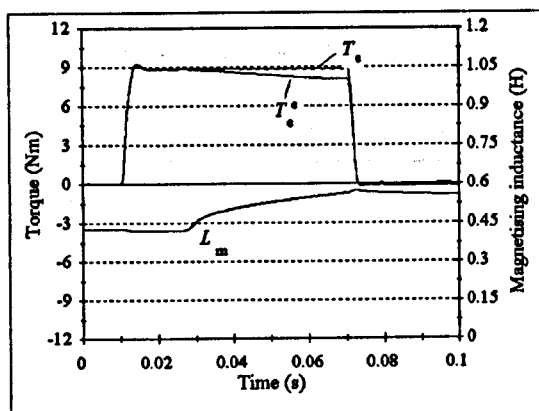
a. angular speed and rotor flux



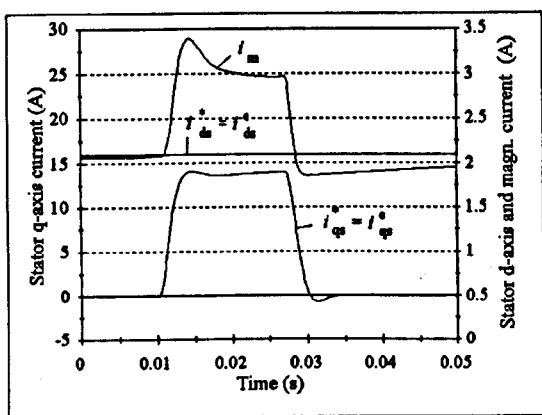
a. angular speed and rotor flux



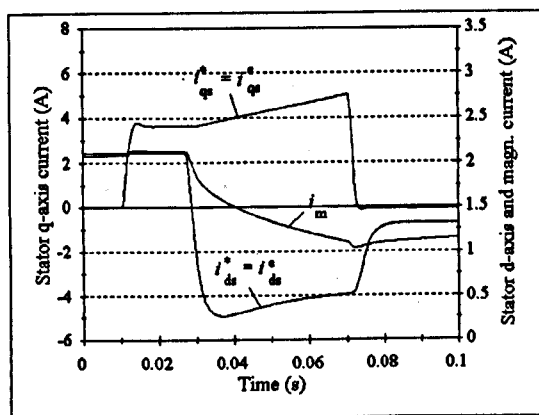
b. torque and mutual inductance



b. torque and mutual inductance



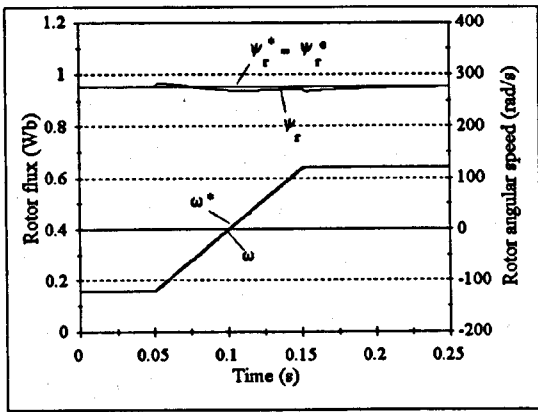
c. currents



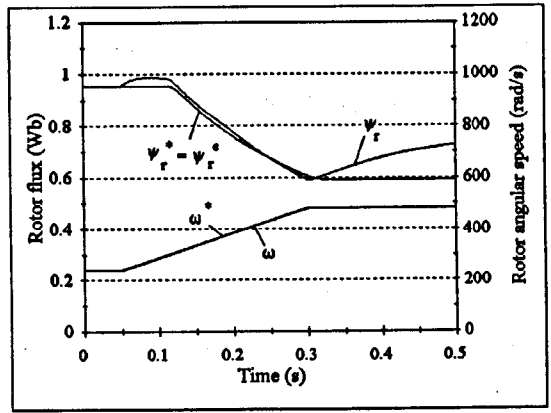
c. currents

Figure 4.20 : Transient responses for fast reversing transient without load, 0.75 kW machine.

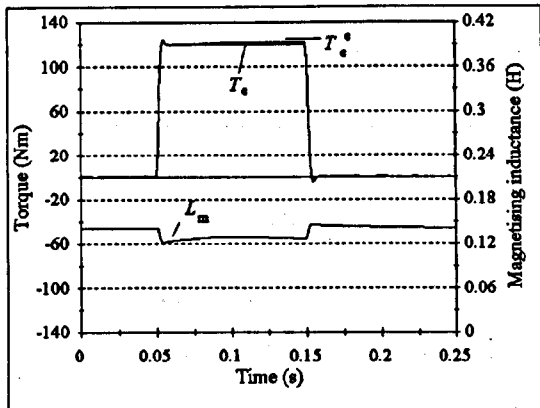
Figure 4.21 : Transient responses for no-load acceleration into the field-weakening region, 0.75 kW machine.



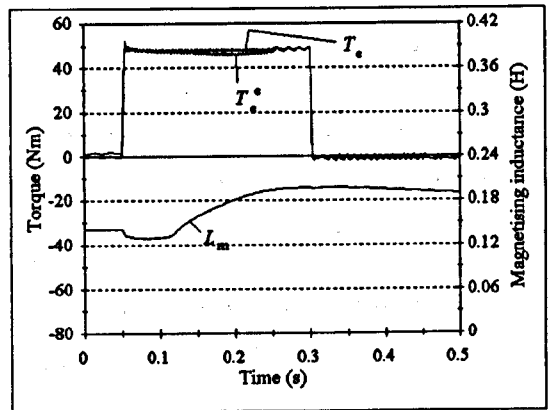
a. angular speed and rotor flux



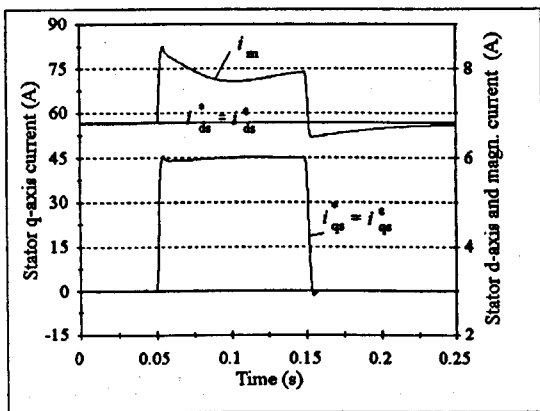
a. angular speed and rotor flux



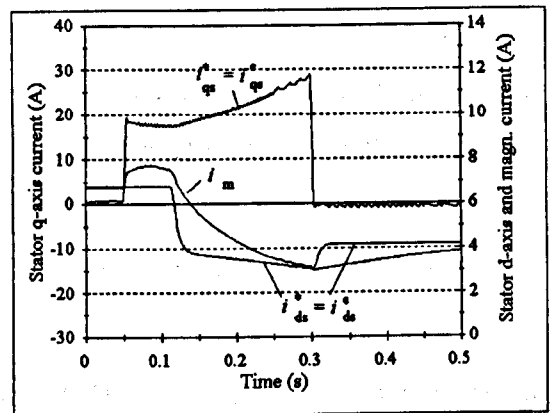
b. torque and mutual inductance



b. torque and mutual inductance



c. currents



c. currents

Figure 4.22 : Transient responses for fast reversing transient without load, 4 kW machine.

Figure 4.23 : Transient responses for no-load acceleration into the field-weakening region, 4 kW machine.

4.6.3. Transient detuning due to iron loss only

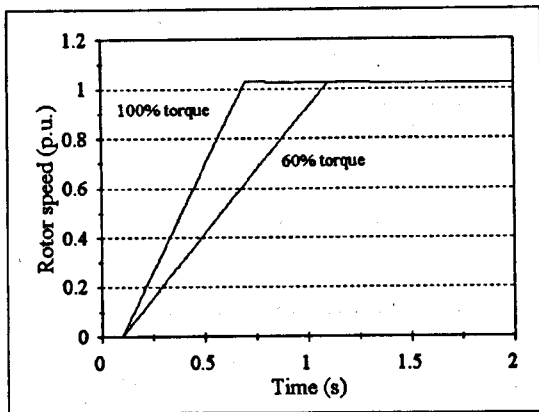
This is the topic that represents one of the entirely original contributions of this thesis. In order to investigate transient detuning due to iron loss, the feedback vector controller with the CPM-based estimator is simulated along with an appropriate reduced-order model with iron loss. Both torque mode of operation (speed loop open) and speed mode of operation are analysed. Two models with different iron loss representation (R_{Fe} and R_{ir}) are elaborated.

4.6.3.1. Torque mode of operation, R_{Fe} iron loss representation

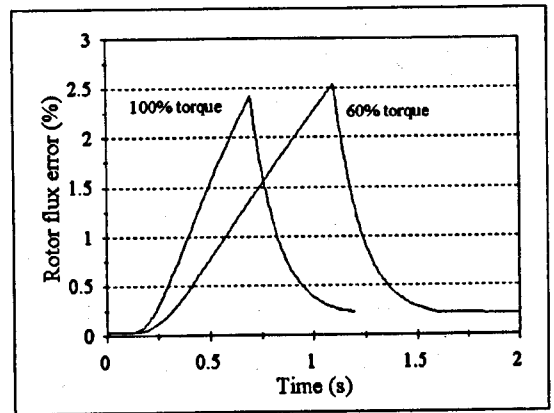
The machine is represented by the $i_s - \psi_m - \psi_r$ reduced-order model in the $d^* - q^*$ reference frame, which is derived from the model of 3.3.2.2 by adopting $\omega_d = \omega_r^*$. In the torque mode of operation the speed controller in the control system of Fig. 2.2 is disabled and the torque command is applied as the control input. No-load acceleration of the 4 kW machine from standstill is simulated. The rotor flux in the machine is already established by the stator d -axis current and then a torque pulse of certain amplitude and certain duration is applied. Two situations that are simulated are the torque pulse of 100% amplitude and 0.6 seconds duration and the torque pulse of 60% amplitude and 1 second duration. The second value of 60% of the rated torque corresponds to the load torque at which maximum iron loss induced detuning occurs in steady-state operation in the base speed region. In perfectly tuned conditions, these two torque pulses force the machine to accelerate up to the nominal no-load speed, which is 4% higher than the rated speed. All the parameters of the machine are taken as equal to those in the vector controller.

Figure 4.24 [Levi et al., 1995b; Sokola et al., 1996] shows responses of the angular speed and detuning parameters for this transient. Due to fast action of the torque controller, the estimated and the commanded torque are basically equal. Meanwhile, due to iron loss, the actual torque has a smaller value during acceleration. Hence the torque error is positive and it increases with the speed, as iron loss increases with the frequency. Due to such detuning, the final speed is slightly lower than expected. It appears that the torque error is roughly identical for the two levels of the commanded torque, but this is only in relative terms, as defined by (4.4). The absolute difference between the commanded and the actual torque is greater for the 100% torque command

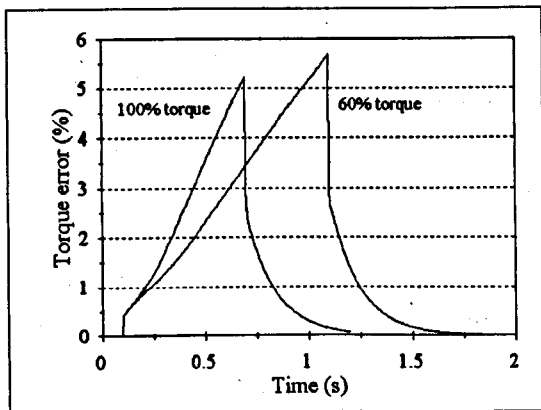
than for the 60% one. The rotor flux error is similar for the two analysed cases, while the angle error for 60% torque command is slightly bigger than for the 100% torque command. Such behaviour is expected from the analysis of steady-state detuning, performed in sub-section 4.4.4.1. The orientation angle error increases with the speed in a roughly linear manner and then it settles to the no-load value after the acceleration is finished.



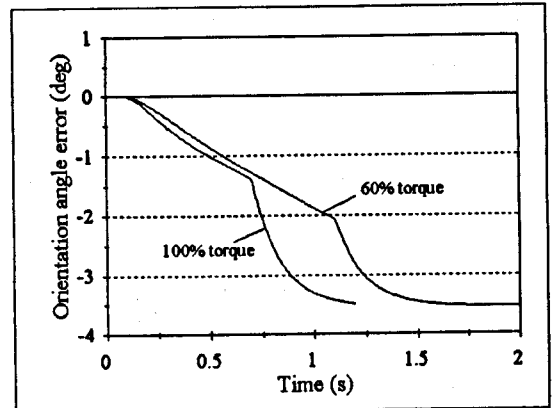
a. angular rotor speed



c. rotor flux error



b. torque error



d. orientation angle error

Figure 4.24 : Transient detuning due to iron loss (R_{Fe} representation) during no-load acceleration, torque mode of operation, 4 kW machine.

4.6.3.2. Torque mode of operation, R_{ir} iron loss representation

The same no-load acceleration transients are simulated again, but this time with R_{ir} iron loss representation. The machine is represented by the $\underline{i}_s - \underline{\psi}_m - \underline{\psi}_r$ reduced-order model of 3.3.2.3. and the results are shown in Fig. 4.25 [Sokola et al., 1996]. The responses are very similar to the responses obtained with R_{Fe} iron loss representation, Fig. 4.24. The speed responses are identical, as well as the behaviour of the orientation angle error.

The torque error and the rotor flux error have slightly smaller values than those they had with R_{Fe} iron loss representation.

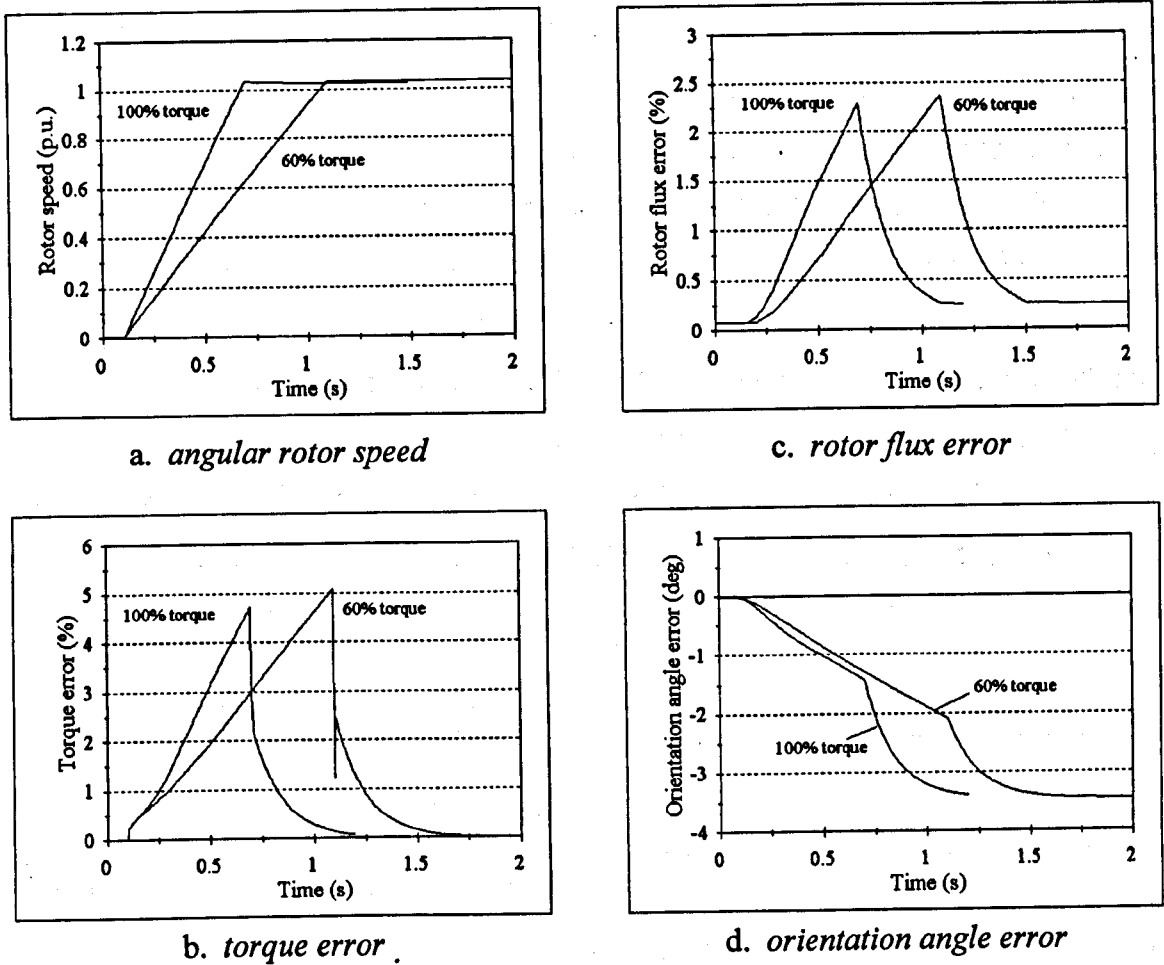
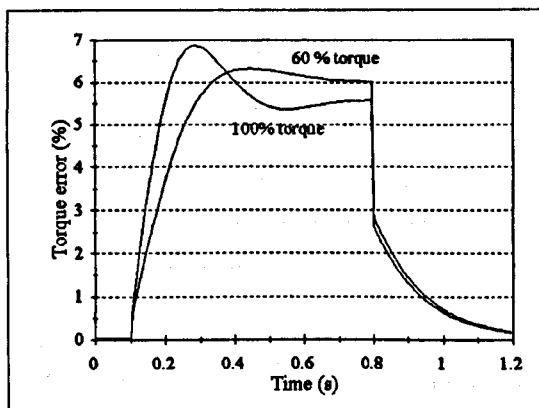


Figure 4.25 : Transient detuning due to iron loss (R_r representation) during no-load acceleration, torque mode of operation, 4 kW machine.

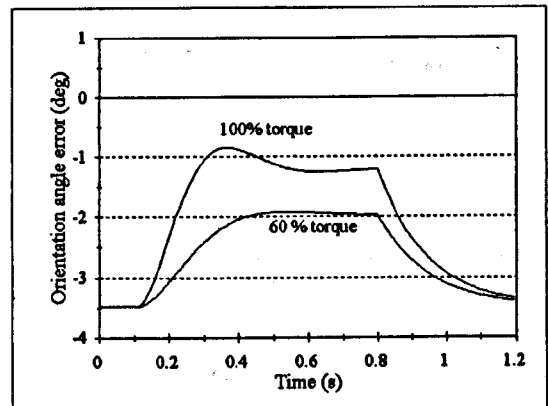
4.6.3.3. Speed mode of operation, R_{Fe} iron loss representation

When the speed controller is enabled and the speed command is imposed as the input, the drive operates in the speed mode. The transients simulated in this case are stepwise application and removal of the load. Two levels of the applied load torque are analysed - 100% of the rated load and 60% of the rated load (at which maximum detuning occurs, as seen in steady state-characteristic from Fig. 4.11). The commanded speed and the actual speed are of the rated level, as maximum detuning due to iron loss occurs at the rated speed.

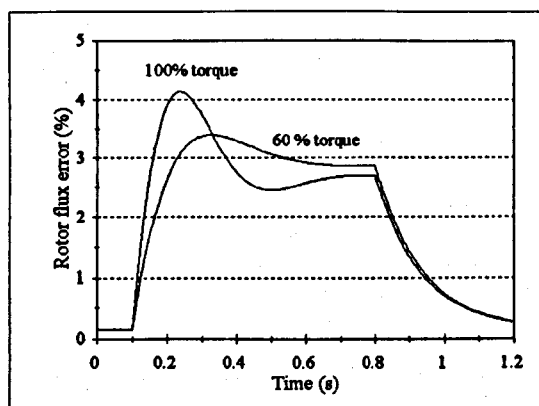
The results are shown in Fig. 4.26 [Levi et al., 1995b]. Due to fast action of the control system, change in the speed caused by the application or the removal of the load is negligibly small and hence the speed response is not shown. Figure 4.26.a. presents the responses of the torque error while Fig. 4.26.b presents the responses of the rotor flux error. The developed torque equals the applied load torque, but the values of the commanded and the estimated torque are higher. As far as the rotor flux is concerned, commanded and estimated values are rated (and thus the flux controller is inactive), while the actual flux experiences decrease due to loading of the machine. For loading with the rated load, the responses are oscillatory, with the torque error peak at almost 7% and the rotor flux error peak at more than 4%. When the load is 60% of rated, the peaks in errors are smaller, while the errors after the loading transient has settled are greater. The orientation angle error is shown in Fig. 4.26.c. As expected, it decreases with loading. After settling, all values of detuning quantities correspond to the steady-state values from Fig. 4.10 to 4.12.



a. torque error



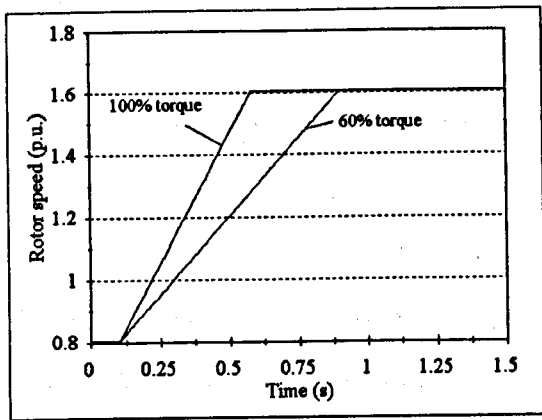
c. orientation angle error



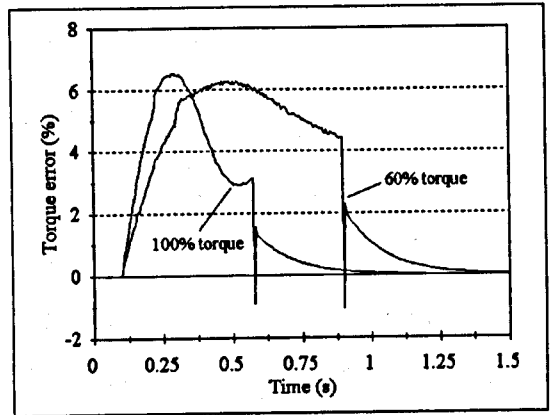
b. rotor flux error

Figure 4.26 : Transient detuning due to iron loss (R_{Fe} representation) during loading and unloading at the rated speed, speed mode of operation, 4 kW machine.

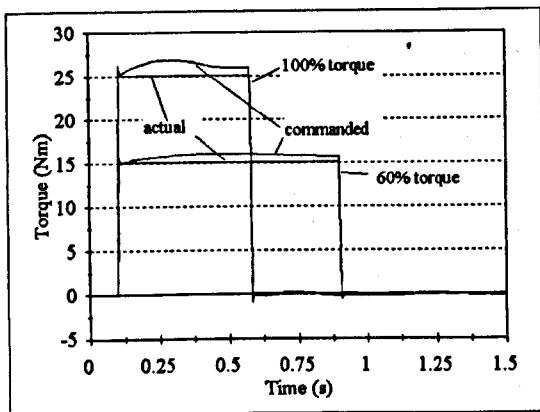
The next simulated transient is acceleration into the field-weakening region. The CPM-based feedback vector control system, operating in the speed mode is simulated. The 4 kW induction machine is represented by the $i_s - \psi_m - \psi_r$ reduced-order model with iron loss, while main flux saturation is neglected. The responses are shown in Fig. 4.27, for



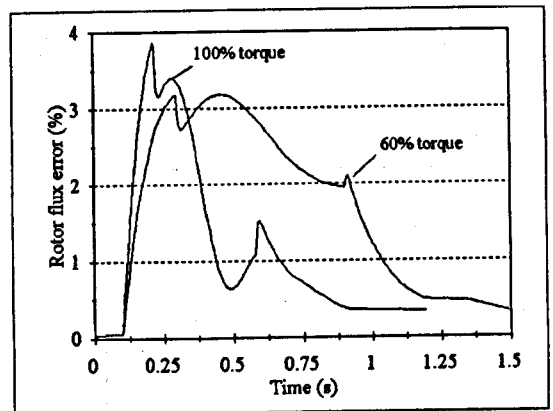
a. angular speed



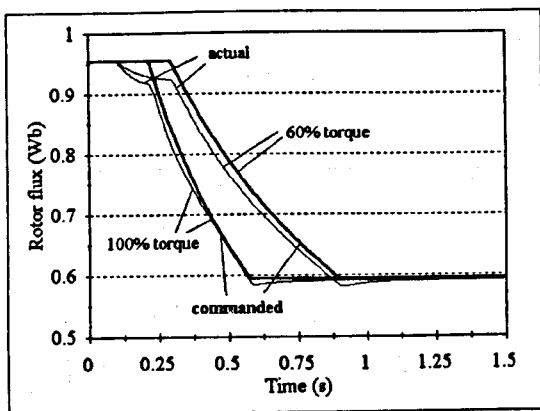
d. torque error



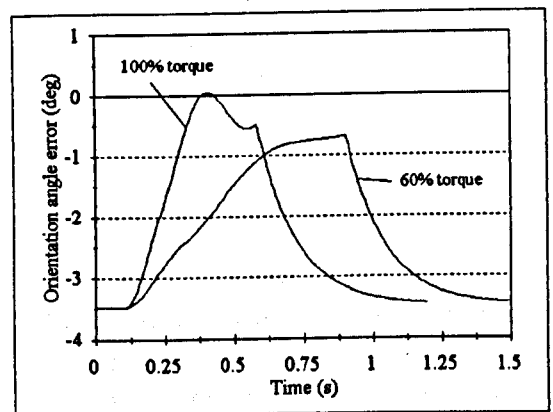
b. commanded and developed torque



e. rotor flux error



c. commanded and actual rotor flux



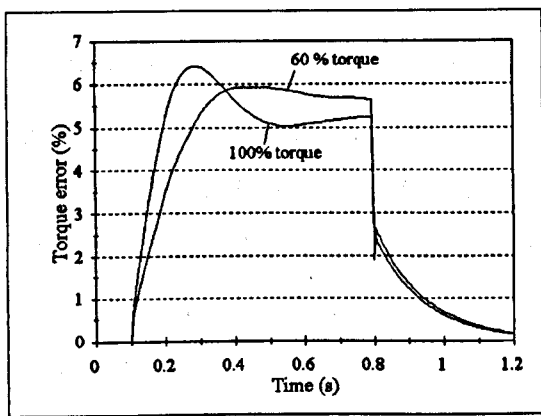
f. orientation angle error

Figure 4.27 : Transient detuning due to iron loss (R_{Fe} representation) for acceleration into the field-weakening region, speed mode of operation, 4 kW machine.

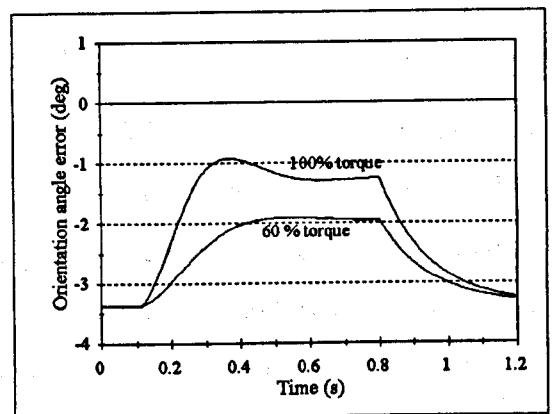
two ramps of the commanded speed that result in acceleration with 100% or 60% of the rated torque. The developed torque assumes value needed to achieve such an acceleration so that speed exactly follows the commanded speed. The commanded torque has a higher value in order to cover for iron loss, that is not recognised by the CPM-based estimator. Estimated flux follows the commanded flux, but the actual flux is smaller. Therefore errors in torque and rotor flux are positive.

4.6.3.4. Speed mode of operation, R_{ir} iron loss representation

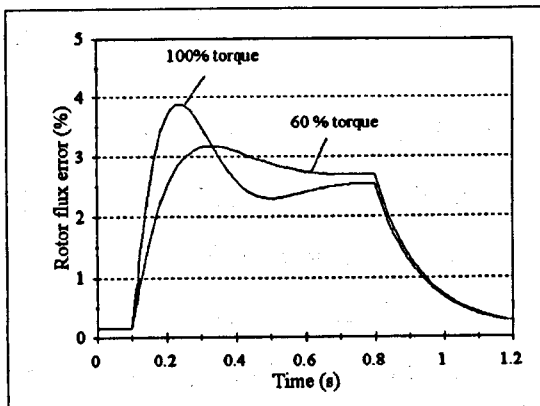
Simulation of the loading and unloading transients at the rated speed are repeated, but now utilising the reduced-order model with R_{ir} iron loss representation of sub-section 3.3.2.3. The results are shown in Fig. 4.28 [Sokola et al., 1996]. No significant changes exist between responses of Fig. 4.28 and Fig. 4.26. As expected, the torque error and the rotor flux error are slightly smaller (both peak values and values after settling) for both loads than for R_{Fe} iron loss representation. Responses of the orientation angle error are almost identical to the ones from Fig. 4.26.c.



a. torque error



c. orientation angle error



b. rotor flux error

Figure 4.28 : Transient detuning due to iron loss (R_{ir} representation) during loading and unloading at the rated speed, speed mode of operation, 4 kW machine.

This identity of responses in transient operation again confirms the hypothesis that R_{Fe} and R_{ir} representations of iron loss yield practically the same results. Therefore only R_{Fe} representation is used further on in the study of combined detuning effects of iron loss and main flux saturation.

4.6.4. Transient detuning due to both iron loss and main flux saturation, R_{Fe} iron loss representation

Transient detuning due to combined influence of iron loss and main flux saturation is analysed. The feedback vector control system again includes the CPM-based estimator. Induction machine is now represented by the $i_s - \psi_m - \psi_r$ reduced-order model with both iron loss and main flux saturation, presented in sub-section 3.4.4. Since the way of iron loss representation has negligible influence on simulation results, R_{Fe} iron loss representation, that yields simpler model, is analysed. Three transients are elaborated - acceleration from standstill to the rated speed in the torque mode of operation, loading and unloading at rated speed in the speed mode of operation and acceleration into the field weakening region. In all the cases simulations are done for two load torque levels.

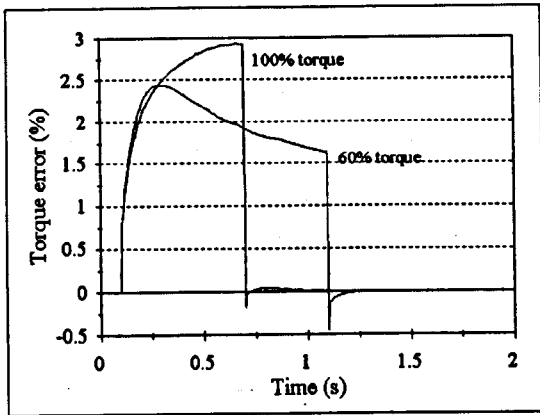
4.6.4.1. Torque mode of operation

The same acceleration transients as in sub-section 4.6.3.1. are simulated, but the main flux saturation is now included in the machine model. The responses are shown in Fig. 4.29. As predicted by steady-state analysis of detuning for such a case (Fig. 4.13), errors in torque and rotor flux are generally smaller than for the case without main flux saturation and errors for 100% torque command are bigger than for the 60% torque command. The shape of responses is also altered and errors do not rise in a linear manner with speed. Torque error for 60% torque command is higher at low speeds (beginning of the acceleration transient) than at higher speeds.

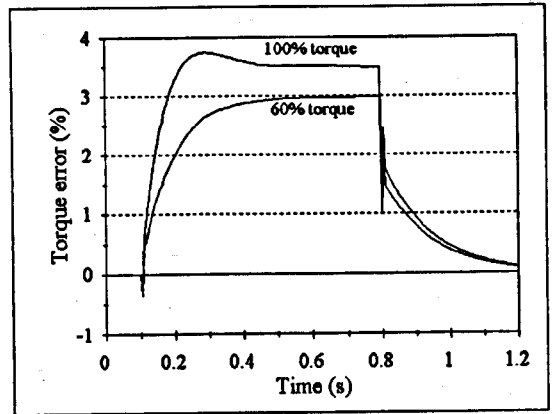
4.6.4.2. Speed mode of operation

Simulation of loading and unloading at rated speed is simulated again, with both iron loss and main flux saturation incorporated in the machine model. The responses are shown in Fig. 4.30. The shape of the responses remains quite similar to the ones obtained with main flux saturation neglected (Fig. 4.26) but values are different. Errors in torque and rotor flux are smaller while the orientation angle error is bigger.

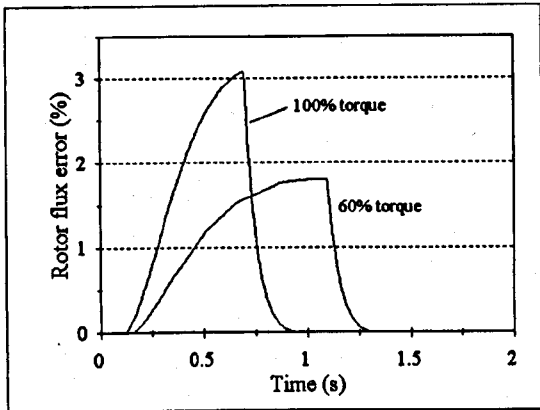
Responses are less oscillatory, especially for 60% torque. Values obtained after loading transient has settled are reversed - detuning at full load is now greater than at 60% load. This is in accordance with the steady-state characteristics of Fig. 4.13.



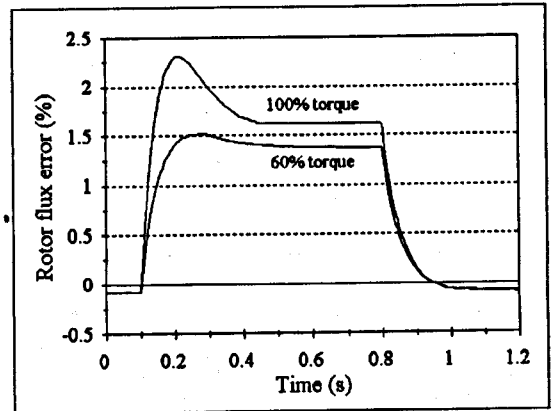
a. torque error



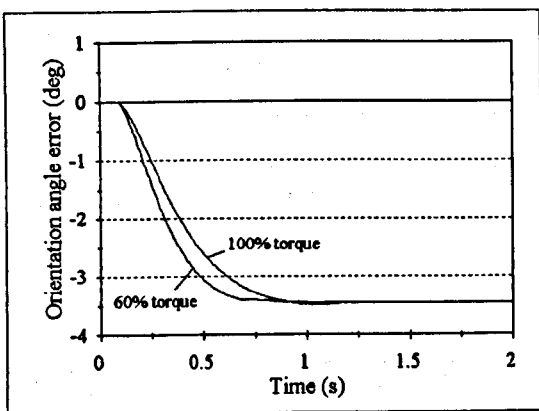
a. torque error



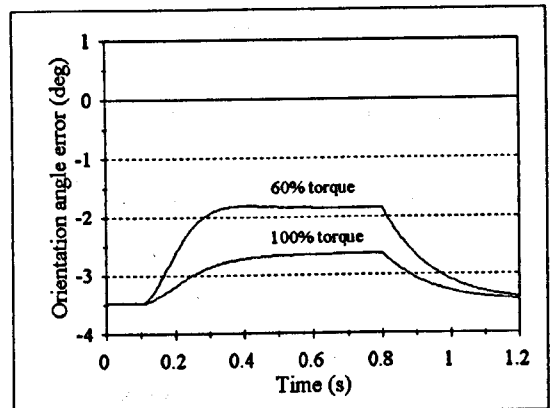
b. rotor flux error



b. rotor flux error



c. orientation angle error

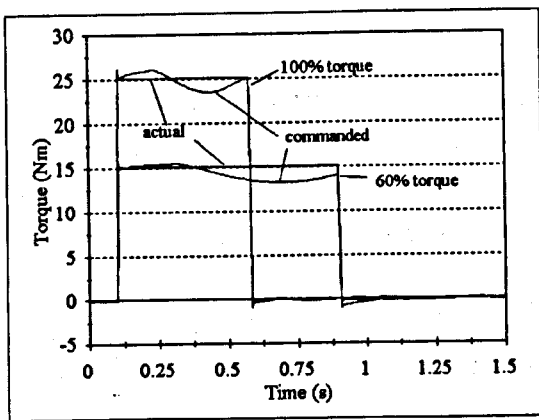


c. orientation angle error

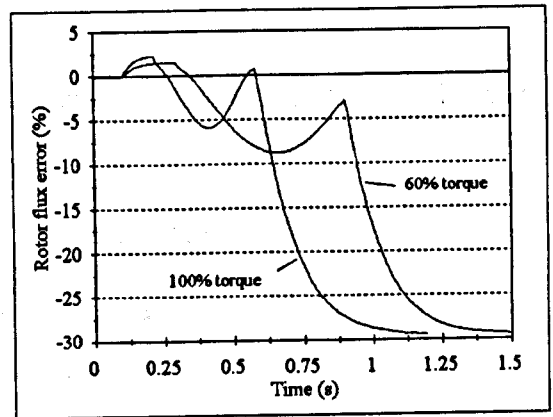
Figure 4.29 : Transient detuning due to combined influence of iron loss and main flux saturation during no-load acceleration, torque mode of operation, 4 kW machine.

Figure 4.30 : Transient detuning due to combined influence of iron loss and main flux saturation during loading and unloading at rated speed, speed mode of operation, 4 kW machine.

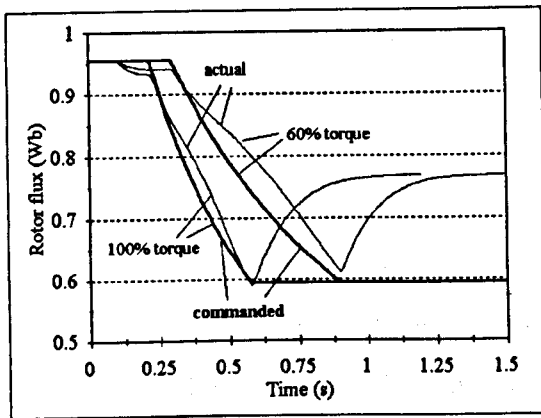
The final transient elaborated in conjunction with the CPM-based controllers is the acceleration into the field-weakening region. The responses, shown in Fig. 4.31, are a combination of responses obtained for analyses of detuning due to main flux saturation (Fig. 4.23) and of detuning due to iron loss only (Fig. 4.28). The responses of the commanded torque are oscillatory. The actual flux deviates from the commanded flux during acceleration and even more after the transient is finished, while the orientation angle error reaches almost 10 degrees.



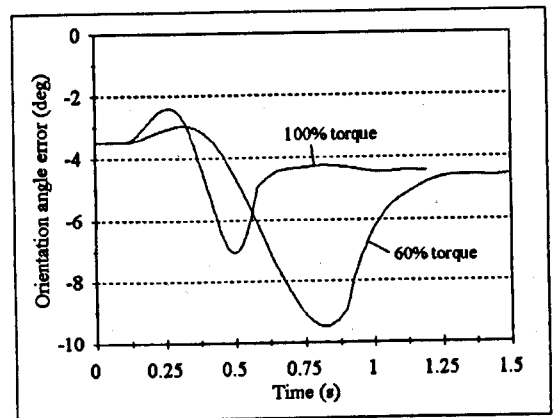
a. developed and commanded torque



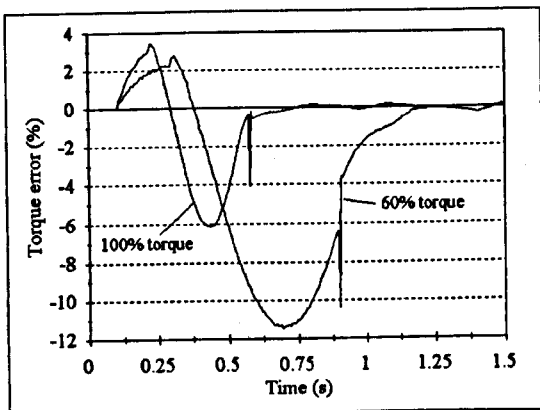
d. rotor flux error



b. commanded and actual rotor flux



e. orientation angle error



c. torque error

Figure 4.31 : Transient detuning due to combined influence of iron loss and main flux saturation during acceleration into the field-weakening region, speed mode of operation, 4 kW machine.

4.7. SUMMARY

Detailed analyses of detuning in the rotor-flux-oriented induction machine drives, when the CPM-based estimator is utilised, were performed. Quantitative analyses of steady-state detuning due to four different phenomena were presented. Expressions that describe detuning were derived for each of these phenomena. It was shown that two ways of iron loss representation, although described by different detuning expressions, resulted in almost identical detuning characteristics. Comparative analysis revealed the following :

- detuning due to rotor leakage inductance variations and uncertainties is much smaller than detuning triggered by other phenomena,
- detuning due to iron loss can become significant at light loads,
- variations and uncertainties in rotor resistance and mutual inductance cause significant detuning at medium and higher loads,
- in the field-weakening region, main flux saturation (variations in mutual inductance) plays major detuning role.

Several transients were simulated. It was shown that inaccurate knowledge of the rotor resistance can seriously endanger the proper orientation. It was also shown that main flux saturation had a major detuning role in the field-weakening region, while it is actually damping the detuning influence of iron loss in the base speed region. The fact that it does not matter which of the two iron loss representation is employed is confirmed to be true in transients as well.

5. COMPENSATION OF DETUNING USING IMPROVED VECTOR CONTROLLERS

5.1. INTRODUCTION

Detuning effects that occur due to main flux saturation and due to iron loss can be compensated by using improved vector controllers. The feedback type of improved RFO controllers incorporate the improved rotor flux estimators of Chapter 3. This type of compensation can be classified as an open-loop technique, since the influence of main flux saturation and/or iron loss is compensated on the basis of the measured signals and pre-determined non-linear functions that describe these two phenomena.

On the other hand, detuning due to temperature effects (i.e. thermally induced rotor resistance variations) is possible to be compensated only by some additional auxiliary circuit for R_r or T_r on-line identification. Since temperature effects are generally difficult to predict, the auxiliary circuit should be of closed-loop type. This will be elaborated in detail in chapter 6.

The two investigation approaches used in chapter 4 are used here again. Steady-state analyses in section 5.2 are performed on the basis of detuning expressions, which in turn are obtained by combining a steady-state machine model and a steady-state model of an improved estimator. Analyses of detuning in transient operation, presented in section 5.3, are performed by simulation of the whole improved vector-controlled drive.

5.2. DETUNING IN STEADY-STATE OPERATION USING IMPROVED CONTROLLERS

5.2.1 Analyses of steady-state detuning using improved vector controllers with main flux saturation

For analyses performed in this sub-section, any of the three improved estimators with main flux saturation (using different representations) can be utilised. The $L_m(\psi_m)$ representation, with improved model from sub-section 3.2.1 and improved estimator of Fig. 3.1, is elaborated in detail, but the results obtained are valid for the other two

representations of main flux saturation. In any steady state, the improved estimator with main flux saturation using $L_m(\psi_m)$ representation becomes:

$$\psi_r^e = \psi_r^* = \psi_{dm}^e = L_m^e i_{ds}^* , \quad (5.1)$$

$$\omega_{sl} = \omega_{sl}^* = \omega_{sl}^e = \frac{L_m^e i_{qs}^*}{T_r^e \psi_r^*} = \frac{2}{3P} \frac{R_r^*}{\psi_r^{*2}} T_e^* , \quad (5.2)$$

$$\psi_{qm}^e = \omega_{sl}^* T_{lr}^* \psi_r^* , \quad (5.3)$$

$$T_e^e = T_e^* = \frac{3}{2} P \frac{1}{L_{lr}^*} \psi_r^* \psi_{qm}^e , \quad (5.4)$$

$$\psi_m^e = \sqrt{\psi_{dm}^{e2} + \psi_{qm}^{e2}} , \quad (5.5)$$

$$L_m^e = f(\psi_m^e) . \quad (5.6)$$

As the improved estimator compensates for main flux saturation, it requires knowledge about non-linear function $L_m(\psi_m)$, which is obtained from no-load tests. Combining (5.1) and (5.2) the following relationship can be obtained :

$$i_{qs}^* = \omega_{sl}^* T_r^e i_{ds}^* . \quad (5.7)$$

Since the current-regulated PWM inverter is assumed to be ideal, the actual and the commanded values of the stator current components are equal :

$$i_{qs} = i_{qs}^* ; \quad i_{ds} = i_{ds}^* . \quad (4.10)$$

Steady-state detuning due to two phenomena is elaborated in the following sub-sections. They include rotor resistance variations and iron loss.

5.2.1.1. Steady-state detuning due to rotor resistance variations using improved estimator with main flux saturation

For this analysis, induction machine is represented by the $\underline{\psi}_m - \underline{\psi}_r$ reduced-order steady-state model with main flux saturation, in the $d^* - q^*$ reference frame determined by the RFO controller, presented in the sub-section 4.4.1. by (4.11)-(4.14). Following the same procedure as in 4.4.1, this model is now combined with the improved estimator steady-state model (5.1)-(5.7) and the following detuning expressions are obtained :

$$\Delta\varphi_r = \arctan \frac{\psi_{qr}}{\psi_{dr}} = \arctan \frac{\omega_{sl}^* (T_r^e - T_r^*)}{1 + \omega_{sl}^{*2} T_r^e T_r^*}, \quad (5.8)$$

$$\frac{\psi_r}{\psi_r^*} = \frac{L_m}{L_m^*} \sqrt{\frac{1 + \omega_{sl}^{*2} T_r^{e2}}{1 + \omega_{sl}^{*2} T_r^{*2}}}, \quad (5.9)$$

$$\frac{T_e}{T_e^*} = \frac{R_r^* \left(\frac{\psi_r}{\psi_r^*}\right)^2}{R_r \left(\frac{\psi_r^*}{\psi_r^*}\right)^2} = \frac{R_r^* \left(\frac{L_m}{L_m^*}\right)^2}{R_r \left(\frac{L_m^*}{L_m^*}\right)^2} \frac{1 + \omega_{sl}^{*2} T_r^{e2}}{1 + \omega_{sl}^{*2} T_r^{*2}}, \quad (5.10)$$

$$T_e^{*3} g^2 \frac{R_r^* \left(\frac{L_m}{L_m^*}\right)^2}{R_r \left(\frac{L_m^*}{L_m^*}\right)^2} T_r^{e2} - T_e^{*2} g^2 T_L T_r^2 + T_e^* \frac{R_r^* \left(\frac{L_m}{L_m^*}\right)^2}{R_r \left(\frac{L_m^*}{L_m^*}\right)^2} - T_L = 0, \quad (5.11)$$

where g is still :

$$g = \frac{2}{3P} \frac{R_r^*}{\psi_r^{*2}} = \frac{\omega_{sl}^*}{T_e^*}. \quad (4.20)$$

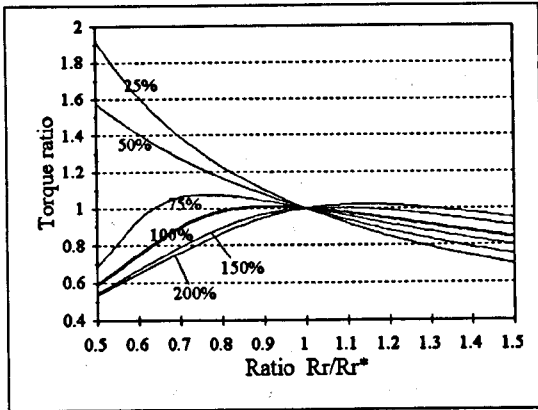
These detuning expressions are very similar to the detuning expressions obtained with the CPM-based estimator (4.15)-(4.20). The only difference is that in the CPM-based estimator the mutual inductance and the rotor time constant were assumed to be constant (L_m^* and T_r^*) while in the improved estimator their values are estimated on the basis of (5.6) and these estimates (L_m^e and T_r^e) are used for estimation of rotor flux, torque, slip angular speed and rotor flux position.

The results of the quantitative study of detuning due to rotor resistance variations, for the 4 kW machine, based on the above expressions, are shown in Figs. 5.1 and 5.2. When they are compared with detuning characteristics obtained with the CPM-based estimator (Figs. 4.3 and 4.4), it can be seen that inclusion of main flux saturation has no effect on operation in the base speed region, while it has a small influence in the field-weakening region. Indeed, the orientation angle error in the field-weakening (Fig. 5.2.c) is reduced if the ratio R_r/R_r^* is close to unity.

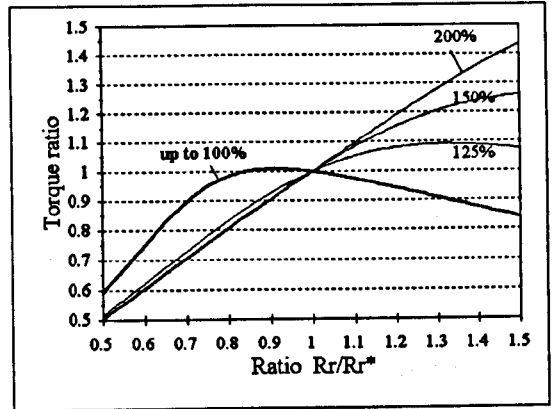
5.2.1.2. Steady-state detuning due to iron loss using improved estimator with main flux saturation

It was shown in sub-section 4.4.4.2 that main flux saturation actually reduces detuning due to iron loss in the base speed region. At the same time, main flux saturation has a

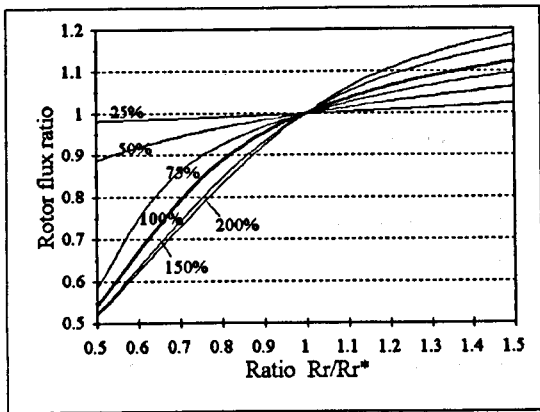
major detuning role in the field-weakening region (Fig. 4.14) especially at light loads. Main flux saturation is compensated by using the improved estimator of Fig. 3.1.



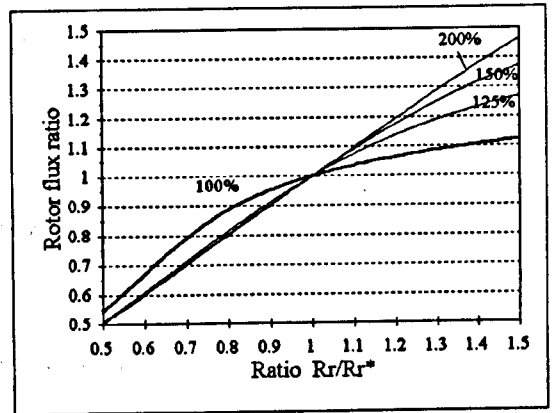
a. torque ratio



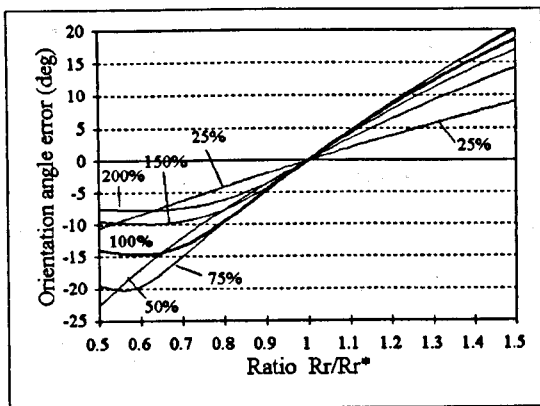
a. torque ratio



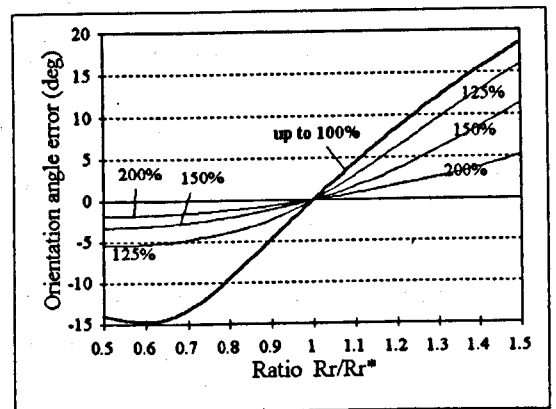
b. rotor flux ratio



b. rotor flux ratio



c. orientation angle error



c. orientation angle error

Figure 5.1 : Steady-state detuning due to R_r variations, improved estimator with main flux saturation, operation at the rated speed, load torque in % as parameter, 4 kW machine.

Figure 5.2 : Steady-state detuning due to R_r variations, improved estimator with main flux saturation, operation with the rated load torque, speed in % as parameter, 4 kW machine.

Steady-state machine model with both iron loss and main flux saturation from sub-section 4.4.4.2 is combined with the steady-state model of improved estimator (5.1)-(5.7), resulting in the following detuning expressions:

$$\Delta\varphi_r = \arctan \frac{\psi_{qr}}{\psi_{dr}} = \arctan \frac{-B + \omega_{sl}^* T_r^e A}{A + \omega_{sl}^* T_r^e B}, \quad (5.12)$$

$$\frac{\psi_r}{\psi_r^*} = \frac{L_m}{L_m^e} \sqrt{\frac{1 + \omega_{sl}^{*2} T_r^{e2}}{A^2 + B^2}}, \quad (5.13)$$

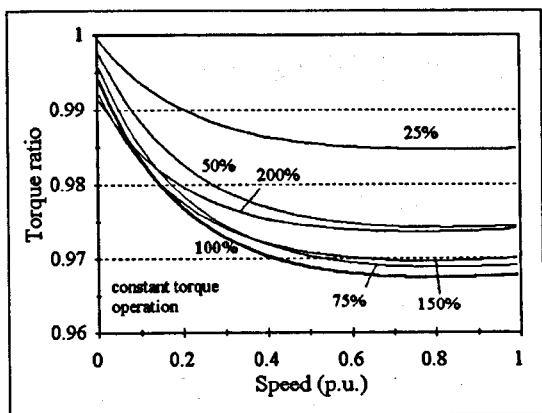
$$\frac{T_e}{T_e^*} = \left(\frac{\psi_r}{\psi_r^*} \right)^2 = \left(\frac{L_m}{L_m^e} \right)^2 \frac{1 + \omega_{sl}^{*2} T_r^{e2}}{A^2 + B^2}, \quad (5.14)$$

$$\begin{aligned} & T_e^{*4} g^4 T_L T_{Fe}^2 T_{lr}^2 + T_e^{*3} g^2 \left(2g T_L \omega T_{Fe}^2 T_{lr}^2 - T_r^{e2} \frac{L_m^2}{L_m^e{}^2} \right) + \\ & + T_e^{*2} g^2 T_L \left((T_r + T_{Fe})^2 + \omega^2 T_{Fe}^2 T_{lr}^2 - 2T_{Fe} T_{lr} \right) + \\ & + T_e^* \left(2g T_L \omega T_{Fe} (T_{Fe} + T_r - T_{lr}) - \frac{L_m^2}{L_m^e{}^2} \right) + T_L (1 + \omega^2 T_{Fe}^2) = 0 \end{aligned} \quad (5.15)$$

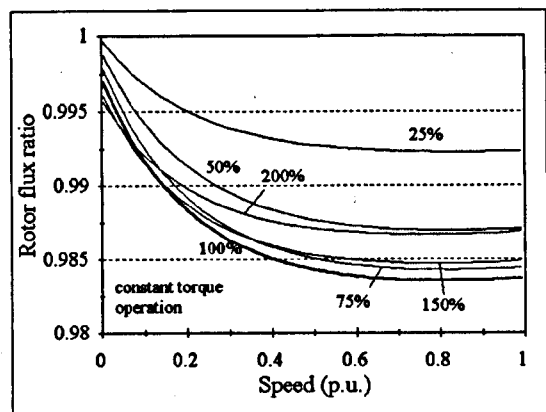
where A and B are defined by (4.25) and g is given with (4.20).

The above detuning expressions differ from those given in sub-section 4.4.4.2 in two details - instead of constant values for magnetising inductance and rotor time constant (L_m^* and T_r^* , respectively) the estimated values (L_m^e and T_r^e) are used.

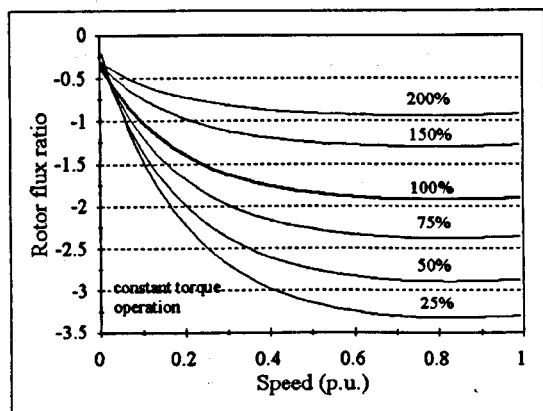
Steady-state detuning characteristics for this case are shown in Figs. 5.3. and 5.4 [Sokola and Levi, 1996], for operation in the base speed region and in a wide speed region, respectively. Comparison with Figs. 4.13 and 4.14 leads to the conclusion that the improved estimator with main flux saturation greatly reduces detuning in the field weakening region (note that scales in Fig. 5.4 differ from scales in Fig. 4.14) and confirms that at speeds above rated the influence of main flux saturation is much greater than the influence of iron loss.



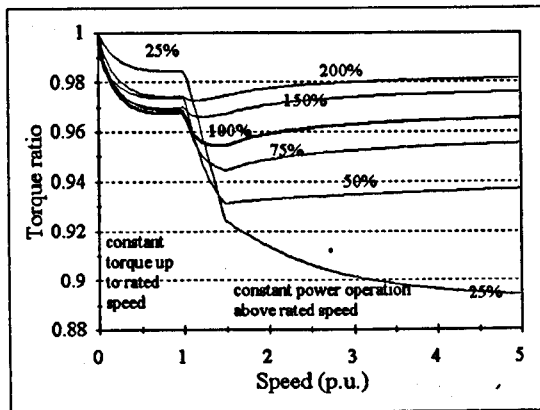
a. torque ratio



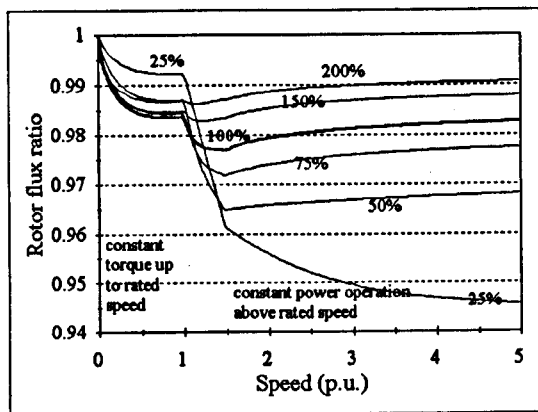
b. rotor flux ratio



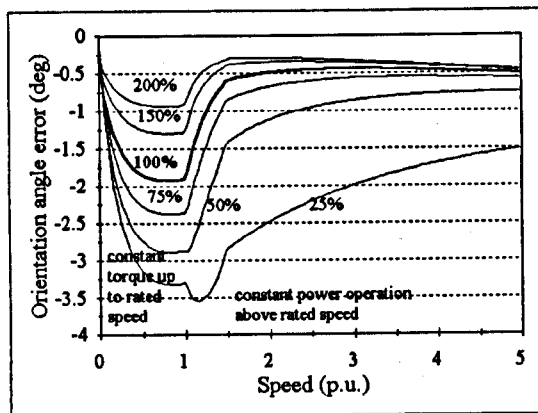
c. orientation angle error



a. torque ratio



b. rotor flux ratio



c. orientation angle error

Figure 5.3 : Steady-state detuning due to iron loss, R_{Fe} representation, improved estimator with main flux saturation, operation in the base speed region, load torque in % as parameter, 4 kW machine.

Figure 5.4 : Steady-state detuning due to iron loss, R_{Fe} representation, improved estimator with main flux saturation, operation in a wide speed region, load torque and output power in % as parameters, 4 kW machine.

5.2.2. Analyses of steady-state detuning using improved vector controllers with iron loss only

For these analyses, improved vector controllers that incorporate either of the two estimators presented in sub-section 3.3.4. (full, Fig. 3.3. or simplified, Fig 3.4) can be used, since their performance in steady-state operation is identical. Both estimators are in steady-states described by the following equations :

$$\psi_r^e = \psi_r^* = \psi_{dm}^e = L_m^* i_{ds}^* + \omega_r^* T_{Fe}^e \psi_{qm}^e , \quad (5.16)$$

$$\omega_{sl} = \omega_{sl}^* = \omega_{sl}^e = \frac{L_m^* i_{qs}^*}{T_r^* \psi_r^*} = \frac{2}{3P} \frac{R_r^*}{\psi_r^{*2}} T_e^* , \quad (5.17)$$

$$\psi_{qm}^e = \omega_{sl}^* T_{lr}^* \psi_r^* , \quad (5.3)$$

$$T_e^e = T_e^* = \frac{3}{2} P \frac{1}{L_{lr}^*} \psi_r^* \psi_{qm}^e , \quad (5.4)$$

where :

$$T_{Fe}^e = \frac{L_m^*}{R_{Fe}^e} ; \quad R_{Fe}^e = f(\omega_r^e) . \quad (5.18)$$

As the improved estimators compensate for iron loss, they require knowledge about non-linear function $R_{Fe}(\omega_r)$. Combining (5.16) and (5.17), the following relationships can be obtained :

$$i_{ds}^* = A^e \frac{\psi_r^*}{L_m^*} , \quad (5.19)$$

$$i_{qs}^* = B^e \frac{\psi_r^*}{L_m^*} , \quad (5.20)$$

where :

$$A^e = 1 - \omega_r^* \omega_{sl}^* T_{Fe}^e T_{lr}^* \quad \text{and} \quad B^e = \omega_{sl}^* T_r^* + \omega_r^* T_{Fe}^e . \quad (5.21)$$

The current-regulated PWM inverter is assumed to be ideal, so that the actual and the commanded values of the stator current components are equal :

$$i_{qs} = i_{qs}^* ; \quad i_{ds} = i_{ds}^* . \quad (4.10)$$

5.2.2.1. Steady-state detuning due to main flux saturation using improved estimator with iron loss

In order to derive expressions for detuning due to main flux saturation, the above steady-state model of improved estimator with iron loss is combined with the steady-state reduced-order model with both iron loss and main flux saturation, given in subsection 4.4.4.2. The resulting detuning expressions are :

$$\Delta\varphi_r = \arctan \frac{\psi_{qr}}{\psi_{dr}} = \arctan \frac{AB^e - A^e B}{AA^e + BB^e} \quad (5.22)$$

$$\frac{\psi_r}{\psi_r^*} = \frac{L_m}{L_m^e} \sqrt{\frac{A^{e2} + B^{e2}}{A^2 + B^2}} \quad (5.23)$$

$$\frac{T_e}{T_e^*} = \left(\frac{\psi_r}{\psi_r^*} \right)^2 = \left(\frac{L_m}{L_m^e} \right)^2 \frac{A^{e2} + B^{e2}}{A^2 + B^2} \quad (5.24)$$

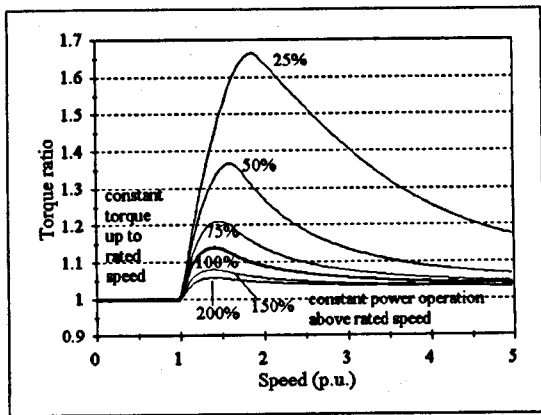
where A^e and B^e are defined by (5.21).

In the speed mode of operation, the additional detuning equation for commanded torque is now of the fifth order :

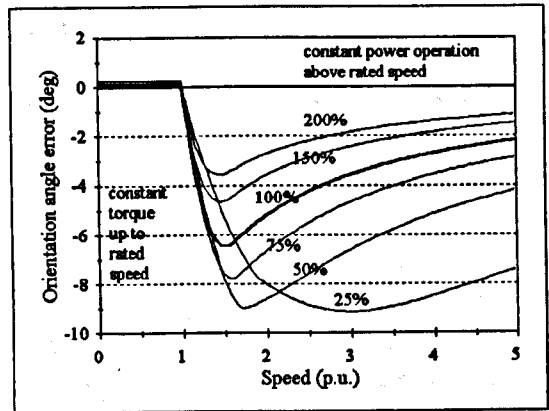
$$\begin{aligned} & -T_e^{*5} g^4 T_{Fe}^2 T_{lr}^2 \frac{L_m^2}{L_m^{*2}} + T_e^{*4} \left[g^4 T_L T_{Fe}^2 T_{lr}^2 - 2g^3 \frac{L_m^2}{L_m^{*2}} \omega T_{Fe}^2 T_{lr}^2 \right] + \\ & + T_e^{*3} \left[2g^3 T_L \omega T_{Fe}^2 T_{lr}^2 - g^2 \frac{L_m^2}{L_m^{*2}} \left((T_r^* + T_{Fe}^e)^2 + \omega^2 T_{Fe}^2 T_{lr}^2 - 2T_{Fe}^e T_{lr} \right) \right] + \\ & + T_e^{*2} \left[g^2 T_L \left((T_r + T_{Fe}^e)^2 + \omega^2 T_{Fe}^2 T_{lr}^2 - 2T_{Fe}^e T_{lr} \right) - g \frac{L_m^2}{L_m^{*2}} 2\omega T_{Fe}^e (T_{Fe}^e + T_r^* - T_{lr}) \right] + \\ & + T_e^* \left[2g T_L \omega T_{Fe} (T_{Fe}^e + T_r - T_{lr}) - \frac{L_m^2}{L_m^{*2}} (1 + \omega^2 T_{Fe}^2) \right] + T_L (1 + \omega^2 T_{Fe}^2) = 0 \end{aligned} \quad (5.25)$$

where g is given with (4.20).

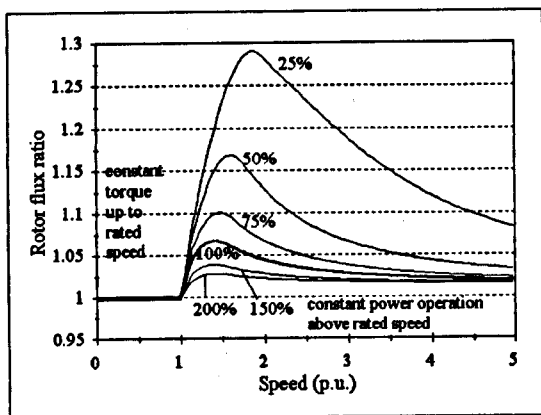
Detuning characteristics for such a case are shown in Fig. 5.5. Utilisation of the improved estimator with iron loss enables compensation of detuning in the base speed region only. Because main flux saturation is not compensated, it still has a major detuning influence in the field-weakening region, in which characteristics are similar to the ones from Fig. 4.14, with just slightly different values.



a. torque ratio



c. orientation angle error



b. rotor flux ratio

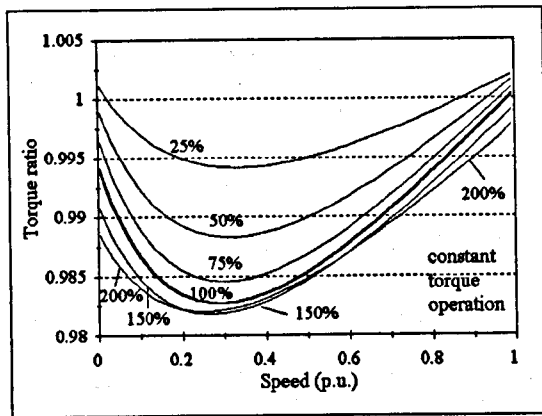
Figure 5.5 : Steady-state detuning due to main flux saturation, improved estimator with iron loss compensation, operation in a wide speed region, load torque in % and output power in % as parameters, 4 kW machine.

5.2.2.2. Steady-state detuning in the base speed region due to main flux saturation using improved estimator with iron loss with constant R_{Fe} value

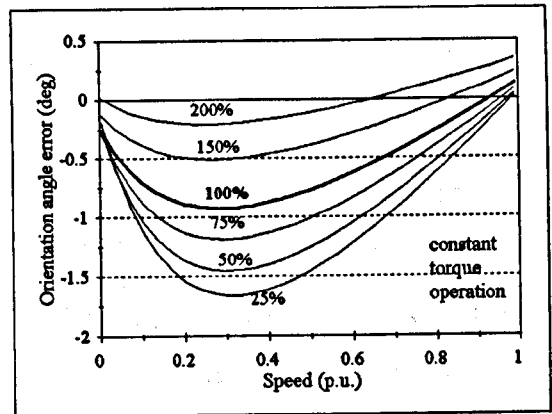
In order to further simplify the estimator and to reduce the number of calculations needed for real-time execution of the estimation process, it is possible to use a constant value of the equivalent iron loss resistance instead of a look-up table describing non-linear relationship $R_{Fe}(\omega_r)$. Results of the previous sub-section have indicated that only detuning in the base speed region can be reduced with improved estimator with iron loss only and the idea here is to investigate operation with the simplest form of the improved estimator. The same detuning expression (5.21)-(5.24) can be used, but the values of R_{Fe}^e and T_{Fe}^e are now considered to be constant.

Detuning characteristics shown in Fig. 5.6 are obtained utilising improved estimator in which iron loss is represented by a constant value of R_{Fe} that corresponds to operation at rated speed and rated flux. It can be seen that this estimator does not provide full compensation even in the base speed region. Nevertheless, partial compensation is

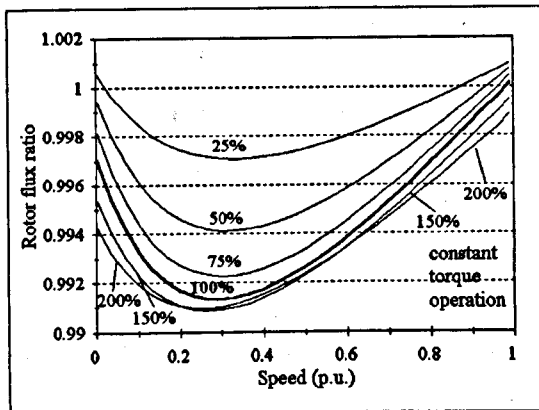
achieved, as detuning of Fig. 5.6. is smaller than detuning with the CPM-based estimator (Fig. 4.13). This is especially true for operation at speeds closer to the rated speed.



a. torque ratio



c. orientation angle error



b. rotor flux ratio

Figure 5.6 : Steady-state detuning due to main flux saturation, improved estimator with iron loss represented by a constant value of R_{Fe} , operation in the base speed region, load torque in % as parameter, 4 kW machine.

5.2.3. Analyses of steady-state detuning using improved vector controllers with both iron loss and main flux saturation

This section investigates steady-state detuning obtained when improved estimators of Figs. 3.6-3.9 are employed. The procedure for derivation of detuning expressions is the same as the one described in 5.2.2, with a difference that estimated values of the mutual inductance and the rotor time constant (L_m^e and T_r^e) are used instead of constant values (L_m^* and T_r^*) in equations (5.16)-(5.25). Three cases are been elaborated - the case when both equivalent iron loss resistance and mutual inductance are correctly estimated, the case when the iron loss resistance is inaccurately estimated and the case when the mutual inductance is inaccurately estimated.

5.2.3.1. Steady state detuning using improved estimator with both iron loss and main flux saturation, R_{Fe} and L_m correctly estimated

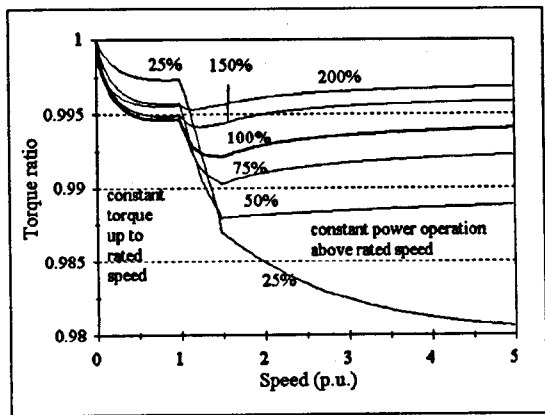
Detuning characteristics with improved estimator with both iron loss and main flux saturation when the value of R_{Fe} is correctly estimated are not shown. The torque ratio and the rotor flux ratio are always equal to unity, while the orientation angle errors are zero, showing that full compensation is achieved.

5.2.3.2. Steady state detuning using improved estimator with both iron loss and main flux saturation, R_{Fe} incorrectly estimated

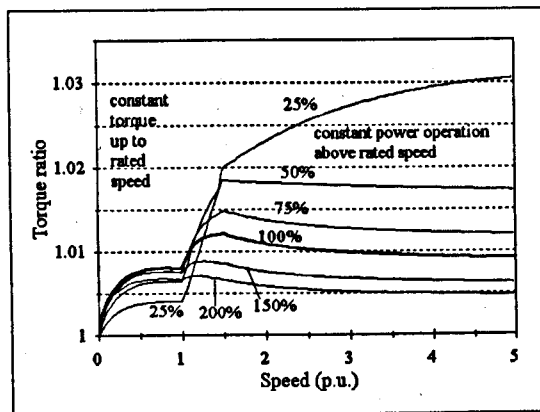
Accurate identification of the equivalent iron loss resistance is not an easy task and some errors during commissioning procedure might occur. Hence the performance of the drive for the case when the non-linear function $R_{Fe}(\omega_r)$, used in the improved estimator, is incorrectly estimated, is investigated. Improved estimator with both iron loss and main flux saturation is analysed. Detuning characteristics when the non-linear function $R_{Fe}(\omega_r)$ is estimated with errors of +20% and -20% are shown in Figs. 5.7 and 5.8, respectively. It can be seen that detuning is quite small, especially in the base speed region. Torque errors amount to several percent, errors in the rotor flux are up to 1.5%, while the orientation angle deviates for less than one degree. It can be concluded that moderate uncertainties in R_{Fe} estimation have very small impact on the compensation capabilities of the improved estimator in steady states.

5.2.3.3. Steady state detuning using improved estimator with both iron loss and main flux saturation, L_m incorrectly estimated

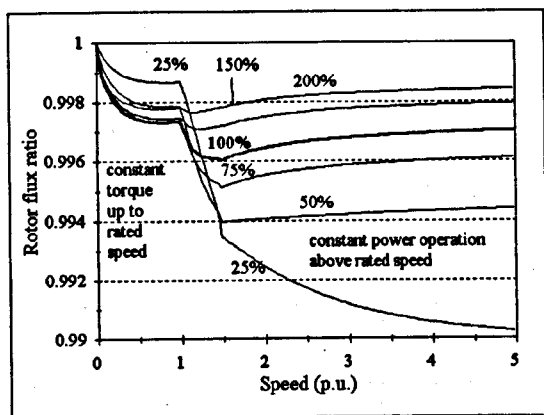
Identification of the magnetising curve and non-linear function $L_m(\psi_m)$ can also be performed with some uncertainties. Detuning characteristics for the 4 kW machine when the non-linear function $L_m(\psi_m)$ is estimated with errors of +20% and -20% are shown in Figs. 5.9 and 5.10, respectively. They reveal that under-estimation of L_m (Fig. 5.10) leads to increased rotor flux and more pronounced saturation, while over-estimation of L_m (Fig. 5.9) reduces the rotor flux. Under-estimation of L_m results in bigger detuning than over-estimation of L_m . It can be concluded that accurate determination of the magnetising curve is more significant than accurate determination of iron loss.



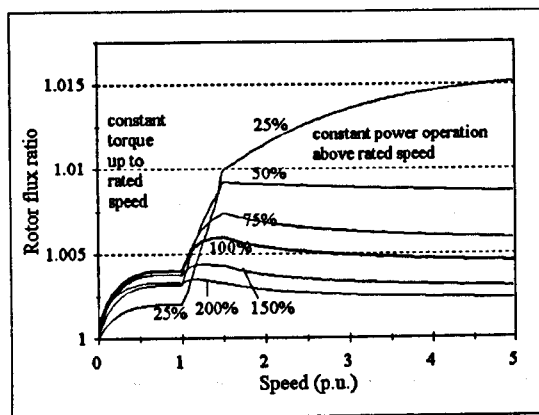
a. torque ratio



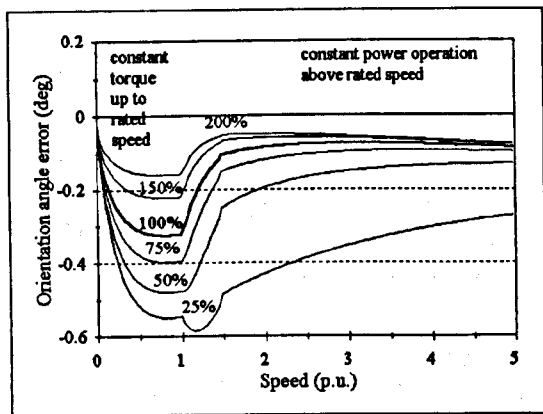
a. torque ratio



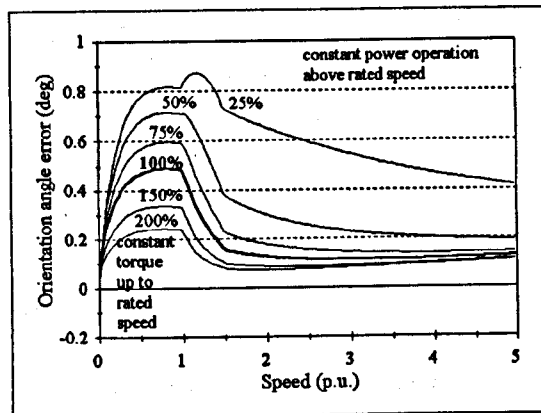
b. rotor flux ratio



b. rotor flux ratio



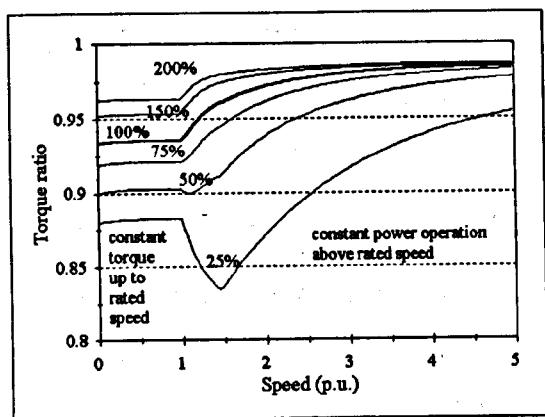
c. orientation angle error



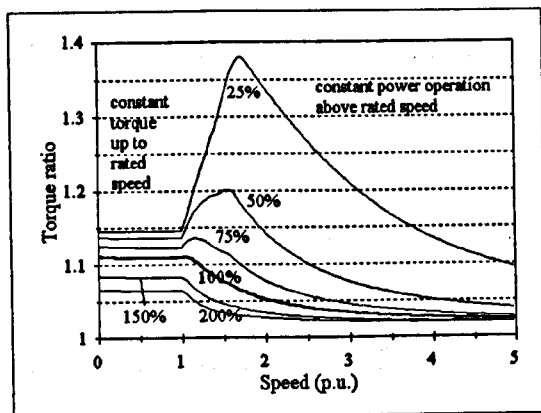
c. orientation angle error

Figure 5.7 : Steady-state detuning with improved estimator with both iron loss and main flux saturation, estimated $R_{Fe}(\omega_r)$ 20% greater than actual, operation in a wide speed region, load torque and output power in % as parameters, 4 kW machine.

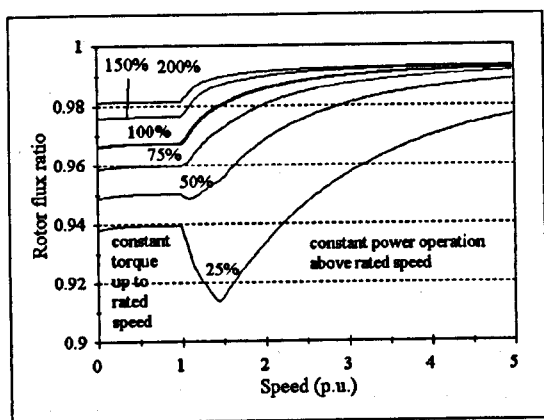
Figure 5.8 : Steady-state detuning with improved estimator with both iron loss and main flux saturation, estimated $R_{Fe}(\omega_r)$ 20% smaller than actual, operation in a wide speed region, load torque and output power in % as parameters, 4 kW machine.



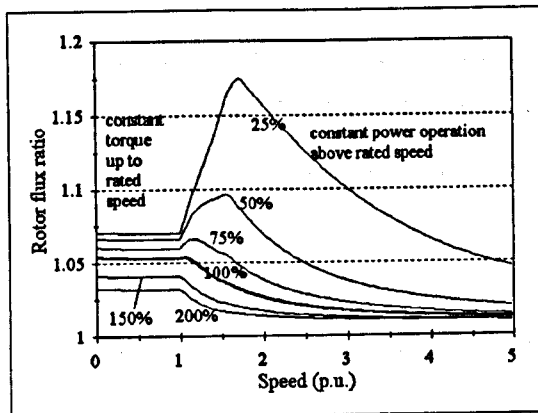
a. torque ratio



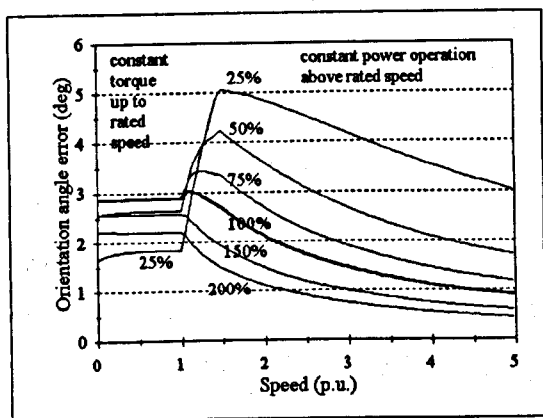
a. torque ratio



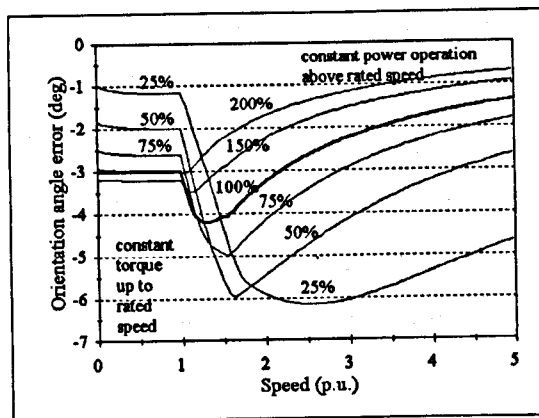
b. rotor flux ratio



b. rotor flux ratio



c. orientation angle error



c. orientation angle error

Figure 5.9 : Steady-state detuning with improved estimator with iron loss and main flux saturation, estimated $L_m(\psi_m)$ 20% greater than actual, operation in a wide speed region, load torque and output power in % as parameters, 4 kW machine.

Figure 5.10 : Steady-state detuning with improved estimator with iron loss and main flux saturation, estimated $L_m(\psi_m)$ 20% smaller than actual, operation in a wide speed region, load torque and output power in % as parameters, 4 kW machine.

5.3. DETUNING IN TRANSIENT OPERATION USING IMPROVED VECTOR CONTROLLERS

5.3.1. Transient detuning using estimators with main flux saturation

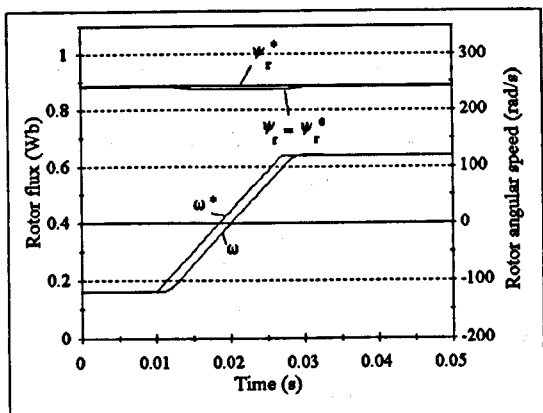
Transient operation of the drive that utilises improved estimator with main flux saturation will be investigated in this sub-section. The first group of simulations incorporates analyses of transient performance of different improved estimators with various representations of main flux saturation. For this purpose, only saturation is included in the machine model, while iron loss is neglected. The analysed transients are reversing in the base speed region and acceleration into field-weakening. The second group of simulations involves only improved estimator with $L_m(\psi_m)$ representation, but now both main flux saturation and iron loss are included in the machine model. The analysed transients are acceleration within the base speed region in the torque mode of operation, loading and unloading at the rated speed in the speed mode of operation and acceleration into the field-weakening region in the speed mode of operation.

5.3.1.1. Transient detuning due to main flux saturation using improved estimators with main flux saturation

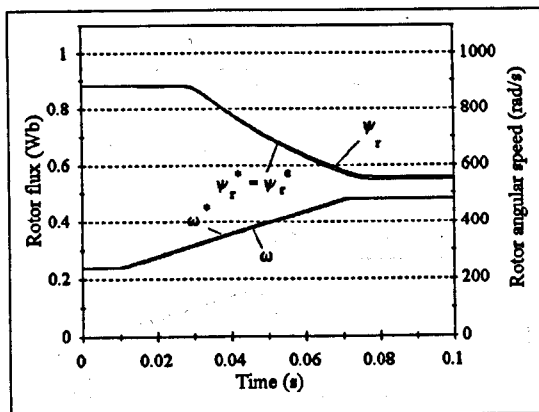
Since improved estimators of Figs. 2.9, 3.1 and 3.2 are derived using the same model as the starting point, it is expected that they will behave in an identical manner. This hypothesis is confirmed by simulations in this sub-section. The three improved estimators are employed for simulations of reversing in the base speed region and of acceleration into the field-weakening region.

The responses of the 0.75 kW machine are shown in Figures 5.11-5.12 [Levi, 1994a] for the improved estimator with $i_m(\psi_m)$ representation and in Figures 5.13-5.14 [Levi and Sokola, 1997] for the improved estimator with $L_r(\Psi)$ representation. Responses to the same transients obtained employing the improved estimator with $L_m(\psi_m)$ representation are identical and therefore not repeated. Responses of Figs. 5.11-5.14 reveal that improved estimators yield practically identical response and that detuning influence of main flux saturation is fully compensated, as shown in [Levi, 1994a; Levi and Sokola, 1997]. During reversing (Figs. 5.11 and 5.13), reductions in the mutual inductance and in the rotor flux are recognised and the control system reacts by increasing the stator d -

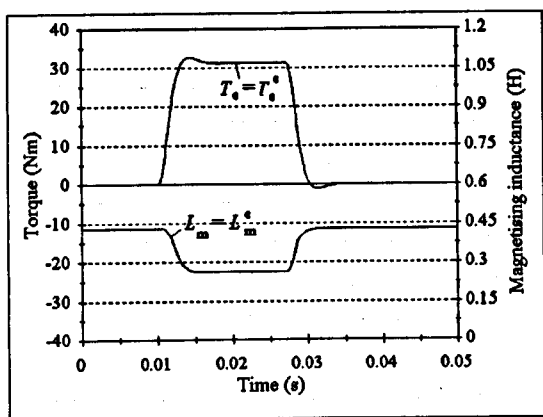
axis current command. During acceleration into the field-weakening region (Figs. 5.12 and 5.14), the control system significantly reduces the stator d -axis current command in



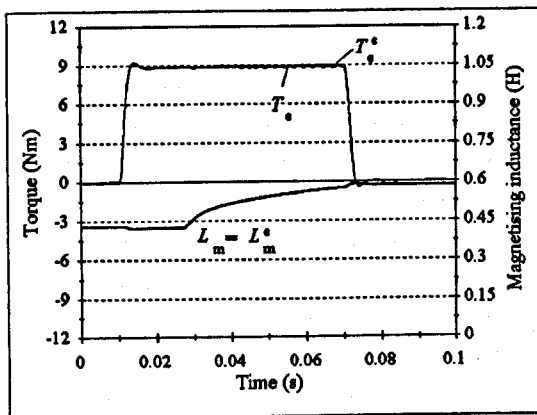
a. angular speed and rotor flux



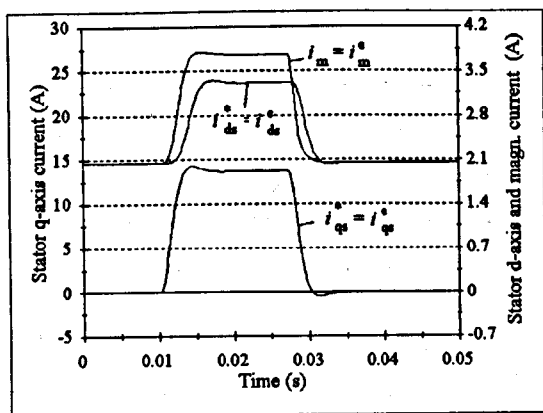
a. angular speed and rotor flux



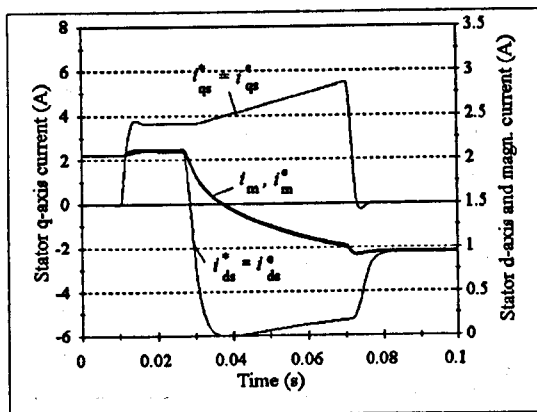
b. torque and mutual inductance



b. torque and mutual inductance



c. currents

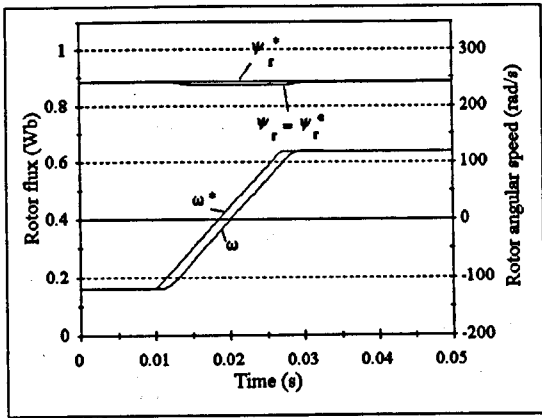


c. currents

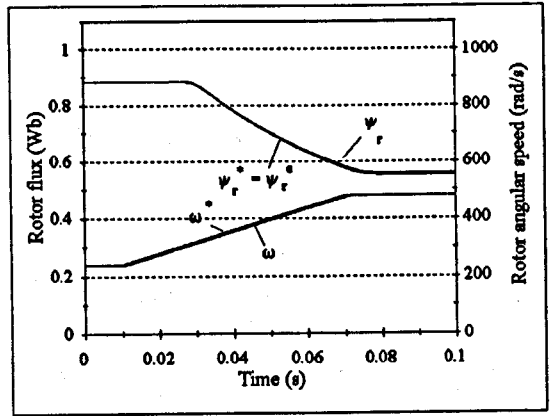
Figure 5.11 : Transient responses during fast reversing without load, improved estimator with $i_m(\psi_m)$ representation, 0.75 kW machine.

Figure 5.12 : Transient responses during no-load acceleration into the field-weakening region, improved estimator with $i_m(\psi_m)$ representation, 0.75 kW machine.

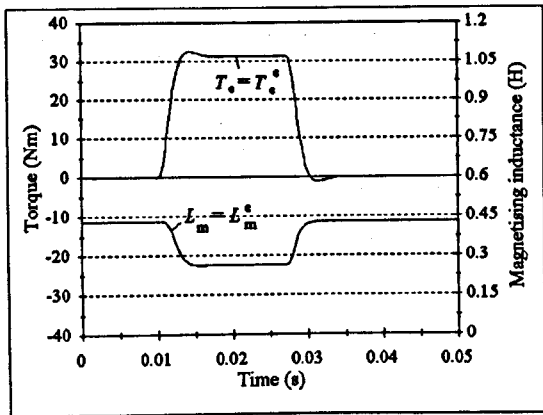
order to bring down the rotor flux to the commanded level. After the acceleration is finished, the stator d -axis current command is returned to the appropriate steady-state value.



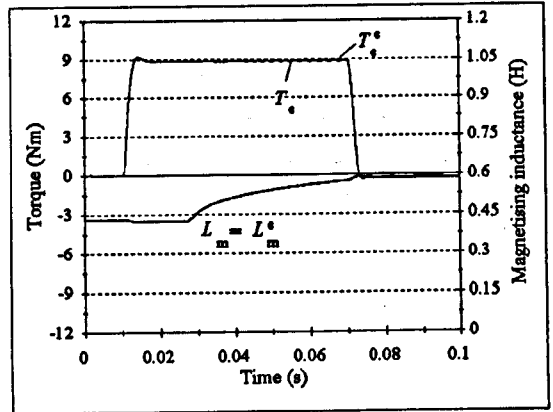
a. angular speed and rotor flux



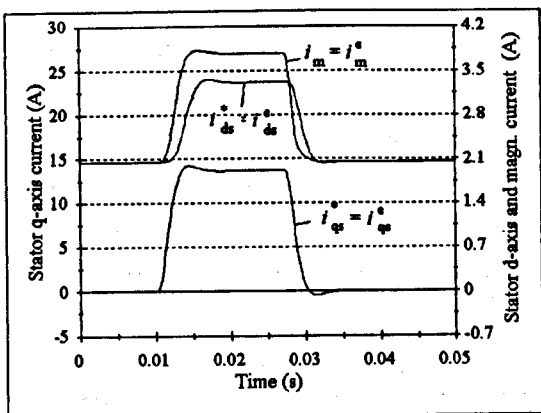
a. angular speed and rotor flux



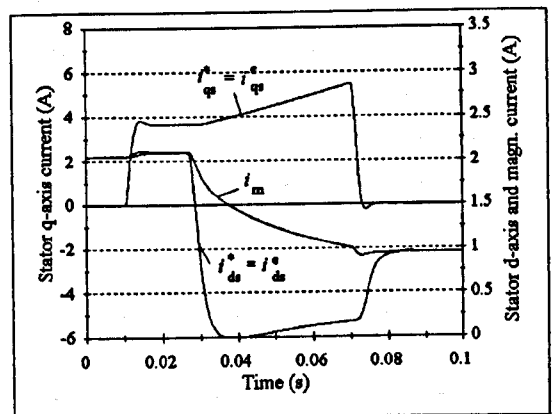
b. torque and mutual inductance



b. torque and mutual inductance



c. currents

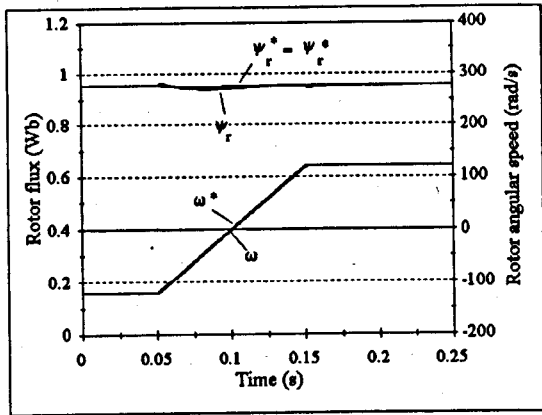


c. currents

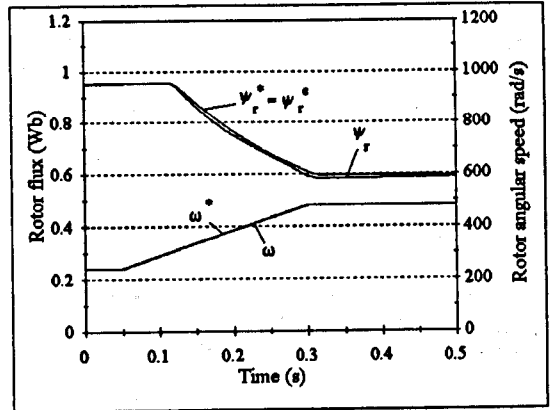
Figure 5.13 : Transient responses during fast reversing without load, improved estimator with L_r (Ψ) representation, 0.75 kW machine.

Figure 5.14 : Transient responses during no-load acceleration into the field-weakening region, improved estimator with L_r (Ψ) representation, 0.75 kW machine.

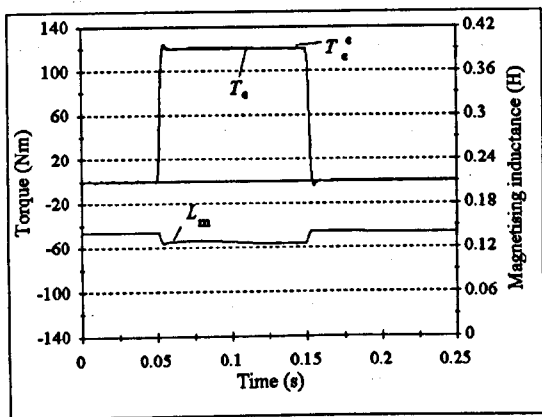
The same simulation studies are repeated for the 4 kW machine, with results shown in Figs. 5.15-5.16 for the improved estimator with $i_m (\psi_m)$ representation. Responses exhibit the same trends as in the case with the 0.75 kW machine. Responses obtained with the other two representations of main flux saturation are identical.



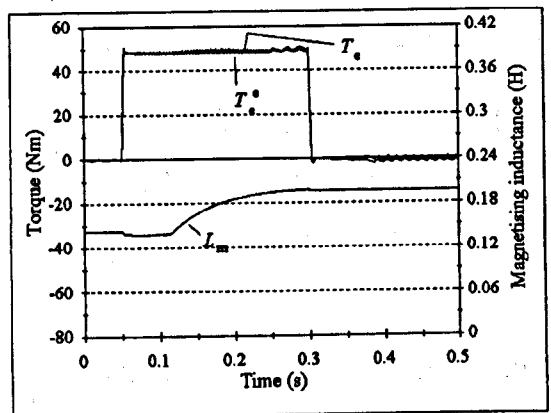
a. angular speed and rotor flux



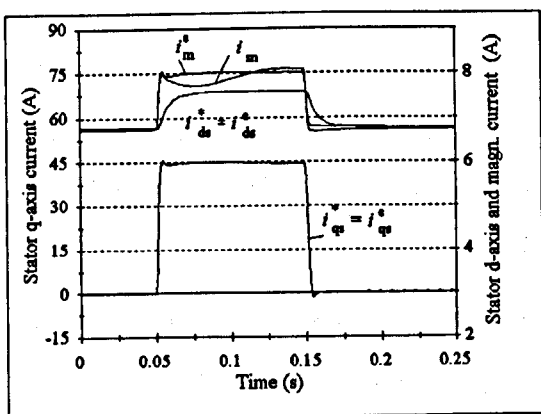
a. angular speed and rotor flux



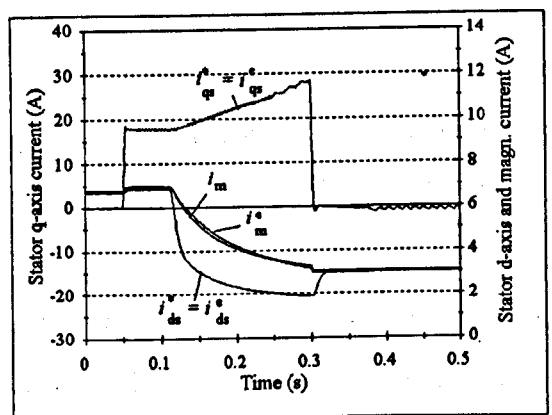
b. torque and mutual inductance



b. torque and mutual inductance



c. currents



c. currents

Figure 5.15 : Transient responses during fast reversing without load, improved estimator with $i_m (\psi_m)$ representation, 4 kW machine.

Figure 5.16 : Transient responses during no-load acceleration into the field-weakening region, improved estimator with $i_m (\psi_m)$ representation, 4 kW machine.

5.3.1.2. Transient detuning due to iron loss using estimators with main flux saturation

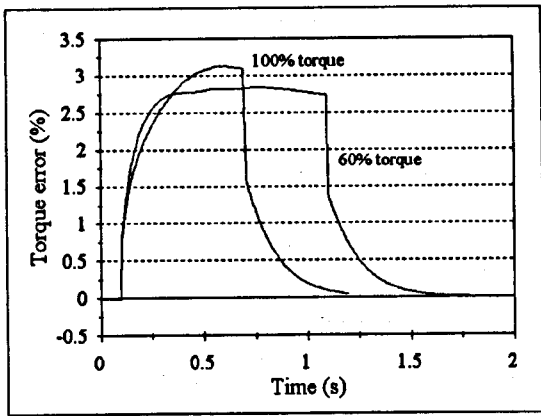
This sub-section presents an analysis of transient detuning due to combined influence of main flux saturation and iron loss, when the improved estimator with main flux saturation only is employed. Therefore the machine model includes both iron loss and main flux saturation, while the estimator incorporates main flux saturation only. The first simulated transient is no-load acceleration in the base speed region, with control system operating in the torque mode (speed control loop open). Torque commands of 100% and 60% are analysed and responses are shown in Fig. 5.17. Speed responses are practically identical to the ones from Fig. 4.24.a and therefore not repeated. Torque error during the transient with 100% torque command is similar to the case of CPM-based estimator (Fig. 4.29.a). The torque error for 60% torque command is smaller at low speeds and greater at higher speed than the one obtained with the CPM-based estimator. Errors in the rotor flux amplitude and in the orientation angle are reduced.

The second simulation represents sudden application and sudden removal of the load while the machine operates at the rated speed. The speed control loop is closed. The responses are shown in Fig. 5.18. They are very similar to the ones obtained with the CPM-based estimator, shown in Fig. 4.30.

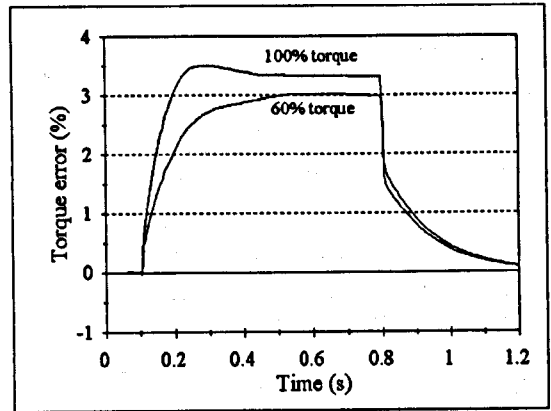
The results of Figs. 5.17 and 5.18, as well as steady-state results of Fig. 5.3, suggest that compensation of main flux saturation cannot yield a significant improvement as far as operation in the base speed region is concerned. One of the reasons for such a behaviour is that the commanded flux is kept at rated value and cross-saturation is not pronounced for considered loads, so that the influence of the main flux saturation is generally small. On the other hand, the other source of detuning (iron loss), being ignored in these improved estimators, remains uncompensated.

Acceleration into the field-weakening region, transient equivalent to the one analysed in sub-section 4.6.4.2. is simulated next, with speed control loop closed. The responses are shown in Fig. 5.19 [Sokola and Levi, 1996]. When responses are compared with the ones obtained with the CPM-based estimator (Fig. 4.31), it can be seen that detuning in the field-weakening region is significantly reduced by using the improved estimator with main flux saturation. Errors in the torque and in the orientation angle are slightly smaller, while deviations of rotor flux from commanded are significantly reduced.

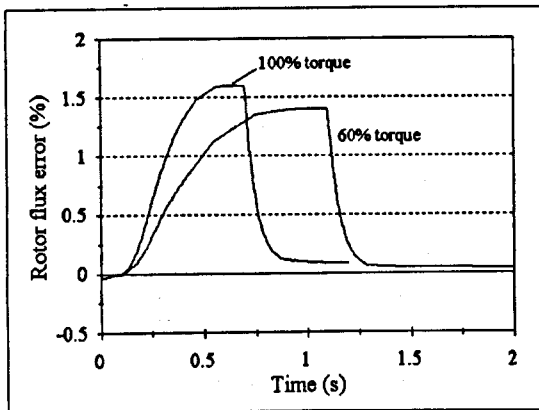
Additionally, responses of commanded torque are less oscillatory. It can be concluded that utilisation of the improved estimator with main flux saturation results in much better performance of the drive in the field-weakening region.



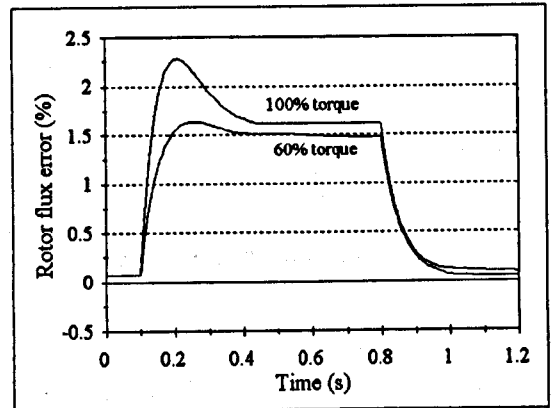
a. torque error



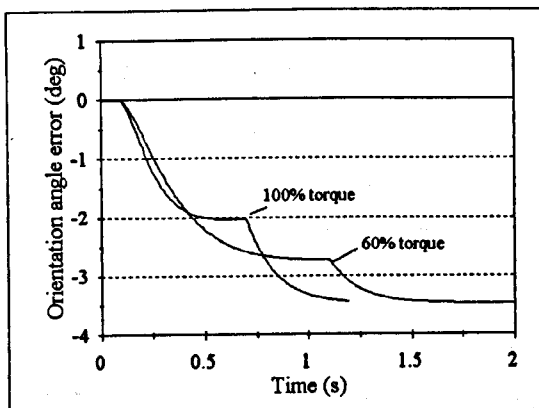
a. torque error



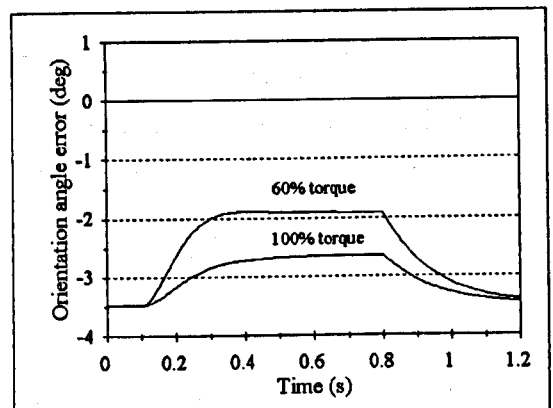
b. rotor flux error



b. rotor flux error



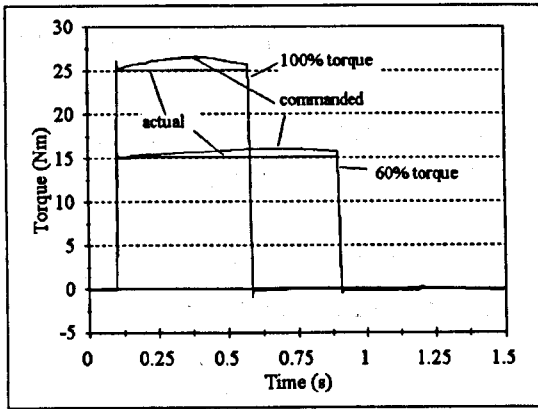
c. orientation angle error



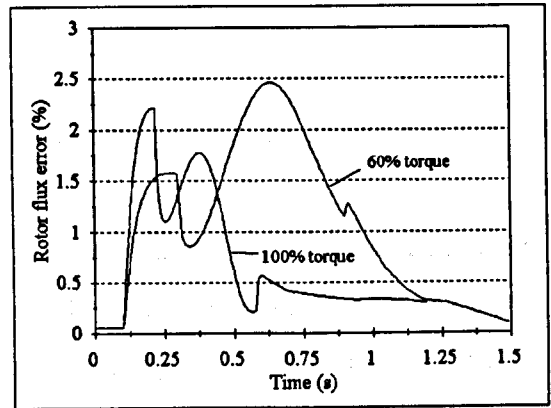
c. orientation angle error

Figure 5.17 : Transient detuning due to combined influence of iron loss and main flux saturation during no-load acceleration, torque mode of operation, improved estimator with main flux saturation, 4 kW machine.

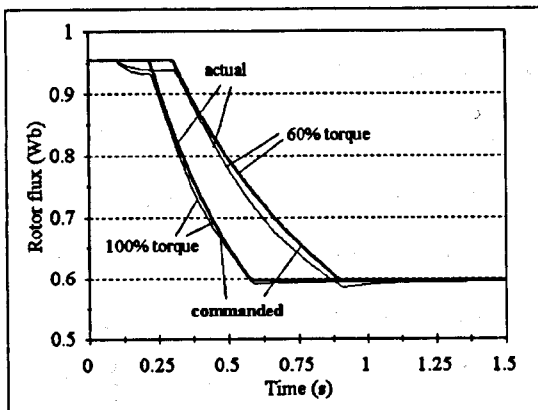
Figure 5.18 : Transient detuning due to combined influence of iron loss and main flux saturation during loading and unloading at rated speed, speed mode of operation, improved estimator with main flux saturation, 4 kW machine.



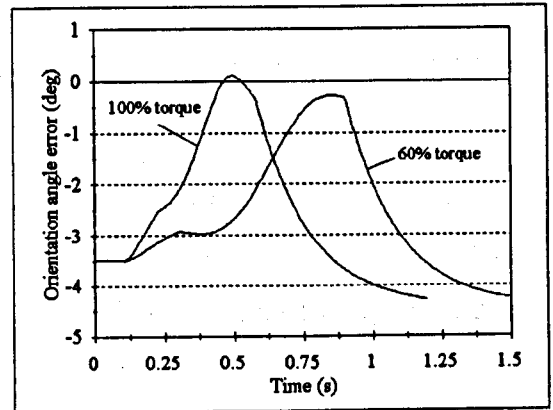
a. commanded and developed torque



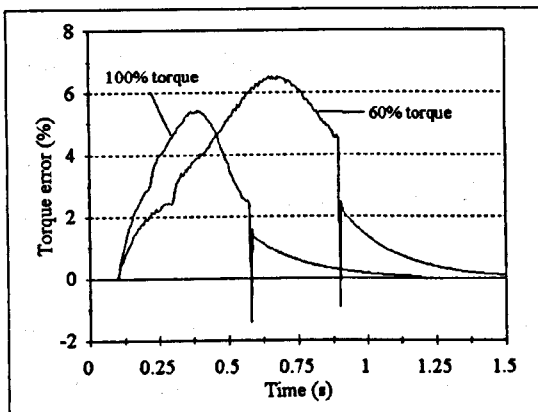
d. rotor flux error



b. commanded and actual rotor flux



e. orientation angle error



c. torque error

Figure 5.19 : Transient detuning due to combined influence of iron loss and main flux saturation during no-load acceleration into the field-weakening region, speed mode of operation, improved estimator with main flux saturation, 4 kW machine.

5.3.2. Transient detuning using improved estimators with iron loss only

Operation of the drive when improved estimators with compensation of iron loss only are utilised will be analysed. Performance of the full estimator of Fig. 3.3 and the simplified estimator of Fig. 3.4 is simulated. Both main flux saturation and iron loss are included in the machine model. The analysed transients are acceleration in the base

speed region in the torque mode of operation and loading and unloading at rated speed in the speed mode of operation.

5.3.2.1. Transient detuning during acceleration in the base speed region, torque mode of operation

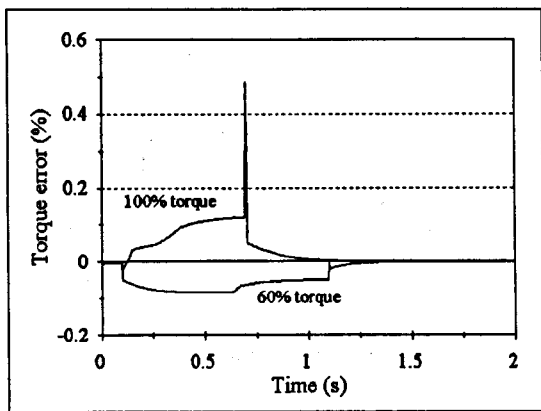
Results of the simulation study for the no-load acceleration in the base speed region when the full improved estimator of Fig. 3.3 is employed are shown in Fig. 5.20. Again, two torque commands of 100% and 60% are analysed. Speed responses are practically identical to the ones from Fig. 4.25.a and therefore are not repeated. Results of Fig. 5.20 reveal that practically full compensation of detuning is achieved. Errors in torque and rotor flux are just a fraction of percent and errors in the orientation angle are less than 0.1 degree.

The same transient of no-load acceleration in the base speed region is simulated again, but this time the simplified improved estimator of Fig. 3.4. is employed. The results are shown in Fig. 5.21. It can be seen that performance is very similar to the performance obtained with the full estimator, Fig. 5.20. This confirms the hypothesis from subsection 3.3.4 that the equivalent time constant $\frac{L_m}{L_r} T_{IFe}$ has a negligible influence on the estimator dynamics.

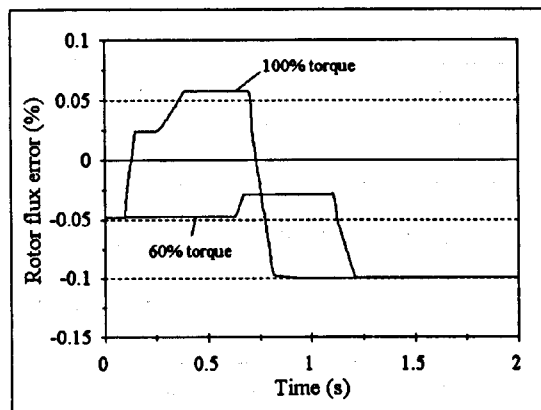
5.3.2.2. Transient detuning during loading and unloading at the rated speed, speed mode of operation

Responses to loading and unloading while the machine operates at the rated speed in the speed mode, when the full improved estimator with iron loss is employed, are shown in Fig. 5.22. Detuning is again very small, proving that almost full compensation can be achieved in the base speed region by employing the improved estimator with iron loss.

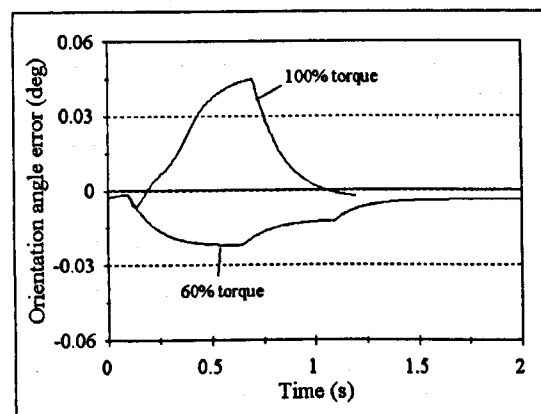
Responses to loading and unloading while the machine operates at the rated speed in the speed mode, when the simplified improved estimator with iron loss is employed, are shown in Fig. 5.23. All responses are very similar to responses obtained with the full estimator (Fig. 5.22), again confirming the effectiveness of the simplified estimator.



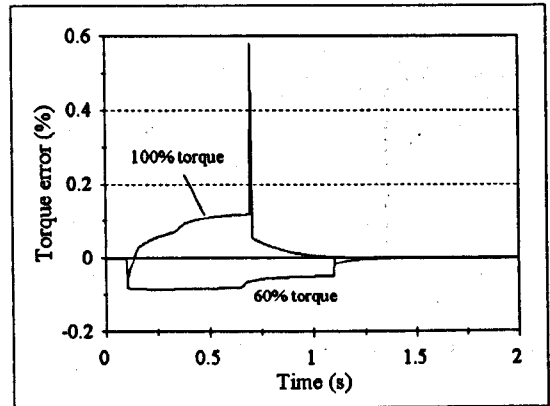
a. torque error



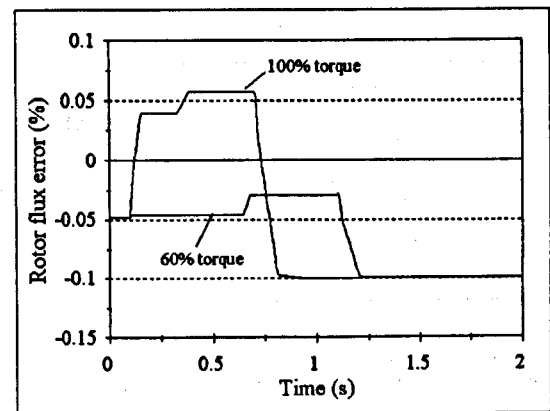
b. rotor flux error



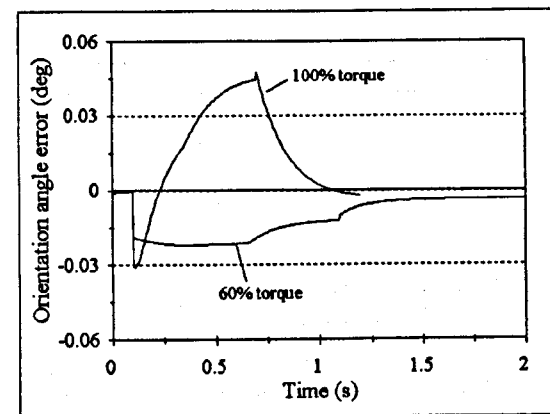
c. orientation angle error



a. torque error



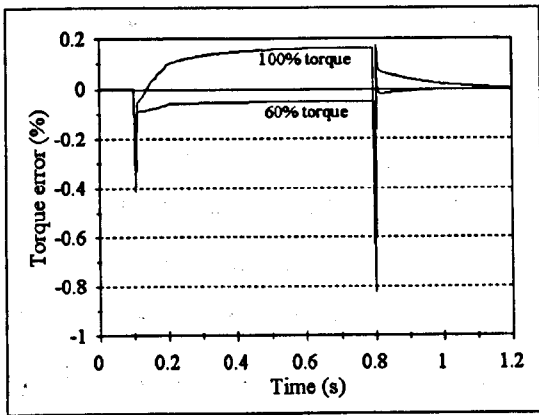
b. rotor flux error



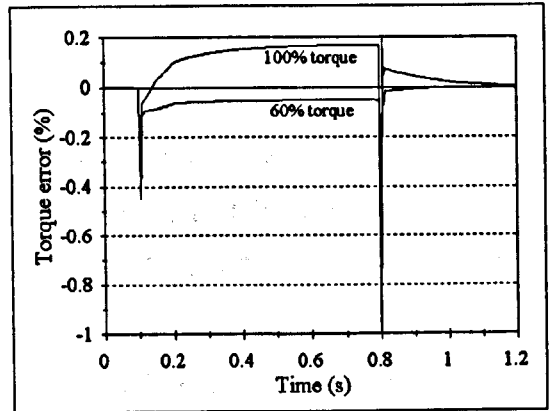
c. orientation angle error

Figure 5.20 : Transient detuning due to combined influence of iron loss and main flux saturation during no-load acceleration, torque mode of operation, the full improved estimator with iron loss, 4 kW machine.

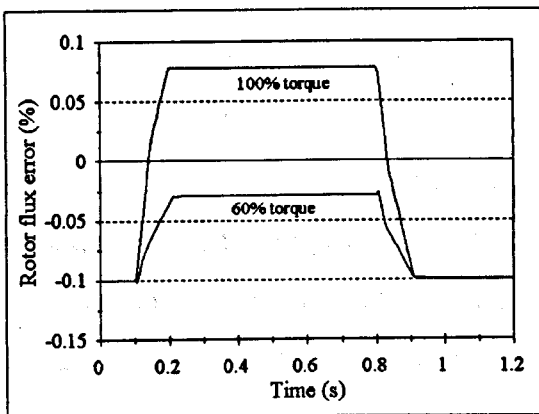
Figure 5.21 : Transient detuning due to combined influence of iron loss and main flux saturation during no-load acceleration, torque mode of operation, the simplified improved estimator with iron loss, 4 kW machine.



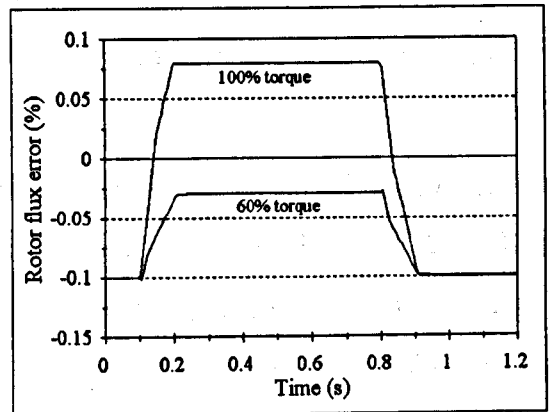
a. torque error



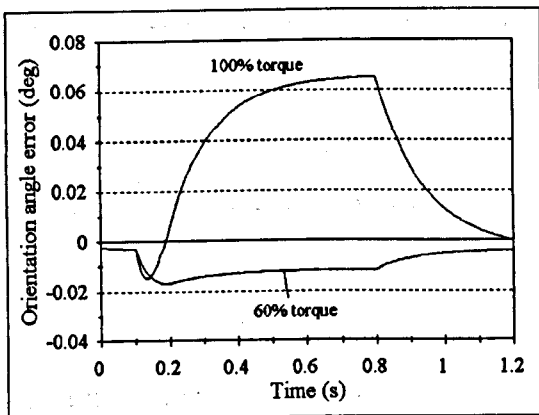
a. torque error



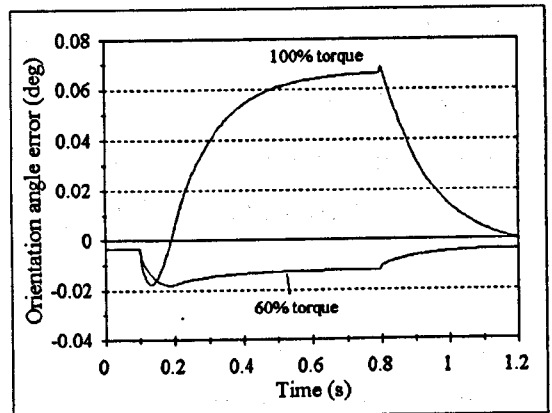
b. rotor flux error



b. rotor flux error



c. orientation angle error



c. orientation angle error

Figure 5.22 : Transient detuning due to combined influence of iron loss and main flux saturation during loading and unloading at the rated speed, speed mode of operation, the full improved estimator with iron loss, 4 kW machine.

Figure 5.23 : Transient detuning due to combined influence of iron loss and main flux saturation during loading and unloading at the rated speed, speed mode of operation, the simplified improved estimator with iron loss, 4 kW machine.

5.3.3. Transient detuning using improved vector controllers with both iron loss and main flux saturation

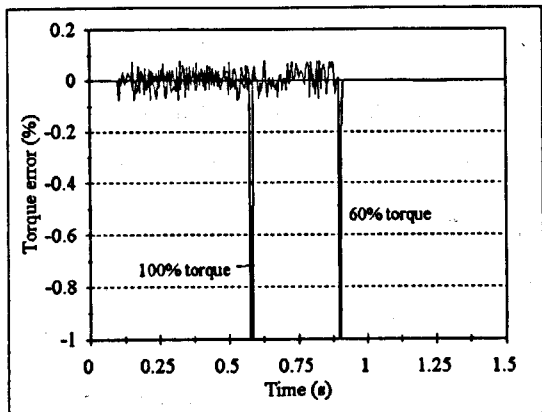
Analysis of the drive operation using improved vector controllers with both iron loss and main flux saturation is presented. Vector controllers that incorporate either full estimators of Figs. 3.6 and 3.8 or simplified estimator of Figs. 3.7 and 3.9 are simulated. Both main flux saturation and iron loss are included in the machine model. In the previous section it was shown that inclusion of iron loss has significantly reduced detuning in the base speed region. Therefore improved estimators with both iron loss and main flux saturation are necessary to be employed only if the drive is to be operated at speeds above rated. Hence the only transient analysed here is acceleration into the field-weakening region.

Results of the simulation study for the no-load acceleration from 80% speed to 160% speed, utilising the improved estimator of in Fig. 3.6, are shown in Fig. 5.24. The estimator includes both iron loss and main flux saturation ($L_m(\psi_m)$ representation). Two commanded speed profiles, that correspond to torque commands of 100% and 60%, are analysed. Speed responses are identical to the ones from Fig. 4.25.a. Errors in torque and in orientation angle are very small, indicating that almost perfect orientation is achieved. Hence results of Fig. 5.24 reveal that the improved estimator with both iron loss and main flux saturation enables practically full compensation of detuning. Errors in rotor flux are negative when the rated speed is surpassed, indicating that decrease in the actual rotor flux is delayed with respect to change in the reference flux.

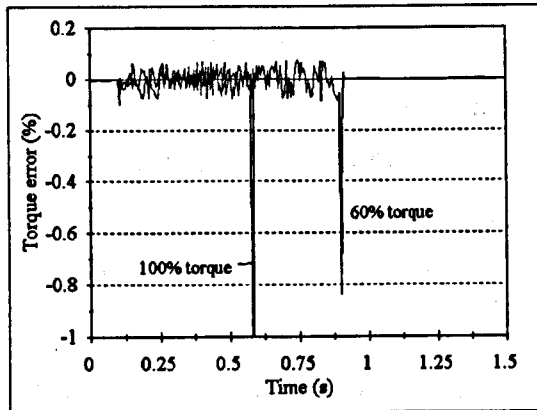
The same no-load acceleration transient is simulated in conjunction with the improved estimator of Fig. 3.8, where $i_m(\psi_m)$ representation of main flux saturation is utilised. The results are identical to the results of Fig. 5.24, again confirming that the way how main flux is represented does not influence the performance of an estimator.

The same transient of no-load acceleration into the field-weakening region, but when the simplified improved estimator of Fig. 3.7 is employed, is simulated again. The results are shown in Fig. 5.25. It can be seen that performance is very similar to the performance obtained with the full estimator, Fig. 5.24. Responses of the torque error and rotor flux error are identical to the ones obtained with the full estimator, while the orientation angle is bigger, but still very small (note that the scales in Figs. 5.24.c and

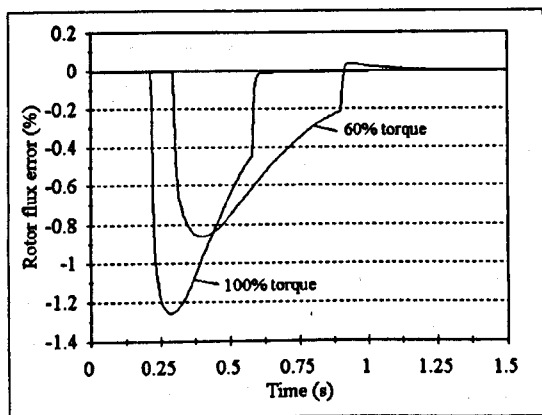
5.25.c differ). This again confirms the hypothesis from sub-section 3.3.4 that the equivalent time constant $\frac{L_m}{L_r} T_{IFe}$ has a negligible influence on the performance of the improved estimator.



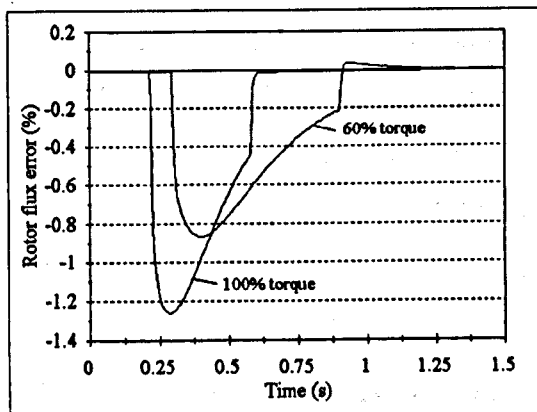
a. torque error



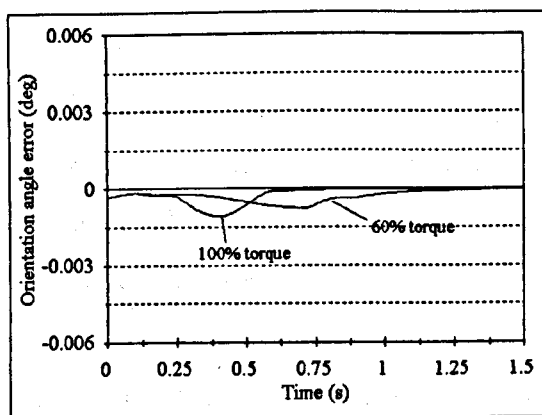
a. torque error



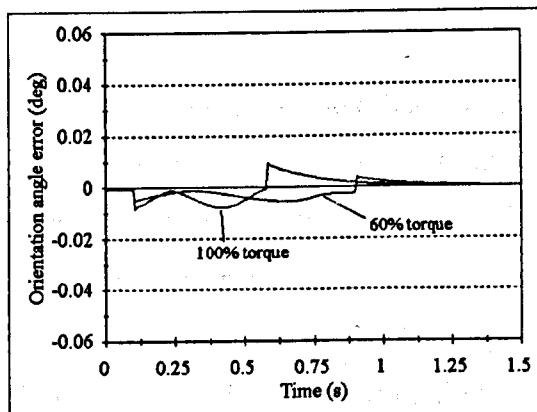
b. rotor flux error



b. rotor flux error



c. orientation angle error



c. orientation angle error

Figure 5.24 : Transient detuning for acceleration into the field-weakening, speed mode of operation, full improved estimator with both iron loss and main flux saturation, 4 kW machine.

Figure 5.25 : Transient detuning for acceleration into the field-weakening, speed mode of operation, simplified improved estimator with both iron loss and main flux saturation, 4 kW machine.

5.4. SUMMARY

The chapter discussed compensation of detuning due to iron loss and/or main flux saturation by using improved vector controllers. Novel detuning expressions that describe steady-state detuning with improved controllers were derived for each type of controller and consequently utilised for quantitative analyses of steady-state detuning.

Improved controllers with main flux saturation were elaborated first. It was shown that they cannot compensate detuning due to rotor resistance variations, apart of reducing the orientation angle error in the field-weakening region. On the other hand, they provide partial reduction of detuning due to iron loss in the base speed region and significant reduction of detuning in the field-weakening region. Improved controllers with iron loss were studied next. They can quite successfully compensate detuning in the base speed region, even if their simplest possible form, with a constant value of the equivalent iron loss resistance, is employed. However, as detuning in the field-weakening stems chiefly from main flux saturation, it cannot be compensated by improved controllers with iron loss. Finally, improved controllers with both iron loss and main flux saturation were studied. Steady-state analyses showed that full compensation of detuning was achieved if both non-linear relationships $R_{Fe}(\omega_r)$ and $L_m(\psi_m)$ were accurately determined. Furthermore, steady-state operation with inaccurately determined equivalent iron loss resistance or mutual inductance was studied. If R_{Fe} was estimated with 20% error, the remaining detuning was quite small. If, however, L_m was estimated with 20% error, detuning was not negligible.

Analyses of detuning in transients were presented next. They confirmed that detuning can be significantly reduced by using improved estimators with main flux saturation. The adopted hypothesis that the choice of non-linear function that describes saturation does not influence the performance was verified. Transient simulations of improved controllers with iron loss validated the compensation obtainable in the base speed region. Furthermore, it was shown that simplified estimator with iron loss performs as good as the full one. As far as utilisation of estimators with both iron loss and main flux saturation is concerned, only acceleration into the field-weakening region was elaborated. It was shown that both full and simplified estimators enable almost perfect compensation of detuning.

6. ON-LINE IDENTIFICATION OF THE ROTOR RESISTANCE

6.1. INTRODUCTION

Detuning that occurs due to temperature effects is difficult to predict and it is not viable to use some pre-determined functions in order to try to compensate for it. Therefore, methods for on-line identification of either rotor resistance or rotor time constant have been developed. Methods of identification and compensation of rotor resistance variations were reviewed in sub-section 2.4.4. and the particular one that is to be elaborated in detail in this chapter was explained in sub-section 2.5.3.

Performance of the R_r identification scheme, based on the CPM machine model and the MRAC theory is investigated in section 6.2. The whole vector controlled drive, including the R_r identification scheme, is simulated. The influence of iron loss and main flux saturation on the operation of the identification scheme is analysed for different operating conditions. Therefore both iron loss and main flux saturation are included in the machine model throughout the chapter. It is shown that these two phenomena spoil the accuracy of identification and that their influence varies with operating conditions. Possible remedy for this situation is to employ novel schemes for R_r on-line identification, that include one or both these phenomena. Novel R_r identifiers, based on improved models of chapter 3, are then proposed in section 6.3. Their performance is again evaluated by simulation. It is shown that they can improve the identification when they are employed alongside novel vector controllers, proposed in chapter 3.

6.2. IDENTIFICATION SCHEME BASED ON THE CONSTANT PARAMETER MODEL

The CPM-based R_r identification scheme, that uses reactive power method, is shown in Figure 6.1. Being based on equations 2.89 and 2.91, the scheme is very similar to the one shown in Fig. 2.14. The difference is that R_r is identified instead of T_r . The scheme is to be used in conjunction with the feedback vector control scheme.

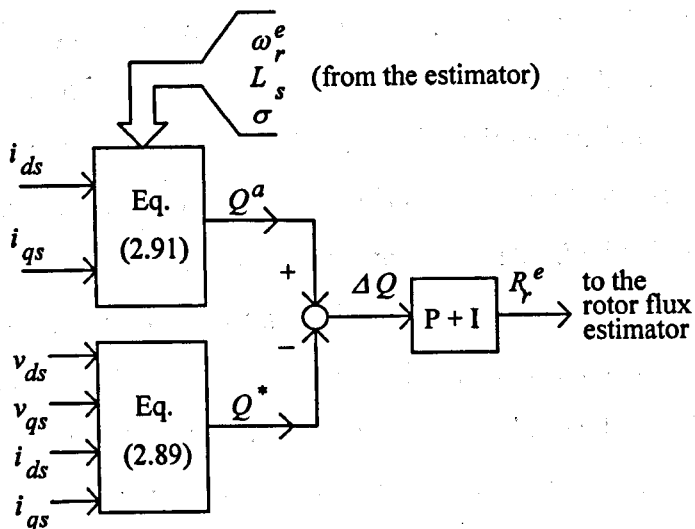


Figure 6.1 : The R_r identification scheme, using the reactive power method.

The performance of the CPM-based R_r identification scheme is analysed by means of simulations. The CPM-based estimator, identical to the one from Fig. 2.3, has a variable value of the rotor resistance R_r^e (and hence T_r^e as well). The information on R_r^e is supplied from the CPM-based R_r identification scheme. Both iron loss and main flux saturation are included in the machine model. The speed control loop is closed and the commanded speed is constant. Three values of the actual R_r are used in simulations - 100%, 120% and 80%. For each of them, three levels of the load torque are considered - 100%, 60 % and 25%. The value of R_r^e is set to the rated level at the beginning of the simulation and the identification is enabled after 0.1 seconds.

Due to different levels of the commanded flux and hence different influence of main flux saturation, results for the base speed region and for the field-weakening region are presented separately.

6.2.1 Operation in the base speed region

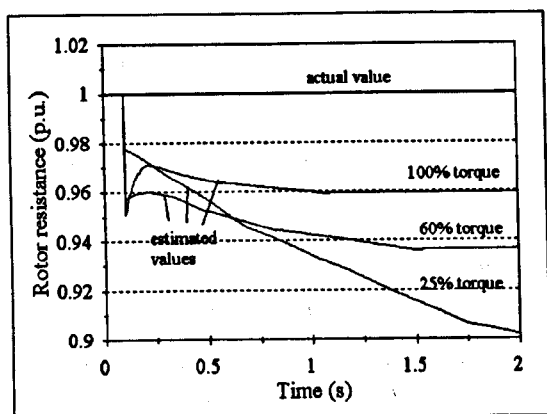
Performance of the CPM-based R_r identification scheme at rated speed is analysed. The drive operation at rated speed is simulated and the simulation results for the three values of actual R_r are shown in figures 6.2 to 6.4.

Figure 6.2 presents the operation of the drive at the rated speed when the actual R_r is of rated value ($R_r = R_{rn}$). Figure 6.2.a shows the actual and the identified R_r , while Figs. 6.2.b and 6.2.c represent the rotor flux error and the orientation angle error, respectively. In the beginning of the simulation the identification algorithm is disabled, the identified

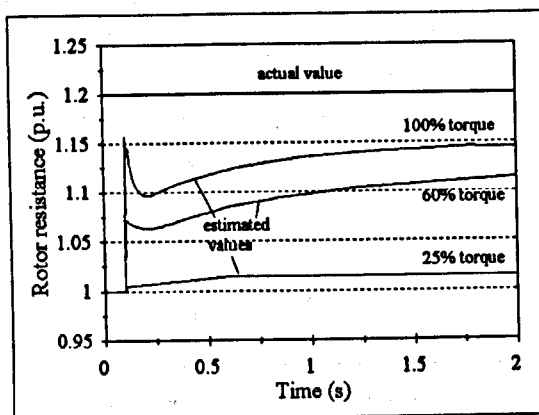
R_r is of rated value and some detuning is present, due to main flux saturation and iron loss. The amount of initial detuning is determined by the load and the values correspond to those from Fig. 4.13. After the identification is enabled, the identifier drives R_r^e to a smaller value so that detuning is reduced and both the rotor flux error and the orientation angle error are slowly driven to zero. The final value of R_r^e , as well as the speed of convergence depend on load. At higher loads, the final value of R_r^e is closer to the actual R_r (difference of about 4% and 6% for 100% and 60% loads, respectively) and the identification process is completed after 1 to 1.5 seconds. At light load the identification converges slower and takes even longer than the shown simulation time. The final R_r^e is identified with an error of about 15%. This confirms the well-known fact that this type of R_r identification schemes operate poorly at light load and do not work at zero load.

Figures 6.3 and 6.4 present the operation of the drive at the rated speed when the actual R_r is 20% bigger and smaller than rated, respectively. In these cases detuning is a combination of three detuning sources: R_r variations, iron loss and main flux saturation. When $R_r = 1.2 R_{rn}$ (Fig. 6.3.) and the load is light, the initial detuning is very small as the three phenomena almost cancel each others' influence. The increase in R_r tends to increase the flux, the existence of iron loss decreases the flux, while main flux saturation has quite small influence in the base speed region. For higher loads, detuning due to R_r variations prevails and the total detuning increases. When enabled, the identifier increases R_r^e and hence reduces detuning. The final values of R_r^e are still smaller than the actual R_r . Errors in R_r estimation are about 6% and 8% for 100% and 60% loads, respectively. For light load operation, the increase in R_r^e is very small as the initial detuning is quite small and therefore R_r^e is identified with error of about 18%. Nevertheless, R_r adaptation greatly reduces detuning as the errors in the rotor flux and in the orientation angle are driven to a very small values.

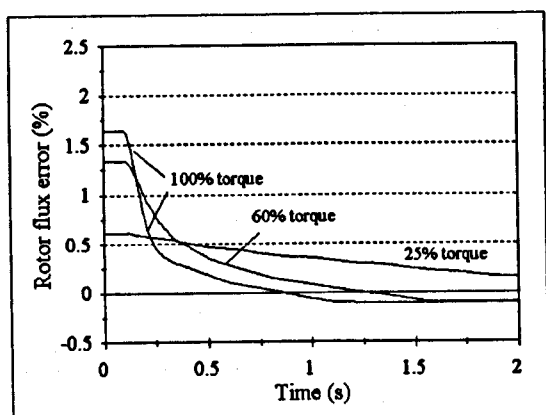
Simulation results for the $R_r = 0.8 R_{rn}$ case are shown in the Fig. 6.4. The initial detuning is bigger than in the previous case, because both R_r variation and iron loss tend to reduce the flux. The rotor resistance is again identified with errors, especially at operation with light load, when it amounts to 20%. This cannot be seen in Fig. 6.4, as the identification process is slower than in the previous two cases and takes about 5 seconds with 25% load.



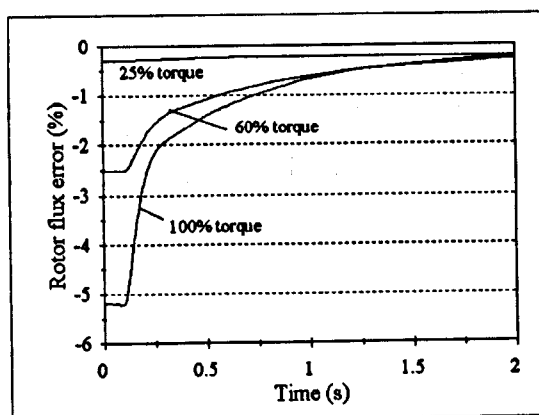
a. rotor resistance



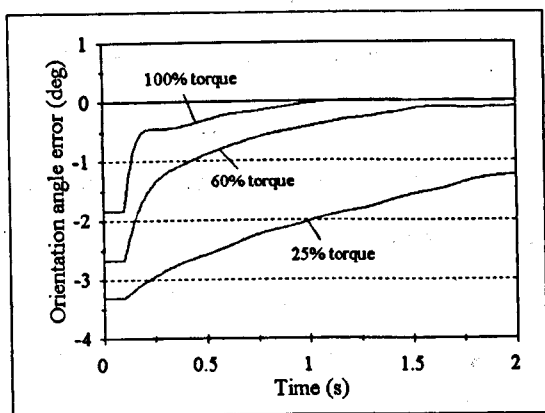
a. rotor resistance



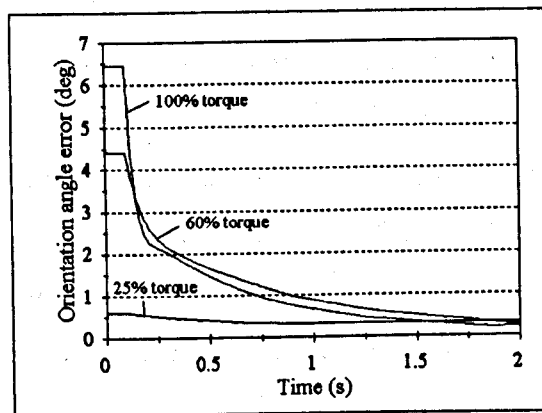
b. rotor flux error



b. rotor flux error



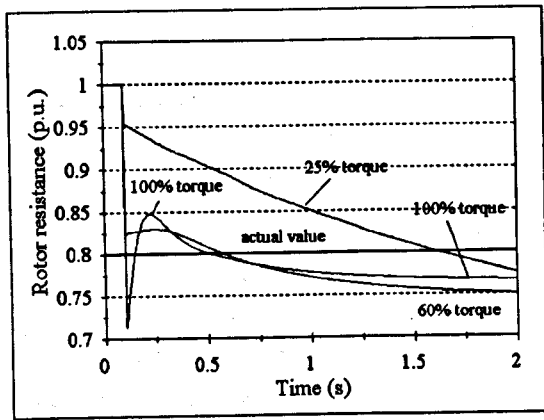
c. orientation angle error



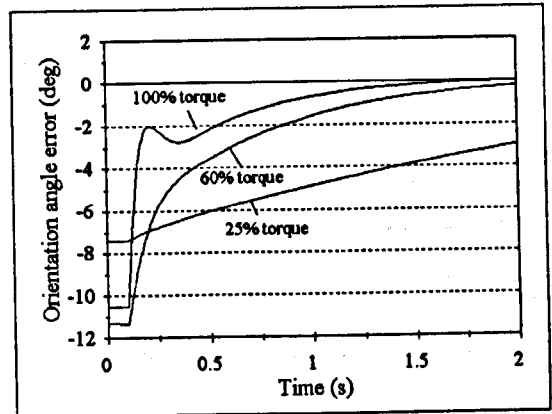
c. orientation angle error

Figure 6.2 : Identification of R_r by the CPM-based identifier at the rated speed, $R_r = R_{rn}$, load torque in % as parameter, 4kW machine.

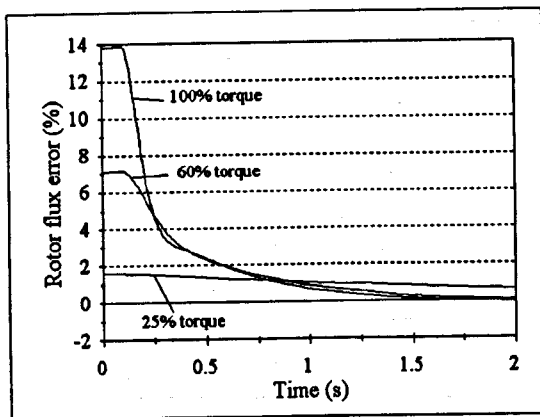
Figure 6.3 : Identification of R_r by the CPM-based identifier at the rated speed, $R_r = 1.2 R_{rn}$, load torque in % as parameter, 4kW machine.



a. rotor resistance



c. orientation angle error



b. rotor flux error

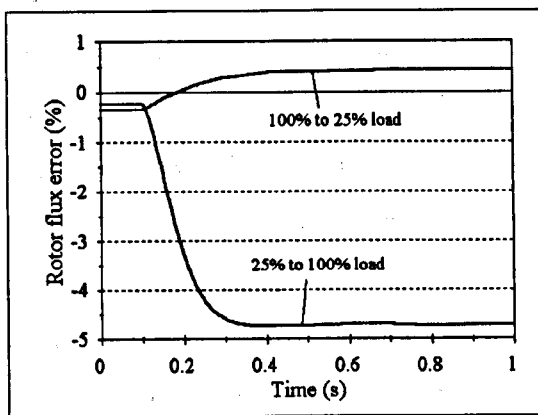
Figure 6.4 : Identification of R_r by the CPM-based identifier at the rated speed, $R_r = 0.8 R_{rn}$, load torque in % as parameter, 4 kW machine.

It can be concluded that the CPM-based R_r identifier delivers a wrong information about R_r^e due to unmodelled iron loss. Such wrong R_r^e values compensate for the iron-loss-induced detuning in the amplitude and orientation of the rotor flux and appears that R_r identifier is a good solution for elimination of detuning. However, this is not true. The identified R_r^e is useful only in that particular operating condition. When the load and/or speed are changed, detuning will reappear in the new steady-state operation and the identification process has to be performed again. As the identification lasts for more than one second, high-performance servo-like operation of the drive, with continuously changing speed and torque, is impossible.

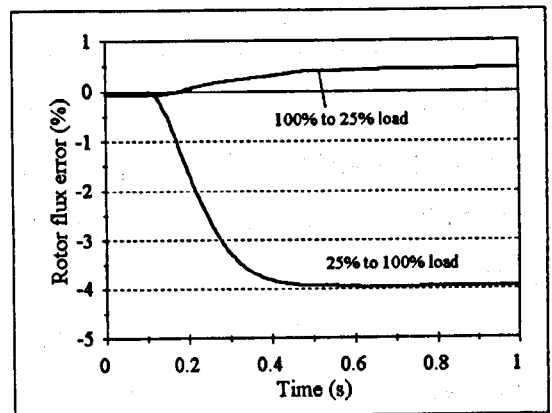
Reappearing of detuning when the load is changed is confirmed by simulations. Figure 6.5. shows the responses of the rotor flux error and the orientation angle error after a change in load. Two values of the actual rotor resistance are shown : $R_r = 1.2 R_{rn}$ (Figs. 6.5.a. and 6.5.b.) and $R_r = 0.8 R_{rn}$ (Figs. 6.5.c. and 6.5.d.). For both cases, two changes in load torque are shown - the reduction in the load from 100% down to 25% and the increase in the load from 25% to 100% load. The R_r identifier is disabled and

the previously identified values of R_r^e are used. The commanded speed is constant and equal to rated.

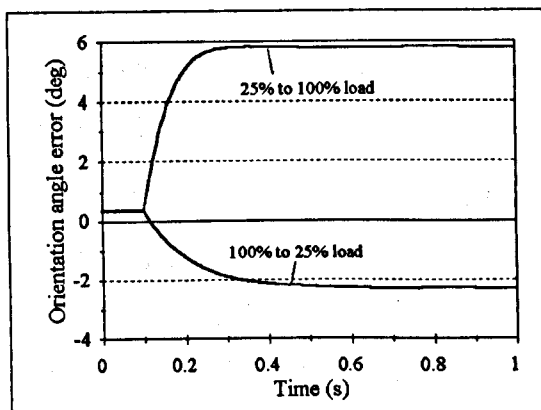
From Figure 6.5. it can be seen that responses are similar for the two levels of the actual R_r - there is only small difference in the amounts of the final detuning values. The reduction in load torque results in a small detuning, but the reappearing of detuning after the increase in load is not negligible. To eliminate that detuning, identification process has to be performed again.



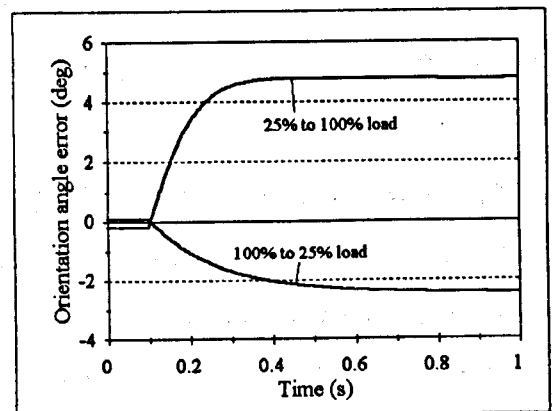
a. rotor flux error, $R_r = 1.2 R_{rn}$



c. rotor flux error, $R_r = 0.8 R_{rn}$



b. orientation angle error, $R_r = 1.2 R_{rn}$



d. orientation angle error, $R_r = 0.8 R_{rn}$

Figure 6.5 : Responses to the changes in load, operation at the rated speed, R_r identification disabled.

6.2.2. Operation in the field-weakening region

Operation in the base speed region, with the rated level of the commanded rotor flux, means that the actual values of the machine inductances are very close to their rated values, which are used in the CPM-based control system. When the commanded flux is reduced in the field-weakening region, main flux saturation now plays a major detuning

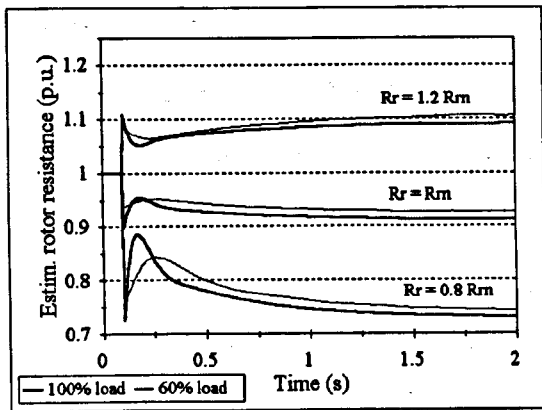
role, so that the actual values of the machine inductances differ from the rated values. This is expected to cause problems in the operation of the R_r identifier.

Simulations of the CPM-based R_r identification scheme and performance analyses for operation in the field-weakening region are performed for several speeds. The drive operation at 125% speed is shown in Figure 6.6 while the operation at 150% speed is shown in Figure 6.7.

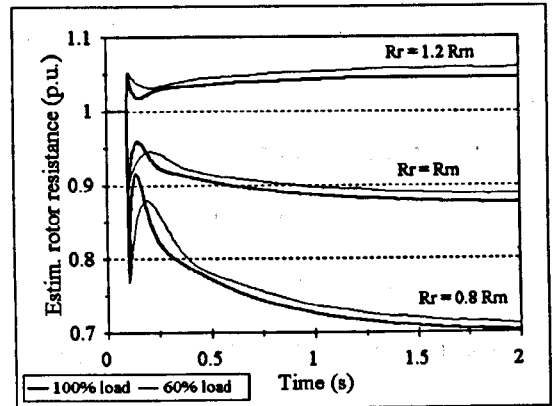
Figure 6.6 presents the operation of the drive at 125% speed, for three cases of R_r and for two load levels. The total detuning is a combination of three detuning sources: R_r variations, iron loss and main flux saturation. The initial values of detuning for the $R_r = R_{r,m}$ case correspond to those from Fig. 4.14. After the identification is started, the identifier drives R_r^e to a value that makes the reactive power of the adaptive part of the R_r identifier equal to the measured reactive power. In all cases, R_r^e is wrongly identified. It is again under-estimated by about 5 to 10 %, depending on the operating conditions. This error occurs due to the neglect of both iron loss and main flux saturation in both R_r identifier and rotor flux estimator. The rotor flux is driven to a value about 8% higher than commanded, while the responses of the orientation angle error depend on load, the final values being approximately -2.5° , -4.5° and -11° for load torque levels of 100%, 60% and 25%, respectively (the case with 25% load is not shown in Fig. 6.6).

Figure 6.7 presents the operation of the drive at 150% speed. Trends observed at 125% speed are repeated and even more pronounced. The rotor resistance is under-estimated by about 10-15%. The final value of the rotor flux is about 10% higher than commanded, while the orientation angle error is driven to values of approximately -3° , -5° and -12° for 100%, 60% and 25% loads, respectively.

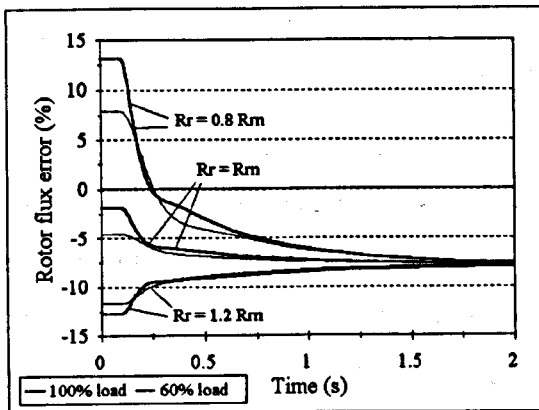
It can be concluded that the CPM-based R_r identifier is not able to compensate detuning in the field-weakening region. Decreased level of main flux saturation and subsequent increase in L_m , as well as iron loss, are responsible for this.



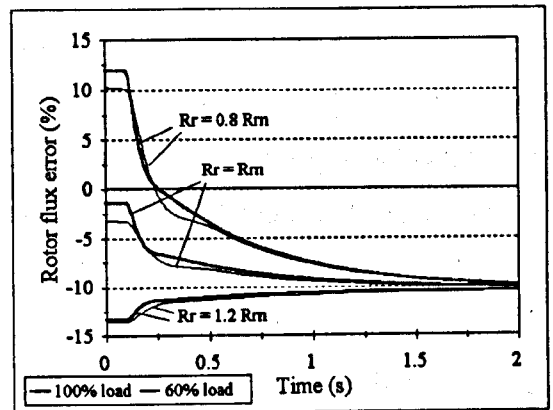
a. rotor resistance



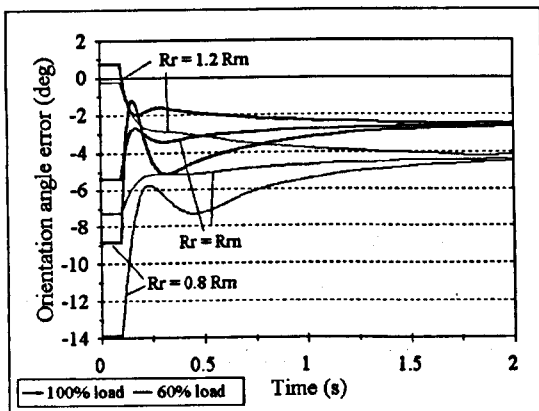
a. rotor resistance



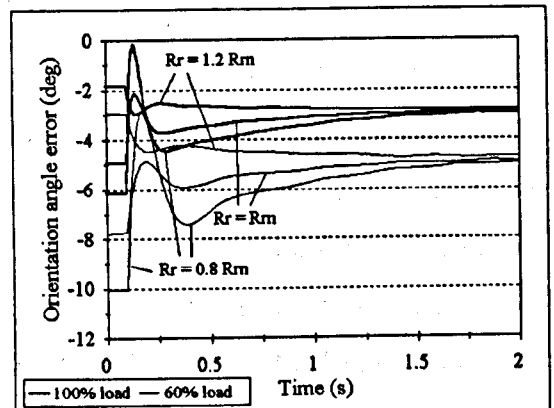
b. rotor flux error



b. rotor flux error



c. orientation angle error



c. orientation angle error

Figure 6.6 : Identification of R_r by the CPM-based identifier in the field-weakening region, 125% speed, load torque in % and the actual value of R_r as parameters, 4 kW machine.

Figure 6.7 : Identification of R_r by the CPM-based identifier in the field-weakening region, 150% speed, load torque in % and the actual value of R_r as parameters, 4 kW machine.

6.2.3. Sensitivity of the CPM-based identifier

As discussed in chapter 2, accuracy of any R_r identification scheme depends on precise information about some of the induction machine parameters. Influences of the mutual inductance L_m and leakage inductances L_{ls} and L_{lr} are analysed here.

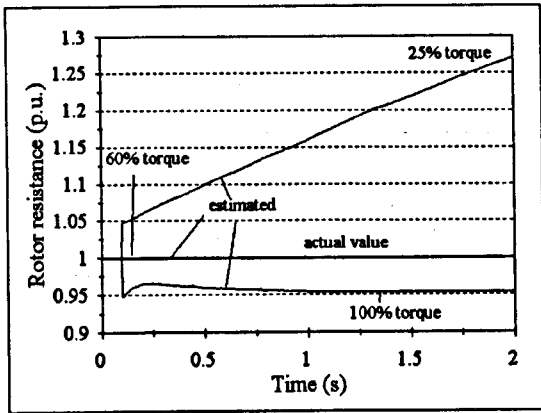
Figures 6.8 and 6.9 present simulated responses of the CPM-based R_r identifier in the base speed region when the L_m value used in both estimator and identifier (L_m^*) is 20% smaller and 20% bigger than rated, respectively. The actual L_m is varied in accordance with the magnetising curve of the 4 kW machine.

When L_m^* is smaller than rated (Fig. 6.8), the machine becomes more saturated due to an increased level of the commanded i_{ds}^* current. This greatly affects the identification process. The overall result is that R_r identification is very accurate for 60% load, while there are errors in other cases - R_r is under-estimated at full load and greatly over-estimated for 25% load. The convergence is slower than in the Figs. 6.1-6.3, the slowest being the case shown in Fig. 6.8.b. Responses of the flux error and the orientation angle error, omitted here, exhibit the following trends : in all cases, the rotor flux is driven to a value about 5-6% higher than commanded; the orientation angle error is forced to values of about -3° , -5° , and -9° , for load levels of 100%, 60% and 25% , respectively.

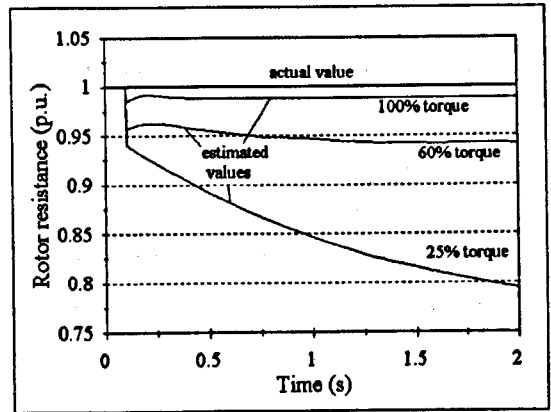
When L_m^* is bigger than rated (Fig. 6.9), the commanded i_{ds}^* current decreases and the machine becomes less saturated. The identification at full load becomes reasonably accurate, while the R_r^e is under-estimated at lower loads. Trends of the flux error and the orientation angle error are different than in the previous case. The final value of the rotor flux is about 5% lower than commanded, while the final values of orientation angle error are 1.5° , 2.5° , and 5° , for load levels of 100%, 60% and 25% , respectively.

The influence of the leakage inductances on R_r identification accuracy is investigated as well and results for the rated speed are shown in Figures 6.10 and 6.11. Figure 6.10 shows responses of the CPM-based R_r identifier at different loads when both L_{ls} and L_{lr} values in the identifier are 20% smaller than the actual leakage inductances. Figure 6.11 presents responses when both L_{ls} and L_{lr} values in the identifier are 20% bigger than the actual leakage inductances. It can be seen that behaviour of the identifier is very similar to the cases with correctly set leakage inductances (section 6.2.1). The final values of R_r^e with wrong leakage inductances differ from the final values of R_r^e with correct

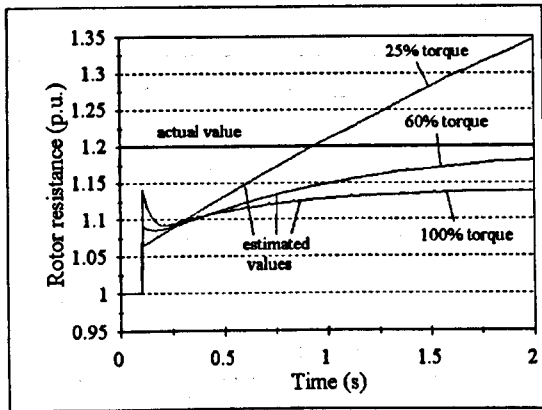
leakage inductances (Figs. 6.2 to 6.4) by approximately 2%. The rotor flux amplitude and orientation angle error (neither shown here) are reduced to within 2% and 2°, respectively.



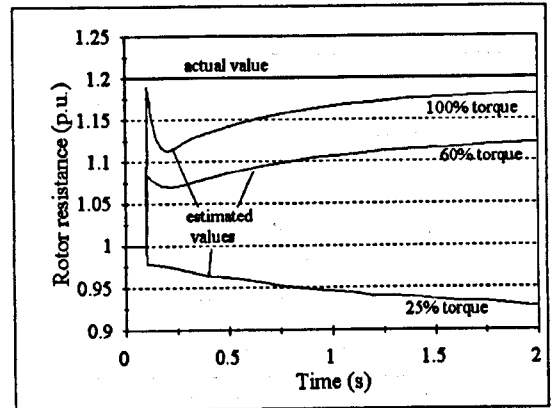
a. $R_r = R_{rn}$



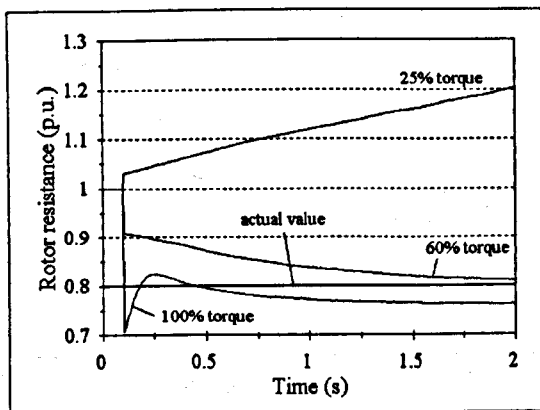
a. $R_r = R_{rn}$



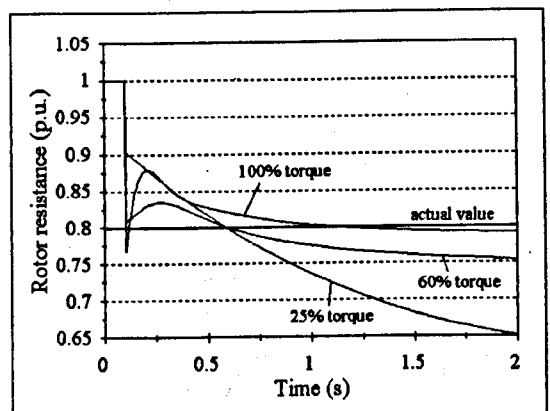
b. $R_r = 1.2 R_{rn}$



b. $R_r = 1.2 R_{rn}$



c. $R_r = 0.8 R_{rn}$

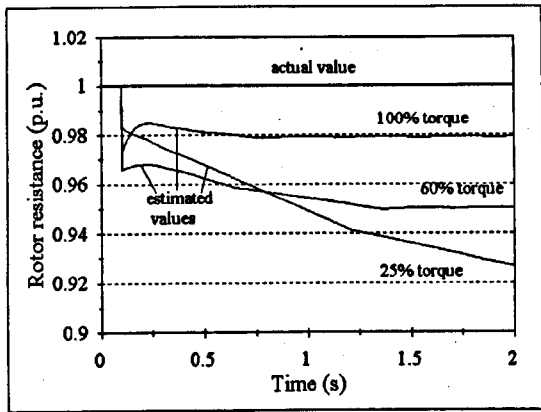


c. $R_r = 0.8 R_{rn}$

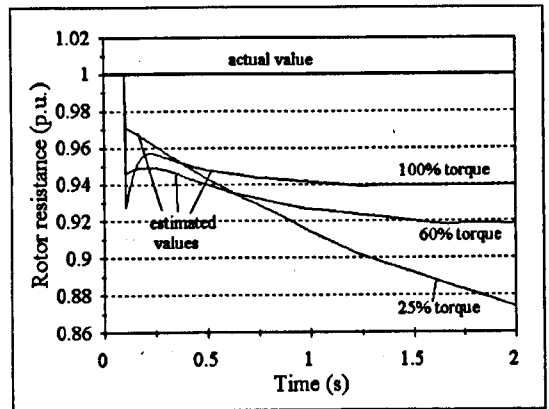
Figure 6.8 : Identification of R_r by the CPM-based identifier at the rated speed, $L_m^* = 0.8 L_{mn}$, load torque in % as parameter, 4kW machine.

Figure 6.9 : Identification of R_r by the CPM-based identifier at the rated speed, $L_m^* = 1.2 L_{mn}$, load torque in % as parameter, 4kW machine.

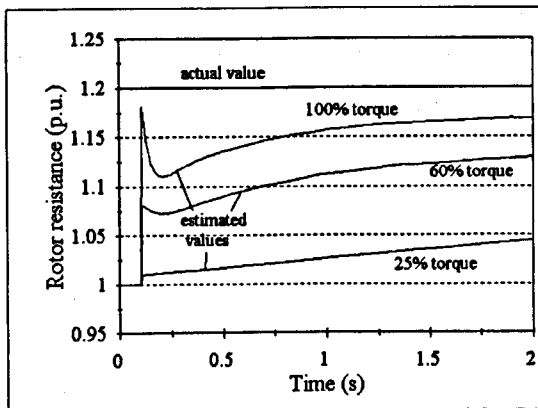
It can be concluded that the accuracy of CPM-based R_r identifier is quite dependent on the accurate knowledge about the mutual inductance while it is reasonably robust to the inaccuracies in the leakage inductances.



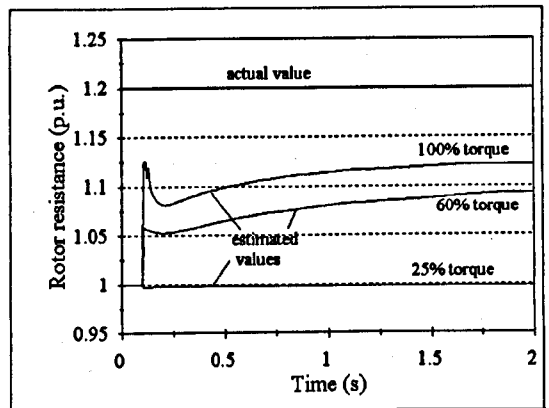
a. $R_r = R_{rn}$



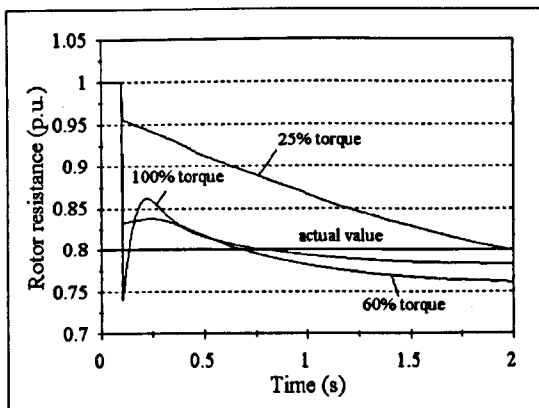
a. $R_r = R_{rn}$



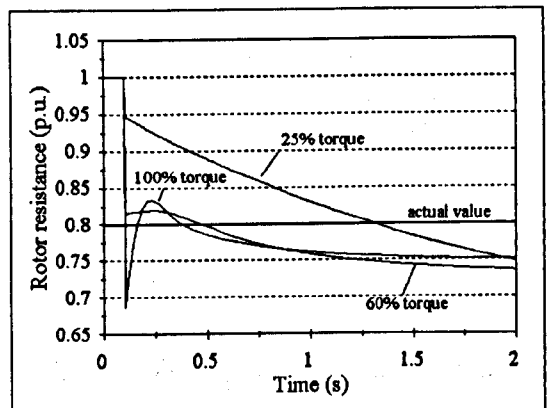
b. $R_r = 1.2 R_{rn}$



b. $R_r = 1.2 R_{rn}$



c. $R_r = 0.8 R_{rn}$



c. $R_r = 0.8 R_{rn}$

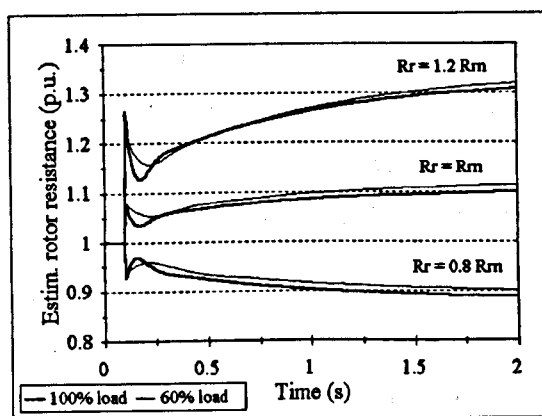
Figure 6.10 : Identification of R_r by the CPM-based identifier at the rated speed, $L_{ls}^* = 0.8 L_{lsn}$ and $L_{lr}^* = 0.8 L_{lrn}$, load torque in % as parameter, 4 kW machine.

Figure 6.11 : Identification of R_r by the CPM-based identifier at the rated speed, $L_{ls}^* = 0.8 L_{lsn}$ and $L_{lr}^* = 0.8 L_{lrn}$, load torque in % as parameter, 4 kW machine.

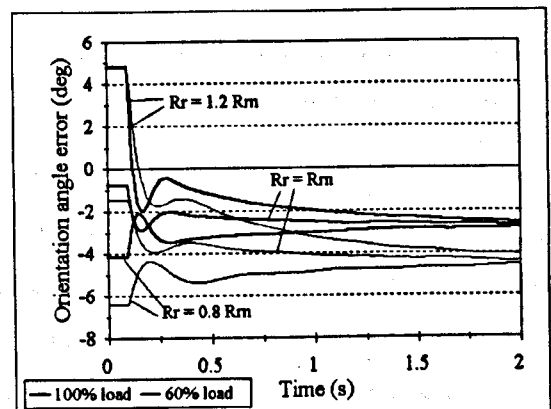
6.2.4. Operation with the CPM-based R_r identifier and saturation-adaptive rotor flux estimator

The improved rotor flux estimator with L_m (ψ_m) representation (Fig. 3.1) is in the following simulations used for processing the feedback signals. At this stage, information about the estimated mutual inductance L_m^e is not passed from the estimator to the R_r identifier, so that the CPM-based R_r identifier is still used.

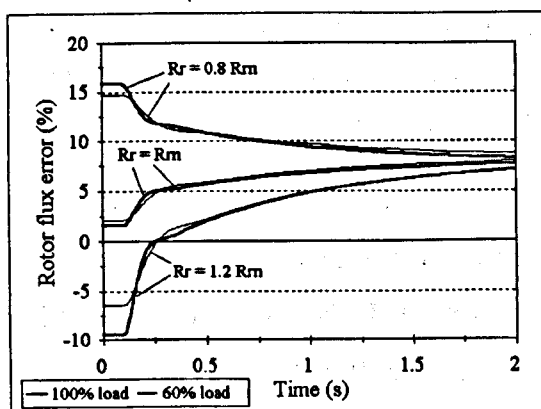
As main flux saturation effects are not pronounced in the base speed region, this change in controller configuration has no effect on operation up to rated speed. On the other hand, main flux saturation has a dominant detuning influence in the field-weakening region. Hence the performance of this vector control scheme is investigated in the field-weakening region only. The simulated responses during operation at 125% speed are shown in Figure 6.12, for two levels of load torque and three values of the actual R_r . They reveal that in all the cases identification gives greatly over-estimated values of R_r , with the errors between 8 and 15%. The final values of detuning in rotor flux error and orientation angle error are identical to the ones obtained in sub-section 6.2.2. for 125%



a. rotor resistance



c. orientation angle error



b. rotor flux error

Figure 6.12 : Identification of R_r by the CPM-based identifier in conjunction with the saturation-adaptive rotor flux estimator, operation in the field-weakening region, 125% speed, $R_r = R_{rm}$ load torque in % as parameter, 4 kW machine.

speed. It can be seen that the final detuning in the for $R_r = R_{r,m}$ case is even greater than the initial detuning that existed before the identification was enabled.

The above discussion shows that a combination of CPM-based R_r identifier and a saturation-adaptive rotor flux estimator is not a viable solution for on-line R_r identification in the field-weakening region. This is due to the fact that the estimated mutual inductance L_m^e , obtained by the improved estimator, is used for control purposes, but not for R_r identification purposes..

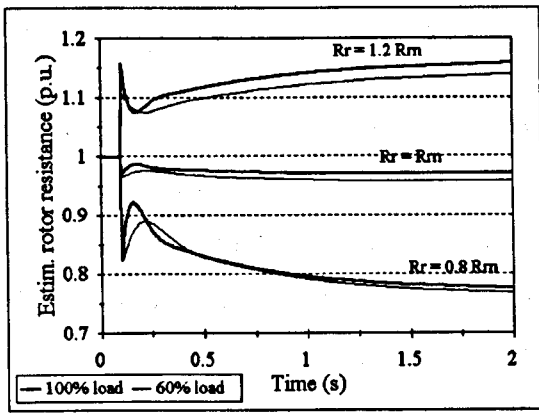
6.3. IDENTIFICATION SCHEMES BASED ON THE IMPROVED MODELS

Successful improvements in the process of R_r identification can be achieved when the induction machine model, on which identification scheme is based, is adapted to include some of the neglected phenomena, such as main flux saturation and iron loss.

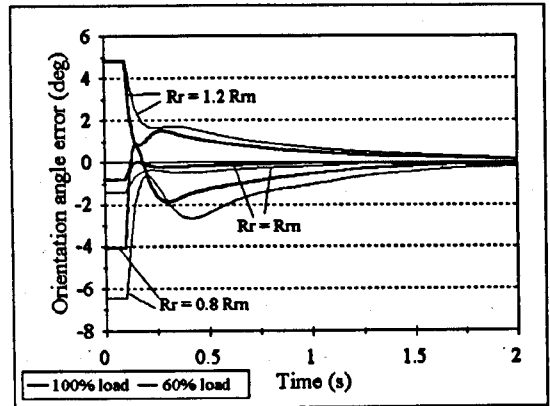
6.3.1. Identification scheme based on the improved model with main flux saturation

The simplest possible improvement of the already analysed CPM-based R_r identifier of Fig. 6.1. is to use the estimated values of machine mutual inductance instead of the rated value. This information is available when a saturation-adaptive rotor flux estimator is used to process the feedback signals. The major benefit is expected to take place in the field-weakening region, when the saturation level is reduced due to reduced flux command. The operation of such vector controlled drive is simulated in both base speed region and field-weakening region. As expected, the responses at the rated speed are practically identical to the ones from Figs. 6.2-6.4 and therefore not repeated.

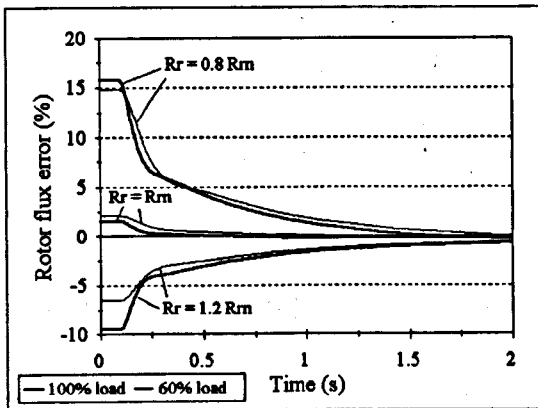
Improvements in drive performance in the field-weakening are illustrated in Fig. 6.13, for 125% speed. Responses are generally similar to the ones obtained at the rated speed with the CPM-based identifier. The final values of the identified R_r are wrong, about 4 to 8% smaller than the actual rotor resistance. However, this is an improvement over the responses obtained at 125% speed with the CPM-based identifier (Figs 6.6 and 6.12), since detuning in final steady-state is practically eliminated. Both amplitude and orientation of the rotor flux converge towards their commanded values and the orientation becomes almost perfect.



a. Rotor resistance



c. Orientation angle error



b. rotor flux error

Figure 6.13 : Identification of R_r by the saturation-adaptive identifier in the field-weakening region, 125% speed, $R_r = R_m$, saturation-adaptive rotor flux estimator, load torque in % as parameter, 4 kW machine.

6.3.2. Identification scheme based on the improved model with iron loss

In chapter 5 it was shown that utilisation of an improved estimator with iron loss can improve the performance of the drive in the base speed region. From those results stems the idea of using an improved R_r identifier with iron loss. The inclusion of iron loss in the R_r identifier can be performed in a number of ways. A possible procedure is to design the identifier on the basis of the improved model of sub-section 3.3.1.2. In the RFO reference frame, the steady-state voltage equations of the $i_s - \psi_m - \psi_r$ mixed current-flux model with iron loss (sub-section 3.3.1.2) are obtained as:

$$\begin{aligned} v_{ds} &= R_s i_{ds} - \omega_r L_{ls} i_{qs} - \omega_r \psi_{qm} \\ v_{qs} &= R_s i_{qs} + \omega_r L_{ls} i_{ds} + \omega_r \psi_{dm} \end{aligned} \quad (6.1)$$

Substitution of (6.1) into (2.89) yields the expression for the reactive power of the adaptive part of the improved identifier :

$$Q^a = \frac{3}{2}(\omega + \omega_{sl}) \left(L_{ls}(i_{ds}^2 + i_{qs}^2) + \psi_{qm} i_{qs} + \psi_{dm} i_{ds} \right) . \quad (6.2)$$

The improved identification scheme is constructed using (2.89) and (6.2) and the structure of the identifier is shown in Fig. 6.14. Information on ψ_{dm} and ψ_{qm} is obtained from an improved rotor flux estimator with iron loss. Either full estimator of Fig. 3.3 or simplified one of Fig. 3.4. can be utilised, since their behaviour in a steady-state is identical. For the following simulations, the simplified estimator is utilised.

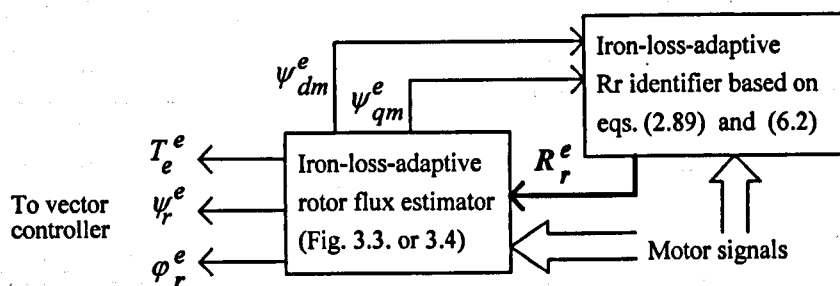
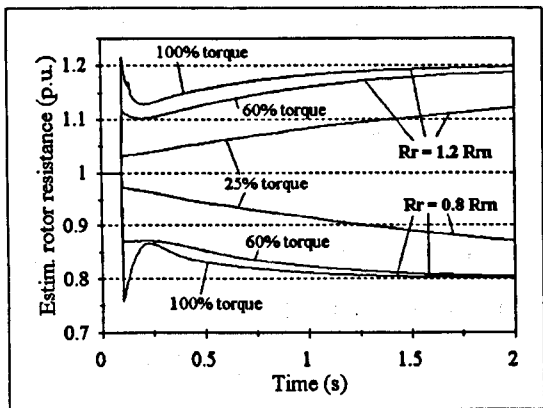


Figure 6.14 : Rotor resistance identification with inclusion of iron loss.

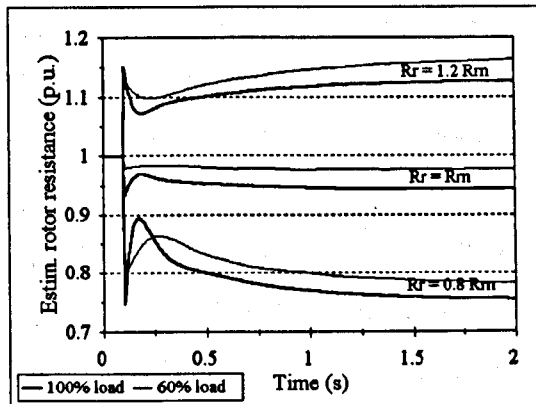
The responses of the drive obtained with the improved R_r identifier with iron loss are shown in Figures 6.15. and 6.16, for operation at 100% speed and 125% speed, respectively. Figure 6.15. presents only the operation with the actual R_r values of 120% and 80% , since there is no initial detuning for the case $R_r = R_{rn}$ in the base speed region. Figure 6.15 suggests that utilisation of the iron-loss-adaptive identifier yields very accurate identified values and, at the same time, elimination detuning in the base speed region. However, as seen in Fig. 6.16, the above identification system still operates erroneously in the field weakening region. Since this improved R_r identifier does not include main flux saturation, it cannot compensate detuning in the field-weakening region.

6.3.3. Identification scheme based on the improved model with both main flux saturation and iron loss

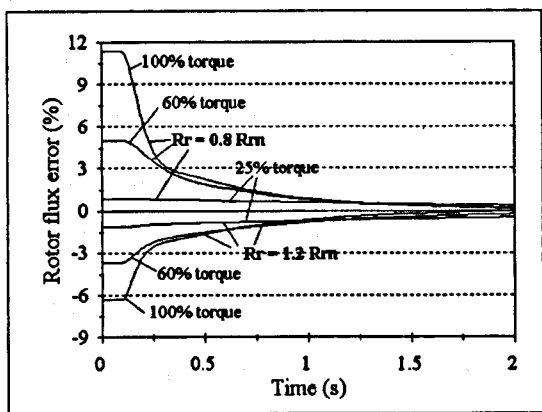
An identification system with both main flux saturation and iron loss is obtained when R_r identification scheme based on equation (2.89) and (6.2) is combined with an improved estimator with both main flux saturation and iron loss. Any of the four estimators presented in sub-section 3.4.6 (Figs. 3.6-3.9) can be utilised. Hence the overall structure remains identical to the one of Fig. 6.14.



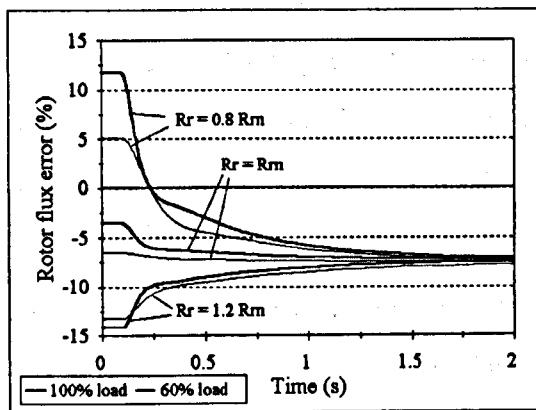
a. rotor resistance



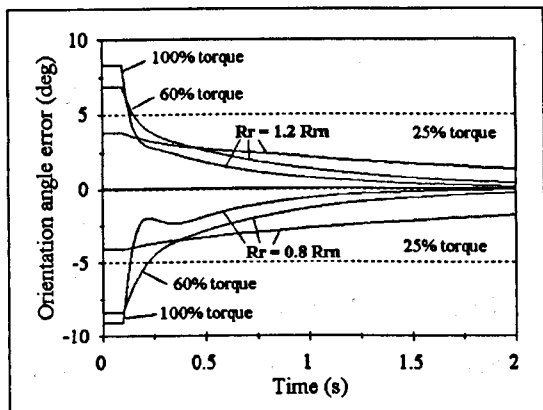
a. rotor resistance



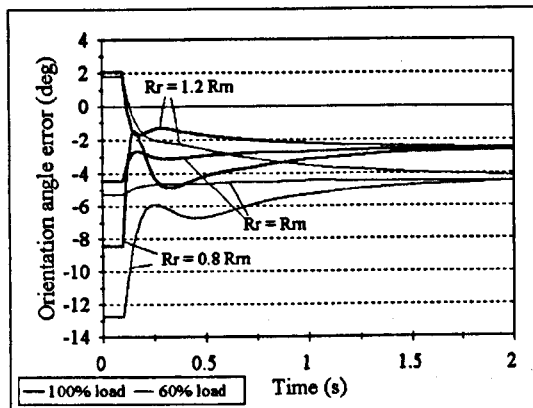
b. rotor flux error



b. rotor flux error



c. orientation angle error



c. orientation angle error

Figure 6.15 : Identification of R_r by the iron-loss-adaptive identifier at the rated speed, rotor flux estimator with iron loss, 4 kW machine.

Figure 6.16 : Identification of R_r by the iron-loss-adaptive identifier in the field-weakening region, 125% speed, rotor flux estimator with iron loss, 4 kW machine.

Operation of the drive in the base speed region is shown in Fig. 6.17, for two values of the actual R_r and three levels of load torque. The simplified estimator of Fig. 3.7, with a variable value of R_r (and hence T_{lr}) is considered. As the $R_r = R_{rn}$ case results in no initial detuning, it is omitted from the Fig. 6.17. It can be seen that R_r identification works very well for 100% and 60% torque levels, with accurate identification of R_r and final detuning lower than 1% for the rotor flux error and less than 1° for the orientation angle error. The convergence of the identification process is, as expected, quite slow for the 25% load.

Figure 6.18 presents the responses for operation in the field-weakening region, for 100% and 60% load torque. There is no initial detuning in the case $R_r = R_{rn}$ and therefore the identifier remains inactive. For the other two values of the actual R_r , identification is accurate and it is performed with a satisfactory speed of convergence. The initial detuning is fully compensated after the identification is initiated.

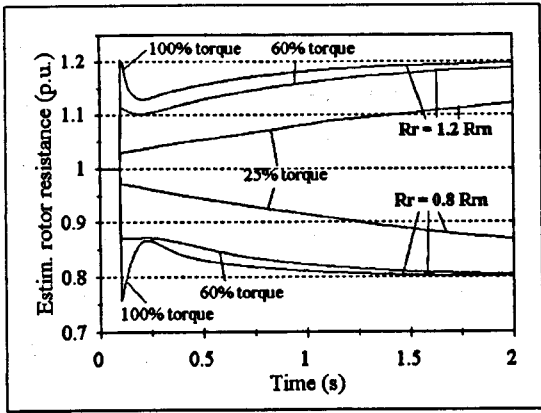
The above discussion suggests that full compensation of detuning can be achieved in both base speed and field-weakening regions by utilising the combination of the R_r identification scheme based on equations (2.89) and (6.2) and an improved estimator with both main flux saturation and iron loss.

6.4. SUMMARY

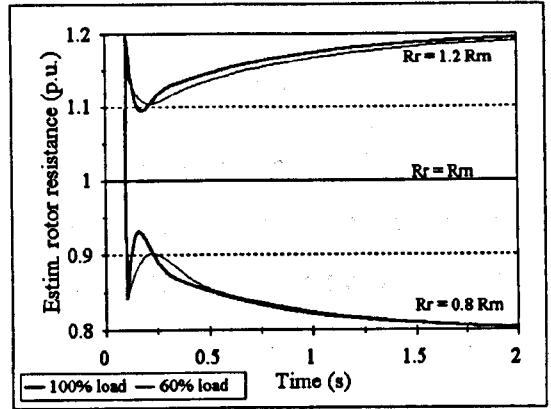
The chapter investigated the identification of the rotor resistance using 'model reference adaptive control' method based on the reactive power.

The performance of the CPM-based identification scheme was investigated first. It was shown that R_r identification at light load is performed slowly and with big errors, indicating that identification would not work at zero load at all. The CPM-based identifier exhibited poor performance in certain cases, due to neglect of main flux saturation and/or iron loss. It was able to compensate detuning due to iron loss in the base speed region, although at the expense of the R_r identification accuracy. The identified values of R_r were 5% to 20% smaller than the actual ones, depending on the load. Although the initial detuning was compensated, these wrong values of R_r imposed the problem that detuning reappeared in the new steady-state operation, when the load was changed. It was concluded that iron loss was the main contributor to the erroneous R_r identification in the base speed region. On the other hand, main flux saturation had a

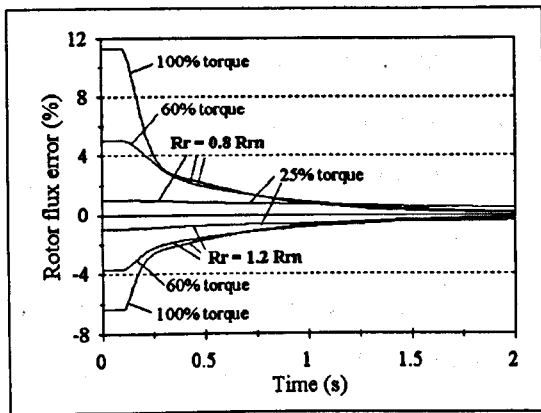
dominant detuning influence in the field-weakening region. It was shown that not only R_r was wrongly identified, but the errors in R_r were greater than in the base speed region, amounting to about 10% and 15% for 125% and 150% speed, respectively. Furthermore, the final detuning still existed. The final values of the rotor flux error



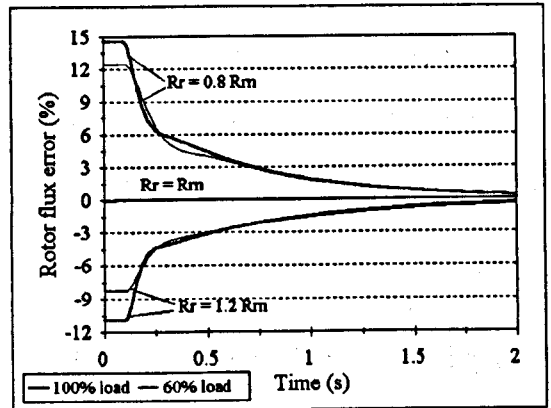
a. Rotor resistance



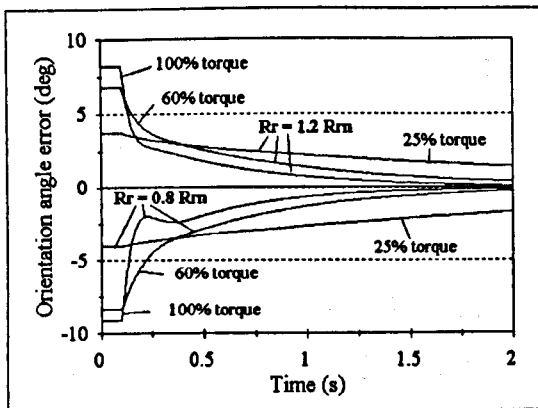
a. Rotor resistance



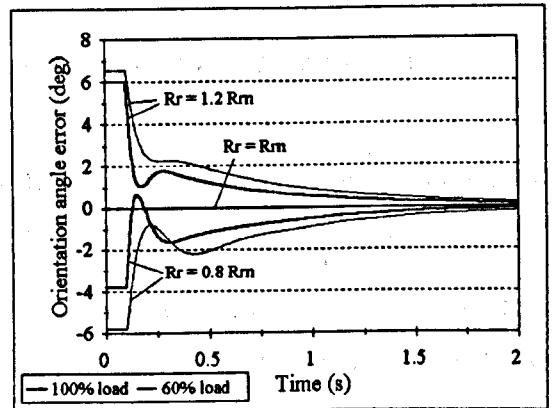
b. Rotor flux error



b. Rotor flux error



c. Orientation angle error



c. Orientation angle error

Figure 6.17 : Identification of R_r at the rated speed, both main flux saturation and iron loss included in both rotor flux estimator and R_r identifier, 4 kW machine.

Figure 6.18 : Identification of R_r in the field-weakening region, 125% speed, both main flux saturation and iron loss included in both rotor flux estimator and R_r identifier, 4 kW machine.

depend on speed only, while the final values of the orientation angle error depend on both speed and load torque.

Sensitivity of the CPM-based R_r identification scheme to inaccurate knowledge about machine inductances was elaborated next. It was confirmed that both the accuracy of the identifier and the speed of convergence are dependent on the accurate knowledge about the mutual inductance. Moderate changes in leakage inductances did not have a significant effect on the performance of the CPM-based R_r identifier.

Analyses of drive operation when the CPM-based R_r identifier was used in conjunction with a saturation-adaptive estimator suggested that this is not a good solution in the field weakening. It was shown that in certain cases the final detuning was even greater than the initial detuning, suggesting that the drive operates better with no identifier at all.

Two improved R_r identifiers were proposed. The first one has the structure identical to CPM-based R_r identifier, but it incorporates main flux saturation. It is intended to be used in conjunction with a saturation-adaptive rotor flux estimator, from which it obtains information on the estimated mutual inductance. The simulation analysis revealed that this improved R_r identifier was fully capable of eliminating detuning in the steady-state operation, but the problem of wrongly identified R_r still remained.

The second improved R_r identifier includes iron loss. The iron loss can be included in the identifier in several different ways. As the improved identifier should be used together with an improved rotor flux estimator that includes iron loss, the design which results in a simple improved R_r identifier was proposed. The improved identifier acquires information on magnetising flux components from an improved estimator. At the same time it provides the information on identified R_r to the estimator. The improved R_r identifier performed very well in the base speed region for medium loads and full load.

Finally, the second improved R_r identifier was combined with an improved rotor flux estimator that includes both main flux saturation and iron loss. Again, the information on magnetising flux components is provided from an improved estimator. Simulation analysis showed that this combination provided full compensation of detuning in both base speed region and field-weakening region.

7. EXPERIMENTAL INVESTIGATION

7.1. INTRODUCTION

This chapter presents an extract of the experiments conducted within the research project. The vector-controlled drive and the measuring equipment are described in section 7.2, while section 7.3. deals with identification of the machine parameters from standard tests. A novel method for identification of the inverse magnetising curve, that utilises both PWM inverter and the vector-controlled drive that are later used for normal operation, is proposed and verified in section 7.4. Section 7.5. presents the experiments concerned with determination of the slip gain. Finally, experiments concerned with detuning in the RFO drive due to parameter variation are described and results presented in sections 7.6 for steady-state operation and in section 7.7 for transient operation. Section 7.8. summarises the chapter.

7.2. DESCRIPTION OF THE DRIVE AND OF THE MEASURING EQUIPMENT

7.2.1. The vector-controlled drive

The experiments are conducted using the drive produced by the Vickers company. The three-phase 50 Hz four-pole induction motor of 2.3 kW rating is supplied by the DBS 04 type controller that incorporates 8/22 inverter (8 A rms is the nominal current, while 22 A is the peak current of the inverter). The control circuitry is based around 8051 microcontroller and TMS30C14 digital signal processor. While the speed control and field orientation are digital, the current control loop is analogue, resulting in the hybrid realisation.

The induction motor incorporates a resolver as a position sensor. An interesting feature of the motor is that it does not have a cooling fan. The current-controlled voltage source inverter operates at 10 kHz switching frequency. The current control loop is equipped with two current sensors that provide feedback signals. DC bus voltage is detected for protection purposes only and the drive is disabled if undervoltage occurs. The excessive DC voltage that occurs during braking is suppressed by an internal braking resistor.

Certain drive parameters can be set and changed digitally, either via special Vickers keyboard or via serial link of a PC. Some of them are protected by a password. The operation of the drive can be controlled either by these two digital links or by analogue signal of ± 10 V brought to the appropriate connector on the front panel of the drive.

The control algorithm is of feed-forward (indirect) type. It is a simplified version of the indirect feed-forward rotor flux vector controller proposed in [Levi et al., 1990], that incorporates provision for compensation of main flux saturation in the field-weakening region. Operation in the field-weakening region is enabled by reducing the rotor flux reference above the base speed. Hence the rotor flux reference is equal to the rated rotor flux below the base speed while it is reduced above the base speed using a pre-programmed law. The maximum speed in the field weakening is 8000 rpm. Although several papers suggested that there are certain laws that enable achieving higher torque/ampere ratio, [Kim and Sul, 1997; Seibel et al., 1997; Bünthe et al., 1996], the drive under consideration here utilises the traditional law for variation of the rotor flux reference in the field-weakening region [Joetten et al., 1983]:

$$\psi_r^* = \psi_m \frac{\omega_B}{\omega} \quad , \quad (7.1)$$

Operation with reduced rotor flux leads to an increase in the magnetising inductance in the machine. If stator d -axis current command is to be correctly set, it is necessary to compensate for the variation of main flux saturation in the machine, by including the inverse of the magnetising curve in the control system. As shown in [Levi et al., 1990], an indirect feed-forward rotor flux oriented controller with partial compensation of main flux saturation can be described with the following equations :

$$\psi_m = \psi_r^* + T_{lr} \frac{d\psi_r^*}{dt} \quad , \quad (7.2)$$

$$i_{ds}^* = i_m(\psi_m) + \frac{T_{lr}}{L_{lr}} \frac{d\psi_r^*}{dt}$$

$$\omega_{sl}^* = K_1 \frac{i_{qs}^*}{\psi_r^*} \quad K_1 = \frac{L_{mn}^*}{T_m^*} = \text{const.} \quad (7.3)$$

$$i_{qs}^* = \frac{1}{K_2} \frac{T_e^*}{\psi_r^*} \quad K_2 = \frac{3}{2} P \frac{L_{mn}^*}{L_m^*} = \text{const.}$$

Indirect vector controller described with the above relationships neglects cross-saturation (i.e., impact of variation of q -axis magnetising current on the value of the

magnetising inductance) and variation in the ratio of magnetising inductance to rotor inductance in (7.3), [Levi et al., 1990]. If rotor speed is assumed to vary much slower than the electromagnetic transients, then rate of change of rotor flux reference in (7.2) is slow. It is therefore possible to neglect the rate of change of rotor flux reference, so that eqs. (7.2) reduce to :

$$\psi_m = \psi_r^* \quad i_{ds}^* = i_m(\psi_m^*) \quad (7.4)$$

The rated value of the rotor flux is in general not known. However, rated magnetising current can be estimated from the rated stator current and the rated power factor. It should be noted that the magnetising curve identification method, that is to be described in the Section 7.3, does not depend on accuracy with which rated magnetising current is determined. If the rated magnetising current is taken as an independent input into the system, it is possible to introduce normalised rotor flux value and normalised inverse magnetising curve. Indirect feed-forward rotor flux oriented controller then takes the form shown in Fig. 7.1. The output of the PI speed controller in Fig. 7.1. is the stator q -axis current command. This is slightly different than the law given by (7.3), and the explanation is that the division by both constant K_2 and the commanded rotor flux value are taken care of by the speed controller and its internal scaling system. Stator d -axis current command is generated as the product of the rated value and a per unit value, which is obtained at the output of the inverse magnetising curve as function of the per unit rotor flux command (which is function of speed). All the per unit values in Fig. 7.1 are identified with the index *p.u.* Slip gain (SG) is a constant parameter, given from (7.3) with :

$$SG = \frac{L_{mn}^*}{T_m^* \psi_m^*} \quad (7.5)$$

Parameters that can be changed by the user are gains of the PI controller (called KP and KI), cut-off frequency of the speed error filter (DF), rated stator d -axis current (ID), base speed at which field-weakening starts (MN), two parameters of the magnetising curve (FB and FS) and the slip gain K_{sl} (SG). Such a variety of user-adjustable parameters enables pairing of an inverter to any motor that has rated power up to the inverter capability. Additionally, this enables great versatility of the drive and results in a very good performance in various applications, pending appropriate setting of these parameters.

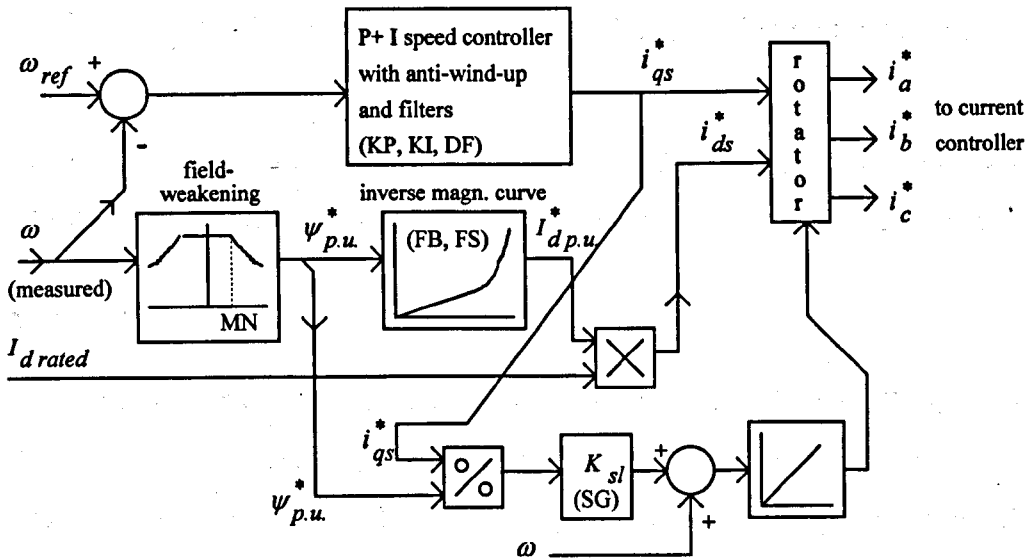


Figure 7.1: The indirect RFO scheme implemented in the Vickers drive.

7.2.2. Measuring equipment

For experiments utilising the sinusoidal supply, three Tektronix CDM250 digital multimeters are used as Am-meters, while two Metrix MX545 digital multimeters are used as Volt-meters. Additionally, two Feedback EW604 electronic Watt-meters are utilised for measurements of input active power. A stroboscope is employed for checking that slip is negligible during no-load test.

When the motor is operated as the vector-controlled drive, the motor phase current is recorded using the Tektronix AM6203 Hall-effect probe and Tektronix AM503 amplifier. This system can accurately record currents of up to 25 A with frequencies from 0 Hz to 20 MHz. The amplifier is designed to be connected to an oscilloscope to which it provides analogue signal of up to ± 50 mV. The Hewlett-Packard HP35665A dynamic signal analyser is used for recording the current waveforms and/or spectra.

For recording the PWM voltages, a potential divider is used in conjunction with oscilloscope probes with attenuation of 10. Additionally, a low-pass filter has been designed in order to reduce the high-frequency components since only the fundamental harmonic of the voltage will be of interest in the tests that are to be described. Line voltage is recorded by connecting two oscilloscope probes to two attenuated and filtered phase voltage signals. Using such an arrangement the influence of the EMC noise is suppressed. The two signals are recorded by the HP35665A analyser and consequently

processed, in order to obtain the voltage spectra and information on fundamental voltage harmonic.

Information on the speed is obtained from the controller as an analogue ± 10 V signal, with resolution of 800 rpm/V. The signal is also recorded using HP35665A analyser.

7.2.3. Load characteristics

Loading of the vector-controlled induction machine is provided by a DC machine. It is operated as a generator, feeding a resistor bank. The load torque therefore linearly rises with speed for a given resistor bank switch position, while the power rises with the square of speed, as shown in Fig. 7.2. The field current of the DC machine is adjusted in such a way that 100%, 70%, 50% and 20% of the rated torque is obtained at 1500 rpm (1 p.u.) with the switch on the resistor bank positioned to 10, 7, 5 and 2, respectively. The power and torque profiles of the Fig. 7.2 are obtained using the assumption that efficiency of the DC machine is 0.87 throughout the considered speed range.

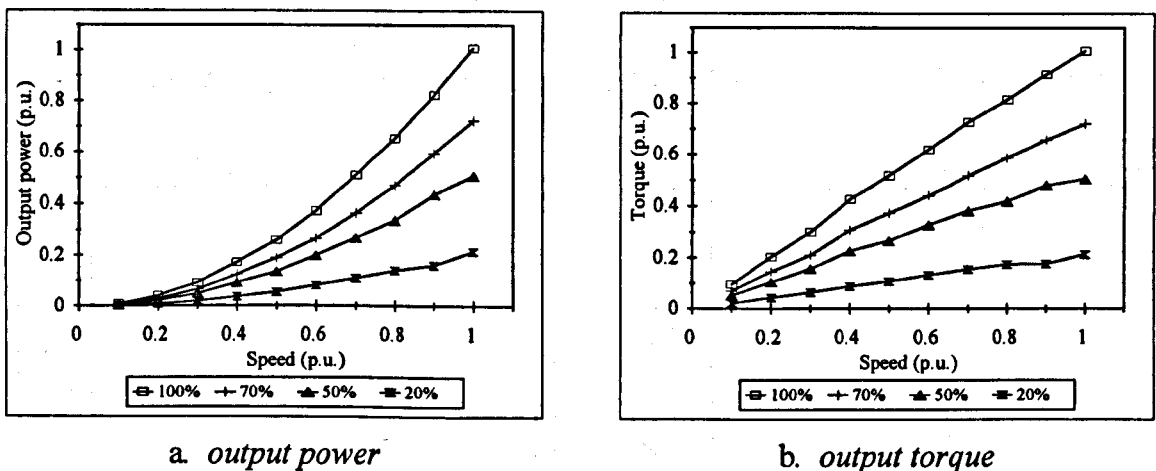


Figure 7.2 : Variations of output power and output torque with speed for several positions of the resistor bank switch.

7.3. IDENTIFICATION OF THE MACHINE PARAMETERS BY STANDARD TESTS

The standard set of identification experiments was performed. The DC test for identification of the stator resistance included the power cable and the identified per-

phase value was 0.7Ω . The blocked-rotor test with reduced voltage was performed next. The current and input power recorded during blocked rotor test performed with 50 Hz sinusoidal supply are shown in Figure 7.3.

Consequent processing of these data has resulted in the following values :

$$R_r = 0.926 \Omega ; L_{ls} + L_{lr} = 7.723 \text{ mH} .$$

As the next step, two series of no-load tests with sine-wave 50 Hz supply were performed. The voltage was changed by an autotransformer. Variations of no-load current and input power with no-load line-to-line voltage are shown in Fig. 7.4.

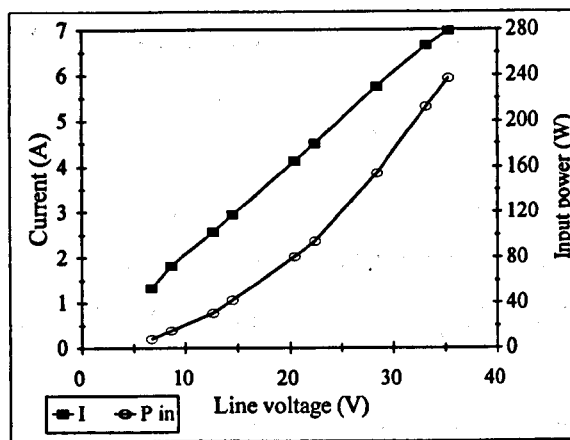
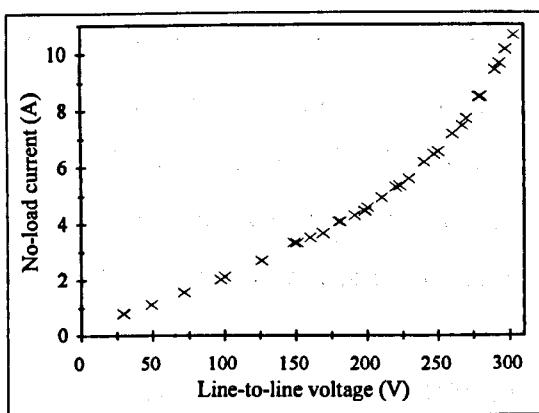
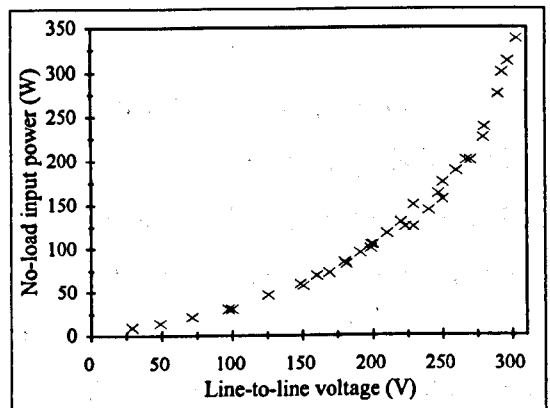


Figure 7.3 : Current and input power during locked rotor test of the 2.3 kW motor.



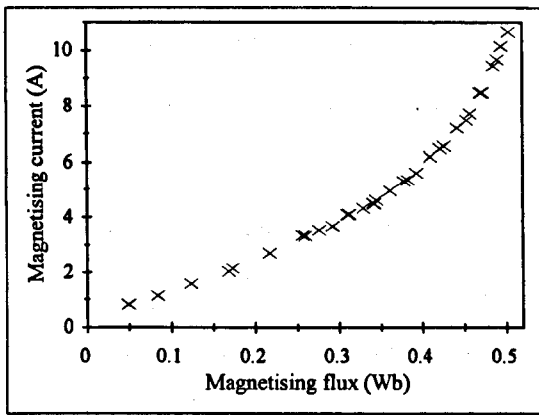
a. current in no-load experiments



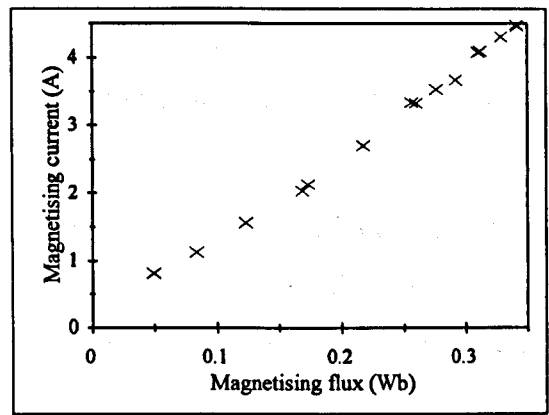
b. input power in no-load experiments

Figure 7.4 : Results of no-load experiments with sinusoidal supply - 2.3 kW motor.

The recorded data are processed and the resulting inverse magnetising curve is shown in Figure 7.5. Figure 7.5.a shows the whole inverse magnetising curve while Fig. 7.5.b shows only the operating region that is later used for vector-controlled operation.



a. full inverse magnetising curve



b. part of the inverse magnetising curve

Figure 7.5 : The inverse magnetising curve obtained from no-load experiments with sinusoidal supply - 2.3 kW motor.

From the results of the no-load tests, the mechanical losses of the motor are estimated by the extrapolation method. They are found to be about 12 W at 1500 rpm, which is negligible 0.5% of the motor's rated power. The reason for so untypical value is the absence of the cooling fan. Rated iron loss is estimated to be 60 W.

7.4. NOVEL METHOD FOR MAGNETISING CURVE IDENTIFICATION

7.4.1. Overview of the existing methods

Numerous applications of rotor flux oriented induction machines require operation in wide field weakening region [Kim and Sul, 1997]. As the available voltage is limited in this region, it is necessary to reduce the rotor flux reference as the speed increases. The issue of optimal rotor flux reference variation in the field weakening region has been extensively investigated in recent times [Kim and Sul, 1997; Seibel et al., 1997; Grotstollen and Wiesing, 1995; Bunte et al., 1996]. The oldest and the simplest method is to vary rotor flux reference above base speed in an open-loop manner, in inverse proportion to the speed of rotation [Joetten et al., 1983]. Such a variation was found to be far from optimal [Kim and Sul, 1997; Seibel et al., 1997; Bunte et al., 1996] and a number of control schemes have been proposed for improving the operation of induction machine drives at high speeds. Their good feature is that, as stator d -axis current reference is obtained by means of a voltage controller, information on the magnetising inductance is not required. Control is therefore insensitive to variation of the

magnetising inductance, caused by variation in flux setting. Improved operation in the field-weakening region is however achieved at the expense of substantially increased complexity of the control scheme, in which some form of a voltage controller is required.

From the point of view of a drive manufacturer, control system should be as simple as possible [Vickers, 1996]. The standard solution in drives available on the market is to provide operation in the field-weakening region without additional voltage controllers. The rotor flux reference is changed in inverse proportion to the speed, by the law given with (7.1). Such an approach, although not optimal, continues to treat the machine as current-fed even in the field-weakening region. Simple structure of the control systems is therefore retained in the whole speed range. The drawback of this approach is that variation of the actual magnetising inductance significantly affects operation of the drive. It is therefore necessary to compensate for this variation, by either embedding the magnetising curve in the control system [Levi et al., 1990; Wieser, 1997] or by providing on-line identification of the magnetising inductance [Choi et al., 1997]. The former method is actually an open-loop (feed-forward) compensation of magnetic saturation, achieved by a suitably modified control system. This approach requires knowledge of the magnetising curve, which has to be identified off-line, during commissioning of the drive.

Several identification methods that utilise special supply and special measurement equipment have been proposed. The method proposed in [Boldea and Nasar, 1987b] identifies the stator inductance but requires integration of the current. A simple method for identification of the magnetising inductance, proposed by [Stankovic et al., 1997], utilises a switched DC excitation and, in conjunction with standard no-load tests, enables accurate determination of the stator leakage inductance. Drawbacks of these methods are that voltage integration is required and the neutral of the machine has to be accessible.

Identification of the magnetising curve, using vector control system and PWM inverter, has been extensively investigated as well. An ideal method should enable identification at standstill with single-phase AC or DC supply, should require measurement of currents only, should be simple to implement and should be accurate. Unfortunately, such a method is not available at present.

If identification is performed on the basis of only current measurements at standstill, it is in general necessary to apply statistical methods in data processing, such as recursive least squares [Ruff and Grotstollen, 1994, 1996]. Accuracy of the method significantly deteriorates below certain magnetising current value, therefore this approach is neither simple nor accurate enough.

If measurement of stator voltages is allowed, it is possible to avoid use of statistical methods. The use of reference voltages instead of measured voltages, [Rasmussen et al., 1996], is in general unsatisfactory due to inverter non-linearity which is very pronounced at low voltage levels. Therefore identification is performed from measured data. Methods of this group [Klaes, 1991; Kwon et al., 1994], that are purely experimental in nature, are good enough for commissioning but are not applicable for self-commissioning as drives are usually not equipped with voltage sensors.

A rather different approach is described in [Levi, 1992]. Although identification is performed at standstill, all the three-phases of the machine are energised and standstill condition is achieved by means of closed loop speed control. Only current measurement is needed, but the method requires that the vector controlled induction motor is coupled mechanically to a controllable load. It is therefore not suitable for either self-commissioning or commissioning of the drive.

This section describes a simple and accurate experimental method for the magnetising curve identification in rotor flux oriented induction machines. The method is developed for indirect feed-forward control scheme and is applicable when inverse magnetising curve is included in the controller as a suitably chosen analytical function with unknown coefficients. Identification is performed on the basis of measurement of stator voltage fundamental component in steady-state (this is the only required measurement) under no-load conditions at various operating speeds in the field weakening region. As the machine rotates and as voltage measurement is required, the method is not suitable for self-commissioning. However, its simplicity and accuracy make it a good choice for commissioning, provided that the machine is not coupled to the load and that the voltage measuring equipment is available on-site.

Implementation of the method requires that rated magnetising current of the machine is known and that stator leakage inductance has already been identified. Rated magnetising current of the machine can be estimated from nameplate data (rated stator

current and power factor), while stator leakage inductance can be obtained from numerous already available procedures for induction motor parameter identification during commissioning stage. If an accurate value is not available, an estimate is sufficient - as will be shown later, sensitivity of the method to inaccurate value of stator leakage inductance is small.

7.4.2. Approximation of the inverse magnetising curve

Implementation of the scheme of Fig. 7.1 requires analytical representation of the inverse magnetising curve. In the drive dealt with here the curve is given in terms of per unit values, so it is represented with a simple two-parameter function [Vickers, 1996] :

$$i_{m(pu)} = a\psi_{m(pu)} + (1-a)\psi_{m(pu)}^b \quad (7.6)$$

The connection between coefficients a and b and the user-adjustable parameters FS and FB of the drive are : FS= b , while FB = (1- a)x255 [Vickers, 1996]. Coefficients a and b (i.e. FB and FS) are unknown and will be determined by the process of the inverse magnetising curve identification. It should be noted that the region of interest is only from the rated flux value downwards. Figures 7.6 and 7.7. illustrate the approximation given with (7.7). Figure 7.6. results from varying the coefficient b while the coefficient a is fixed, while figure 7.7. results from varying the coefficient a while the coefficient b is fixed. As can be seen from Fig. 7.7, influence of the coefficient b on the inverse magnetising curve approximation is very small for flux values from zero up to 1 p.u.. Higher the value of the coefficient a is (i.e. less saturated a machine is), lower the influence of coefficient b is.

Therefore, identification process can be reduced to determination of the coefficient a only, by fixing the coefficient b in advance (adopted here as $b=7$). Such a simplification can be advantageous for on-site commissioning. However, it should be pointed out that this simplification is only a further possibility and that the developed identification method does not rely on this simplification. As that reduction of the problem to the identification of the coefficient a is not mandatory, it is possible to perform fitting of both coefficient a and b from experimentally obtained data. The only constraint in such case is that coefficient b should be integer.

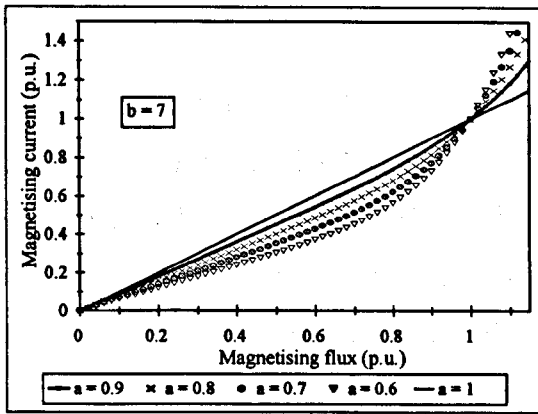
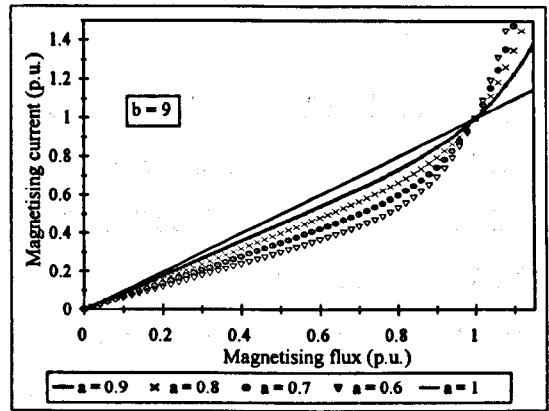

 a. coefficient $b=7$

 b. coefficient $b=9$

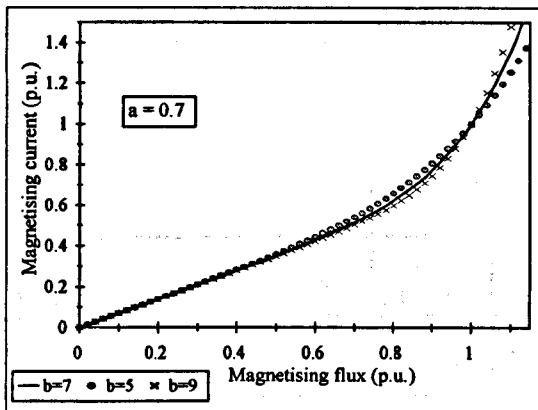
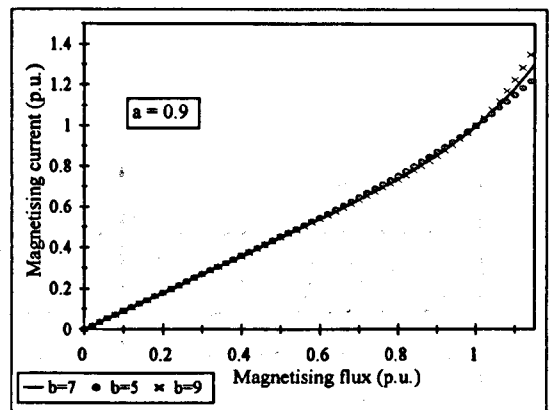
 Figure 7.6: Impact of the coefficient a on the inverse magnetising curve approximation.

 a. highly saturated curve ($a=0.7$)

 b. less saturated curve ($a=0.9$)

 Figure 7.7: Impact of the coefficient b on the inverse magnetising curve approximation.

7.4.3. Theoretical background of the novel procedure

In steady-state no-load conditions ($i_{qs}^* = 0$, $\omega_{sl} = 0$), the model of 2.2.5. (iron losses neglected) reduces to :

$$v_{ds} = R_s i_{ds}^* \quad (7.7)$$

$$v_{qs} = \omega_r L_s i_{ds}^* \quad (7.8)$$

The amplitude of the no-load voltage is :

$$v = \sqrt{v_{ds}^2 + v_{qs}^2} = i_{ds}^* \sqrt{R_s^2 + (\omega_r L_s)^2} \quad (7.9)$$

As R_s is much smaller than the product $\omega_r L_s$ (provided that ω_r is sufficiently large) the stator resistance can be neglected, yielding :

$$v \approx v_{qs} = \omega_r L_s \dot{i}_{ds}^* \quad (7.10)$$

In order to confirm the validity of this approximation, calculations of no-load voltage for both 50 Hz and 20 Hz operation of the three induction machines have been performed and the results are shown in the Table 7.1. The flux and the magnetising current are of rated value and the errors that result using approximate expression (7.10) are negligibly small. At lower speed the errors increase but are still quite small, at least for the 2.3 kW and 4 kW motors. On the other hand, there is the benefit of smaller mechanical and iron losses at lower speeds [Levi et al., 1996a,b], that are neglected in the consideration. This loss reduction actually balances the smaller accuracy due to neglectation of the stator resistance. Therefore it is recommended to perform experiments at lower frequencies, i.e. to start field-weakening at a lower speed than rated.

Table 7.1:

			no-load operation at 50 Hz			no-load operation at 20 Hz		
param. Machine	R_s	L_s	V_{exact} (7.6)	V_{approx} (7.7)	error	V_{exact} (7.6)	V_{approx} (7.7)	error
2.3 kW	0.64 Ω	0.08 H	104.30 V	104.34 V	0.036 %	41.82 V	41.736 V	0.2 %
4 kW	1.37 Ω	0.146 H	218.72 V	218.82 V	0.05 %	87.813 V	87.569 V	0.278 %
0.75 kW	10 Ω	0.46 H	215.1 V	214.59 V	0.239 %	87.111 V	85.836 V	1.486 %

As the next step, the change of voltage in the field-weakening region is considered. When the machine operates in the field weakening region, with rotor flux reference value determined with the traditional law (7.1), stator d-axis current reference is :

$$i_{ds}^* = \frac{\psi_m \omega_B}{L_m^* \omega} \quad (7.11)$$

where ω_B is the base speed at which field weakening is initiated. The commanded magnetising inductance L_m^* is a variable parameter, whose value for each speed setting depends on the actual values of coefficients a and b of the inverse magnetising curve approximation (7.6) that is implemented in the controller. On the other hand, value of the slip gain parameter (SG) is irrelevant in no-load operation, as stator q -axis current command is zero. Existence of mechanical and fundamental harmonic iron losses is

neglected, and rotor electrical speed of rotation ω is regarded as equal to the stator fundamental angular frequency ω_s .

Combining (7.10) and (7.11), the fundamental stator voltage can be given with :

$$v = \psi_m \omega_B \frac{L_{ls} + L_m}{L_m^*} \quad (7.12)$$

Taking the product of rated rotor flux and base speed as 1 p.u., equation (7.12) can be re-written as :

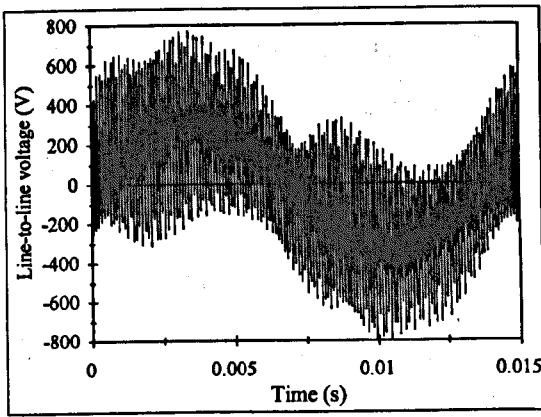
$$v_{pu} = \frac{L_{ls}}{L_m^*} + \frac{L_m}{L_m^*} \quad (7.13)$$

If the inverse magnetising curve approximation in the controller exactly matches the actual magnetising curve, then at all speeds $L_m \equiv L_m^*$. Variation of voltage in (7.12) and (7.13) with increase in speed then occurs only due to variation in term L_{ls} / L_m^* , as magnetising inductance in the controller changes from rated towards unsaturated value. This variation is negligibly small for most machines - it only becomes important for very small machines, with relatively high leakage inductance.

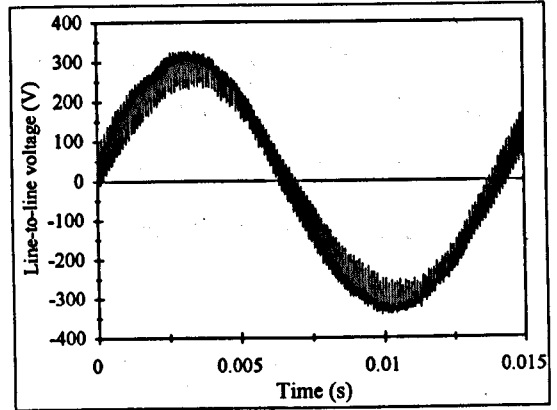
If, however, the inverse magnetising curve approximation in the controller is incorrect, variation in voltage (7.12) can be substantial, as it will be shown in the next section.

7.4.4. Measurement of the currents and voltages

When the machine is supplied from a PWM inverter, problems associated with current and voltage measurements arise. They stem from the existence of the higher harmonics in both current and, especially, voltage waveforms. As only fundamental harmonic of the voltage is of the interest here, there are two possible approaches to extract this information from the PWM voltage: utilisation of a good (like 4th or 6th order Butterworth) low-pass filter [Healey, 1995] or utilisation of a spectrum analyser with some simple low-pass filtering. The second approach, using a voltage divider and a simple first-order passive filter, is utilised here. Figure 7.8 shows the waveforms of unfiltered and filtered voltages. It can be seen that just a simple first-order filter significantly reduces the PWM harmonics.



a. unfiltered voltage

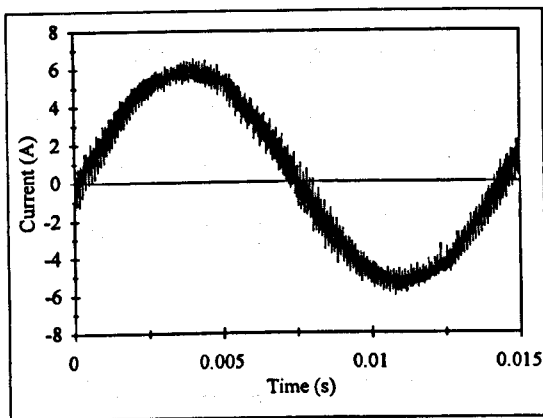


b. filtered voltage

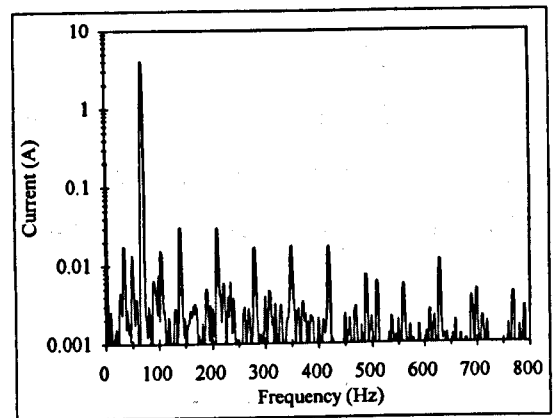
Figure 7.8 : Voltage waveforms during PWM no-load operation at 2100 rpm.

As mentioned earlier, the waveforms of the current are recorded using Tektronix current probe and HP35665A dynamic signal analyser. The current waveform for operation at 2100 rpm (70 Hz) is shown in Fig. 7.9.a.

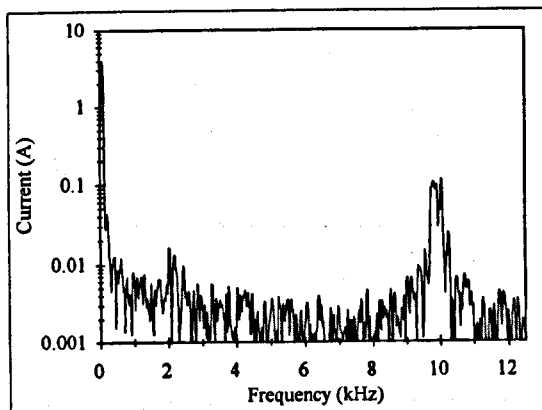
For both current and voltage waveforms, the HP signal analyser is able to process the recorded data and produce a spectra. The spectra of the current are shown in Fig. 7.9.



a. current waveform



c. spectrum up to 0.8 kHz



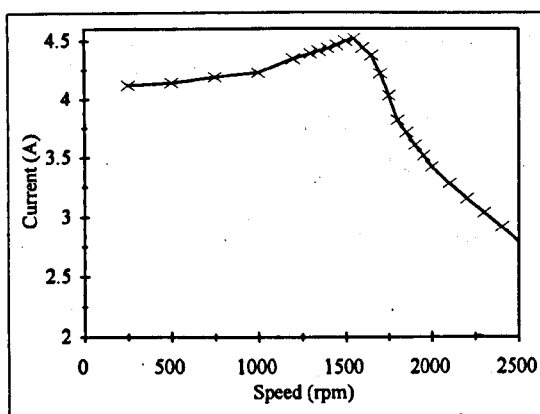
b. spectrum up to 12.8 kHz

Figure 7.9 : Current waveforms and spectra during PWM no-load operation at 2100 rpm.

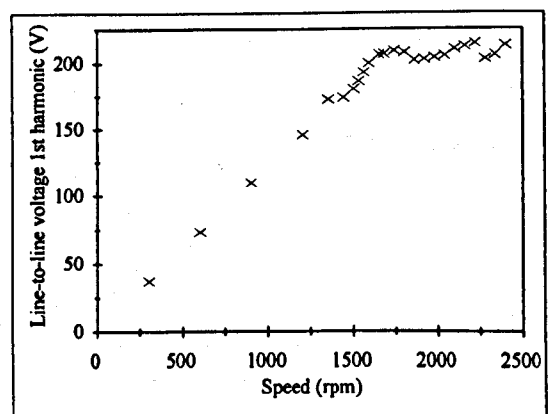
The wider frequency range (Fig. 7.9.b) reveals pronounced high-order harmonics around 10 kHz, which is the inverter switching frequency. From the narrow range spectra (Fig. 7.9.c) it is possible to extract the information on the frequency and amplitude of the fundamental component for a given speed and use those information for the identification procedure.

The procedure for conducting the experiments is as follows. At first, it is necessary to set parameters a and b (i.e. FB and FS) and base speed (MN) and then run the machine at certain speed, without any load. At the moment the choice for these values is irrelevant, as long as they are in some reasonable ranges. Next, line-to-line voltage and phase current are measured in steady-state no-load operation and information on fundamental harmonics of these two is noted. Measurement of the current is not necessary, as it will be shown later. After this, the running speed is changed to obtain another operating point and the new values of current and voltage are noted. The process is repeated until the whole speed region of interest is covered.

The results of the no-load experiments with coefficient settings $a=0.9$, $b=7$ and the base speed 1500 rpm are given in Fig. 7.10. It shows variation of the no-load current and the no-load voltage fundamental harmonics versus speed. It can be seen that there is an increase in the no-load current towards the end of the base speed region and then significant reduction after the field-weakening is entered. Meanwhile, the voltage rises with the frequency in the base speed region and is relatively constant in the field-weakening region.



a. no-load current (fundamental)

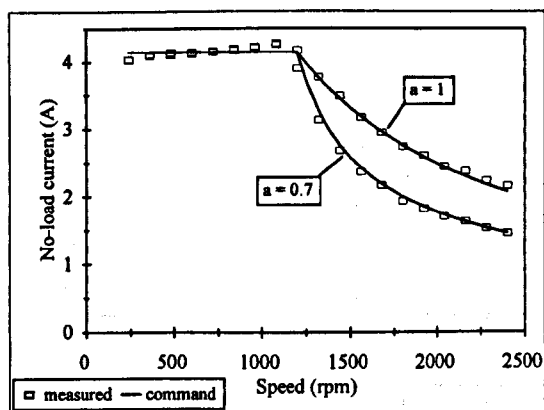


b. no-load voltage (fundamental)

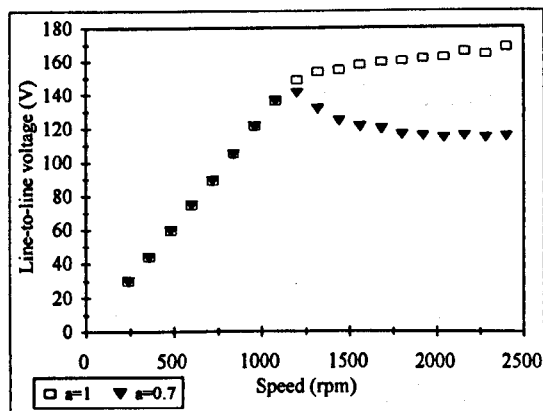
Figure 7.10 : No-load experiments with inverter supply, 1500 rpm base speed.

The increase in the no-load current is caused by increases in both mechanical and iron losses as the frequency rises. Therefore the no-load experiments are repeated but with the field-weakening starting at lower speeds. As fundamental iron loss is of the highest value at rated frequency [Levi et al., 1996a], and as mechanical loss increases with speed, base speed is taken lower than 1500 rpm in an attempt to reduce effects of the neglected losses on accuracy of the subsequent magnetising curve identification. There is another benefit of starting the field-weakening at lower speeds - lower flux values (i.e. deeper field-weakening) can be achieved with reasonable speeds. No-load current for base speed of 1150 rpm is shown in Fig. 7.11.a, for two settings of the coefficient a . The increase of the no-load current in the base speed region is now much smaller and the measured current closely corresponds to the commanded d -axis current, also includes in the Fig. 7.11.a. This confirms the fact that measurement of the stator current is not necessary - the stator d -axis current command can be used instead.

Figure 7.11.b depicts measured fundamental component of the stator line-to-line voltage for two incorrect settings of the coefficient a , with coefficient b set to 7. This figure confirms that variation in voltage (7.12) can be substantial when the inverse magnetising curve approximation in the controller is incorrect. If main flux saturation is neglected in the controller ($a=1$), stator voltage increases in the field weakening region, so that voltage margin available for current control reduces. On the other hand, if saturation is over-compensated ($a=0.7$), voltage in the field weakening decreases. In such a case the stator d -axis current is reduced too much (Fig. 7.11.a), leading to an unnecessary decrease in the motor's transient torque capability.



a. no-load current (fundamental)



b. no-load voltage (fundamental)

Figure 7.11: No-load current and voltage for two incorrect values of coefficient a , 1150 rpm base speed.

7.4.5. Determination of the magnetising curve

Equations (7.10) and (7.11) can be used for calculation of the magnetising inductance as function of the magnetising current (i.e., stator d -axis current reference). If the influence of the stator resistance is neglected, the magnetising inductance can be obtained as :

$$L_m = \frac{v}{\omega} \frac{1}{i_{ds}} - L_{ls} \quad (7.14)$$

It is therefore necessary to measure only the fundamental component of the stator voltage. Speed of rotation equals commanded speed and stator d -axis current reference is used instead of the measured stator no-load current. Knowledge of the stator leakage inductance is required. As mentioned previously, it was determined using standard locked rotor test with sinusoidal supply and the value of $L_{ls} = 3.86$ mH was obtained.

Figure 7.12 illustrates set of measurement results. Field weakening is initiated at 1150 rpm. Fundamental components of the stator current and the stator voltage are measured for different speeds. Measurements are repeated for several values of the coefficient a in the control system. The same experiments are repeated for the base speed of 650 rpm, and the results are given in Fig. 7.13.

For each set of points, that corresponds to one value of the coefficient a , magnetising inductance is calculated using (7.14) at all speed settings. As the no-load current was measured anyway, measured values rather than commanded values of the d -axis stator current are used. Every setting of the coefficient a and every speed correlate to a speci-

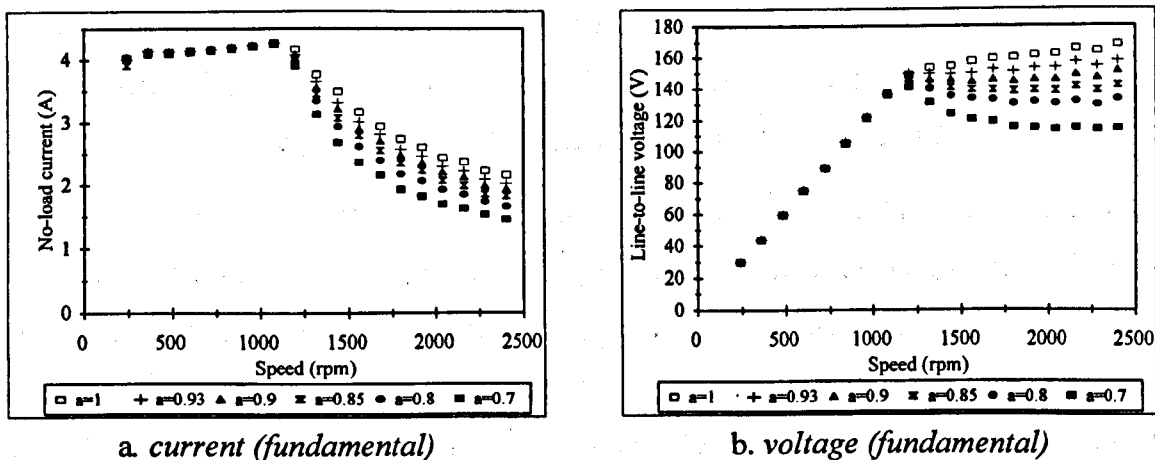
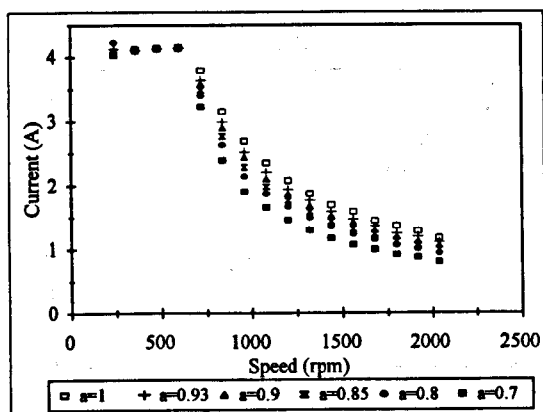
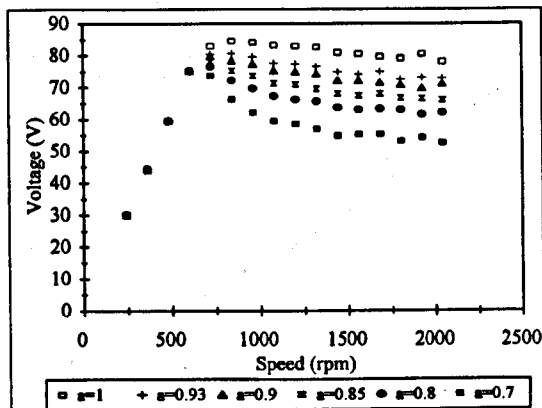


Figure 7.12 : No-load currents and voltages for different settings of coefficient a , 1150 rpm base speed.



a. current (fundamental)



b. voltage (fundamental)

Figure 7.13 : No-load currents and voltages for different settings of coefficient a , 650 rpm base speed.

fic point on the inverse magnetising curve. Aggregation of different points produces the identified inverse magnetising curve of the machine, shown in Fig. 7.14. Figure 7.14.a represents the data obtained for the base speed of 1150 rpm (Fig. 7.12), while Fig. 7.14.b shows the inverse magnetising curve obtained for the base speed of 650 rpm (Fig. 7.13). In the Figure 7.14.b., the points identified by the standard procedure using sinusoidal 50 Hz voltage are shown as well. Agreement between the identified curves using two different procedures is very good.

Figure 7.14 shows that, regardless of the setting of either parameter a or base speed in the indirect vector controller, identified points will always belong to the same curve. This fact proves the accuracy of the procedure and indicates that it is sufficient to execute the described no-load test in the field weakening region with a single pair of value of the coefficients a and b . From Fig. 7.14, the rated magnetising inductance is obtained as 78 mH. Rated rotor flux is therefore 0.33 Wb (or 0.458 Wb peak), for the rated magnetising current of 4.15 A rms. Using these values, fitting of the curves of Fig. 7.14 yields the required values of coefficients as $a = 0.9$ and $b = 7$.

Each of the set of measured stator voltages and currents in Figs. 7.12 and 7.13 encompasses base speed region. Thus large number of measurements are performed with rated rotor flux reference and all these points are supposed to yield the single, rated operating point on the magnetising curve. Some errors in measurements are inevitable and this explains existence of a number of flux values in Fig. 7.14 in vicinity of rated magnetising current.

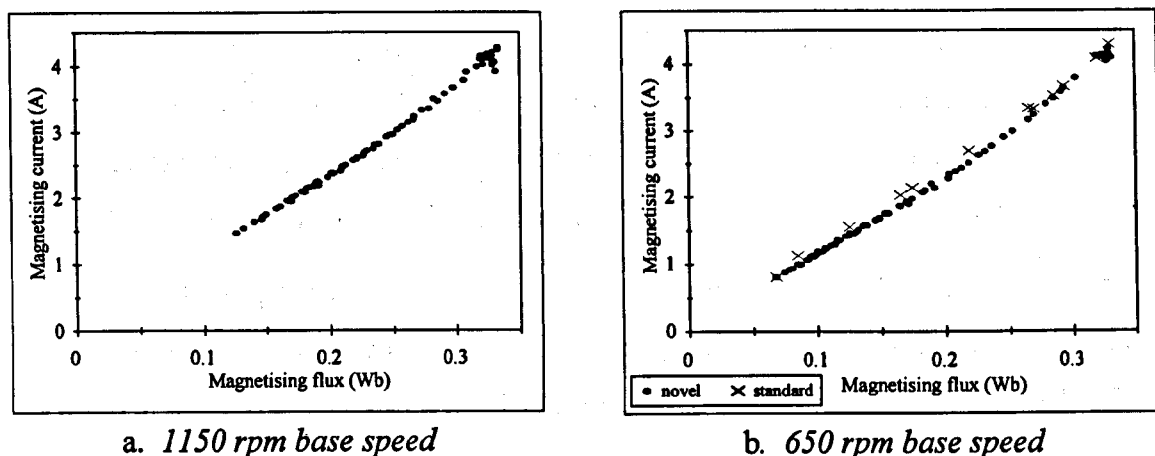


Figure 7.14 : The inverse magnetising curve identified by the novel method, comparison with standard no-load test results included in (b).

7.4.6. Accuracy of the proposed identification method

The proposed procedure requires that inverse magnetising curve is implemented in the controller by means of (7.6), that the machine can run under no-load conditions, that fundamental harmonic of the stator voltage can be measured, that rated magnetising current is known and that stator leakage inductance is determined in advance.

Accuracy with which rated magnetising current is known has no impact on the identification process itself. This is so because the identified portion of the curve is from zero up to the rated value, whatever the rated values is. The rated value of the magnetising current merely sets the rated value of rotor flux, which is subsequently used for operation in the base speed region. However, correct setting of the rated magnetising current (i.e. rated flux) is obviously important for correct operation of the RFO drive.

Selection of the base speed at which field weakening is started appears to be rather arbitrary, but some guidelines are as follows. In order to reduce the influence of neglected losses on the accuracy, it should be lower than rated speed. On the other hand, reduction of base speed compromises the accuracy due to the influence of the stator resistance. The base speed should therefore not be too low. Practically identical results were obtained with base speeds of 1150 rpm and 650 rpm. However, for the base speed of 650 rpm a greater section of the inverse magnetising curve is covered because experiments went deeper into the field weakening region (up to several times the base speed) while still operating at speed lower than twice the machine rated speed.

As mentioned earlier, this particular machine does not have a cooling fan and the mechanical losses are very low. Therefore their contribution to the no-load losses is very small, even for speeds above 2000 rpm. For the standard motor construction, the author advises to (if possible) detach the fan and thus reduce the mechanical losses and their influence on the identification procedure.

Sensitivity of the procedure to an incorrect value of the stator leakage inductance is examined by reconstructing magnetising curve, by means of (7.14), from data obtained for $a = 0.9$, $b = 7$ and base speed of 1150 rpm. Three traces are shown in Fig. 7.15. The first one corresponds to the correct value of the stator leakage inductance ($L_{ls} = L_{lsn}$). This trace at the same time verifies that a single set of voltage measurements in the field weakening region, for any pair of values of the parameters a and b , is sufficient for reconstruction of the magnetising curve. The other two traces are obtained with an underestimate (50% of L_{lsn}) and an overestimate (200% of L_{lsn}) of the stator leakage inductance, respectively. Error in magnetising curve reconstruction appears to be very small if error in stator leakage inductance is up to 50%. It only becomes significant if the error approaches 100%. Figure 7.15 confirms that exact knowledge of the stator leakage inductance is not necessary and that reasonable accuracy is obtained with a moderately correct estimate of the stator leakage inductance.

It should be pointed out that the developed identification method has limited accuracy in the very low flux region, if the magnetising curve of the particular machine has a point of inflexion [Ruff and Grotstollen, 1994, 1996]. The adopted inverse magnetising curve approximation treats the initial part of the curve as a straight line through the origin.

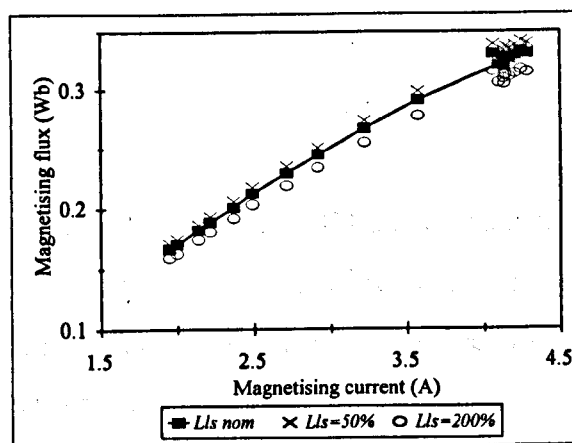


Figure 7.15 : Sensitivity of the proposed identification procedure to incorrect value of the stator leakage inductance.

7.5. DETERMINATION OF THE SLIP GAIN

Accurate determination of the slip gain is essential for proper operation of a vector-controlled drive throughout the whole operating region. Calculation of the slip gain using (7.5) is feasible only if all three parameters on the right-hand side of (7.5) are accurately determined. Hence some other ways of slip gain determination have been devised. The manufacturer of the drive under consideration suggest that the following expression is used :

$$SG = 1.475 \omega_{sl\ nom} \frac{I_{peak}}{I_{qs\ nom}} , \quad (7.15)$$

where 1.475 is internal DSP constant, I_{peak} is the peak current of the inverter and $I_{qs\ nom}$ is the rated torque-producing current of the motor. In this way the matching of motor and inverter is provided. Using this expression, a value of 39 is obtained. However, the matching of the 2.3 kW motor and 8/22A inverter is not perfect. The rated motor current is 10 A while the rated inverter current is 8 A. The maximum commanded d -axis current depends on the inverter rating and the maximum value obtained with this 8/22A inverter is still smaller than the rated magnetising current of the 2.3 kW motor. Therefore the machine is less saturated and the actual rated value of the rotor flux in (7.5) is lower than the manufacturer predicted. The lower level of saturation means that the nominal value of the magnetising inductance is higher than the manufacturer expected it to be. Therefore the value obtained using (7.15) should be increased.

In order to determine the correct value of the slip gain, a simple experimental method, described in [Levi, 1992] and aimed at magnetising curve identification, is used here for slip gain identification.

7.5.1. Procedure

The basic idea of the method of [Levi, 1992] stems from the vector control theory. When the flux command is constant (base speed region, for instance) and the slip gain is correctly set, the actual rotor flux is kept at constant value. In such a case the developed torque is directly proportional to the torque-producing current :

$$T_e^* = T_L = k i_{qs}^* , \quad (7.16)$$

and the relationship $T_e^* = f(I_{qs}^*)$ is a straight line. If, however, the slip gain is incorrectly set, detuned operation occurs and one of the consequences is that actual rotor flux changes. In such a case the relationship $T_e^* = f(I_{qs}^*)$ becomes a non-linear curve.

Hence the method requires to perform measurements with different values of the load torque (which is equal to the developed torque in steady-states) with several settings of the slip gain and then obtain and analyse the function $T_e^* = f(I_{qs}^*)$. The slip gain setting that results in a linear relationship is the correct one.

7.5.2. Measurements

In the following experiments, the system comprising the vector-controlled induction machine and the DC machine (running as a generator) is operated in steady-states. Load levels depend on the operating speed and the resistance of the resistor bank, as the field current is kept constant. Two load profiles of Fig. 7.2 (100% and 50%) are analysed. Phase current of the induction machine is measured using the current probe and the information on the fundamental harmonic is extracted using dynamic signal analyser. The recorded phase currents are shown in Figs. 7.16 and 7.17, for base speed set to 1500 rpm and 1150 rpm, respectively. Four settings of the slip gain have been analysed: 31, 39, 47 and 59, denoted as 66%, 83%, 100% and 125%, respectively.

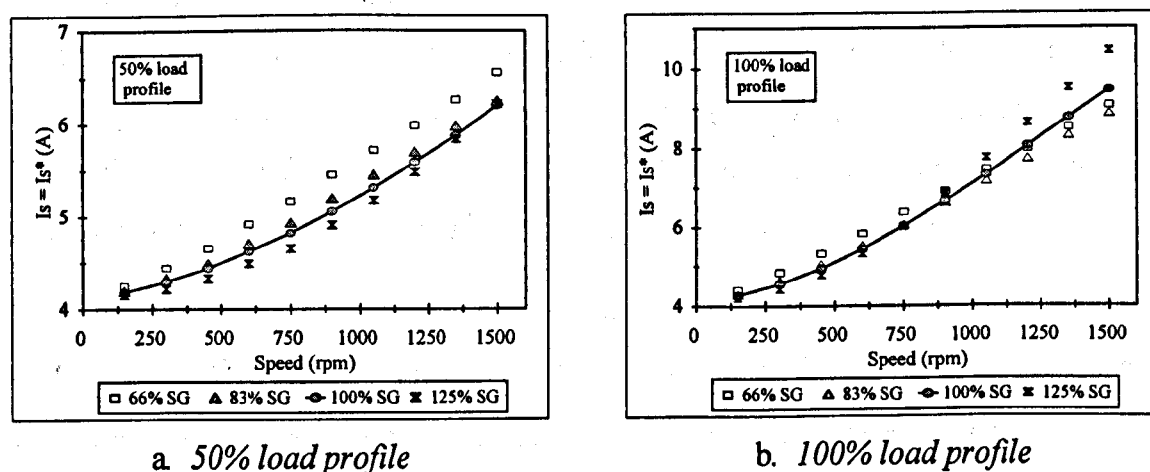
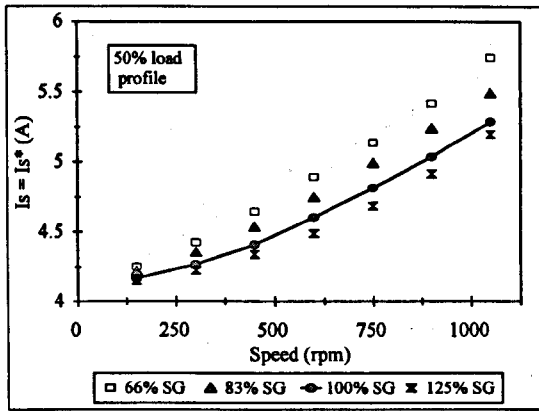
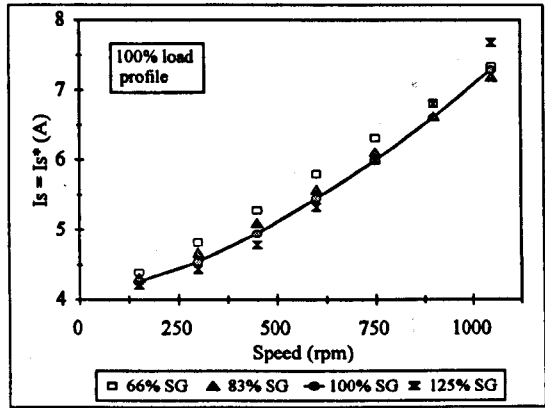


Figure 7.16 : Phase currents (rms fundamental component) with various values of slip gain, operation in the base speed region, 1500 rpm base speed.



a. 50% load profile



b. 100% load profile

Figure 7.17 : Phase currents (rms fundamental component) with various values of slip gain, operation in the base speed region, 1150 rpm base speed.

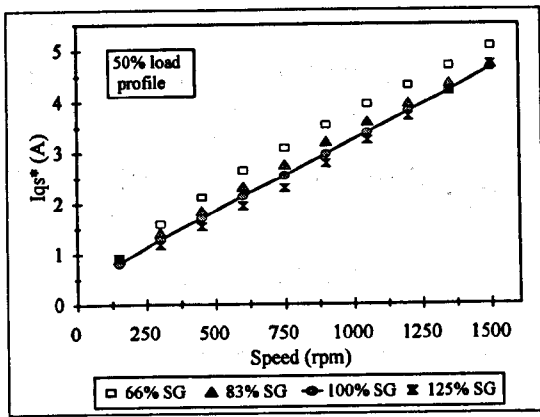
7.5.3. Evaluation of the slip gain

In order to make measurements as simple as possible, two simplifications are adopted. Firstly, since the load torque for the given resistance of the resistor bank is proportional to the speed (see Fig. 7.2.b), the requirement for linearity of the function $T_e^* = f(I_{qs}^*)$ is translated into requirement for linearity of the function $I_{qs}^* = f(n)$. Secondly, since the information on I_{qs}^* is not available from the drive, it is calculated using :

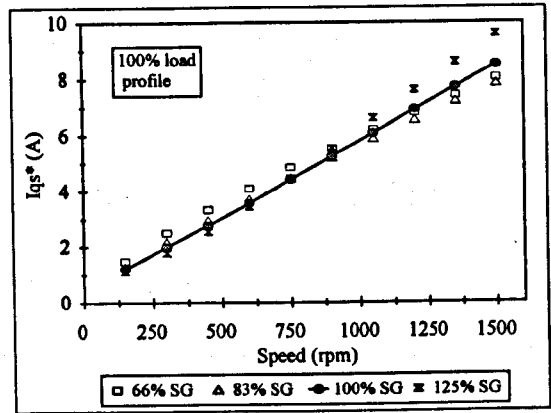
$$I_{qs}^* = \sqrt{I_s^2 - I_{ds}^{*2}} \quad (7.17)$$

The value of I_{ds}^* is already known from the no-load experiments described in the previous section. Meanwhile, as discussed in section 2.4, the commanded stator current is equal to the actual (i.e. measured) stator current ($I_s^* = I_s$), regardless of detuning. Hence the recorded data from Figs. 7.16. and 7.17 are processed using the expression (7.17) and the obtained functions $I_{qs}^* = f(n)$ are shown in Figs. 7.18 and 7.19.

It can be seen that slip gain setting of 100% (SG=47) is the correct one, since it results in a linear relationship $I_{qs}^* = f(n)$. Other settings of the slip gain produce non-linear curves, which can clearly be seen for 100% load profile, Figs. 7.18.b and 7.19.b.

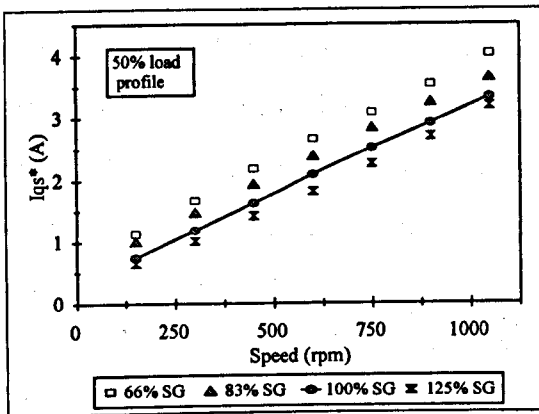


a. 50% load profile

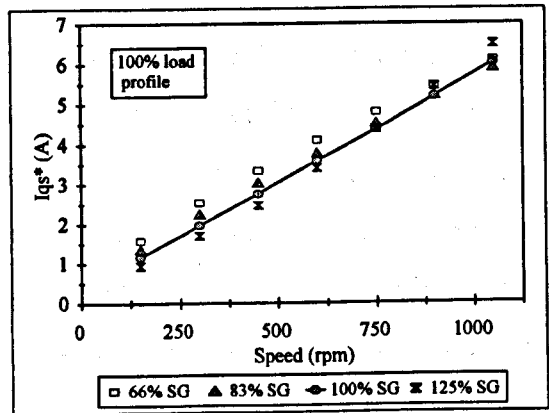


b. 100% load profile

Figure 7.18 : Estimated I_{qs}^* (rms fundamental component) with various values of slip gain, operation in the base speed region, 1500 rpm base speed.



a. 50% load profile



b. 100% load profile

Figure 7.19 : Estimated I_{qs}^* (rms fundamental component) with various values of slip gain, operation in the base speed region, 1150 rpm base speed.

7.6. DETUNING OF THE VECTOR-CONTROLLED INDUCTION MACHINE DRIVE IN STEADY-STATE OPERATION

The three detuning sources, investigated experimentally in this section, are errors in the slip gain setting, thermally induced variations of the actual rotor resistance and errors in the identified magnetising curve. Detuning in the base speed region and in the field-weakening region are analysed separately. Analyses of detuning due to errors in the slip gain were performed using four settings - 66%, 83%, 100% and 125%. Meanwhile analyses of detuning due to thermal effects were performed using rated (100%) slip gain but operating the induction machine in two different thermal situations. Finally,

detuning effects of inaccurate setting of the magnetising curve are analysed for three values of parameter a : 0.9 (the correct one), 1 and 0.7 , with $b = 7$.

7.6.1. Steady-state detuning due to errors in the slip gain setting

7.6.1.1. Steady-state detuning in the base speed region

The base speed n_B for these experiments is set to either 1500 rpm or 1150 rpm and only operation at speeds up to the base speed is analysed, so that induction machine operates with constant flux command (i.e. constant I_{ds}^* command). The recorded amplitudes of the phase currents and the estimated I_{qs}^* are already shown in Figures 7.16-7.19.

Let us at first examine operation with bigger slip gain (125%) setting and compare it with operation with exact slip gain (100%). Operation with light load (up to 50%) with slip gain set to 125% results in a decrease in phase current and I_{qs}^* . This is expected since such an error in the commanded slip gain actually results in the situation depicted in Fig. 2.7. The actual rotor flux ψ_r lags the commanded and its amplitude is smaller than the commanded. Hence the actual I_{ds} is smaller than the commanded. Since the actual total current is equal to the commanded total current, the actual I_{qs} is bigger than commanded. With light load torque, I_{qs} is relatively small and I_{ds} is dominant. Therefore reduction in I_{ds} results in reduction of the total current with respect to the total current obtained with the correct value of the slip gain. However, for operation with torque around 50% (50% load profile at 1500 rpm speed or 100% load profile at medium speeds) I_{qs} starts to play bigger role in the total current. Therefore the curves for 100% slip gain and 125% slip gain start to converge as the load increases. This trend is continued as the load is increased (100% load profile at speeds above 750 rpm) and it can be seen that both phase current and I_{qs}^* for 125% slip gain become bigger than for 100% slip gain as the torque approaches its rated value. It can be concluded that operation with reduced flux level can at light loads be beneficial for efficiency (lower copper loss and lower iron loss), as it was shown in [Kirchen et al., 1987], but that is not the case for heavy loads.

When the machine operates with slip gains of 66% and 83%, a situation opposite to the one explained in the above paragraph results. The actual values of rotor flux ψ_r and I_{ds} become bigger than their commanded values, while I_{qs} becomes smaller than its

command. While the load is light, I_{ds} is dominant and the total current is bigger than the total current obtained with 100% slip gain. As in the previous case, the difference between the currents becomes smaller as the load increases. Finally, as the load approaches rated value, the phase current and I_{qs} become smaller than for the correct value of the slip gain. This happens because an increase in flux level decreases I_{qs} , which becomes dominant at heavy loads.

7.6.1.2. Steady-state detuning in the field-weakening region

In order to investigate detuning in the field-weakening region, the base speed n_B is reduced rather than to operate the machine at speeds higher than 1500 rpm. This is done so because the nominal operating speed of the DC machine is 1500 rpm and field-weakening operation cannot be achieved if the base speed is kept at 1500 rpm. Two lower base speeds are considered - 1150 rpm and 650 rpm - and the recorded phase currents (fundamental harmonic) are shown in Figures 7.20 and 7.21, respectively. From these, the estimated I_{qs}^* values are calculated using (7.17) and shown in Figures 7.22 and 7.23.

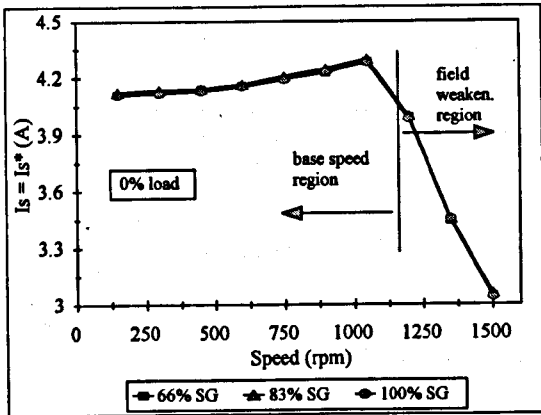
Detuning effects are very small for no-load operation, as can be seen in Figs. 7.20.a and 7.21.a. It could have been expected that there should be no detuning (i.e. no differences in currents) at no-load operation, regardless of slip gain setting. However, mechanical losses of the DC machine represent a small, but not negligible load and some detuning occurs for operation in deep field-weakening (Fig. 7.21.a).

The behaviour in the base speed region with load is the same as discussed in the previous sub-section. The trends observed in the base speed region are also valid in the field-weakening region. Actually, these trends become more pronounced.

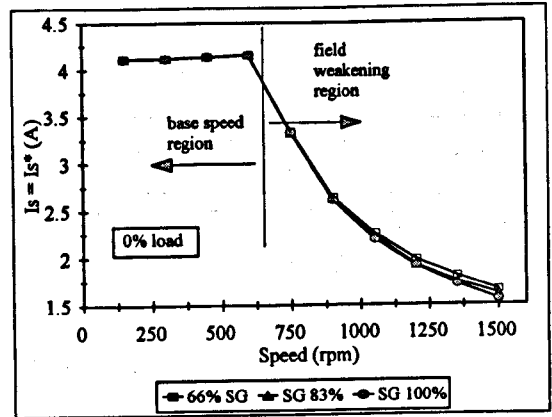
For field-weakening operation with 125% slip gain, flux is reduced both due to reduced flux command and due to detuning. Therefore higher I_{qs} than with 100% slip gain is needed for producing the same torque. As the load increases I_{qs} becomes dominant and the total current with 125% slip gain becomes much bigger than with the 100% slip gain. The differences increase with an increase in both loading and the ratio of operating speed to base speed (n/n_B i.e. ω/ω_B).

The opposite situation is encountered for field-weakening operation with lower slip gains (66% and 83% SG) - the actual flux is bigger than commanded. Hence lower I_{qs}

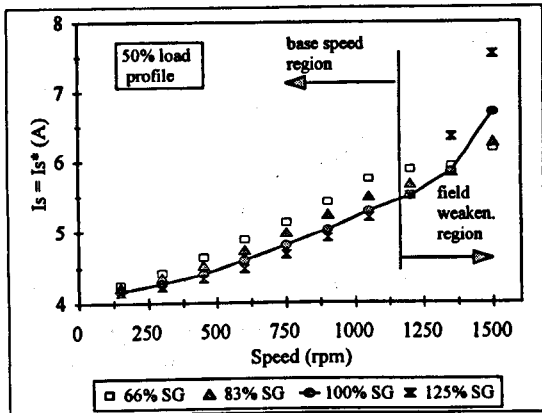
is needed for producing the same torque and the total currents with lower slip gain settings become smaller than the current with the 100% slip gain. The differences in current increase as both load and ω/ω_B ratio increase, as well as with the error in the slip gain command. Although smaller overall current is beneficial for the machine efficiency, the increased flux induces higher emf and therefore the supply voltage has to



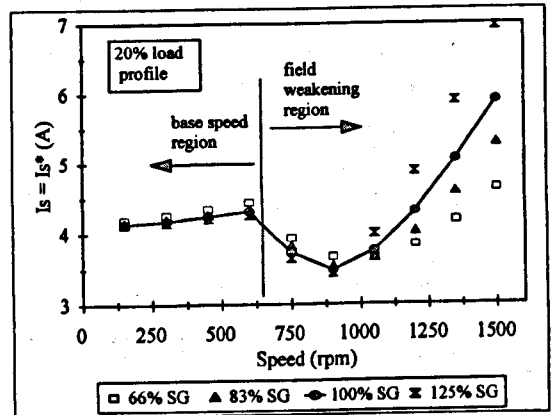
a. no load



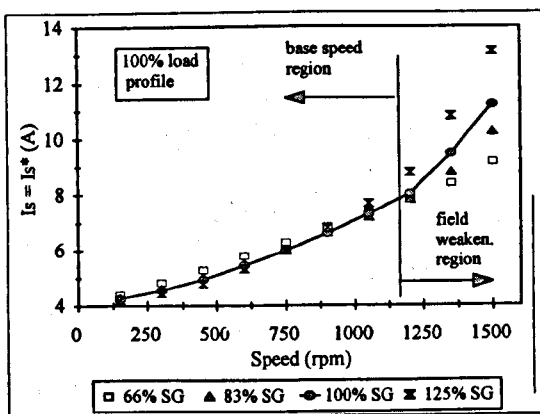
a. no load



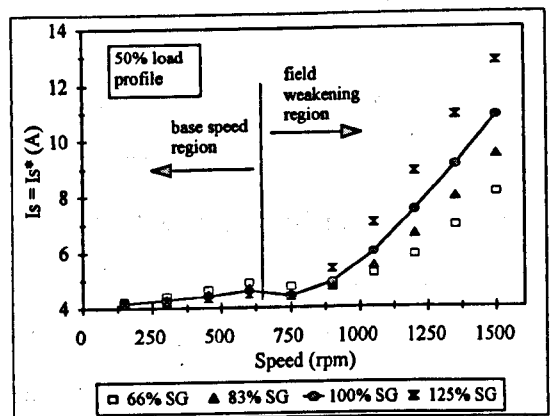
b. 50% load profile



b. 20% load profile



c. 100% load profile

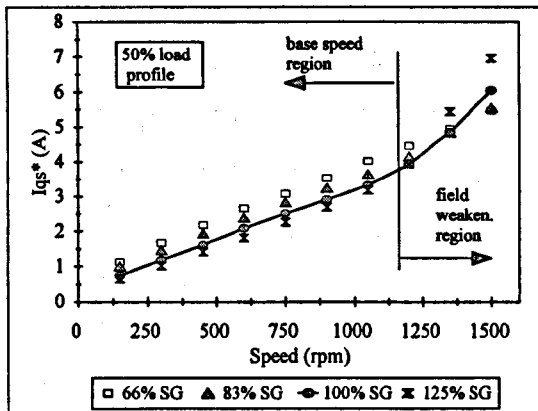


c. 50% load profile

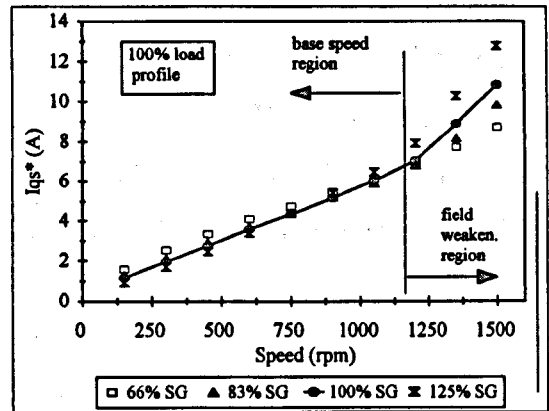
Figure 7.20 : Phase currents (fundamental component) for detuning due to errors in slip gain settings, 1150 rpm base speed.

Figure 7.21 : Phase currents (fundamental component) for detuning due to errors in slip gain setting, 650 rpm base speed.

rise. If the base speed was set as equal to rated (1500 rpm), the voltage margin of the inverter might have been endangered and proper current control could have been lost.

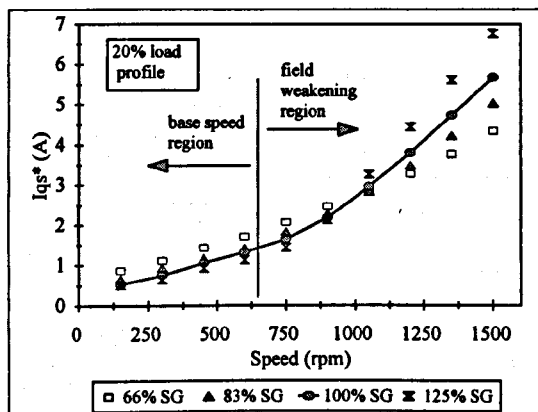


a. 50% load profile

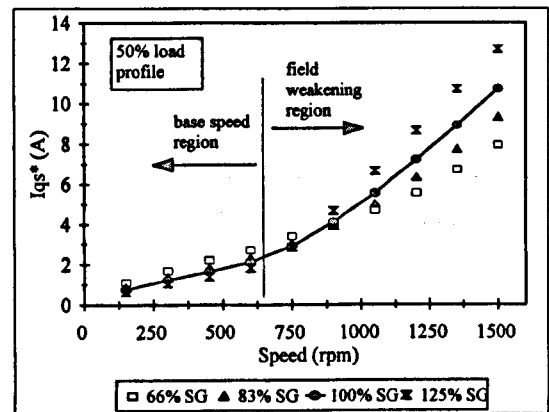


b. 100% load profile

Figure 7.22 : Estimated I_{qs}^* (rms fundamental component) for detuning due to errors in slip gain setting, 1150 rpm base speed.



a. 20% load profile



b. 50% load profile

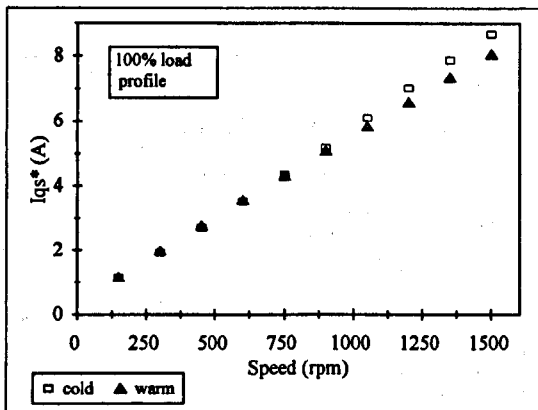
Figure 7.23 : Estimated I_{qs}^* (rms fundamental component) for detuning due to errors in slip gain setting, 650 rpm base speed.

7.6.2. Steady-state detuning due to thermal variations

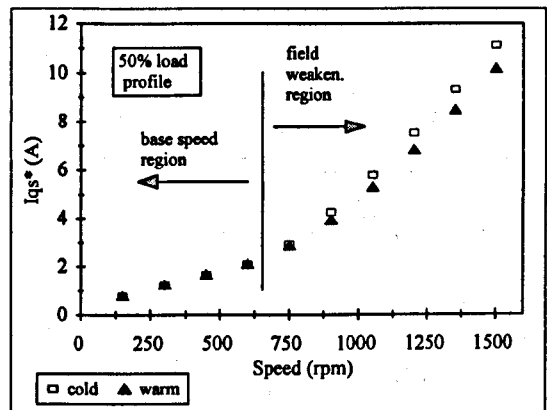
This section analyses operation with exact setting of the slip gain (100%), but the thermal situation of the machine is different. In 'cold' experiments the temperature of the machine is close to the ambient temperature (about 20°C). Then the machine is left to run at full load for an hour and the second series of measurements, marked as 'warm' is conducted. The stator temperature in the 'warm' case is about 60°C. Therefore the rotor resistance in the 'cold' case is smaller than in the 'warm' case. As this change is not recognised by the controller, detuning occurs. Three base speeds (1500, 1150 and 650 rpm) are analysed and the estimated I_{qs}^* curves, as a function of speed, are shown in

Fig. 7.24. Load profiles of 100% for 1500 and 1150 rpm base speeds and 50% for 650 rpm base speed are shown. Detuning with light loads is small and therefore omitted.

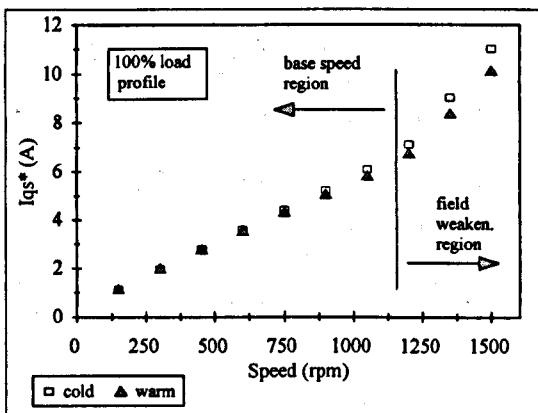
From Fig. 7.24 it can be seen that an increase in the actual rotor resistance leads to a decrease in I_{qs}^* , as expected. The 'warm' case is similar to operation with lower slip gain setting (for instance, 83% setting in Figs. 7.16 to 7.21). Detuning is relatively small for light loads in the base speed region and increases with the loading. Additionally, the trend of reduced I_{qs}^* in the 'warm' case becomes more pronounced in the field-weakening region.



a. base speed 1500 rpm, 100% load profile



c. base speed 650 rpm, 50% load profile



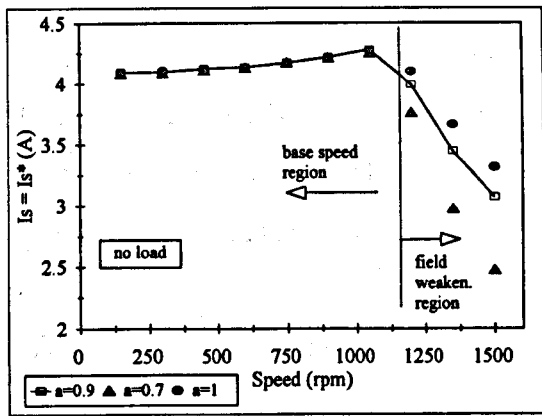
b. base speed 1150 rpm, 100% load profile

Figure 7.24 : Estimated I_{qs}^* (rms fundamental component) with detuning due to thermal effects.

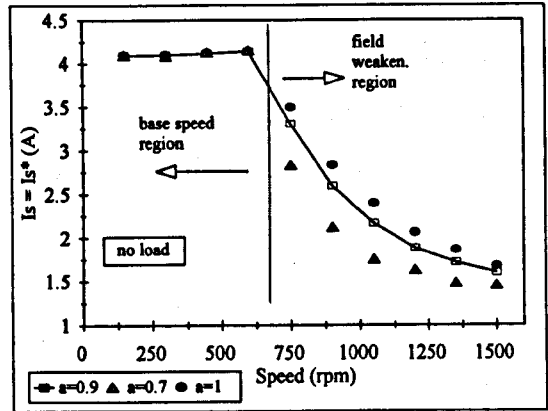
7.6.3. Steady-state detuning due to incorrect magnetising curve approximation

Detuning effects of inaccurate setting of the magnetising curve are analysed for three values of parameter a - 0.9 (the correct one), 1 and 0.7 (all with $b = 7$). Figure 7.25 shows no-load currents with these three values of parameter a , for base speeds of 1150 and 650 rpm, while Figure 7.26 shows estimated I_{qs}^* .

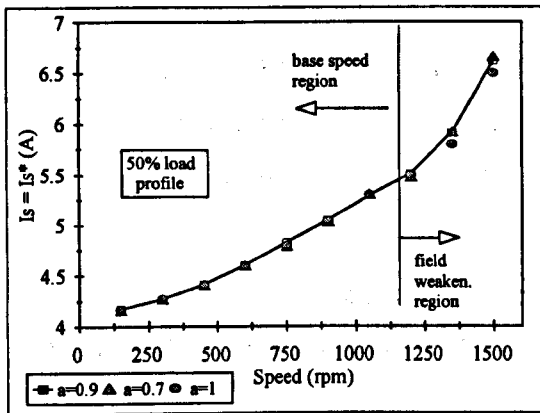
As expected, no-load current (and the rotor flux) for case $a = 0.7$ is reduced more than it should be for proper operation since too saturated magnetising curve is assumed in the controller (Figs. 7.25.a and 7.25.c). Therefore voltage capabilities of the inverter are not



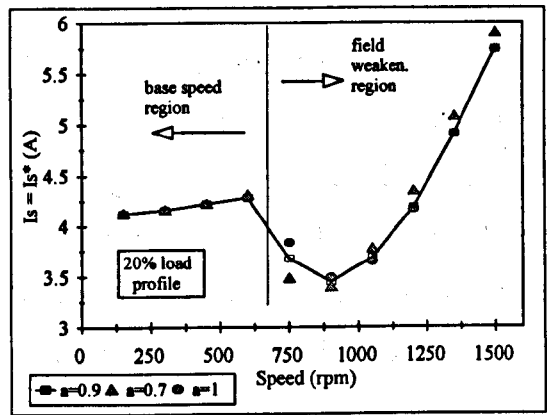
a. base speed 1150 rpm, no load



c. base speed 650 rpm, no load

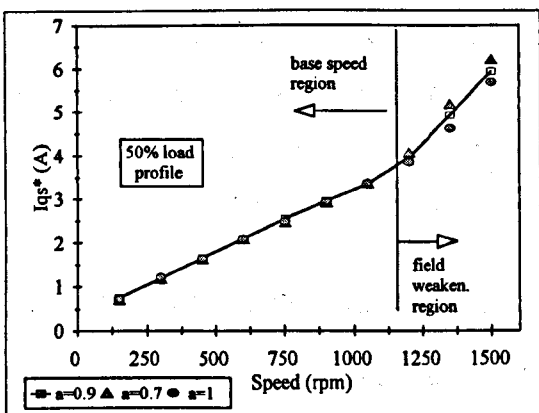


b. base speed 1150 rpm, 50% load profile

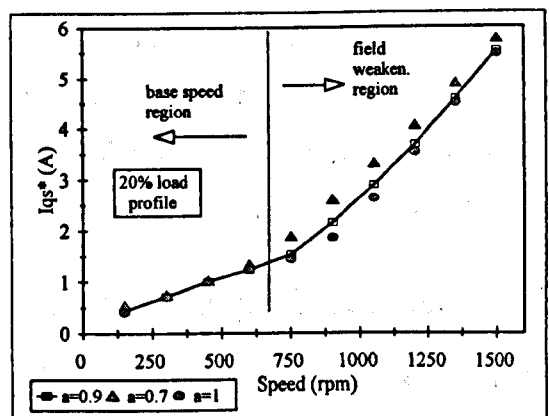


d. base speed 650 rpm, 20% load profile

Figure 7.25 : Phase currents (fundamental component) in no-load operation with various magnetising curves in the controller.



a. base speed 1150 rpm, 50% load profile



b. base speed 650 rpm, 20% load profile

Figure 7.26 : Estimated I_{qs}^* (rms fundamental component) with detuning due to incorrect magnetising curve.

fully utilised and the voltage will drop, as already shown in Fig. 7.11.b. When the motor is required to develop some torque, too low flux means that higher I_{qs} is necessary and the total current is higher than for the properly identified magnetising curve (Figs. 7.25.b, 7.25.d and 7.26).

For the case of neglected saturation ($a=1$) the rotor flux is not reduced enough. Hence the no-load current is higher than for the case $a=0.9$ and the voltage will rise in the field-weakening region (Fig. 7.11.b). On the other hand, such setting results in slightly lower I_{qs} when the load is applied.

7.7. DETUNING IN TRANSIENT OPERATION

Two transients are analysed in this section - acceleration from 200 rpm up to 1500 rpm and deceleration from 1500 rpm down to 200 rpm. The commanded speed is changed very quickly (ramp of 80,000 rpm/s) so that the step change can be assumed. Both transients are performed with 3 load profiles of the DC generator (0%, 50% and 100%). Two detuning sources are analysed - errors in slip gain and errors in the identified magnetising curve. For most experiments the base speed is set to 1500 rpm and in those cases transients cover base speed region only. In some experiments the base speed is set to lower values (1150 rpm or 650 rpm) so that both base speed and field-weakening regions are encompassed during the transients.

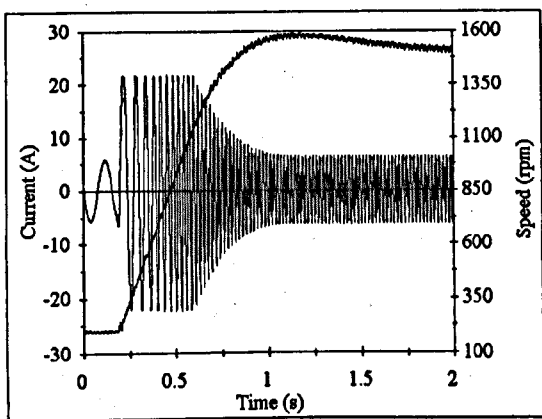
7.7.1. Transients with various slip gain settings

The following experiments present the recordings of the phase current and the rotor speed responses during the two analysed transients, for different settings of the slip gain in the controller. All other settings in the vector controller, like gains of the PI controller, cut-off frequency of the digital filter, the rated d -axis current and the coefficients that determine the commanded magnetising curve, are kept unchanged.

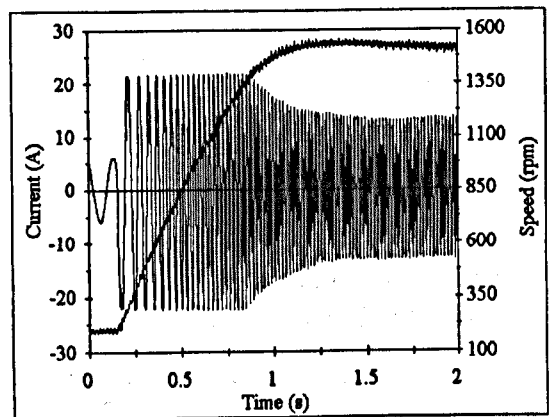
7.7.1.1. Transients with exact slip gain setting, 1500 rpm base speed

Acceleration transient with the exact slip gain setting (100%) is presented first. Recorded phase current and rotor speed responses during acceleration are shown in Figure 7.27, for the three load profiles of the DC machine. Additionally, Figure 7.27.d. reveals the influence of the load on the rotor speed responses.

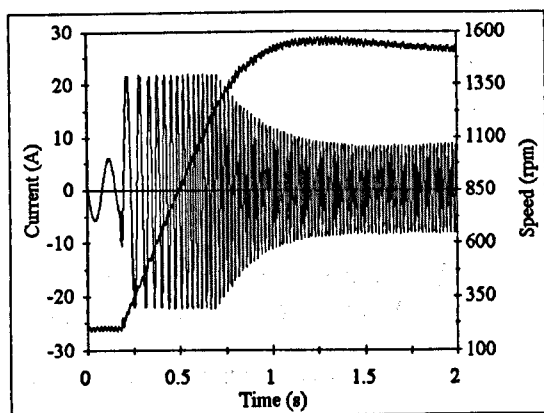
It can be seen that the controller pushes the current to its limit very soon after the commanded speed is changed. Maximum possible torque is developed, maximum possible acceleration takes place and the rotor speed rises sharply. After reaching about 80% of the commanded speed, the amplitude of the phase currents exits the limit and in aperiodical manner falls to its steady-state value, which is dependent on the loading. Since this fall of the current is not fast enough, a small overshoot in the speed response occurs. Figure 7.27.d. enables comparison of the speed responses for different load profiles. It can be seen that influence of the loading is small at the beginning of the acceleration, but increases with speed. The explanation to this is that more torque is required for generation as the speed increases and hence less torque is available for acceleration. The size of the overshoot also depends on loading and is greatest at no-load acceleration.



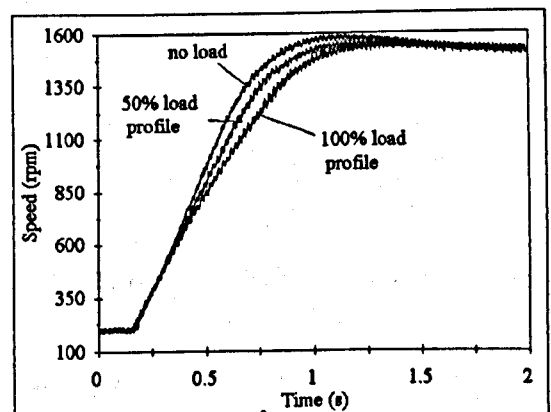
a. responses of phase current and speed, no-load acceleration



c. responses of phase current and speed, acceleration with 100% load profile



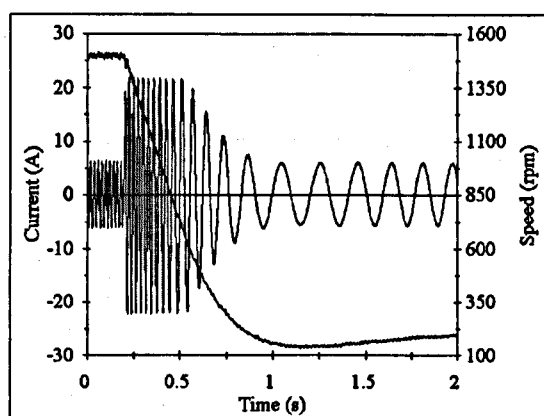
b. responses of phase current and speed, acceleration with 50% load profile



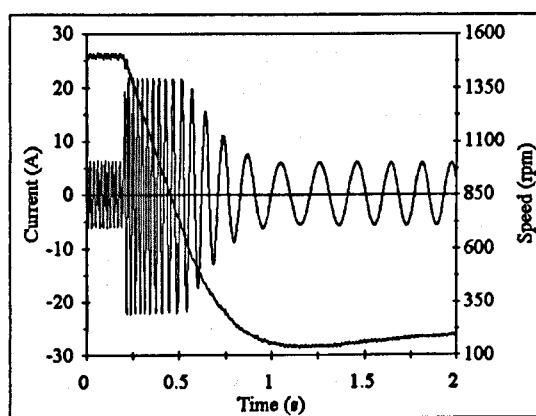
d. speed responses for acceleration with various loads

Figure 7.27 : Acceleration transients with the exact slip gain, 1500 rpm base speed.

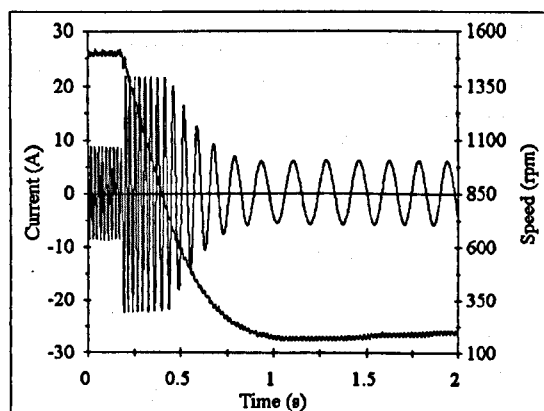
Recorded responses of the phase current and the rotor speed during deceleration, using the exact value of slip gain (100%), are shown in Figure 7.28. The stator current is pushed to its limit during the first part of deceleration, hard braking occurs and the rotor speed drops sharply. After a while, the stator current exits the limit and aperiodically falls to the value required for the 200 rpm operation. There is some undershoot during braking and it again depends on load. Fig. 7.28.d. also reveals that load profile has an influence on the speed response. The situation is the opposite to the one met in acceleration transient. No-load deceleration is slowest, while deceleration with 100% load profile is fastest, since the load actually helps slowing down.



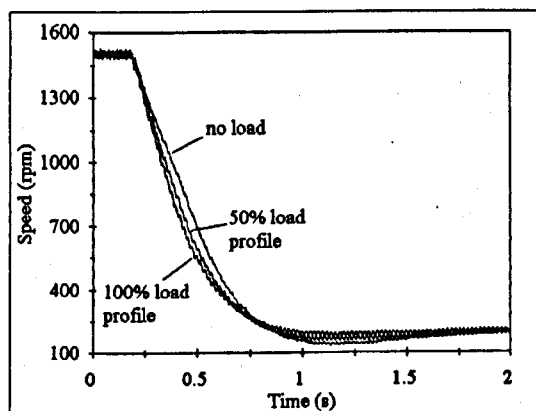
a. responses of phase current and speed, no-load deceleration



c. responses of phase current and speed, deceleration with 100% load profile



b. responses of phase current and speed, deceleration with 50% load profile



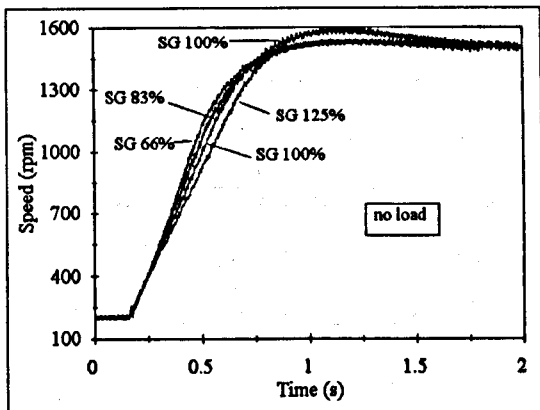
d. speed responses for deceleration with various loads

Figure 7.28 : Deceleration transients with the exact slip gain, 1500 rpm base speed.

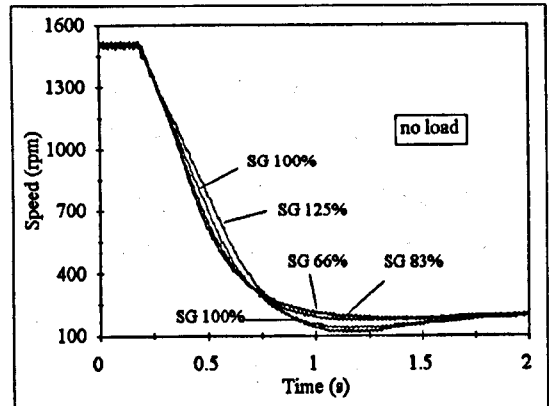
7.7.1.2. Transients with various slip gain settings, 1500 rpm base speed

The transients are performed again, but this time with the slip gain settings of 66%, 83% and 125%. The recorded speed responses are shown in Figures 7.29 (acceleration) and

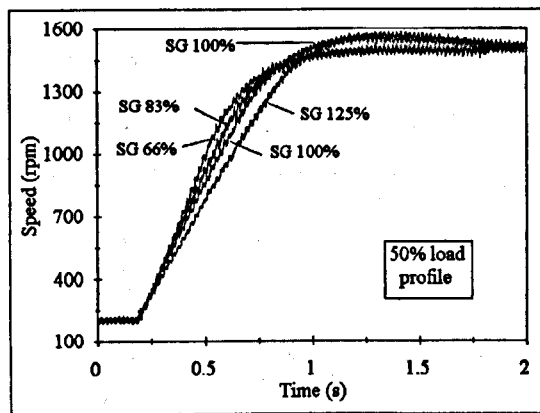
7.30 (deceleration). The responses of phase currents are quite similar to the responses from Figs. 7.27 and 7.28. and therefore omitted.



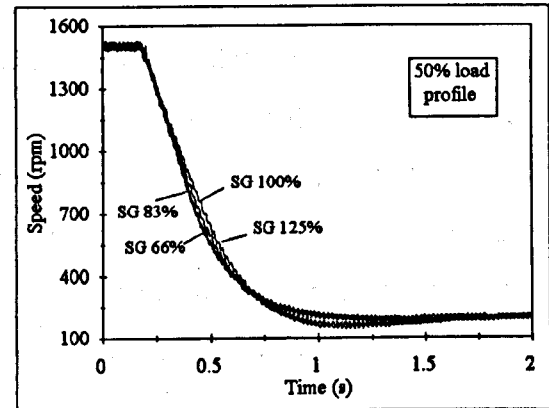
a. no-load acceleration



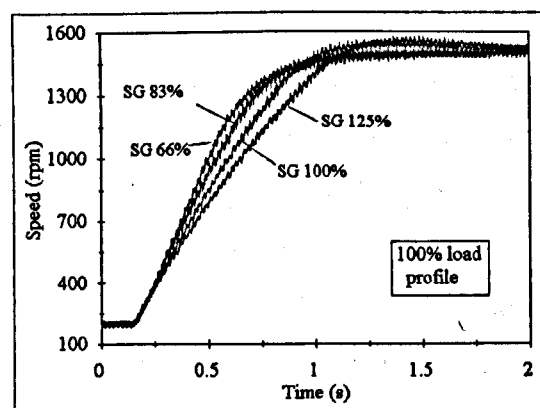
a. no-load deceleration



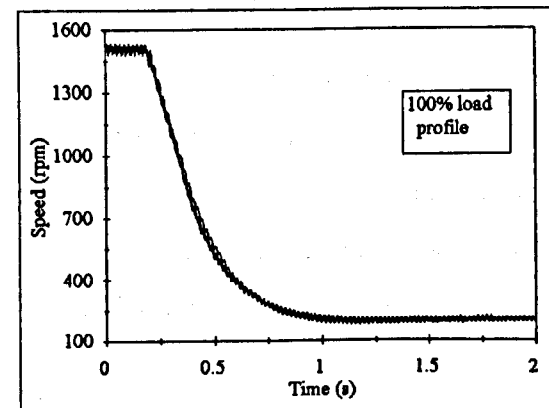
b. acceleration with 50% load profile



b. deceleration with 50% load profile



c. acceleration with 100% load profile



c. deceleration with 100% load profile

Figure 7.29 : Speed response in acceleration transients with various loads and various slip gains, 1500 rpm base speed.

Figure 7.30 : Speed responses in deceleration transients with various loads and various slip gains, 1500 rpm base speed.

Speed responses during acceleration (Fig. 7.29) reveal that faster responses are obtained with lower settings of the slip gain. This can be explained using the steady-state characteristics of Fig 7.16.b and the discussion in sub-section 7.6.1.1. about operation with heavy load torque. There it was observed that steady-state detuning is such that a lower current was needed to develop the rated torque (at 1500 rpm) with a lower slip gain settings and vice versa - higher current was needed for 125% slip gain setting. The situation of Fig. 7.29 should be analysed from the opposite point of view. The current is limited and hence a higher torque can be developed with a lower slip gain setting. Therefore acceleration is more rapid and speed responses are faster for lower slip gain settings. This happens independently of the load profile. Differences in speed responses with various slip gain settings are smaller for no-load acceleration (Fig. 7.29.a) and increase with loading.

Speed responses during deceleration transients (Fig. 7.30) reveal that responses are more dependent on the slip gain setting when there is no load (Fig. 7.30.a), since there is no generation to help the braking. Similarly to the acceleration transient, the speed response with 125% slip gain setting is slowest. The size of an undershoot also depends on the slip gain setting and the greatest undershoot is obtained with 125% slip gain setting. The responses become almost identical when the load profile of 100% is applied (Fig. 7.30.c).

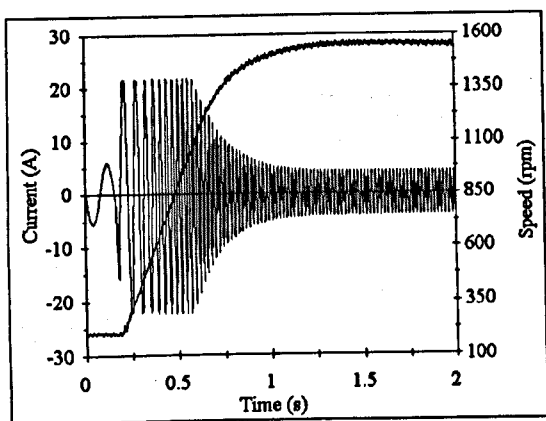
7.7.1.3. Transients with the exact slip gain setting, 1150 rpm base speed

This section presents responses during acceleration and deceleration that covers both base speed and field-weakening regions. As it was the case for steady-state analyses, the base speed is reduced to 1150 rpm rather than operating at speeds higher than 1500 rpm. The slip gain is set to the exact value (100%). Recorded phase current and speed responses during acceleration are shown in Figure 7.31, while the same responses during deceleration are shown in Figure 7.32.

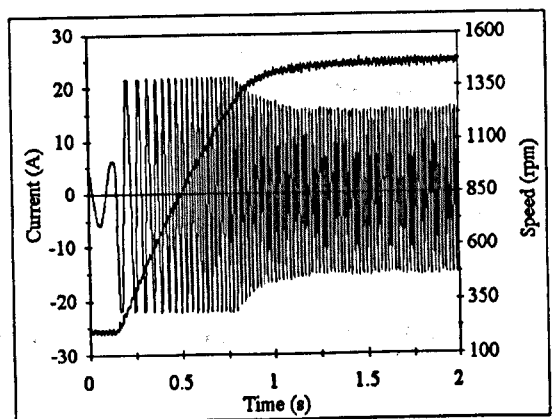
There are several differences between responses of Fig. 7.31 and responses of Fig. 7.27. The overshoot in the speed response during no-load acceleration (Fig. 7.31.a) is smaller in amplitude, but longer in duration. There is no overshoot for 50% load profile. For 100% load profile, the speed response towards the end of transient is slower and the commanded speed is not fully reached after the recorded 1.8 seconds. The explanation

to these three observations lies in the structure of the controller. As discussed in section 7.2, there is no division of the PI controller's output by the commanded flux in the controller under consideration. Therefore the gains of the speed control loop are not increased when the flux is reduced in the field-weakening region, as they should be. The net result is that the gains of the speed control loop are effectively reduced in the field-weakening region and therefore the speed responses become more sluggish when the field-weakening region is entered.

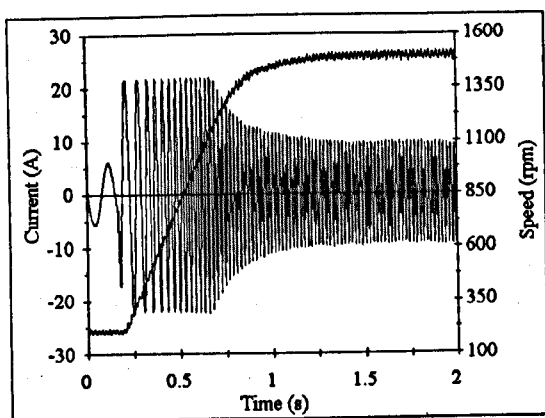
The responses during deceleration transients (Fig 7.32) are very similar to the ones obtained with the base speed set to 1500 rpm (Fig 7.28). There are three small differences : the braking is slower due to lower available flux, there is no undershoot in Fig. 7.32, and the initial values of the steady-state current (before the speed reference is reduced) are different to those of Fig. 7.28.



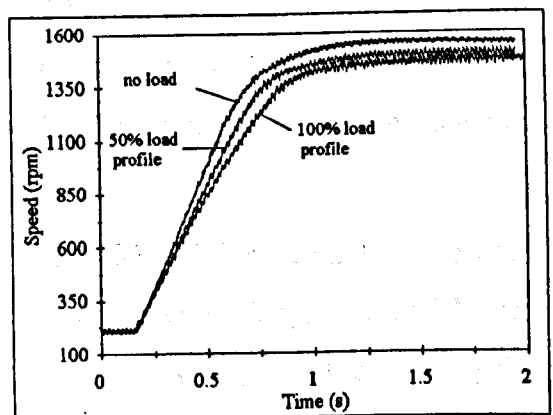
a. responses of phase current and speed, no-load acceleration.



c. responses of phase current and speed, acceleration with 100% load profile.

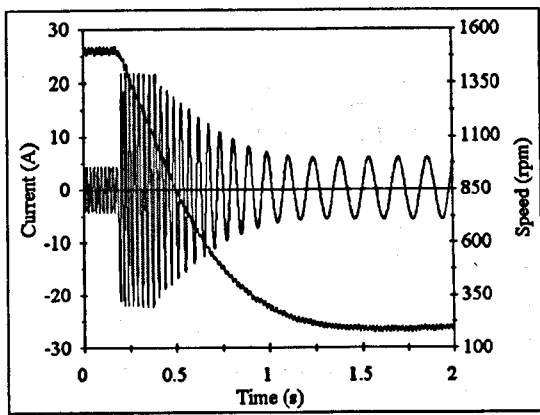


b. responses of phase current and speed, acceleration with 50% load profile

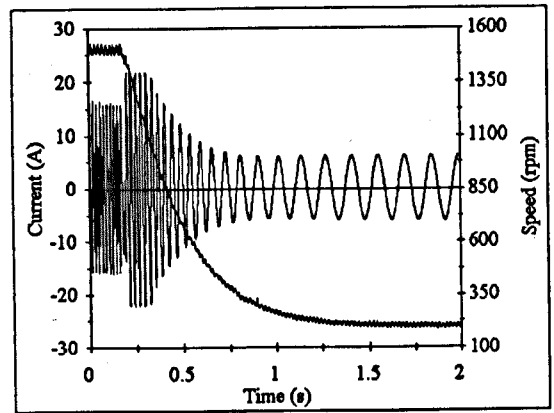


d. speed responses for acceleration with various loads

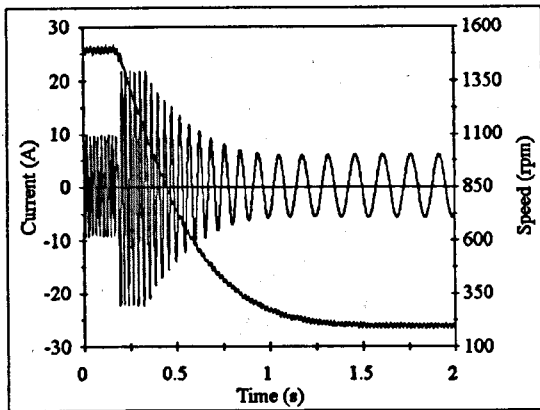
Figure 7.31 : Acceleration transients with the exact slip gain, 1150 rpm base speed.



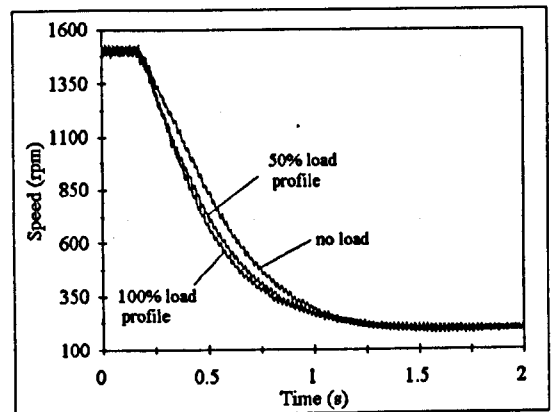
a. responses of phase current and speed, no-load deceleration



c. responses of phase current and speed, deceleration with 100% load profile



b. responses of phase current and speed, deceleration with 50% load profile



d. speed responses for deceleration with various loads

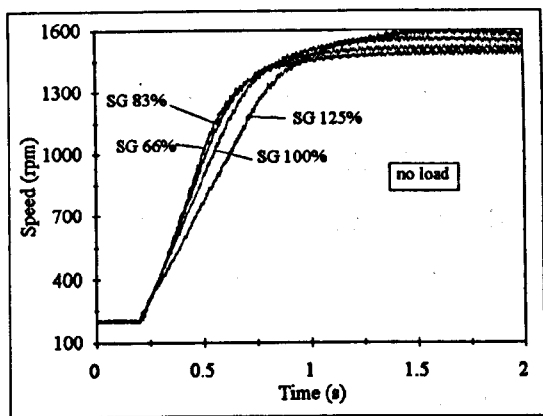
Figure 7.32 : Deceleration transients with the exact slip gain, 1150 rpm base speed.

7.7.1.4. Transients with various slip gain settings, 1150 rpm base speed

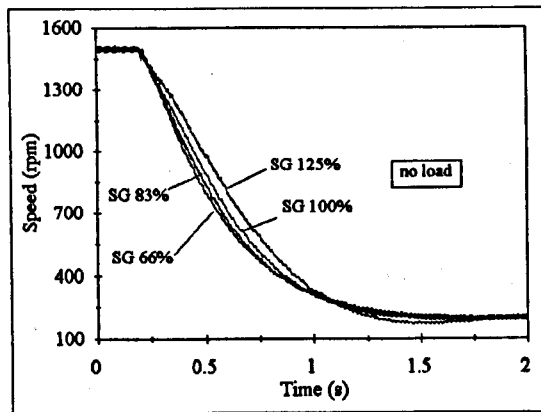
The same transients of acceleration from 200 to 1500 rpm and deceleration from 1500 rpm to 200 rpm, using the four slip gain settings - 66%, 83%, 100% and 125%, are performed with the base speed set to 1150 rpm and the responses of speed are shown in Fig 7.33 and Fig. 7.34.

Speed responses for acceleration are shown in Figure 7.33 and they are in some respect similar to the responses obtained with the base speed set to 1500 rpm. At all loads, acceleration is fastest with 66% slip gain setting and slowest with 125% slip gain setting. This is expected since the results of no-load operation indicated that lower current was needed to develop the rated torque when the slip gain was set to a lower value (Fig 7.20.c). During no-load acceleration (Fig. 7.33.a), the speed overshoots are obtained with 100% setting and 125% setting. The overshoots are of similar amplitude

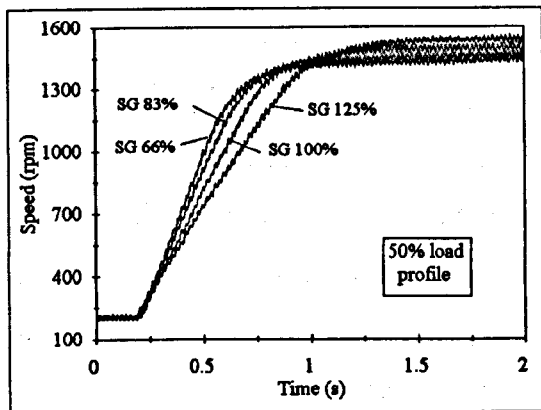
as they were for the 1500 rpm base speed (Fig. 7.29). However, there are some differences between speed responses of Fig 7.33 and Fig. 7.29. As expected, the speed responses towards the end of acceleration, after field-weakening is entered, are slower.



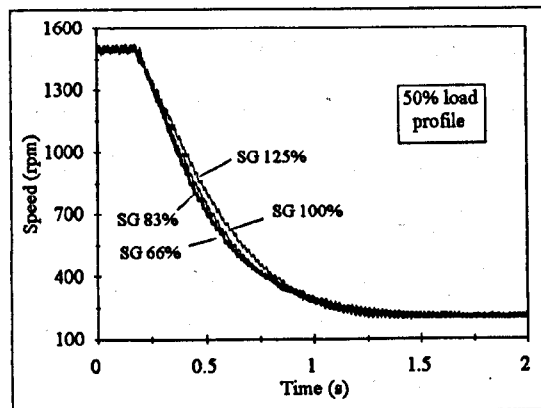
a. no-load acceleration



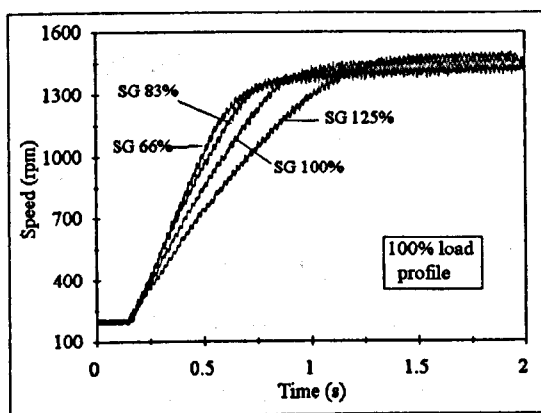
a. no-load deceleration



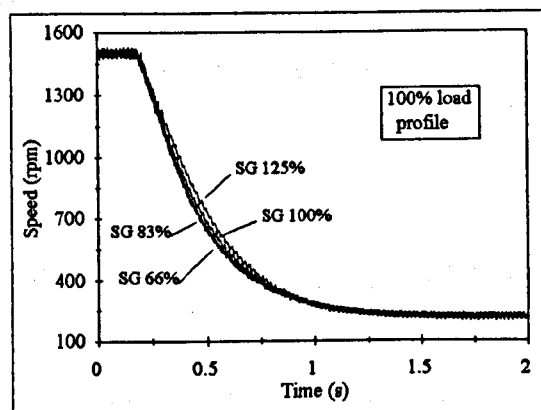
b. acceleration with 50% load profile



b. deceleration with 50% load profile



c. acceleration with 100% load profile



c. deceleration with 100% load profile

Figure 7.33 :Speed responses in acceleration transients with various loads and various slip gains, 1150 rpm base speed.

Figure 7.34 :Speed responses in deceleration transients with various loads and various slip gains, 1150 rpm base speed.

The overshoots in no-load case last longer and the return to the commanded speed is slower. There is no overshoot when the load is present. The commanded speed is not reached within the recorded time period when acceleration is performed with 50% load profile and slip gain settings of 66% and 83%. Moreover, when the 100% load profile is applied, neither of the slip gain settings can ensure that commanded speed is reached within the recorded 1.8 seconds.

Speed responses during deceleration transients are shown in Fig. 7.34. The responses are slower than they were with the base speed of 1500 rpm (Fig. 7.30), and there is no undershoot. Again, responses for lower slip gain settings are faster. The influence of slip gain settings is greater without load (Fig. 7.32.a) than with load. The influence of slip gain setting is observable with 100% load (Fig 7.34.c).

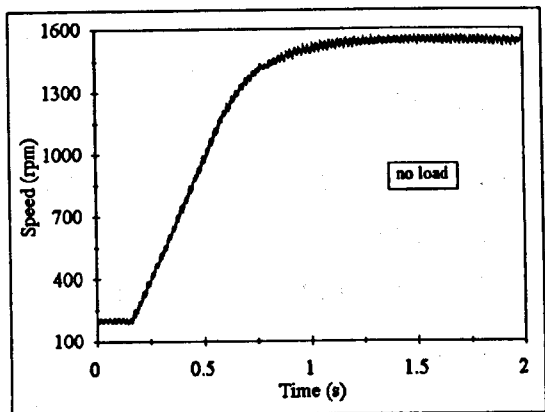
7.7.2. Transients with detuned magnetising curve

The influence of the setting of the coefficient a , that describes the magnetising curve in the controller, is investigated. As the setting of the coefficients a and b has no influence in the base speed region, only operation in the field-weakening region is of interest. Acceleration with base speed set to either 1150 rpm or 650 rpm is performed. The slip gain is set to the exact value. The experiments are performed for three values of the coefficient a - $a = 0.9$ (exact value), $a = 1$ (saturation neglected in the controller), and $a = 0.7$ (too saturated magnetising curve in the controller). Figures 7.35 and 7.36 present the recorded responses of rotor speed during acceleration, for base speeds of 1150 rpm and 650 rpm, respectively. It can be seen that the responses are practically identical and that setting of the parameter a has no influence on this transient.

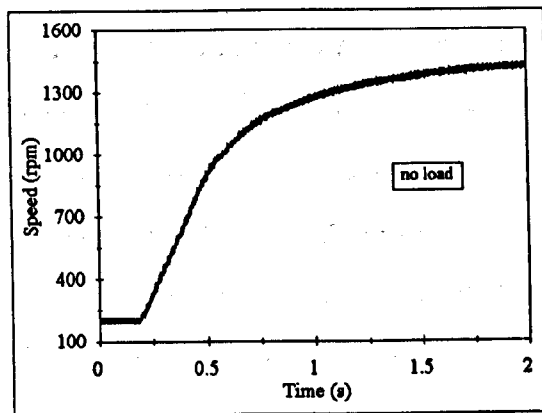
7.8. SUMMARY

The vector controlled drive, the loading machine and the measuring equipment were described in the first instance.

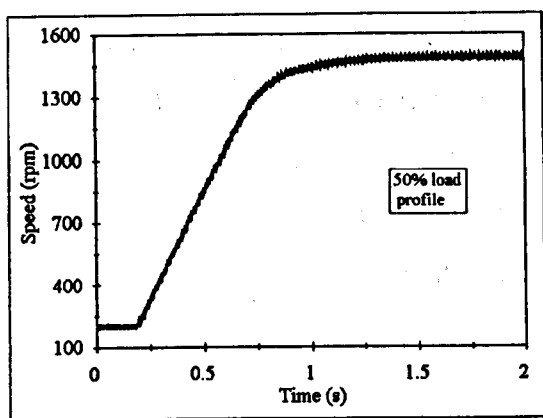
A novel procedure for identification of the inverse magnetising curve was proposed. The procedure is suitable for commissioning of the drive and requires that the induction machine can operate under no-load conditions. Measurement of the fundamental component of the stator voltage is necessary. The identification accuracy is to a certain extent robust to inaccurate knowledge of the stator leakage inductance.



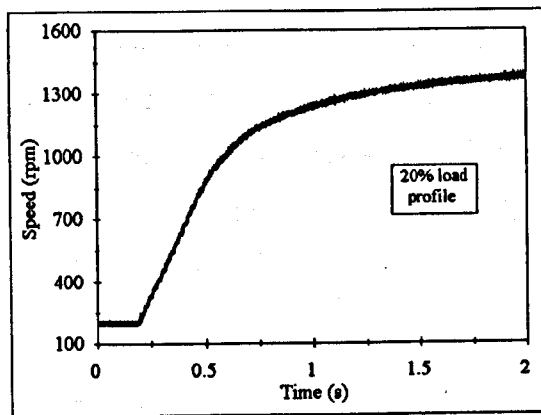
a. no-load acceleration



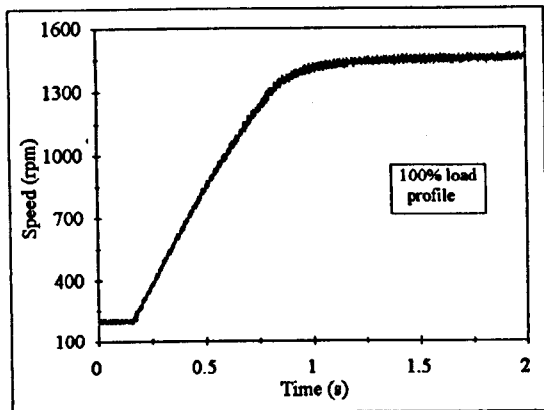
a. no-load acceleration



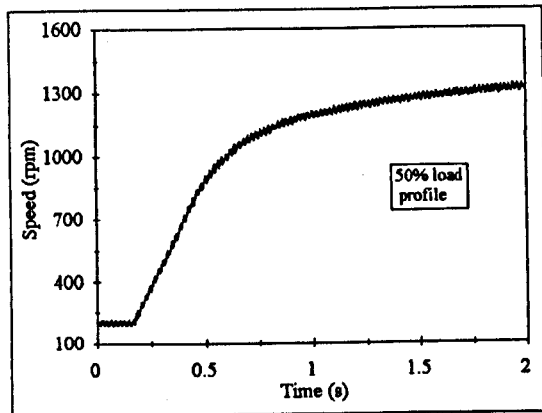
b. 50% load profile



b. 50% load profile



c. 100% load profile



c. 100% load profile

Figure 7.35 : Speed responses for acceleration with three settings of the coefficient α in the vector controller (1, 0.9 and 0.7), the exact slip gain, 1150 rpm base speed.

Figure 7.36 : Speed responses for acceleration with various settings of the coefficient α in the vector controller (1, 0.9 and 0.7), the exact slip gain, 650 rpm base speed.

An existing method, previously utilised for identification of the magnetising curve, was utilised here for determination of the slip gain. The method requires measurement of the fundamental component of the stator current. A controllable load is also necessary.

Experiments concerning steady-state operation showed that the machine operates with non-optimal values of currents, when detuning is present. Detuning due to inaccurate slip gain setting, due to thermal effects, and due to inaccurate magnetising curve was investigated. Operation in both base speed region and field-weakening region were encompassed by the study.

Responses of the phase current and the rotor speed during two transients - fast acceleration and fast deceleration - were recorded. The influence of the slip gain setting was investigated first. It was shown that slip gain setting has some influence on the responses during acceleration, while it has little influence on responses during deceleration. Finally, it was shown that inaccurately determined magnetising curve has no influence during acceleration in the field-weakening region.

8. CONCLUSIONS

8.1. SUMMARY

Detuning in the vector-controlled induction machine drives and compensation of detuning effects represent two topics which have attracted significant research attention in recent years. These two topics are the main themes of the thesis. Detuning due to parameter variations and due to unmodelled phenomena is investigated for both feed-forward type and feedback type of the vector controller with orientation along the rotor flux.

A brief history of vector control theory and practice reveals tremendous growth in less than three decades. Numerous vector control schemes exist and novel ones are still being proposed. They address the problems that are still encountered, searching for the causes of these problems and providing the solutions that enhance the performance of electric drives. Even more impressive is the list of different areas of engineering and science whose developments have contributed to the evolution of the vector control theory and practice. This evolution is still happening and there are more challenges in the future. The problems that engineers and researchers have encountered and the approaches to solving them are underlined briefly in chapter one. The topics that have not been exhaustively investigated so far are identified and research objectives are set.

The basics of vector control theory are reviewed and orientation along different flux vectors is explained in chapter two. Orientation along the rotor flux, in conjunction with current feeding, being the simplest and hence the most common group of vector control methods, is discussed in detail. Step-by-step derivation of mathematical models is illustrated and design of the rotor-flux-oriented vector control scheme is explained using the constant parameter model. The CPM is utilised for design of two vector controlled schemes (feedback and feed-forward).

Vector controllers operate in the reference system attached to the chosen flux. Therefore accurate information on the position of the chosen flux is essential for proper operation. If there are any inaccuracies in obtaining this information, the controller is detuned and the performance of the vector controlled drive deteriorates. Since high performance is the key feature of vector-controlled drives, detuned operation deserves

the attention that it has received in this project. A physical insight into sources and consequences of detuned operation is provided. Detuning due to main flux saturation, iron loss and temperature effects, as well as compensation techniques for these three phenomena, are discussed in detail. Two types of compensation approaches are distinguished : open-loop compensation of main flux saturation and/or iron loss and closed-loop compensation of thermally induced variations in the rotor resistance.

Attempts to compensate some of these detuning sources have been made by many researchers and engineers. Most of the compensation schemes are designed to neutralise effects of only one detuning source. Additionally, in majority of the schemes the controller is designed on the basis of CPM and compensation is enabled by utilising complex adaptation circuitry. The increased complexity puts an additional processing burden on controllers and more powerful microprocessors and DSPs need to be employed, increasing the cost. An alternative approach is to design vector controllers on the basis of improved models of induction machines. Such improved vector controllers can provide enhanced performance with relatively small increase in controller complexity. Some improved controllers have already been proposed in literature, but their numbers and versatility are still limited.

This project attempts to contribute to the model-based approach to compensation of detuning effects. Several novel improved mathematical models of induction machines and novel improved rotor flux estimators for feedback vector control are proposed. Main flux saturation, iron loss and then both of these phenomena are included in improved models. Initially, two novel mathematical models and novel estimators with main flux saturation are developed. Their originality is that two novel representations of the main flux saturation are utilised and the models are obtained by merely changing equations for the magnetising flux components. When these relationships are used, the number of calculations necessary to execute the control algorithm can be reduced with respect to the existing representations of main flux saturation.

As far as iron loss is concerned, several original models that include iron loss have been developed. Iron loss is represented by equivalent iron loss resistance and two possible placements of the equivalent resistance are initially analysed. The first possibility is to place the resistance in parallel with the magnetising branch while the other is to place it immediately after the stator resistance. It is shown that utilisation of the first placement

results in simpler improved models, when current feeding is considered. For the first placement, two sets of state variables are analysed - the first set consist of stator current, magnetising flux and rotor flux $d-q$ components, while the second one consists of stator current, magnetising current and rotor flux $d-q$ components. It is shown that the first state variable set results in more compact model and therefore in a simpler improved estimator than in the case of the second state-variable set. Therefore the first state variable set is utilised for design of the improved estimator with iron loss. As the improved estimator is still quite complicated, a simplification that does not compromise quality of achieved iron loss compensation is proposed.

Novel models and novel estimators that include both iron loss and main flux saturation are proposed as well. Following the suggestions about simplicity of the models from previous considerations, two full-order improved estimators are designed and then their complexity reduced using the same simplification that was used for improved estimator with iron loss only.

Detailed analysis of detuning effects in the rotor-flux-oriented induction machine drives, when the constant-parameter estimator is utilised, is the main issue of chapter four. Comprehensive parameter identification is performed for the 4 kW machine. Stator and rotor resistances, leakage inductances, magnetising curve and changes of iron loss with frequency are identified. Consequently, quantitative analyses of steady-state detuning due to four different phenomena (rotor resistance variations, rotor leakage inductance uncertainties, mutual inductance variations and iron loss) is performed using novel expressions that describe steady-state detuning. In most studies, main flux saturation is included in the machine model, together with the phenomenon whose detuning effects are investigated. It is shown that the two ways of iron loss representation, although described by different detuning expressions, result in almost identical detuning characteristics. Comparative analysis of steady-state detuning has revealed the following:

- detuning due to rotor leakage inductance variations and uncertainties is much smaller than detuning triggered by other phenomena,
- detuning due to iron loss can become significant at light loads,

- variations and uncertainties in both rotor resistance and magnetising inductance cause significant detuning at medium and higher loads,
- in the field-weakening region, main flux saturation (variation of the magnetising inductance) plays the major detuning role.

Detuning during transients is analysed using simulations. It is confirmed that inaccurate knowledge of the rotor resistance can seriously endanger the proper orientation, as indicated by the already existing research. It is also confirmed that main flux saturation has a major detuning role in the field-weakening region. On the other hand, it is found that main flux saturation is actually lessening the detuning effects of iron loss in the base speed region. Identical transient responses are obtained with the two iron loss representations, confirming the findings of the steady-state analysis.

Compensation of detuning, obtainable when novel improved rotor flux estimators developed in chapter three are employed, is analysed in chapter five. Novel detuning expressions are derived for each improved estimator using the same method as in the chapter four. The expressions are utilised for quantitative analyses of steady-state detuning. Utilisation of improved estimators with main flux saturation provides significant reduction of steady-state detuning in the field-weakening region. Additionally, improved estimators with main flux saturation provide a reduction of iron-loss induced steady-state detuning in the base speed region. However, improved estimators with main flux saturation cannot compensate detuning due to rotor resistance variations.

Improved estimators with iron loss (both complete and reduced one) successfully compensate steady-state detuning in the base speed region. In order to simplify them even further, an estimator with a constant value of the equivalent iron loss resistance is employed. It is shown that it can provide partial compensation in the base speed region. However, neither of the estimators with iron loss include main flux saturation and therefore cannot compensate detuning in the field-weakening region.

Improved estimators with both iron loss and main flux saturation enable full compensation of steady-state detuning. Analyses of their sensitivity reveals their robustness to inaccuracies in the identified iron loss resistance. Even if iron loss is estimated with 20% error, the performance of these improved estimators is still very

good. On the other hand, the compensation capability of the improved estimators depends on the accurate knowledge of the magnetising curve. If the mutual inductance is identified with 20% error, the estimators cannot provide good compensation and detuning is not negligible.

Performance of the improved estimators in transient operation is analysed by simulation. The improved operation and reduction of detuning, anticipated on the basis of steady-state analyses, is confirmed. Furthermore, it is shown that the performance of the simplified estimators match that of complete estimators in most cases.

The closed-loop on-line adaptation of the rotor resistance is viable when using the model reference adaptive control approach. The performance of three identification schemes, based on the reactive power, has been analysed by simulation. The first identification scheme, based on the constant parameter model, manages to eliminate detuning in steady-state operation in the base speed region but the convergence speed is slow. It exhibits poor performance in field weakening. Therefore two improved rotor resistance identifiers, based on improved models, are proposed. Their enhanced performance is confirmed by simulations.

Experimentation is undertaken on the vector-controlled laboratory rig that utilises a DC machine operating as a generator and feeding a resistor bank. For correct commissioning of the drive, it is necessary to incorporate the magnetising curve of the motor into the control algorithm. Existing procedures for magnetising curve identification are reviewed and a novel method for identification of the inverse magnetising curve, that utilises both PWM inverter and the vector controlled drive that are later used for normal operation, is proposed. The developed method is suitable for commissioning and requires the induction motor to be decoupled from load. Measurement of the fundamental component of the stator line-to-line voltage is required, but the measurement of current is not. The method is satisfactorily accurate and is quite robust to uncertainties in the value of the stator leakage inductance. An existing method is utilised for determination of the slip gain.

Some of the theoretical quantitative detuning results, that were obtained in chapters four and five, are experimentally verified. Detuning effects due to rotor resistance variations are analysed for changes in both slip gain setting (in the controller) and actual rotor

resistance (due to temperature variations). Detuning due to main flux saturation is triggered by changing the magnetising curve setting in the controller. Detuning in steady-state operation is assessed on the basis of measured amplitude of the phase current. As the commanded d -axis current is known, the commanded q -axis current can be estimated. For the given load, the estimated command of q -axis current assumes different values when a detuning source is introduced. An increase in the estimated command of q -axis current indicates that flux is reduced due to detuning and vice versa. Analyses of detuned operation in transients reveals that settings of the slip gain influences the speed responses during both rapid acceleration and rapid deceleration of the drive. Detuned magnetising curve has no influence on the acceleration in the field-weakening region.

8.2. CONCLUSIONS

The thesis represents a research into the effects of the various phenomena on the performance of the vector-controlled induction machine drive. Research objectives, set in section 1.3.1. are satisfactorily met.

Several novel improved induction machine models that include main flux saturation and/or iron loss are developed. These include mixed current-flux models and rotor-flux oriented models.

Novel expressions, that describe detuning effects introduced by main flux saturation, iron loss and temperature variations, have been derived. On the basis of these expressions, detuning effects of the above phenomena on the standard CPM-based vector controlled drives are quantitatively assessed. It is shown that iron loss, usually neglected, can cause noticeable detuning in certain operating conditions.

Several novel vector controllers are designed on the basis of the proposed improved machine models. Their capability to reduce or even eliminate detuning is investigated by simulations. It is shown that they can significantly reduce detuning and hence improve the overall performance of the drive.

The influence of main flux saturation and iron loss on the performance of an existing rotor resistance identification scheme is investigated. It is found that this identifier inaccurately identifies the rotor resistance value in the field-weakening region.

Therefore two novel rotor resistance identifiers, designed on the basis of improved induction machine models, are proposed. Their improved performance is verified by simulations.

A novel procedure for magnetising curve identification is developed. The procedure utilises the PWM inverter that is used in normal operation of the vector controlled drive. It requires that the induction motor is decoupled from the load and that the fundamental harmonic of the voltage is measured. The procedure is to a certain extent robust to inaccurate determination of the stator leakage inductance.

Finally, experimental confirmation of detuned operation is performed by analysing the amplitude of the induction machine phase current. It is shown that, for a given load, the current assumes different values when a detuning source is introduced, indicating the unwanted changes in the rotor flux.

8.3. FURTHER WORK

The research deals with vector control of induction machines. As mentioned in the introduction, recent competitor to vector control is direct torque control, DTC. The control algorithms of DTC schemes involve estimation of the developed torque and stator flux. Since a machine model is used for this estimation, a possible direction for further research is investigation into the influence of iron loss on the estimation accuracy in DTC. Inclusion of iron loss into the DTC estimation process can be obtained using the proposed improved machine models.

Another recent trend in vector control developments are sensorless drives, where no speed sensor is employed. Since there is no information on rotor position, the position of the chosen flux in sensorless vector control schemes cannot be estimated using estimators that process stator current and rotor speed. Hence some other estimator structures, using other available feedback signals are employed. Sensitivity of these estimators to rotor resistance variations has attracted some research interest in recent years. However, research into the influence of iron loss and/or main flux saturation on the estimation accuracy can be of further interest.

The research reported here applies to induction machines whose rated power ranges from 0.75 kW to 4 kW. In this power range the switching frequency of the modern

inverters can be tens of kilohertz and very fast current control is achieved. This means that current feeding is achieved and relatively simple vector controllers can be employed. These vector controllers are analysed in the thesis. Therefore investigations into the effects of detuning phenomena on the operation of vector controllers with voltage-fed induction machines can be an interesting topic for further research.

Finally, the research is limited to vector control with orientation along the rotor flux. Although some work has been done regarding detuning effects in stator-flux-oriented and air-gap-flux oriented vector controllers, this is another direction for prospective work.

9. REFERENCES

- Atkinson, D.J.; Acarnley, P.P.; Finch, J.W. (1991) : Observers for Induction Motor State and Parameter Estimation, *IEEE Transactions on Industry Applications*, Vol. IA-27, No. 6, pp. 1119-1127.
- Ba-Razzouk, A.; Chériti, A.; Olivier, G. (1996) : Artificial Neural Networks Rotor Time Constant Adaptation in Indirect Field Oriented Control Drives, *Proceedings of the IEEE Power Electronics Specialist Conference PESC'96*, pp.701-707, Baveno, Italy.
- Baliga, B.J. (1994) : Power Semiconductor Devices for Variable-Frequency Drives, *Proceedings of the IEEE*, Vol. 82, No. 8, pp. 1112-1122.
- Bhatnagar, M.; Baliga, B.J. (1993) : Comparison of 6H-SiC, 3C-SiC and Si for power Devices, *IEEE Transactions on Electronic Devices*, Vol. 40, pp. 645-655.
- Blaschke, F. (1971) : Das Prinzip der Feldorientierung, die Grundlage für die TRANSVECTOR- Regelung von Drehfeldmaschinen, *Siemens-Zeitschrift*, Vol. 45, H.10, pp. 757-760.
- Bogletti, A.; Ferraris, P.; Lazzari, M.; Pastorelli, M. (1996) : Influence of the Inverter Characteristics on the Iron Losses in PWM Inverter-Fed Induction Motors, *IEEE Transactions on Industry Applications*, Vol. 32, No. 5, pp. 1190-1194.
- Boldea, I.; Nasar, S.A. (1987a) : A Unified Analysis of Magnetic Saturation in Orthogonal Axis Models of Electrical Machines, *Electrical Machines and Power Systems*, Vol. 12, No. 3, pp. 195-204.
- Boldea, I.; Nasar, S.A. (1987b) : Unified Treatment of Core Losses and Saturation in the Orthogonal-Axis Model of Electrical Machines, *IEE Proceedings, Part B*, Vol. 134, No. 6, pp. 355-363.
- Boldea, I.; Nasar, S.A. (1990) : *Vector Control of AC Drives*; CRC Press.
- Borgard, D.E.; Olsson, G.; Lorenz, R.D. (1995) : Accuracy Issues for Parameter Estimation of Field Oriented Induction Machine Drives, *IEEE Transactions on Industry Applications*, Vol. IA 31, No. 4, pp. 795-801.
- Bose, B.K. (1986) : *Power Electronics and AC Drives*, Prentice-Hall, Englewood Cliffs.
- Bose, B.K. (1994) : Expert System, Fuzzy Logic, and Neural Network Application in Power Electronics and Motion Control, *Proceedings of the IEEE*, Vol. 82, No. 8, pp 1303-1323.
- Bünthe, A.; Grotstollen, H.; Krafka, P. (1996) : Field-Weakening of Induction Motors in a Very Wide Region With Regard to Parameter Uncertainties, *IEEE Power Electronics Specialist Conference PESC'96*, IEEE Cat. No. 96 CH 35962, pp. 944-950, Baveno, Italy.

- Chan, C.C.; Wang, H. (1990) : An Effective Method for Rotor Resistance Identification for High-Performance Induction Motor Vector Control, *IEEE Transactions on Industrial Electronics*, Vol. 37, No. 6, pp. 477-482.
- Choi, D.H.; Cho, S.B.; Hyun, D.S. (1997) : Improved Torque Response by Tuning of the Magnetising Inductance Under Field Weakening Operation Region, *Conference Record of 1997 IEEE IAS Annual Meeting*, pp. 418-425, New Orleans, LA, USA.
- Dalal, D.; Krishnan, R. (1987) : Parameter Compensation of Indirect Vector Controlled Induction Motor Drive Using Estimated Airgap Power, *Conference Record of 1987 IEEE IAS Annual Meeting*, pp. 170-176, Atlanta, Georgia, USA.
- De Buck, F.G.G.; Gistelink, P.; De Baker, D. (1984) : A Simple but Reliable Loss Model for Inverter-Supplied Induction Motors, *IEEE Transactions on Industry Applications*, Vol. IA-20, No. 1, pp. 190-202.
- De Doncker, R.W. (1992) : Field-Oriented Controllers with Deep Bar Compensation Circuits, *IEEE Transactions on Industry Applications*, Vol. 28, No. 5, pp. 1062-1071.
- De Doncker, R.W. (1994) : Parameter Sensitivity of Indirect Universal Field-Oriented Controllers, *IEEE Transactions on Power Electronics*, Vol. 9, No. 4, pp. 367-376.
- De Doncker, R.W.; Vandenput, A.; Geysen, W. (1986) : Thermal Models of Inverter Fed Asynchronous Machines Suited for Adaptive Temperature Compensation of Field Oriented Controllers, *Conference Record of 1986 IEEE IAS Annual Meeting*, pp. 132-139, Denver, CO, USA.
- De Doncker, R.W.; Novotny, D.W. (1988) : The Universal Field Oriented Controller, *IEEE IAS Conference Records*, pp. 450-456.
- De Doncker, R.W.; Profumo, F.; Pastorelli, M. (1994) : Self-Tuning of Tapped Stator Winding Induction Motor Servo Drives Using the Universal Field-Oriented Controller, *IEEE Transactions on Power Electronics*, Vol. 9, No. 4, pp. 357-366.
- Depenbrock, M. (1988) : Direct Self-Control (DSC) of Inverter-Fed Induction Machine, *IEEE Transactions on Power Electronics*, Vol. 3, No. 4, pp. 420-429.
- Dittrich, A. (1994) : Parameter Sensitivity of Procedures for On-Line Adaptation of the Rotor Time Constant of Induction Machines with Field Oriented Control, *IEE Proceedings - Electrical Power Applications*, Vol. 141, No. 6, pp. 353-359.
- Flöter, W.; Ripperger, H. (1971) : Die TRANSVECTOR-Regelung für die feldorientierten Betrieb einer Asynchronmaschine, *Siemens-Zeitschrift*, Vol. 45, H. 10, pp. 761-764.
- Gabriel, R.; Leonhard, W.; Nordby, C.J. (1980) : Field-oriented Control of a Standard AC Motor Using Microprocessors, *IEEE Transactions on Industry Applications*, Vol. 16, No. 2, pp. 186-192.
- Ganji, A.A.; Lataire, P. (1995) : Rotor Time Constant Compensation of an Induction Motor in Indirect Vector Controlled Drives, *Proceedings of the 6th European*

- Conference on Power Electronics and Applications EPE'95*, Sevilla, Spain, Vol. 1, pp. 1.431-1.436.
- Garcés, L.J. (1980) : Parameter Adaptation for the Speed-Controlled Static AC Drive with a Squirrel-Cage Induction Motor, *IEEE Transactions on Industry Applications*, Vol. IA-16, No. 2, pp. 173-178.
- Garcia, G.O.; Santisteban, J.A.; Brignone, S.D. (1994) : Iron Losses Influence on a Field-Oriented Controller, *Proceedings of 1994 IEEE IECON Conference*, pp. 633-638, Bologna, Italy.
- Grotstollen, H.; Wiesing, J. (1995) : Torque Capability and Control of a Saturated Induction Motor Over a Wide Range of Flux Weakening, *IEEE Transactions on Industrial Electronics*, Vol. 42, No. 4, pp. 374-381.
- Healey, R.C. (1995) : The Implementation of a Vector Controlled Scheme Based on an Advanced Motor Model, *Proceedings of the 6th European Conference on Power Electronics and Applications EPE'95*, Vol. 3, pp. 3.017-3.022, Sevilla, Spain.
- Healey, R.C.; Williamson, S.; Smith A.C. (1995) : Improved Cage Rotor Models for Vector Controlled Induction Motors Model, *IEEE Transactions on Industry Applications*, Vol. 31, No. 4, pp. 812-822.
- Heinemann, G. (1989) : Comparison of Several Control Schemes for AC Induction Motors under Steady State and Dynamic Conditions, *Proceedings of the 3rd European Conference on Power Electronics and Applications EPE'89*, pp. 843-848, Aachen, Germany.
- Hewlett-Packard Company (1993) : *HP 35665A Dynamic Signal Analyser - Operator's Reference*, Everett, WA, USA.
- Hintze, D.; Schröder, D. (1992) : Induction Motor Drive with Intelligent Controller and Parameter Adaptation, *Conference Record of 1992 IEEE IAS Annual Meeting*, pp. 970-977, Houston, Texas, USA.
- Hofmann, H.; Sanders, S.R.; Sullivan, C. (1995) : Stator-Flux-Based Vector Control of Induction Machines in Magnetic Saturation, *Conference Record of 1995 IEEE IAS Annual Meeting*, pp. 152-158, Orlando, Florida, USA.
- Hofmann, W.; Liang, Q. (1995a) : An Observer for Field-Oriented AC Drives Using a Novel Dynamical Neural Network, *Proceedings of PCIM'95 Conference*, Nurnberg, Germany.
- Hofmann, W.; Liang, Q. (1995b) : Neural Network-Based Parameter Adaptation for Field-Oriented AC Drives, *Proceedings of the 6th European Conference on Power Electronics and Applications EPE'95*, Sevilla, Spain, Vol. 1, pp. 1.391-1.396.
- Holtz, J. (1994) : Pulsewidth Modulation for Electronic Power Conversion, *Proceedings of the IEEE*, Vol. 82, No. 8, pp 1194-1214.

- Holtz, J. (1995) : State of the Art of Controlled AC Drives without Speed Sensor, *IEEE Conference PEDS'95*, pp. 1-6, Singapore.
- Hori, Y.; Umeno, T. (1989) : Implementation of Robust Flux Observer Field Orientation (FOFO) Controller for Induction Machines, *Conference Record of 1989 IEEE IAS Annual Meeting*, pp. 523-528, San Diego, CA, USA.
- Jaderko, A. (1992) : Simulation of the Induction Motor with Iron Losses, *International Conference on Electrical Drives and Power Electronics*, pp. 384-387, Kosice, CSFR.
- Joensson, R. (1989) : Measurements on a New AC Induction Motor Control System, *Proceedings of the 3rd European Conference on Power Electronics and Applications EPE'89*, pp. 17-22, Aachen, Germany.
- Joetten, R.; Schierling, H. (1983) : Control of the Induction Machine in the Field Weakening Range, *Proceedings of IFAC Symposium on Power Electronics and Electric Drives*, pp. 297-304, Lausanne, Switzerland.
- Karzmierowski, M.P.; Sobczuk, D. (1994) : Improved Neural Network Current Regulator for VS-PWM Inverters, *Proceedings of 1994 IEEE IECON Conference*, pp. 1237-1241, Bologna, Italy.
- Karzmierowski, M.P.; Sulkowski, W. (1986) : Transistor Inverter-Fed Induction Motor Drive with Vector Control System, *Conference Record of 1986 IEEE IAS Annual Meeting*, pp. 162-168, Denver, CO, USA.
- Khater, F.M.H.; Lorenz, R.D.; Novotny, D.W.; Tang, K. (1987) : Selection of Flux Level in Field-Oriented Induction Machine Controllers with Consideration of Magnetic Saturation Effects, *IEEE Transactions on Industry Applications*, Vol. IA-23, No. 2, pp. 277-282.
- Kim, S.H.; Sul, S.K. (1997) : Voltage Control Strategy for Maximum Torque Operation of an Induction Machine in the Field-Weakening Region, *IEEE Transactions on Industrial Electronics*, Vol. 44, No. 4, pp. 512-518.
- Kirschen, D.S.; Novotny, D.W.; Lipo, T.A. (1987) : Optimal Efficiency Control of an Induction Motor Drive, *IEEE Transactions on Energy Conversion*, Vol. EC-2, No. 1, pp. 70-76.
- Klaes, N.R. (1991) : Parameter Identification of an Induction Machine with Regard to Dependencies on Saturation, *Conference Record of 1991 IEEE IAS Annual Meeting*, pp. 21-27, Dearborn, MI, USA.
- Krause, P.C. (1986) : *Analysis of Electric Machinery*, McGraw-Hill Inc.
- Krishnan, R.; Pillay, P. (1986) : Sensitivity Analysis and Comparison of Parameter Compensation Schemes in Vector Controlled Induction Motor Drives, *Conference Record of 1986 IEEE IAS Annual Meeting*, pp. 155-161, Denver, CO, USA.

- Krishnan, R.; Bharadwaj, A.S. (1991) : A Review of Parameter Sensitivity and Adaptation in Indirect Vector Controlled Induction Motor Drive Systems, *IEEE Transactions on Power Electronics*, Vol. 6, No. 4 pp. 695-704.
- Kubota, H.; Matsuse, K. (1992) : Compensation for Core Loss of Adaptive Flux Observer-Based Field-Oriented Induction Motor Drives, *Proceedings of 1992 IEEE IECON Conference*, pp. 67-71, San Diego, CA, USA.
- Kubota, H.; Matsuse, K. (1994) : Speed Sensorless Field-Oriented Control of Induction Motor with Rotor Resistance Adaptation, *IEEE Transactions on Industry Applications*, Vol. 30, No. 5 pp. 1219-1224.
- Kwon, W.H.; Lee, C.H.; Youn, K.S.; Cho, G.H. (1994) : Measurement of Rotor Time Constant Taking Into Account Magnetising Flux in the Induction Motor, *Conference Record of 1994 IEEE IAS Annual Meeting*, pp. 88-92, Denver, CO, USA.
- Lee, C.K.; Pang, W.H. (1994) : Rule-based Adaptive Control in a Servomotor Control System, *CONTROL '94, IEE Conference Publication No. 389*, pp. 1088-1093, Warwick, UK.
- Le-Huy, H. (1994) : Microprocessors and Digital IC's for Motion Control, *Proceedings of the IEEE*, Vol. 82, No. 8, pp. 1140-1163.
- Leonhard, W. (1985) : *Control of Electrical Drives*, Springer-Verlag, Berlin.
- Levi, E.; Vukosavic, S.; Vuckovic (1990) : Saturation Compensation Schemes for Vector Controlled Induction Motor Drives, *IEEE Power Electronics Specialist Conference PESC '90*, pp. 591-598, San Antonio, TX, USA.
- Levi, E. (1992) : Method of Magnetising Curve Identification in Vector Controlled Induction Machines, *European Transactions on Electrical Power Engineering ETEP*, Vol. 2, No. 5, pp. 309-314.
- Levi, E.; Vuckovic, V. (1993): Rotor Flux Computation in Saturated Field-Oriented Induction Machines, *Electric Machines and Power Systems*, Vol. 21, No. 6, pp. 741-754.
- Levi, E. (1994a) : Magnetic Saturation in Rotor-Flux-Oriented Induction Motor Drives: Operating Regimes, Consequences and Open-Loop Compensation, *European Transactions on Electrical Power Engineering ETEP*, Vol. 4, No. 4, pp. 277-286.
- Levi, E. (1994b) : Mathematical Models of Field-Oriented Induction Machines Incorporating the Iron Core Loss, *Proceedings of International Conference on Electrical Machines ICEM '94*, Vol. 2, pp. 683-687, Paris, France.
- Levi, E. (1995a) : A Unified Approach to Main Flux Saturation Modelling in D-Q axis Models of Induction Machines, *IEEE Transactions on Energy Conversion*, Vol. 10, No. 3, pp. 455-461.

- Levi, E. (1995b) : Impact of Iron Loss on Behaviour of Vector Controlled Induction Machines, *IEEE Transactions on Industry Applications*, Vol. 31, No. 6, pp. 1287-1296.
- Levi, E. (1995c) : Modelling of Saturated Induction Machines Using Flux Linkages as State Space Variables, *Proceeding of the International Power Engineering Conference IPEC'95*, Vol. 2, pp. 533-538, Singapore.
- Levi, E.; Boglietti, A.; Lazzari, M. (1995a) : Comparative Study of Detuning Effects in Indirect Rotor Flux Oriented Induction Machines due to Iron Core Losses, *Conference Rec. IEEE Power Electronics and Drive Systems PEDS*, pp. 639-644, Singapore.
- Levi, E.; Vuckovic, V.; Sokola, M. (1995b): Rotor Flux Estimation in Vector Controlled Induction Machines Incorporating the Iron Loss Compensation, *Proceedings of the 6th European Conference on Power Electronics and Applications EPE'95*, Vol. 3, pp. 3.997-3.1002, Sevilla, Spain.
- Levi, E.; Krzeminski, Z. (1996) : Main Flux Saturation Modelling in d-q Axis Models of Induction Machines Using Mixed Current-Flux State-Space Models, *European Transactions on Electrical Power Engineering ETEP*, Vol. 6, No. 3, pp. 207-215.
- Levi, E.; Sokola, M.; Boglietti, A.; Pastorelli, M. (1996a) : Iron Loss in Rotor-Flux-Oriented Induction Machines: Identification, Assessment of Detuning, and Compensation, *IEEE Transactions on Power Electronics*, Vol. 11, No. 5, pp. 698-709.
- Levi, E.; Sokola, M.; Boglietti, A.; Pastorelli, M. (1996b) : Iron Loss Identification and Detuning Evaluation in Rotor Flux Oriented Induction Machines, *IEEE Power Electronics Specialist Conference PESC'96*, IEEE Cat. No. 96 CH 35962, pp. 1555-1561, Baveno, Italy.
- Levi, E.; Sokola, M. (1997) : A Novel Saturation Adaptive Rotor Flux Estimator for Rotor Flux Oriented Induction Machines, *Proceedings of the 7th European Conference on Power Electronics and Applications EPE'97*, Vol. 1, pp. 1.518-1.523, Trondheim, Norway.
- Lipo, T.; Chang K.C. (1986) : A New Approach to Flux and Torque-Sensing in Induction Machines, *IEEE Transactions on Industry Applications*, Vol. IA-22, No. 4, pp. 731-737.
- Lorenz, R.D.; Novotny, D.W. (1990) : Saturation Effects in Field-Oriented Induction Machines, *IEEE Transactions on Industry Application*, Vol. 26, No. 2, pp. 283-289.
- Lorenz, R.D.; Lawson, D.B. (1990) : A Simplified Approach to Continuous On-Line Tuning of Field-Oriented Induction Machine Drives, *IEEE Transactions on Industry Applications*, Vol. 26, No. 3, pp. 420-424.
- Nordin, K.B.; Novotny, D.W.; Zinger, D.S. (1985) : The Influence of Motor Parameter Deviations in Feedforward Field Orientation Drive Systems, *IEEE Transactions on Industry Applications*, Vol. IA-21, No. 4, pp. 1009-1015.

- Ohnishi, K.; Matsui, N.; Hori, Y. (1994) : Estimation, Identification, and Sensorless Control in Motion Control System, *Proceedings of the IEEE*, Vol. 82, No. 8, pp. 1253-1265.
- Ojo, O.; Vipin, M.; Bhat, I. (1994) : Steady-State Performance Evaluation of Saturated Field-Oriented Induction Motors, *IEEE Transactions on Industry Application*, Vol. IA-30, No. 6, pp. 1638-1647.
- Pena, R.S.; Asher, G.M. (1993) : Parameter Sensitivity Studies for Induction Motor Parameter Identification Using Extended Kalman Filters, *Proceedings of the 5th European Conference on Power Electronics and Applications EPE'93*, pp. 306-311, Brighton, UK.
- Rasmussen, H.; Knudsen, M.; Tonnes, M. (1996) : Parameter Estimation of Inverter and Motor Model at Standstill using Measured Currents Only, *Conference Record of IEEE International Symposium on Industrial Electronics*, pp. 331-336, Warsaw, Poland.
- Rowan, T.M.; Kerkman, R.J.; Leggate, D. (1991) : A Simple On-Line Adaptation for Indirect Field Orientation of an Induction Machine, *IEEE Transactions on Industry Application*, Vol. IA-27, No. 4, pp. 720-727.
- Ruff, M.; Grotstollen, H. (1994) : A New Self-Commissioning Scheme for an Asynchronous Motor Drive System, *Conference Record of 1994 IEEE IAS Annual Meeting*, pp. 616-623, Denver, CO, USA.
- Ruff, M.; Grotstollen, H. (1996) : Off-line Identification of the Electrical Parameters of an Industrial Servo Drive Systems, *Conference Record of 1996 IEEE IAS Annual Meeting*, pp. 213-220, San Diego, CA, USA.
- Saitoh, T.; Okuyama, T.; Matsui, T. (1989) : An Automated Secondary Resistance Identification Scheme in Vector Controlled Induction Motor Drives, *Conference Record of 1989 IEEE IAS Annual Meeting*, pp. 594-600, San Diego, USA.
- Sangwongwanich, S.; Ishida, M.; Okuma, S.; Iwata, K. (1988): Manipulation of Rotor Flux for Time-Optimal Single-Step Velocity Response of Field-Oriented Induction Machines, *IEEE Transactions on Industry Application*, Vol. IA-24, No. 2, pp. 262-270.
- Schierling, H. (1988) : Self-commissioning - a Novel Feature of Modern Inverter-Fed Motor Drives, *IEE Conference on Power Electronics and Variable Speed Drives PEVSD, Conference Pub. No. 219*, pp. 287-290, London, UK.
- Sen, P.C. (1989) : *Principles of Electric Machines and Power Electronics*, John Willey & Sons Inc., NY, USA.
- Sharaf, A.M.; Rufer, A.C.; Brientini, L. (1989) : A FAM Voltage Controller for Asynchronous Motor Drives, *Proceedings of the 3rd European Conference on Power Electronics and Applications EPE'89*, pp. 511-514, Aachen, Germany.

- Seibel, B.J.; Rowan, T.M.; Kerkman, R.J. (1997) : Field-Oriented Control of an Induction Motor in the Field-Weakening Region with DC-link and Load Disturbance Rejection, , *IEEE Transactions on Industry Applications*, Vol. 33, No. 6, pp. 1578-1584.
- Simões, M.G.; Bose, B.K. (1995) : Neural Network Based Estimation of Feedback Signals for a Vector Controlled Induction Motor Drive, *IEEE Transactions on Industry Applications*, Vol. 31, No. 3, pp. 620-629.
- Sivakumar, S.; Sharaf, A.M.; Natarajan, K. (1986) : Improving the Performance of Indirect Field Orientation Schemes for Induction Motor Drives, *Conference Record of 1986 IEEE IAS Annual Meeting*, pp. 147-154, Denver, CO, USA.
- Slemon, G.R. (1992) : *Electric Machines and Drives*, Addison-Wesley Inc., Reading, MA.
- Slemon, G.R. (1994) : Electrical Machines for Variable-Frequency Drives, *Proceedings of the IEEE*, Vol. 82, No. 8, pp. 1123-1139.
- Slemon, G.R. (1996) : Modelling of Highly-Saturated Induction Machines for High-Torque Vector Control, *Proceedings of International Conference on Electrical Machines IECM'96*, Vol. 3, pp. 91-96, Vigo, Spain.
- Sokola, M.; Levi, E.; Boglietti, A.; Pastorelli, M. (1995) : Detuned Operation of Rotor Flux Oriented Induction Machines in the Field-Weakening Region due to Iron Loss, *IEE Colloquium on Vector Control and Direct Torque Control of Induction Motors*, pp. 4/1-4/6, London, UK.
- Sokola, M.; Levi, E. (1996) : Combined Impact of Iron Loss and Main Flux Saturation on Operation of Vector Controlled Induction Machines, *IEE International Conference on Power Electronics and Variable Speed Drives PEVD'96*, IEE Conf. Pub. No. 429, pp. 36-41, 1996, Nottingham, UK.
- Sokola, M.; Levi, E.; Jamieson, G.; Williams, D. (1996) : Representation and Compensation of Iron Loss in Rotor Flux Oriented Induction Machines, *IEEE International Conference on Power Electronics, Drives and Energy Systems for Industrial Growth PEDES*, IEEE Cat. No. 96 TH 8111, Vol. 1, pp. 243-249, New Delhi, India.
- Sokola, M.; Levi, E.; Williams, D. (1997) : Comparative Analysis of Parameter Variation Effects in Vector-Controlled Induction Machines, *Universities Power Engineering Conference UPEC'97*, Vol. 2, pp. 1003-1006, Manchester, UK.
- Sousa, G.C.D.; Bose, B.K.; Kim, K.S. (1993) : Fuzzy Logic Based On-line Tuning of Slip Gain for an Indirect Vector Controlled Induction Motor Drive, *Proceedings of the 1993 IEEE IECON Conference*, pp. 1003-1008, Maui, Hawaii, USA.
- Sousa, G.C.D.; Bose, B.K. (1993) : Fuzzy Logic Based On-line Efficiency Optimization Control of an Indirect Vector Controlled Induction Motor Drive, *Proceedings of the 1993 IEEE IECON Conference*, pp. 1168-1174, Maui, Hawaii, USA.

- Stemmler, H. (1994) : High-Power Industrial Drives, *Proceedings of the IEEE*, Vol. 82, No. 8, pp. 1266-1286.
- Stankovic, A.; Benedict, E.R.; John, V.; Lipo, T.A. (1997) : A Novel Method for Measuring Induction Machine Magnetizing Inductance, *Conference Record of 1997 IEEE IAS Annual Meeting*, pp. 234-238, New Orleans, LA, USA.
- Stoll, R.L. (1974) : *The Analysis of Eddy Currents*, Clarendon Press, Oxford.
- Sul, S.K. (1989) : A Novel Technique of Rotor Resistance Estimation Considering Variation of Mutual Inductance, *IEEE Transactions on Industry Applications*, Vol. 25, No. 4, pp. 578-587.
- Sullivan, C.R.; Sanders, S.R. (1995) : Models for Induction Machines with Magnetic Saturation of the Main Flux Path, *IEEE Transactions on Industry Applications*, Vol. 31, No. 4, pp. 907-917.
- Sullivan, C.R.; Kao, C.; Acher, B.M.; Sanders, S.R. (1996) : Control Systems for Induction Machines with Magnetic Saturation, *IEEE Transactions on Industrial Electronics*, Vol. IE-43, No. 1, pp. 142-152.
- Sumner, M.; Asher, G.M.; Pena, R. (1993) : The Experimental Investigation of Rotor Time Constant for Vector Controlled Induction Machine Drives During Transient Operating Conditions, *Proceedings of the 5th European Conference on Power Electronics and Applications EPE'93*, pp. 51-56, Brighton, UK.
- Takahashi, I.; Noguchi, T. (1986) : A New Quick-Response and High-Efficiency Control Strategy of an Induction Motor, *IEEE Transactions on Industry Applications*, Vol. IA-22, No. 5, pp. 820-827.
- Textronix (1992) : *User Manual - AM 503S Current Probe System*
- Tiitonen, P.; Pohjalainen, P.; Lalu, J. (1995) : The Next Generation Motor Control Method: Direct Torque Control (DTC), *EPE Journal*, Vol. 5, No. 1, pp. 14-18.
- Tiitonen, P.; Surandra, M. (1996) : The Next Generation Motor Control Method, DTC Direct Torque Control, *Proceedings of IEEE PEDES Conference*, New Delhi, India, pp. 37-43.
- Toliyat, H.; Arefeen, M.S.; Rahman, K.M.; Ehsani, M. (1995) : Rotor Time Constant Updating Scheme for a Rotor Flux Oriented Induction Motor Drive, *Proceedings of IEEE PESC Conference*, Vol. 2, pp. 1302-1306, Atlanta, GA, USA.
- Trzynadlowski, A.M. (1994) : *The Field Orientation Principle in Control of Induction Motors*, Kluwer Academic Publishers.
- Tungpimolrut, K.; Peng, F.Z.; Fukao, T. (1994) : Robust Vector Control of Induction Motor without Using Stator and Rotor Circuit Time Constants, *IEEE Transactions on Industry Applications*, Vol. 30, No. 5, pp. 1241-1246.

- Umanand, L.; Bhat, S.R. (1994) : Adaptation of the Rotor Time Constant for Variations in Rotor Resistance of an Induction Motor, *Proceedings of IEEE PESC Conference*, Taipei, Taiwan, pp. 738-743.
- Umanand, L.; Bhat, S.R. (1995) : Online Estimation of Stator Resistance of an Induction Motor for Speed Control Applications, *IEE Proceedings - Electrical Power Applications*, Vol. 142, No. 2, pp. 97-103.
- Undeland, T.M.; Mohan, N. (1988) : Overmodulation and Loss Considerations in High-Frequency Modulated Transistorised Induction Motor Drives, *IEEE Transactions on Power Electronics*, Vol. 3, No. 4, pp. 447-452.
- Vas, P.; Alakula, M. (1990) : Field-Oriented Control of Saturated Induction Machine, *IEEE Transactions on Energy Conversion*, Vol. 5, No. 1, pp. 218-224.
- Vas, P. (1990) : *Vector Control of AC Machines*, Clarendon Press, Oxford, UK.
- Vas, P. (1992) : *Electrical Machines and Drives - A Space-Vector Theory Approach*, Clarendon Press, Oxford, UK.
- Vas, P. (1993) : *Parameter Estimation, Condition Monitoring and Diagnosis of Electrical Machines*, Oxford University Press, Oxford, UK.
- Vas, P.; Stronach, A.F.; Neuroth, M. (1995) : DSP-Controlled Intelligent High-Performance AC Drives - Present and Future, *IEE Colloquium on Vector Control and Direct Torque Control of Induction Motors*, London, pp. 7/1-7/8.
- Vergheze, G.C.; Sanders, S.R. (1988) : Observers for Flux Estimation in Induction Machines, *IEEE Transactions on Industrial Electronics*, Vol. 35, No. 1, pp. 85-94.
- Vickers (1996) : *DBS 04 User Manual*.
- Vuckovic, V. (1992) : *General Theory of Electrical Machines* (in Serbian), Nauka, Belgrade, Yugoslavia.
- Vukosavic, S.N.; Stojic, M.R. (1993) : On-Line Tuning of the Rotor Time Constant for Vector-Controlled Induction Motor in Position Control Applications, *IEEE Transactions on Industrial Electronics*, Vol. IE-40, No. 1, pp. 130-138.
- Wade, S.; Dunnigan, M.W.; Williams, B.W (1995) : Improvements for Induction Machine Vector Control, *Proceedings of the 6th European Conference on Power Electronics and Applications EPE'95*, Vol. 1, pp. 1.542-1.546, Sevilla, Spain.
- Wade, S.; Dunnigan, M.W.; Williams, B.W (1997) : A New Method of Rotor Resistance Estimation for Vector-Controlled Induction Machines, *IEEE Transactions on Industrial Electronics*, Vol. 44, No. 2, pp. 247-257.
- Wallace, I.T.; Novotny, D.W.; Lorenz, R.D.; Divan, D.M. (1994): Verification of Enhanced Dynamic Torque per Ampere Capability in Saturated Induction Machines, *IEEE Transactions on Industry Applications*, Vol. IA-30, No. 5, pp. 1193-1200.

- Wieser, R.S. (1997) : Optimal Rotor Flux Regulation for Fast Acceleration Induction Machines in the Field Weakening Region, *Conference Record of 1997 IEEE IAS Annual Meeting*, pp. 401-409, New Orleans, LA, USA.
- Williamson, S.; Healey, R.C. (1996) : Space Vector Representation of Advanced Motor Models for Vector Controlled Induction Motors, *IEE Proceedings - Electrical Power Applications*, Vol. 143, No. 1, pp. 69-77.
- van Wyk, J.D. (1994) : Power Electronic Converters for Motion Control, *Proceedings of the IEEE*, Vol. 82, No. 8, pp. 1164-1193.
- Xu, L.; Xu, X.; Lipo, T.A.; Novotny, D.W. (1991) : Vector Control of a Synchronous Reluctance Motor Including Saturation and Iron Loss, *IEEE Transactions on Industry Applications*, Vol. 27, No. 5, pp. 977-985.
- Yamamura, S. (1986) : *AC Motors for High-Performance Applications - analysis and Control*, Marcel Denner Inc., New York.

APPENDIX A : DATA OF INDUCTION MACHINES**A1 : 4 kW motor :**

4 kW 380 V 8.7 A 1440 rpm

50 Hz stator winding star connected

$R_s = 1.37 \Omega$ $R_r = 1.1 \Omega$ $X_{ls} = 1.53 \Omega$ $X_{lr} = 2.5 \Omega$

$X_{mn} = 44.3 \Omega$ $T_{en} = 1.37 \text{ Nm}$ $P_{Fen} = 194 \text{ W}$ $R_{Fen} = 699 \Omega$

Magnetising curve approximation (in terms of rms values) :

$L_m = 0.1964285 \text{ H}$ for $\psi_m < 0.432 \text{ Wb}$

$L_m = 0.8032 - 0.6087\psi_m - \frac{0.1338}{\psi_m} \text{ (H)}$ for $\psi_m > 0.432 \text{ Wb}$

Iron loss resistance approximation :

$R_{Fe} = 128.92 + 8.242f + 0.7788f^2 \text{ } (\Omega)$ for $f < 50 \text{ Hz}$

$R_{Fe} = 1841 - \frac{55272}{f} \text{ } (\Omega)$ for $f < 50 \text{ Hz}$

A2 : 0.75 kW motor :

0.75 kW 380 V 2.1 A 1390 rpm

50 Hz stator winding star connected

$R_s = 10 \Omega$ $R_r = 6.3 \Omega$ $L_{ls} = 43 \text{ mH}$ $L_{lr} = 40 \text{ mH}$

Magnetising curve and the mutual inductance represented by :

$$\begin{aligned} \psi_m &= 0.86427 \cdot 0.59976 I_m^{1.1211} \\ L_m &= 0.86427 \cdot 0.59976 I_m^{0.1211} && \text{for } I_m \leq 1.95 \text{ A} \\ L &= 0.86427 \cdot 0.59976 I_m^{1.1211} \cdot (1.121 \cdot I_m^{0.1211} - 0.511226 \cdot I_m^{1.1211}) \end{aligned}$$

$$\psi_m = 0.043I_m + 0.5902$$

$$L_m = 0.043 + \frac{0.5902}{I_m} \quad \text{for } I_m > 1.95 \text{ A}$$

$$L = 0.043$$

A3 : 2.3 kW motor :

2.3 kW 380 V 10 A 1450 rpm

50 Hz

$R_s = 0.7 \Omega$ $R_r = 0.926 \Omega$ $L_{ls} + L_{lr} = 7.723 \text{ mH}$

$P_{Fe n} = 60 \text{ W}$ $R_{mech n} = 12 \text{ W}$

For the base d -axis stator current of $i_{d \text{ BASE}} = 4.15 \text{ A}$, and the rated magnetising flux of $\psi_{m \text{ BASE}} = 0.33 \text{ Wb}$, the inverse magnetising curve is :

$$i_{m(pu)} = 0.9\psi_{m(pu)} + 0.1\psi_{m(pu)}^7 .$$

APPENDIX B : PUBLISHED PAPERS**Journal papers :**

- Levi, E.; Sokola, M.; Boglietti, A.; Pastorelli, M. (1996) : Iron Loss in Rotor-Flux-Oriented Induction Machines: Identification, Assessment of Detuning, and Compensation, *IEEE Transactions on Power Electronics*, Vol. 11, No. 5, pp. 698-709.
- Levi, E.; Sokola, M.; Vukosavic, S.N. : A Method for Magnetising Curve Identification in Rotor Flux Oriented Induction Machines, submitted for publishing in the *IEEE Transactions on Energy Conversion* .

Conference papers :

- Sokola, M.; Levi, E.; Boglietti, A.; Pastorelli, M. (1995) : Detuned Operation of Rotor Flux Oriented Induction Machines in the Field-Weakening Region due to Iron Loss, *IEE Colloquium on Vector Control and Direct Torque Control of Induction Motors*, pp. 4/1-4/6, London, UK.
- Levi, E.; Vuckovic, V.; Sokola, M. (1995): Rotor Flux Estimation in Vector Controlled Induction Machines Incorporating the Iron Loss Compensation, *Proceedings of the 6th European Conference on Power Electronics and Applications EPE'95*, Vol. 3, pp. 3.997-3.1002, Sevilla, Spain.
- Levi, E.; Sokola, M.; Boglietti, A.; Pastorelli, M. (1996) : Iron Loss Identification and Detuning Evaluation in Rotor Flux Oriented Induction Machines, *IEEE Power Electronics Specialist Conference PESC'96*, IEEE Cat. No. 96 CH 35962, pp. 1555-1561, Baveno, Italy.
- Sokola, M.; Levi, E. (1996) : Combined Impact of Iron Loss and Main Flux Saturation on Operation of Vector Controlled Induction Machines, *IEE International Conference on Power Electronics and Variable Speed Drives PEVD'96*, IEE Conf. Pub. No. 429, pp. 36-41, 1996, Nottingham, UK.
- Sokola, M.; Levi, E.; Jamieson, G.; Williams, D. (1996) : Representation and Compensation of Iron Loss in Rotor Flux Oriented Induction Machines, *IEEE International Conference on Power Electronics, Drives and Energy Systems for Industrial Growth PEDES*, IEEE Cat. No. 96 TH 8111, Vol. 1, pp. 243-249, New Delhi, India.
- Sokola, M.; Levi, E.; Williams, D. (1997) : Comparative Analysis of Parameter Variation Effects in Vector-Controlled Induction Machines, *Universities Power Engineering Conference UPEC'97*, Vol. 2, pp. 1003-1006, Manchester, UK
- Levi, E.; Sokola, M. (1997) : A Novel Saturation Adaptive Rotor Flux Estimator for Rotor Flux Oriented Induction Machines, *Proceedings of the 7th European Conference on Power Electronics and Applications EPE'97*, Vol. 1, pp. 1.518-1.523, Trondheim, Norway.

PAGE/PAGES
EXCLUDED
UNDER
INSTRUCTION
FROM
UNIVERSITY